Earthquake Source Properties *in the* Hellenic *and* Aleutian Islands Subduction Zones

Fotini Liakopoulou

B.Sc. (Hon), University of Thessaloniki, Greece.

Thesis submitted for the Degree of

Doctor of Philosophy,

University of Edinburgh,

April, 1992.

Στους γονεις μου

ABSTRACT

This thesis provides information on earthquake source properties for recent, moderate-sized ($5.5 < m_b < 6.5$) earthquakes in the Hellenic and Aleutian subduction zones. This is achieved through the analysis of teleseismic observations from the Global Digital Seismograph Network.

The relative amplitude method of Pearce and Rogers is used to determine source orientations for all events studied, placing constraints on fault plane solutions typically to better than 5° in angle. This method is able to compute well-constrained solutions even when *P*-wave first motion polarity cannot be read unambiguously, because it includes polarity and amplitude information for phases other than direct *P*. Body-wave modelling is carried out to determine other earthquake source parameters including depth, seismic moment, seismic source dimensions, rupture velocity and stress drop. Broadband seismograms (recovered from short-period records) are used because they give a more complete representation of the source radiation for moderate-sized earthquakes than do conventional short- or long-period records. A two-dimensional finite dislocation model is used in the calculation of the synthetic seismograms. This model gives a more realistic representation of the earthquake source than does the point-source model. A plane-layer velocity structure both at the source and the receiver areas is assumed.

Seven earthquakes associated with the Hellenic subduction zone are studied. Thrust components are present in the solutions for most events, in agreement with the overall compressional stress regime of the subduction zone. However, strike-slip components are found in events associated with transform faults identified by geological, morphological and seismic data. Forward body-wave modelling is carried out for three of these events.

Seven earthquakes associated with the Aleutian Islands subduction zone are also studied. Most are found to have thrust mechanisms and fault strikes consistent with coupling of the lithospheric plates. One earthquake occurred in the oceanic crust beneath the trench, and is characterized by normal faulting with the tensional axis perpendicular to the arc. Solutions for other events are found to include a strike-slip component, consistent with local variations in deformation (e.g. adjacent to the Amlia fracture zone). One earthquake was situated within the upper part of the double Benioff zone beneath the Kamchatka peninsula. The down-dip direction of compression suggested by the orientation of the *P*-axis for this event is consistent with unbending stresses in the upper half of the subducting lithosphere. Body-wave modelling is carried out for five of these events.

In both regions, focal depths are determined from the time difference between the *pP* and *P* phases where possible, or from body-wave modelling, and are well constrained (to within $\pm$ 2 km). Sources are assumed to be circular or elliptical, and radii are found to

vary from 2.5 to 12 km according to body-wave magnitude. The rupture velocities obtained (2.1 - 4.5 km s^{-1}) lie toward the upper limit imposed by the shear wave velocity. All events have typical stress drops for interplate earthquakes (~ 30 bar), except one event at a depth of approximately 184 km within the subducting plate which has a higher stress drop, and which can be characterized as an intraplate earthquake. Source finiteness is observed for most events, and this allows the discrimination between fault and auxiliary planes. Seismic moment generally increases with earthquake size and source dimensions.

A significant difference identified between the two arcs is in the relationship of the calculated seismic moments to moments published using the centroid-moment tensor (CMT) method of Dziewonski, Chou and Woodhouse. For the Hellenic arc earthquakes, moments determined here are systematically lower than those of the CMT method, whereas for the Aleutian arc events the two moments are similar. It is concluded that this is probably associated with the predominance of oceanic as distinct from continental body-wave raypaths from the Aleutian arc.

ACKNOWLEDGEMENTS

I am greatly indebted to my supervisors Dr. R. G. Pearce and Dr. I. G. Main for their continued guidance, encouragement and expert advice throughout my time in Edinburgh. I thank Prof. G. S. Boulton and Prof. K. M. Creer for kindly making the facilities of the Department of Geology and Geophysics available to me.

I am also grateful to Prof. B. C. Papazachos of the Aristotle University of Thessaloniki for encouraging me to continue my studies in the field of seismology, and for acting as my supervisor for the Greek State Scholarships Foundation (I. K. Y.). My thanks go to I. K. Y. for providing financial support for this project.

This project has benefited from the help and advice of many people, including: Dr. P. Burton (U. E. A., Norwich), Dr. S. Das (Oxford), Dr. B. Dost (ORFEUS, Utrecht), Prof. A. Douglas (M. O. D., Blacknest), R. Sleeman (ORFEUS, Utrecht), Dr. I. Stimpson (Keele), and J. Young (M. O. D., Blacknest). Special thanks go to Rachel Abercrombie (University of S. California) for many fruitful and encouraging discussions. I am also grateful to the other staff and students of the department, both past and present, for all their help during the course of this project and for making my stay in Edinburgh so enjoyable. My thanks must also go to Mrs. Helen McKeating always being willing to help (even on a Friday afternoon!), and to the other secretarial staff for their help.

My studies in Edinburgh would not have been so pleasant without the friendship and support of Prof. and Mrs. Creer.

I would like to thank my parents for their love and continuous support. Special thanks go to my brother, George, especially for those long waiting hours at Athens airport!

Last, but not least, I would like to thank Tony for his love and support, proof reading and putting up with me while I was writing up.

CONTENTS

CHAPTER 1

INTRODUCTION

1.1 INTRODUCTION

Recent years have seen a substantial increase in the number of studies of earthquake source characteristics and seismic radiation. This has been due to a number of factors. For example, modern arrays of sophisticated instruments have become operational and record data both in the local and teleseismic ranges, computer programs able to analyse large amounts of data have become available, and methods of inversion of complex datasets and detailed models of fault slip have been developed. These developments would be expected to lead to a significant decrease in uncertainties about seismic sources. However, this does not appear to be universally the case and several questions remain unanswered. New theories and models of earthquake rupture have been introduced, but the available data and analyses do not always seem to be able to distinguish between the various models with confidence. Complex or multiple sources have been suggested for many earthquakes. However, is it true that simple ruptures are really exceptional? Moreover, how can we distinguish between source complexity and path effects? Are the mechanisms of faulting always associated with the tectonic environment in which the earthquakes occur? If we assume that the source is simple, can we reproduce the observed far-field pulse? What other factors affecting the synthetic pulse should we consider? How much does the source velocity structure affect the results? Is our determination of the triggering mechanism in agreement with the observations on the seismograms?

These questions are of great importance when studying earthquake rupture dynamics and can only be answered by detailed studies of individually selected earthquakes. In this thesis, teleseismically recorded moderate-sized earthquakes from two subduction zones (the Hellenic and the Aleutian Islands arcs) have been selected for detailed study. In addition to using conventional short- and long-period seismograms, broadband records are used. These provide a better representation of the seismic source and can therefore lead to an improved understanding of the earthquake rupture process.

1.2 OBJECTIVES OF THIS STUDY

The availability of worldwide digital seismic data (much of it broadband) offers an opportunity to apply quantitative seismological methods to regional earthquake source

mechanisms and problems in geodynamics. The Hellenic subduction zone is a region of both compressional and extensional continental deformation, and offers a suitable location for investigating several problems which have previously been addressed using analogue seismic data and qualitative seismological methods. Additionally, a study of earthquakes from a similar tectonic environment, such as the Aleutian Islands subduction zone, enables a comparison to made between results obtained using the same methods but from different regions.

The main aims of this study are:

1. To put tight constraints on the focal mechanisms of recent moderate-sized earthquakes from the subduction zones mentioned above, using the relative amplitude method.

2. To compare the results with those obtained using classical (e.g. first motion) and whole waveform inversion methods.

3. To carry out forward body-wave modelling using broadband data in order to determine other source parameters, including seismic moment and rupture geometry.

4. To use simple source models in order to reproduce the far-field *P*-wave pulse and to test the reliability of such models.

5. To compare results from the two study areas and to interpret them in terms of the tectonic environment in which the earthquakes occurred.

1.3 CHARACTERISTICS OF SUBDUCTION ZONE EARTHQUAKES

Most of the global seismic moment release (Fig. 1.01) occurs at subduction zones. The major seismic moment release at subduction zones occurs at the frictional interface between the subducting plate and the overriding plate. This is not strictly a fault, since the two sides were not formed by brittle fracture and modified by continued shear. Instead, as the schematic diagram of Fig. 1.02 (Byrne *et al.*, 1988) shows, one side, which consists of sediment-covered sea floor, is being introduced continuously into the system. The frictional behaviour of the interface affects the degree of subduction and the extent to which subducted material is consolidated and metamorphosed. Furthermore, because of the nearby presence of the subducting slab, major plate-driving forces also affect the stresses on the interface. The variability of the above factors may be important causes of the greater range in seismic behaviour within subduction zones compared to crustal fault zones.

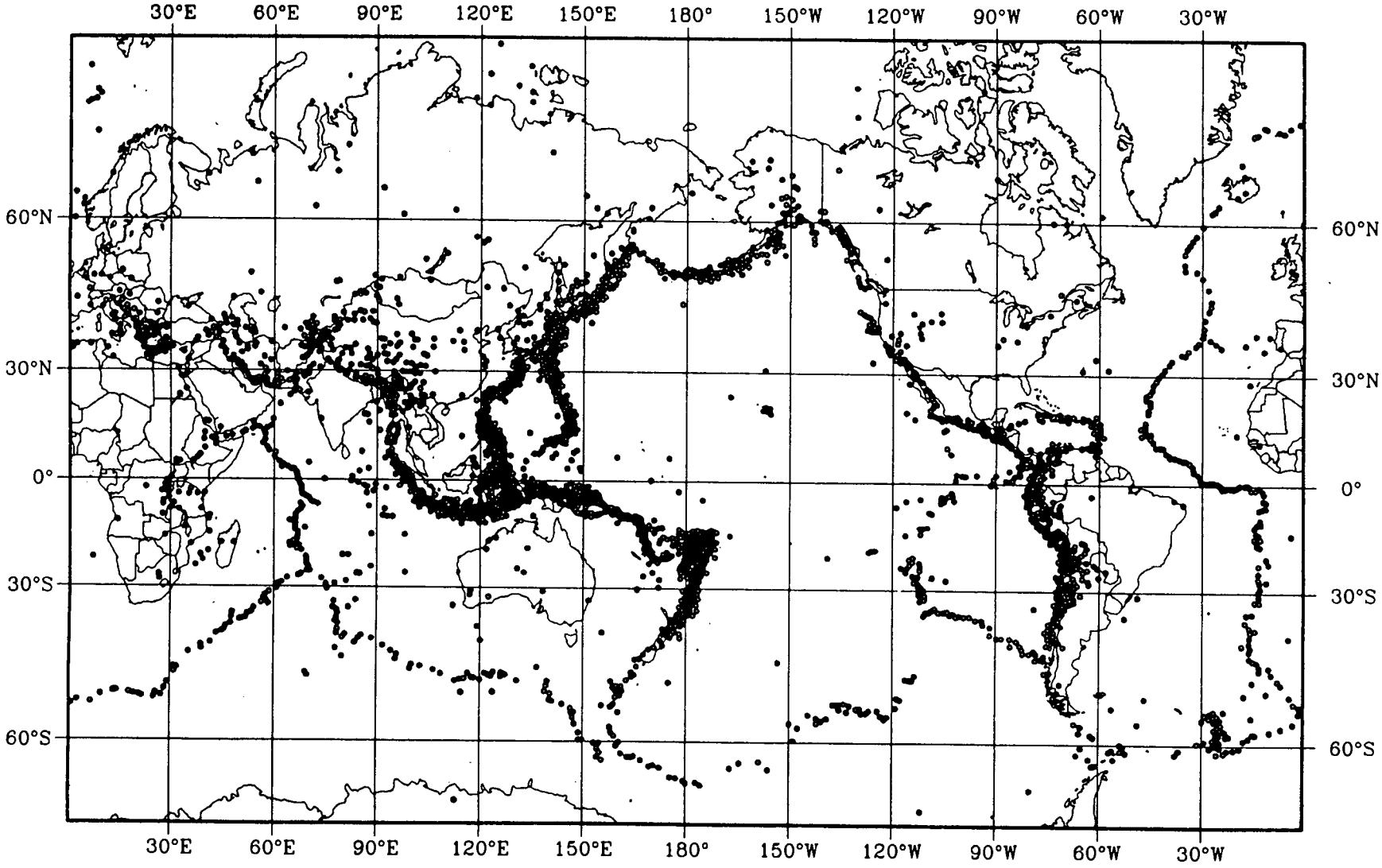

Figure 1.01. Global seismicity. Earthquakes with magnitudes $\geq$ 5.0 for the time period 1980 - 1990. (U. S. Geological Survey, NEIC, 1990).

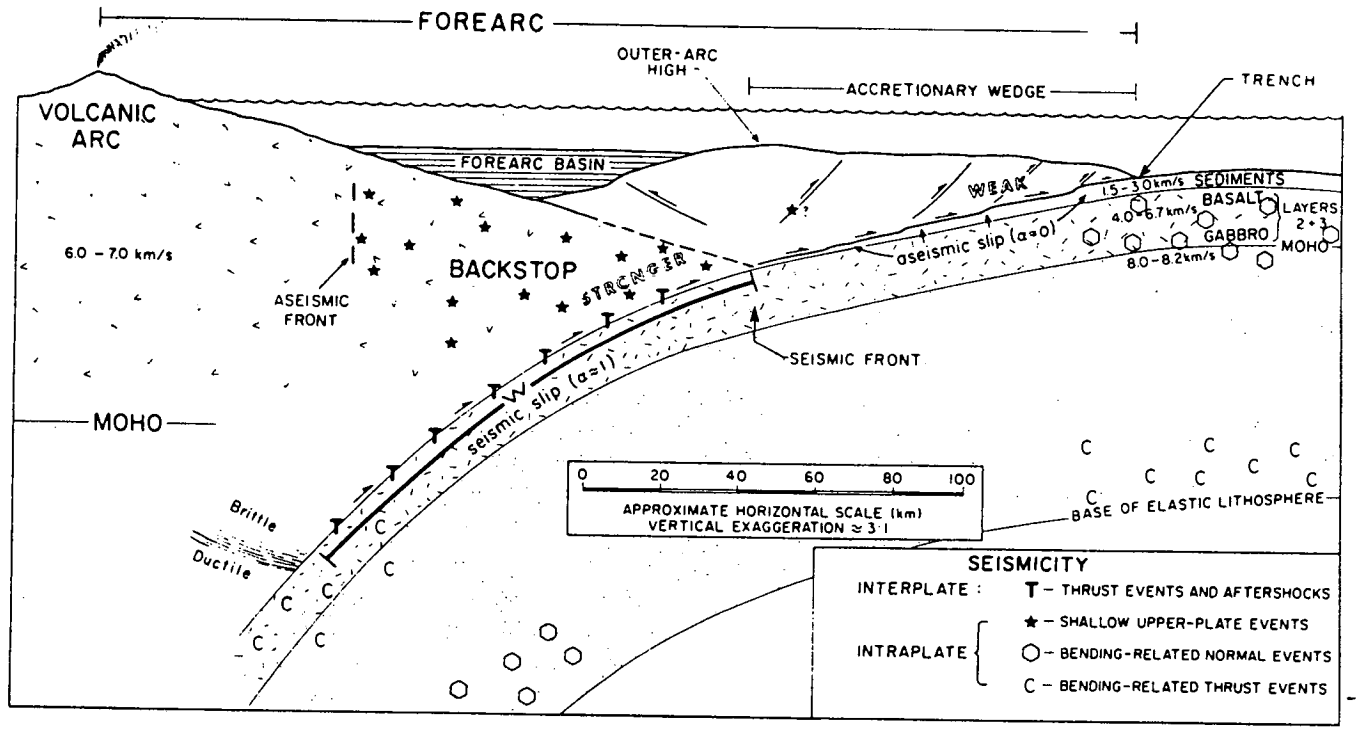

Figure 1.02. Schematic cross section of a subduction zone. Major features are named, a schematic distribution of earthquakes is shown, and some representative *P*-wave velocities are given (from Byrne *et al.*, 1988).

The typical seismicity of subduction zones is shown in Fig. 1.02. The principal moment release occurs by thrusting along the plate interface during great earthquakes. The rupture of such earthquakes apparently does not propagate all the way to the surface and the trench but terminates within the accretionary wedge (Byrne *et al.*, 1988). This is a sedimentary wedge of variable width that has been built up predominantly by scraping of sediments off the subducting sea floor. The down-dip termination of rupture in these earthquakes occurs at depths that vary between 40 and 60 km. Because the dip of the interface is often shallow, the down-dip width of rupture in subduction zones may be very large, often in excess of 200 km. This factor along with their great total length, explains why subduction zones account for the major portion of the world's moment release. This zone of seismicity is called the *main thrust zone* in the present study.

Minor seismicity occurs in both the upper and lower plates. In the upper plate it is confined to an area between the *aseismic front* (Yoshii, 1979), which is a sharp cut-off in seismicity some distance in front of the volcanic arc, and the beginning of the accretionary wedge, which is also aseismic (Engdahl, 1977; Chen *et al.*, 1982; Byrne *et al.*, 1988; Fig. 1.02). Lower plate seismicity results from lithospheric bending of the descending slab and occurs close to the axis of maximum bending. This typically occurs at the outer trench wall and well back from it, but in some cases it might persist further, towards the arc. At greater depth the lower plate earthquakes merge into the Benioff zone, which may extend to depths as great as 650 km. These intermediate- and deep-focus earthquakes reflect internal stresses in the downgoing slab. They exhibit double-couple focal mechanisms and therefore could be analysed by standard seismotectonic techniques. However, they probably do not arise from the type of frictional instability which causes crustal earthquakes because of the very high pressures at those depths. A possible mechanism is a solid-solid phase transition involving pure shear (e.g. Kirby, 1987; Green and Barnley, 1989), or a propagating plantic instability (Hobbs and Ord, 1988).

There is a variety of subduction zone types whose end members have been defined by Uyeda (1982) as the *Chilean* type and the *Mariana* type (Fig. 1.03). The *Chilean* type, which is highly compressional, is characterised by a pronounced *outer rise*, abundant calc-alkaline volcanism, a shallow dipping *Benioff* zone, and great earthquakes along the interface (*main thrust zone*). In contrast, the *Mariana* type is extensional, has back-arc spreading, little or no *outer rise*, few andesites in the arc, a steeply dipping *Benioff* zone, and no great earthquakes. The Hellenic and Aleutian subduction zones, which are studied in the present thesis, are more closely represented by the *Chilean* type. However, it should be noted that back-arc spreading is observed in the Hellenic subduction zone.

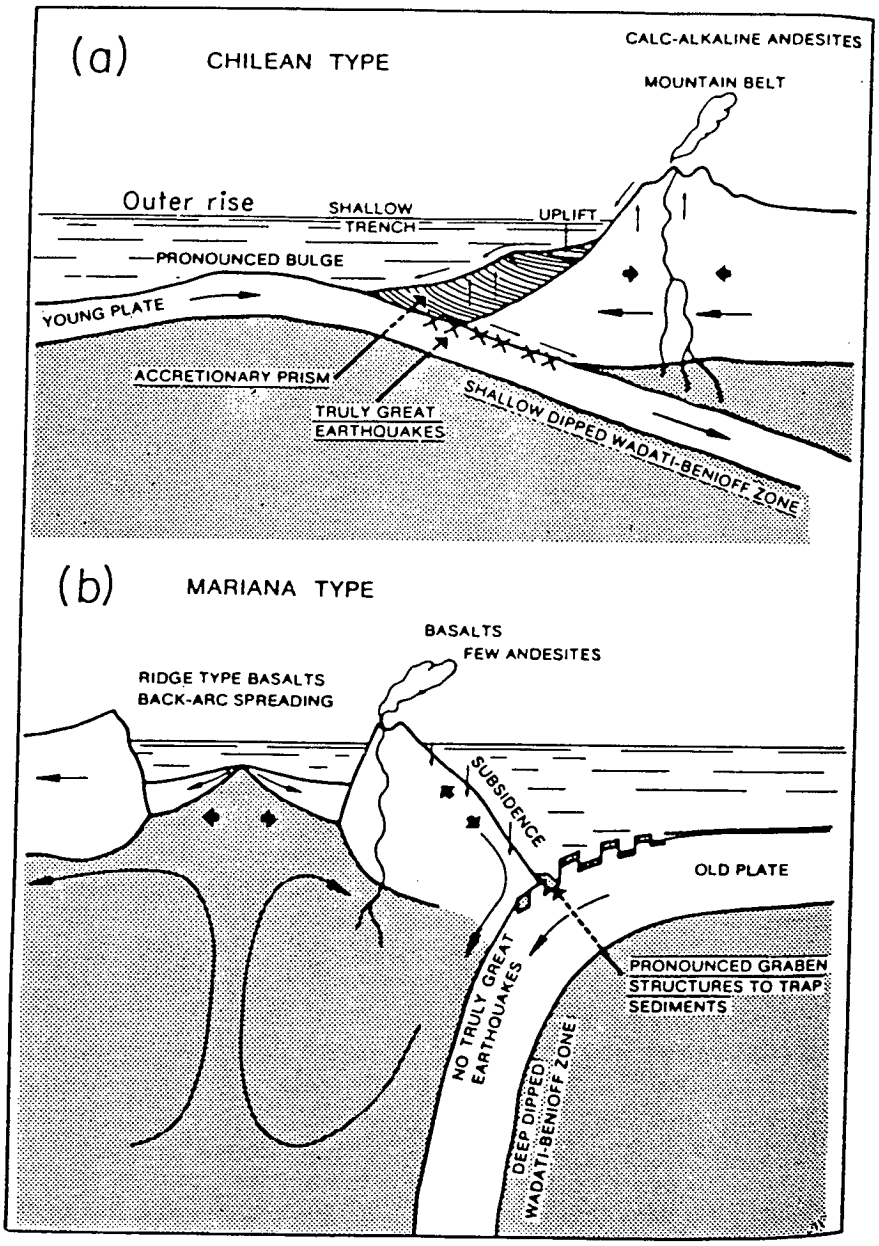

Figure 1.03. Schematic diagram showing the two end members of subduction zone types: a) Chilean type, highly compressional; b) Mariana type, highly extensional. (After Uyeda, 1982).

1.4 LAYOUT OF THESIS

This thesis is divided into four sections. Chapter 2 describes the data and the processing and modelling techniques used, and forms the remainder of the introductory section.

Chapters 3 and 4 deal with the Hellenic subduction zone. Chapter 3 gives a review of the neotectonic setting and seismicity of the region, and Chapter 4 presents the source parameters determined for the earthquakes studied.

The neotectonic characteristics and seismicity of the Aleutian subduction zone are reviewed in Chapter 5. The source parameters obtained for the Aleutian arc earthquakes studied are described in Chapter 6.

Chapter 7 presents a comparison and discussion of the results obtained in the two regions, and finally the overall conclusions of the thesis are presented in Chapter 8.

CHAPTER 2

THEORY AND METHODS

2.1 INTRODUCTION

It was as recently as 1893, when Koto (1893) noted that "it can be confidently asserted that the sudden faulting was the cause (and not the effect) of the earthquake", that it was universally accepted that faults were indeed responsible for earthquakes. One of the most widely accepted explanations of shallow, ground-rupturing earthquakes is Reid's (1911) elastic-rebound theory, which attributes earthquakes to the progressive accumulation of strain energy, followed by faulting when the slip fracture strength is exceeded.

The product of the average slip $\bar{s}$ on a fault plane of area A and rigity μ of the surrounding medium defines the scalar seismic moment:

$$M_0 = \mu A \bar{s} \tag{2.1}$$

Including the orientation of the fault, an earthquake source can be represented by the seismic moment tensor M_{ij}. For a point source in Cartesian coordinates there are three force components and three lever arm directions (Fig. 2.01). The three diagonal elements of the tensor are equivalent to extensions along the orthogonal axes, and the six other elements represent couples. If angular momentum is to be conserved M_{ij} must be symmetric. Several types of source mechanism, in addition to the double couple, have been suggested, especially for deep earthquakes and they can be represented by the moment tensor.

The double couple force system associated with shear fracture within a fault plane is a very plausible earthquake mechanism which has been assumed *a priori* in almost all focal mechanism computations made over the last 20 years. Although the body of supporting observational evidence is not so extensive as the success of the double couple might imply, in most cases there is no reason to believe that this model is incorrect (Pearce and Rogers, 1989). In the present study a double couple source mechanism is assumed throughout.

In this chapter, the method used to determine the fault plane orientation of the earthquakes examined is first outlined. A brief description of other existing methods is given and a comparison between them is made. It is now well known that body waves containing a broad spectral bandwidth (broadband) can give a better resolution of the

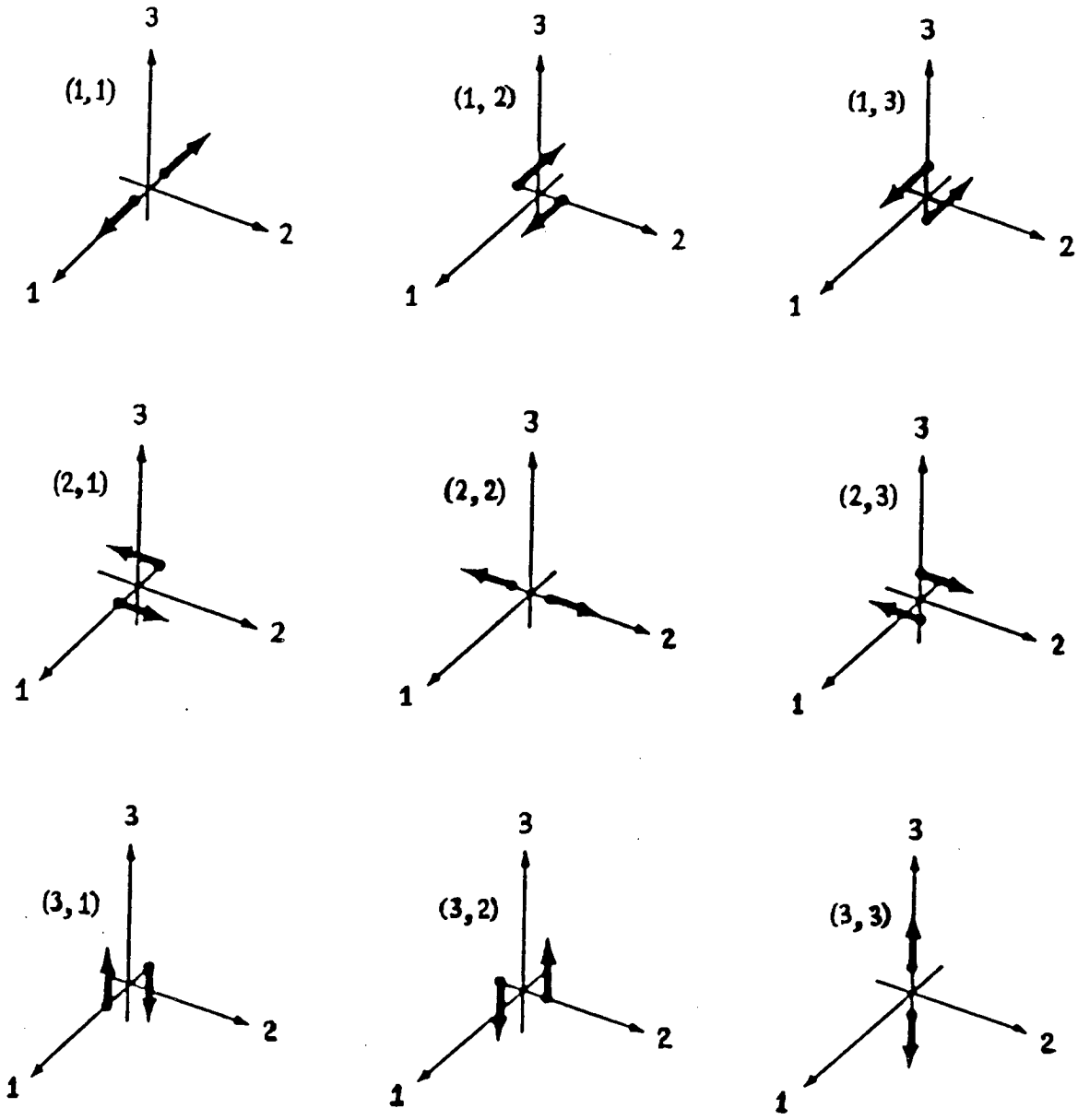

Figure 2.01. The nine possible couples that are required to obtain equivalent forces for a generally oriented displacement discontinuity in an isotropic medium (from Aki & Richards, 1980).

earthquake rupture process than do conventional long-period (20 s) and short-period (1 s) period seismograms (e.g. Choy and Boatwright, 1981, 1982; Choy and Dewey, 1988), despite the microseismic noise at intermediate periods (6 - 8 s). Therefore, the advantages of broadband seismograms over the conventional short-period (SP) and long-period (LP) ones are then discussed, and the standard deconvolution techniques for their retrieval from the conventional SP and LP records are presented. The resulting seismograms are then compared with direct broadband recordings, to verify the validity of the conversion process used in this study. The source parameters, such as magnitude, static seismic moment and stress drop, are discussed and some of the laws governing their relationship are mentioned.

Finally, the two-dimensional kinematic model used in the generation of the synthetic seismograms is described and discussed. The synthetics are used in forward body-wave modelling which is carried out in order to determine the source parameters of the earthquakes. The resolution of the model and the resulting errors in the source parameters are considered.

2.2 SOURCE MECHANISM DETERMINATION

2.2.1 Relative Amplitude Moment Tensor program.

The Relative Amplitude Moment Tensor Program (RAMP) used to calculate the fault plane solutions of the earthquakes presented in this study, is designed to reveal all possible moment tensors for a seismic event (Pearce and Rogers, 1989). This is done by making direct use only of the specific features of the seismogram waveforms which relate to the earthquake radiation pattern, and by minimizing the dependence of the computation upon knowledge of structure and upon effects of the propagation paths. The method is able to test all source types resolvable into three orthogonal dipoles; this includes the pure explosion and source types having an explosive or implosive component.

Its input consists of observations of the relative amplitudes of the phases *P*, *pP*, *sP* and of the three components of direct *S*-waves at a series of teleseismic stations. Each relative amplitude observation takes the form of maximum and minimum permissible amplitudes for a phase and its polarity. Since only relative amplitudes are considered, the amplitude limits may be specified in any units, provided that all phases to be considered together are measured in the same units. These limits are defined to be broad enough so as to cover the effects of noise on the seismogram and possible attenuation of *pP* and *sP* to and from the near surface. The polarity may be specified as positive, negative, or

unknown, or it may be specified as the same as or opposite to the polarity of another observed phase. These amplitude ranges and polarities are converted to equivalent ranges of ratios, which are restored to the appropriate pair of points on the focal sphere, after any correction for amplitude loss by the surface-reflected phases at interfaces above the source (especially the free surface) as described in detail by Pearce (1977, 1980). For each mechanism under test, the theoretical ratio between the amplitudes of each possible pair of the specified phases is calculated, and if it falls within the limits inferred from the measured bounds, then the mechanism is characterized "compatible" with the observations; otherwise it is "incompatible". This operation is repeated for each station at which phases are specified. Those mechanisms compatible with all the phase pairs are considered to be compatible with the dataset.

2.2.2 Source representation

The source is described in terms of the source orientation and its type, which are expressed by separate parameters. The orientation is described by three angles; σ, δ, and ψ (Fig. 2.02). In the case of a double couple mechanism these correspond to the strike, dip and slip angles of the source, respectively. For other source types, the physical meaning of the angles is less clear, but they retain the same relationship with the principal axes of stress.

The source type is described by two parameters, T and k. T expresses the deviatoric component of the source type (ie. the variation between double couple, compensated linear vector dipole (CLVD), and negative CLVD. k represents the portion of the volume change in the source (implosive or explosive component). The total moment tensor is given by:

$$M_{ij} = (1-|k|) \begin{bmatrix} \min(2,2-T) & 0 & 0 \\ 0 & \max(-2,-(2+T)) & 0 \\ 0 & 0 & T \end{bmatrix} + k \begin{bmatrix} 2 & 0 & 0 \\ 0 & 2 & 0 \\ 0 & 0 & 2 \end{bmatrix} \qquad (2.2)$$

where $-1 < T < +1$ and $-1 < k < +1$.

It is seen that the separate expression of the orientation allows the source type to be expressed as a diagonalised moment tensor, independent of the orientation. Since no information on absolute amplitudes is used to calculate source orientation, no parameter is required to describe the magnitude of the source, and hence only five parameters are used.

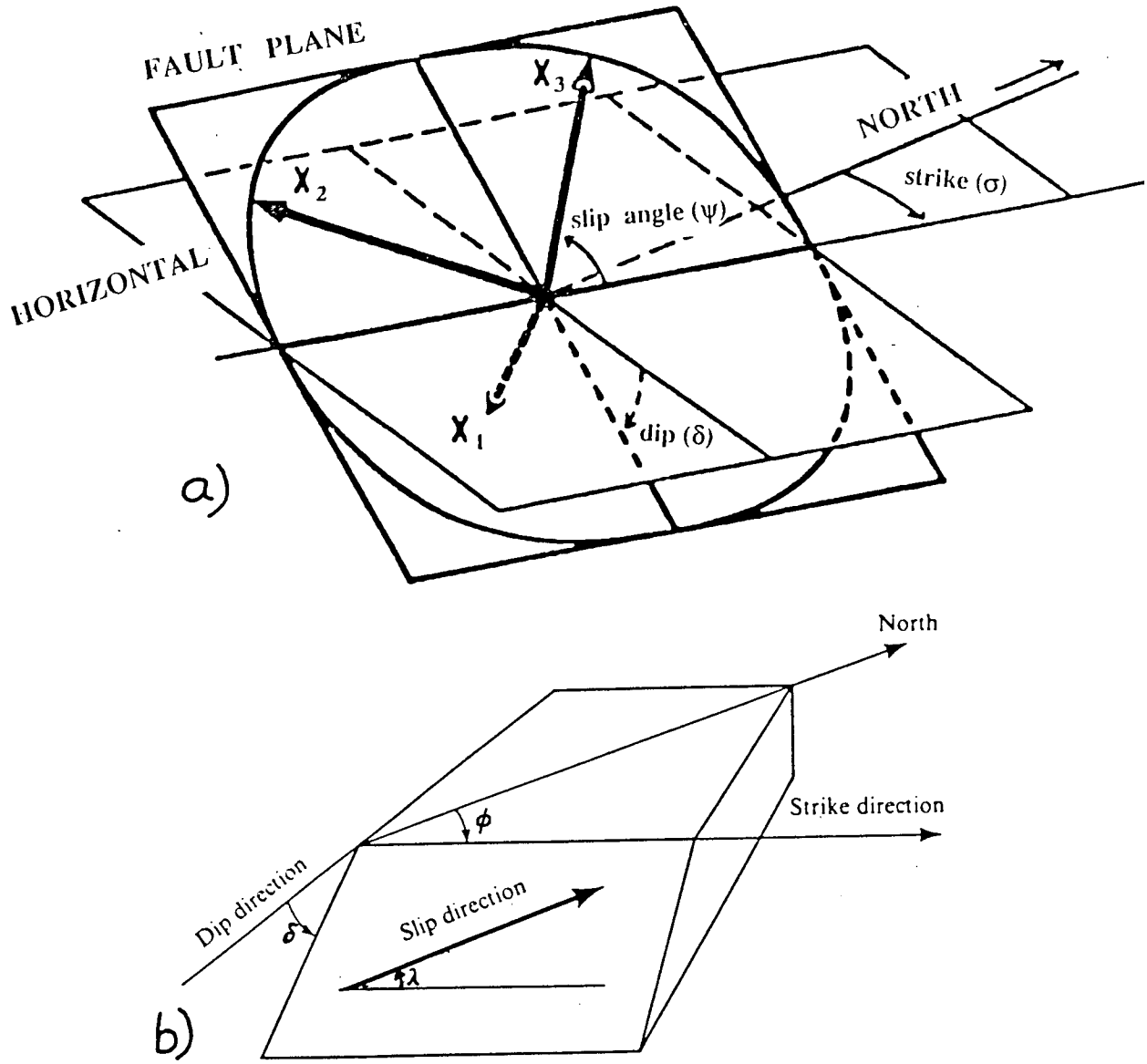

Figure 2.02. a) Definition of source orientation in space (Pearce, 1977). b) Definition of the fault orientation parameters (strike σ, dip δ, rake λ) by Aki and Richards (1980). Strike is measured clockwise from the north, with the fault dipping down to the right of the strike direction: $0 \leq \phi \leq 2\pi$. Dip is measured down from the horizontal: $0 \leq \delta \leq \pi / 2$. Rake is the angle direction between strike direction and slip: $-\pi < \lambda \leq \pi$.

2.2.3 Graphical representation of results

Compatible mechanisms are represented using two types of graphical display; the vectorplot (Pearce, 1977), and the source type plot (Pearce and Rogers, 1989, Hudson *et al.*, 1989). The vectorplot (Fig. 2.03a) is used to display those orientations of a given source type found to be compatible with the input data. A vector is drawn for each compatible orientation, in the position corresponding to its dip, δ, slip, ψ, and at an angle measured clockwise from the vertical of the display equal to strike, σ. The source type plot (Fig. 2.03b) represents a projection of the five-dimensional parameter space onto the two dimensions used for the source type. Circles are drawn on the plot, centred on those source types found to have at least one compatible orientation. Their size is proportional to the number of orientations found to be compatible for this particular source type.

2.2.4 Other methods

There are several methods of determining earthquake source mechanisms. The traditional method involves a forward approach, analysing the *P* radiation pattern using *P*-wave first motions, normally on the LP seismograms. This forward method is considerably extended, in principle to all the body-wave phases, by the RAMP method. Estimation of the earthquake mechanism can also be obtained using an inverse approach. Several schemes for the inversion of seismic waveforms exist:

1. The Centroid Moment Tensor (CMT) method (Dziewonski *et al.*, 1981) uses the inversion of GDSN seismograms which have been filtered so as to remove components with a period of less than 45 seconds and truncated just before the arrival of the first fundamental mode surface waves. The method was later enhanced with the incorporation of mantle wave data, described in Dziewonski and Woodhouse (1983). A further refinement of the method by the introduction of corrections for the aspherical Earth structure is discussed in Woodhouse and Dziewonski (1984). Synthetic seismograms, partial derivatives of synthetic spectra with respect to the moment tensor components and hypocentral coordinates are calculated. An iterative process is used to find the "best fitting" parameters in a least squares sense.

2. In the multichannel signal enhancement (MSE) inversion method (Sipkin, 1982) the Green's functions, representing the response of the earth between the source and the station, are considered to be a multichannel input. The moment rate tensor (the time derivative of the moment tensor) is taken as the convolution filter operating on the input, and the observed seismograms are the desired output. Using a recursive procedure and least squares fitting the moment rate tensor elements are solved to produce the optimum multichannel signal enhancement filter. The multiple vector decomposition (MVD)

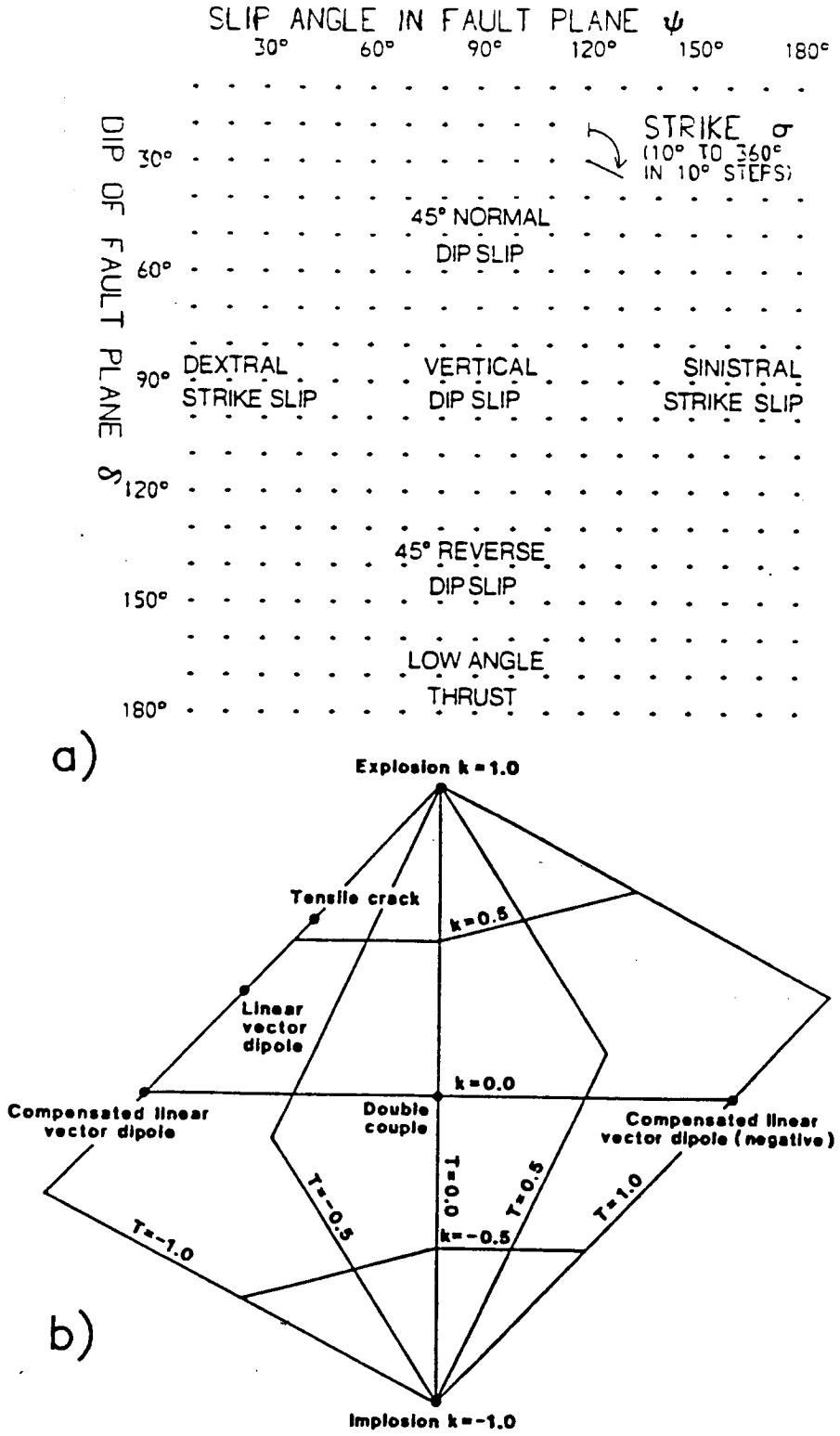

Figure 2.03. a) The vectorplot, annotated to show the position of major fault types. Each vector drawn on such a plot represents a compatible orientation of a specified source type (from Rogers & Pearce, 1987). b) Source type plot which displays all possible source types defined in terms of the two moment tensor parameters T and k of (2.2). The shape of the plot is designed to exhibit equal probability density of source types given no *a priori* constraint on the moment tensor (Pearce & Rogers, 1989).

method, also due to Sipkin (1982), also uses least squares fitting to derive a set of filters which, when deconvolved with the seismogram data, can yield unique time averages of the individual elements of the moment rate tensor.

3. The inversion method by Nabelek (1985) is an iterative maximum likelihood technique for extracting average point source parameters from teleseismic *P*- and *S*-waves. For a layered crustal structure the Earth's response to an arbitrary moment tensor can be cast in terms of four (for *P*- and *SV*-waves) or two (for *SH*-waves) elementary seismograms which do not change in a given layer enabling fast computation. The source time function is parameterized in terms of overlapping isosceles triangles whose amplitudes are determined by the inversion.

4. The method of Riedesel and Jordan (1985) inverts normal mode data taken from the IDA network of accelerometers. The basic data are integrals of the complex spectrum over narrow bandwidths centred on the fundamental modes typically 1 mHz bands from 1 to 11 mHz. Adjustments in the phase of the integrals are computed to compensate for centroid time shifts, the effects of unmodelled Earth structure, and station timing errors.

5. Beisser *et al.* (1990) developed a method which would allow derivation of fairly reliable fault plane solutions based on records from only one station. It is an inversion method for source depth, fault plane orientations, rise time and moment of a point source, and uses digital waveform data of relatively short period (2 - 20 s) body waves. The most important step in this method is the computation of theoretical seismograms for a large number of source parameter variations and a quantitative comparison between theoretical and observed seismograms. It should only be used in the absence of sufficient available data for analysis by the methods described above.

2.2.5 Comparison

Most of the methods described above make inversion of waveforms without operator intervention. They do not require explicit identification of phases and make implicit use of a whole range of body-wave phases, thereby increasing the sampling of the focal sphere. The process can be semi-automated, allowing a large number of earthquakes to be studied routinely. This enables extensive catalogues of data to be compiled. However, they require digital waveform data, which asks for hand digitization of seismograms prior to 1977. The routine processing of the data, without operator intervention, may prove to be a disadvantage in cases of multiple or extensive sources which could be inverted without being considered as such, with consequent errors in location, space and time being transferred to the moment tensor. The least squares best fitting match of synthetic seismograms is dominated by high amplitude *S*-waves, whereas there is an inherent

variation of information content on seismograms with nodal observations usually containing more information.

The relative amplitude moment tensor method, although it depends entirely on correct identification of phases (particularly *pP*, *sP* and *S*), offers an alternative way to study the source parameters of a wide range of teleseismically recorded events (Rogers and Pearce, 1987; Stimpson, 1987; Stimpson and Pearce, 1987) in a more accurate way. The specification of amplitude bounds ensures that the error bounds obtained for the solutions are well founded and relate directly to the quality of the observations (Pearce, 1980). The method successfully isolates those waveform features which are governed by the source radiation, greatly simplifying the need for structural and propagation path information, and the use of simple amplitude measurements enables analogue and digital seismograms to be used. Constraints can be placed upon the moment tensors of the smallest of teleseismically recorded events, which is not possible using other methods. There are three classes of teleseismically recorded earthquakes to which this method can be applied using different types of data:

a) Small shallow earthquakes where a small number of short period discrete *P*, *pP*, and *sP* observations may be available.

b) Large intermediate and deep earthquakes which offer long-period *P*, *pP* and *sP* observations, possibly augmented by those of three-component direct *S*-waves.

c) Large shallow earthquakes, whose interfering direct *P*-waves and surface reflections may offer little relative amplitude information other than *P*-wave polarities, but whose three-component *S*-wave measurements provide the additional information required. Moreover, depth phases can become apparent on broadband seismograms, and their use can improve the input data considerably.

The method is also sensitive to volume-change components of the moment tensor, and offers the best means of testing suggestions that such components may be found among earthquake processes.

2.3 BROADBAND SEISMOGRAMS

To optimize signal detection, the response functions of many seismograph systems like the WWSSN have been shaped inversely to the spectrum of Earth noise. This was often done by splitting the seismograph system into long- and short- period components, which together provided a broad-band response with an effective notch filter between roughly 0.1 - 1.0 Hz. For ray theoretical inversions, which require only arrival times and amplitudes, this type of response was adequate. However, the ability to resolve Earth structure and the earthquake mechanism has been significantly advanced by techniques

using synthetic seismograms, where it is desirable to use all the amplitude and phase information contained in seismic pulse shapes. As each component of the split seismograph system tends to emphasize a narrow band of frequencies about the instrument response, frequency-dependent phenomena, such as attenuation, are also usually suppressed. Another phenomenon that does not become evident with short- and long-period data is directivity, that is the directional variation in body wave pulse shapes generated by a finite source (e.g. Hartzell 1980; Choy and Boatwright 1981). This is because the corner frequency of most teleseismically recorded earthquakes lies in the frequency band of information that is usually filtered out by conventional seismograph systems. The design of the system response in this fashion (LP and SP components), has strongly influenced the analysis of body waves from moderate-sized earthquakes. For instance, records of long-period body waves from events with corner frequencies greater than 0.5 Hz (where generally $m_b < 6.0$) are usually modelled using point sources, i.e., by assuming the source has a finite duration but no spatial extent (Langston and Helmberger, 1975). This assumption greatly simplifies estimation of the average properties of the source such as the moment, the source depth, and the focal mechanism. However, because neither the data nor the source models contain spectral information above the corner frequency, this modelling approach can provide no information about the dynamic character of the rupture process. Recent papers (e.g. Choy and Broatwright, 1981; 1982; Engdahl and Kind, 1986; Bezzeghoud *et al.*, 1985; Choy and Engdahl, 1987; Choy and Kind, 1987, Choy and Dewey, 1988), have shown that body waves containing a broad spectral bandwidth of information (broadband) can provide much higher resolution of the rupture process than narrow band recordings from conventional seismographs; they evaluate the usefulness of broadband seismograms for identifying depth phases and describing source characteristics.

2.3.1 Short Period to Broadband conversion method

As outlined above, broadband seismograms are essential when studying the source characteristics of moderate-sized, teleseismically-recorded earthquakes. Several seismological stations world-wide are equipped with instruments that have a flat response to displacement or velocity over a wide range of frequencies. However, broadband seismograms can also be recovered indirectly by deconvolution of high quality digital SP data (Douglas *et al.*, 1981), or from a combination of SP and LP data (Choy and Kind 1987). Because of the lack of directly recording broadband stations at teleseismic distances, to provide a good coverage of the focal sphere for the events studied here, broadband records are recovered from the GDSN short period seismograms using the method of Douglas *et al.* (1981). According to this method, the short period record is

converted to a displacement broadband seismogram by multiplying its spectrum by the ratio $a_2(\omega)/a_1(\omega)$, where $a_1(\omega)$ is the short period instrument response, and $a_2(\omega)$ is the displacement broadband instrument response, both as functions of angular frequency ω. The displacement broadband instrument response in current use is flat to ground displacement from 0.025 to 10 Hz (Fig. 2.04). In the presence of background noise, multiplication of the record by the ratio of the relevant instrument responses is a more stable process, especially at low frequencies, than dividing out one instrument, and then multiplying by the other, since the latter process inevitably results in near-infinite amplitudes at both ends of the spectrum. The process of multiplication in the frequency domain is identical to deconvolution in the time domain, and therefore the broadband seismograms are referred to here as deconvolved seismograms (Fig. 2.05).

2.3.2 SP and LP to Broadband conversion method

The method of simultaneous deconvolution of SP and LP seismograms (Harvey and Choy, 1982); Choy and Boatwright, 1981) uses digitally recorded waveforms which are first deconvolved to remove the instrument response. The resulting short- and long-period channels can then be combined to form a single broadband record of the ground displacement. The method involves computing the Fourier transforms of the seismograms, dividing out the frequency response of the instrument, and applying frequency windows to the instrument-corrected transforms (Choy and Boatwright, 1981). For the long-period channel, a low-pass filter is applied with a ramp cutoff between 0.04 to 0.08 Hz. Similarly, a high-pass filter with a ramp cutoff in the same frequency band is applied to the short period channel. In the frequency band where the long- and short-period spectra overlap, the falloffs of the two windows sum to unity. An inverse Fourier transform returns the long- and the short-period ground motions, and the two signals are summed, using a cross-over filter to construct the broadband deconvolved ground motion (Fig. 2.06).

Figure 2.07 shows an example of the deconvolution process using data from the 17 January 1983, Ionian islands earthquake recorded at SCP, LON, COL and BDF. The top traces represent the GDSN SP seismograms and those immediately below are the deconvolved broadband velocity records retrieved from the SP seismograms using the method of Douglas *et al.* (1981). The bottom traces show the broadband velocity seismograms recorded directly at the same stations for comparison. The excellent agreement between the deconvolved and the directly recorded broadband records, together with other examples using the same method (Abercrombie, 1991; Douglas *et al.*, 1990), suggests that the additional use of long period data contributes little extra

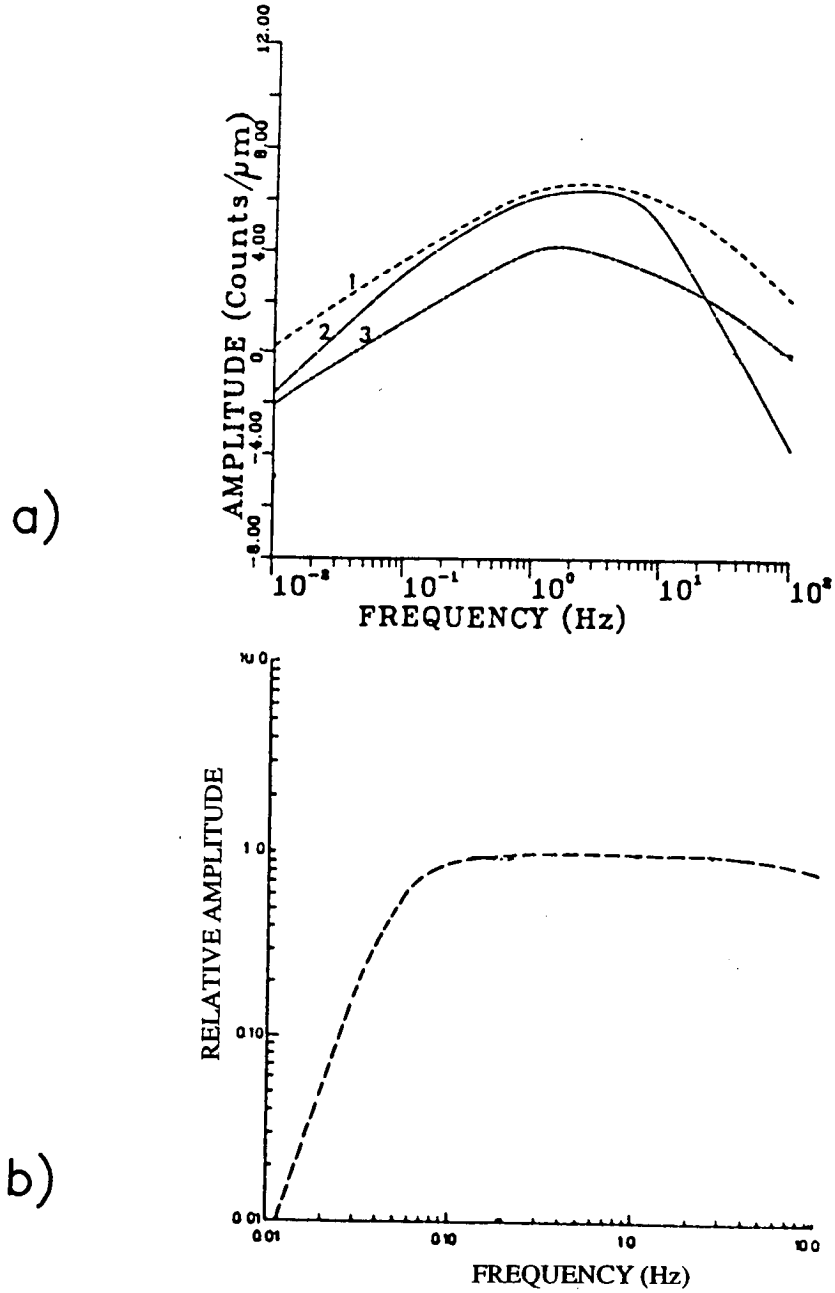

Figure 2.04. a) Amplitude responses of the short-period recordings of the GDSN network: The curves (1), (2) and (3) indicate, respectively, SRO, ASRO and DWWSSN instrument responses. b) Broadband amplitude response as a function of frequency, used in this study to generate the broadband seismograms.

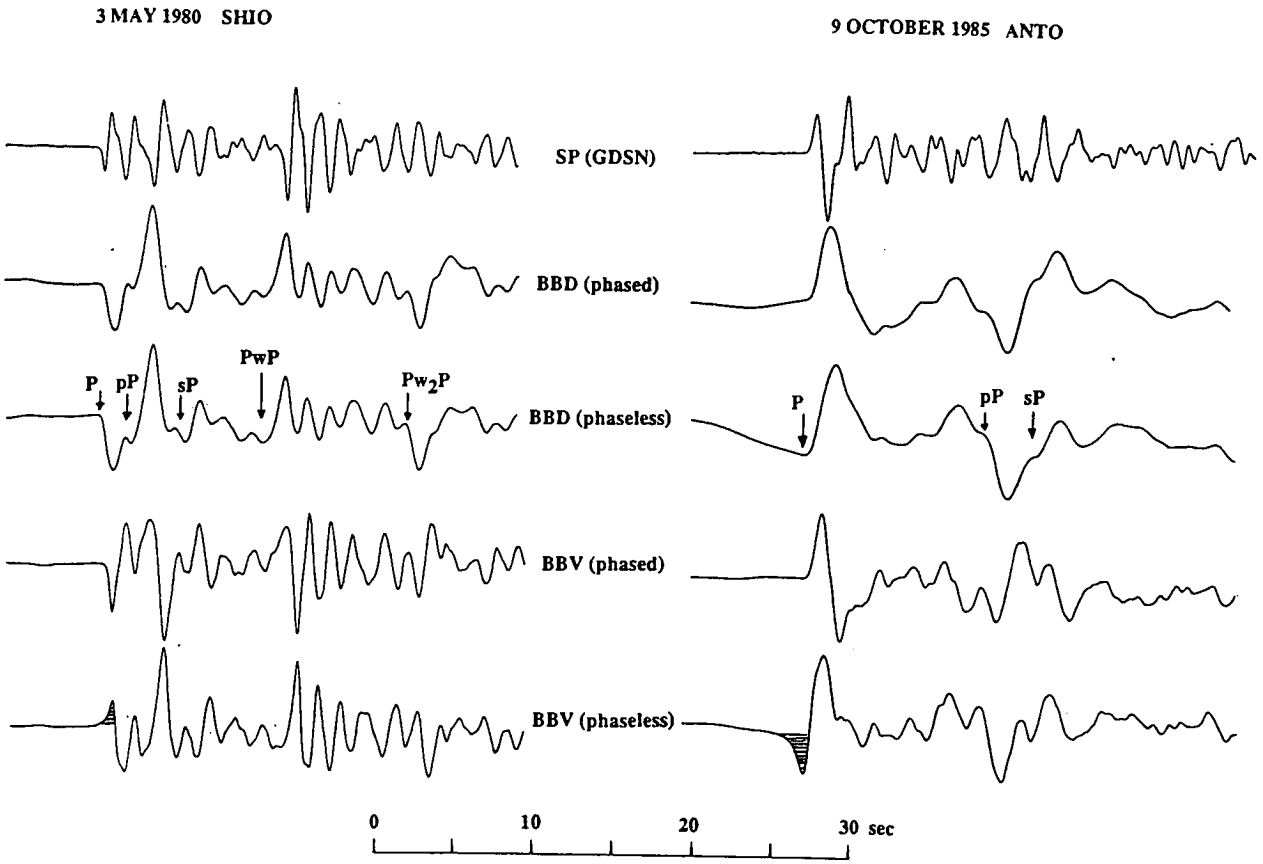

Figure 2.05. Short-period (SP) seismograms *(top traces)* recorded at the stations SHIO and ANTO of the 3 May 1980 and 9 October 1985 earthquakes respectively. The displacement broadband (BBD) and the velocity broadband (BBV) records, as they are deconvolved from the SP, are shown beneath, both as conventional (phased) trace, and with the instrument phase removed (phaseless). This shows how clearly the arrivals and the polarities of the various phases are shown on the BB records. The phaseless waveforms give a better representation of the pulse shape, at the expense of a small precursor of opposite polarity *(shaded areas)* to the polarity of the direct *P*-wave.

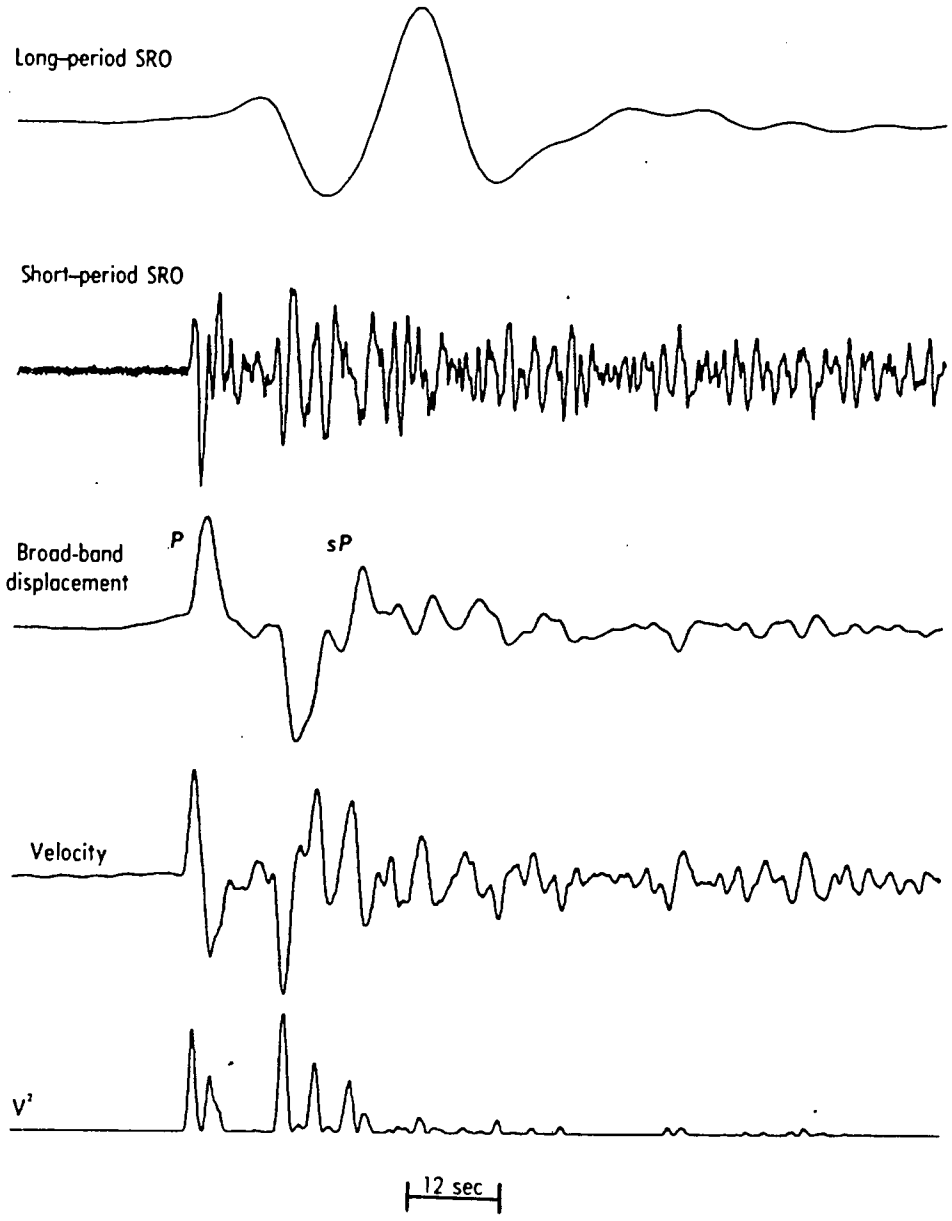

Figure 2.06. (*Top two records*) Digitally recorded long- and short-period vertical component seismograms at station MAIO, containing *P* and *sP* arrivals from the earthquake of 8 November 1976. The LP channel is sampled at 1 Hz while the SP channel is sampled at 20Hz. (*Third record from the top*) The BB record of ground displacement constructed by the simultaneous deconvolution of the instrument response from the original LP and SP records. (*Fourth record from the top*) Corresponding record of velocity. (*Bottom*) Corresponding record of velocity squared (from Choy & Boatwright, 1982).

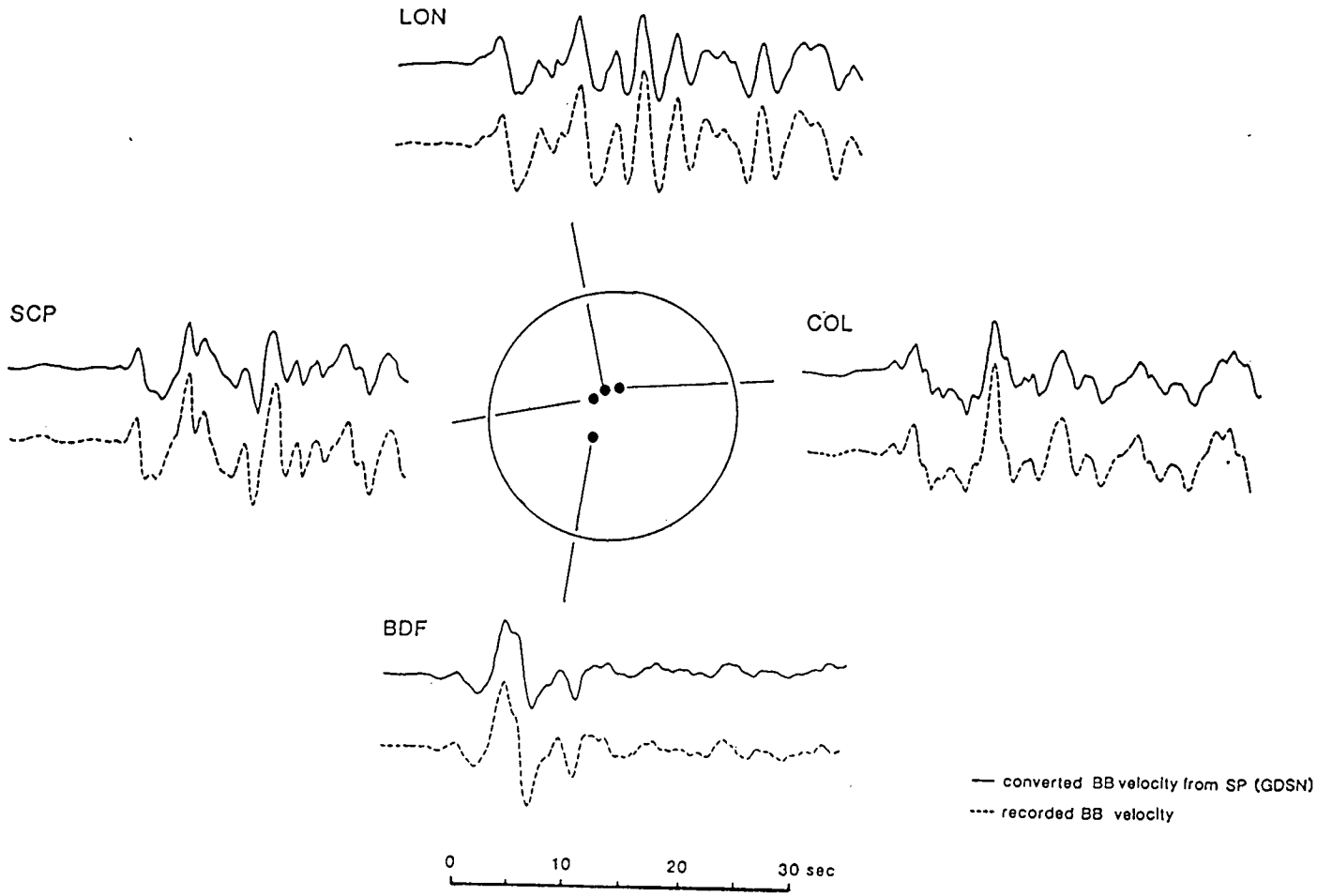

Figure 2.07. Broadband velocity waveforms (converted from SP) for the 17 January 1983 earthquake at four GDSN stations are plotted around the focal sphere *(solid lines)*. Underneath, in dashed lines, are shown the broadband velocity records as they were recorded at the same stations. This demonstrates an excellent agreement.

information to the deconvolved broadband signal for intermediate events ($M_s < 7$) in the areas studied in the present work.

2.3.3 Phaseless seismograms

Phaseless seismograms, which can be thought of as non-causal seismograms that would have been recorded by a system which introduces no phase shifts, sometimes have advantages over standard seismograms in showing more clearly the polarity, width and area of body-wave pulses and are therefore easier to interpret (Stewart and Douglas, 1983; Fig. 2.08). Because seismometers are inertial systems, they cannot record zero frequency displacement (analogous to a DC level in electronics), so the response of any real seismometer to a "spike" pulse must include an overshoot, and the area of the overshoot is equal to the area of the spike (Fig. 2.09a). Phaseless seismometers, however, are able to distribute this "overshoot" both before and after the spike, so decreasing its size at any point, and giving a better representation of the signal. This effect can clearly be seen in observed data. E.g. the *P*-wave of the 13 September 1986 Kalamata earthquake as recorded at COL (Fig. 2.09b), when recorded by the instrument with the phase shifts included, has a distorted direct *P*-wave, and in the case of large shallow earthquakes it is dwarfed by the combination of the surface reflected phases and the overshoot. A phaseless instrument correction, however, represents the waveform much more accurately, at the expense of producing a precursor of opposite polarity to the first arrival.

Phaseless broadband seismograms cannot be recorded directly, but they are easily recovered from the SP records by multiplying by $|a_2(\omega)|/a_1(\omega)$ in the frequency domain and transforming back into the time domain in the same way as for deriving a standard BB record. Such a response generates the artificial precursor described above which makes the onset of a signal difficult to observe. If the filter amplitude response is sufficiently broad, as it is for the broadband seismograph used here, then precursors generated in this way need not be a serious drawback in the interpretation of phaseless seismograms. These artificial precursors are first identified, and simply ignored in any source modelling. For the reasons described above, phaseless seismograms dominate the rest of this study.

2.4 SOURCE PARAMETERS

Understanding earthquake sources is of fundamental interest for many fields of Earth science. The study of earthquake sources helps define active deformation processes; it provides important constraints on the state of the stress of the crust, and it is of primary importance in the understanding and prediction of strong ground motions.

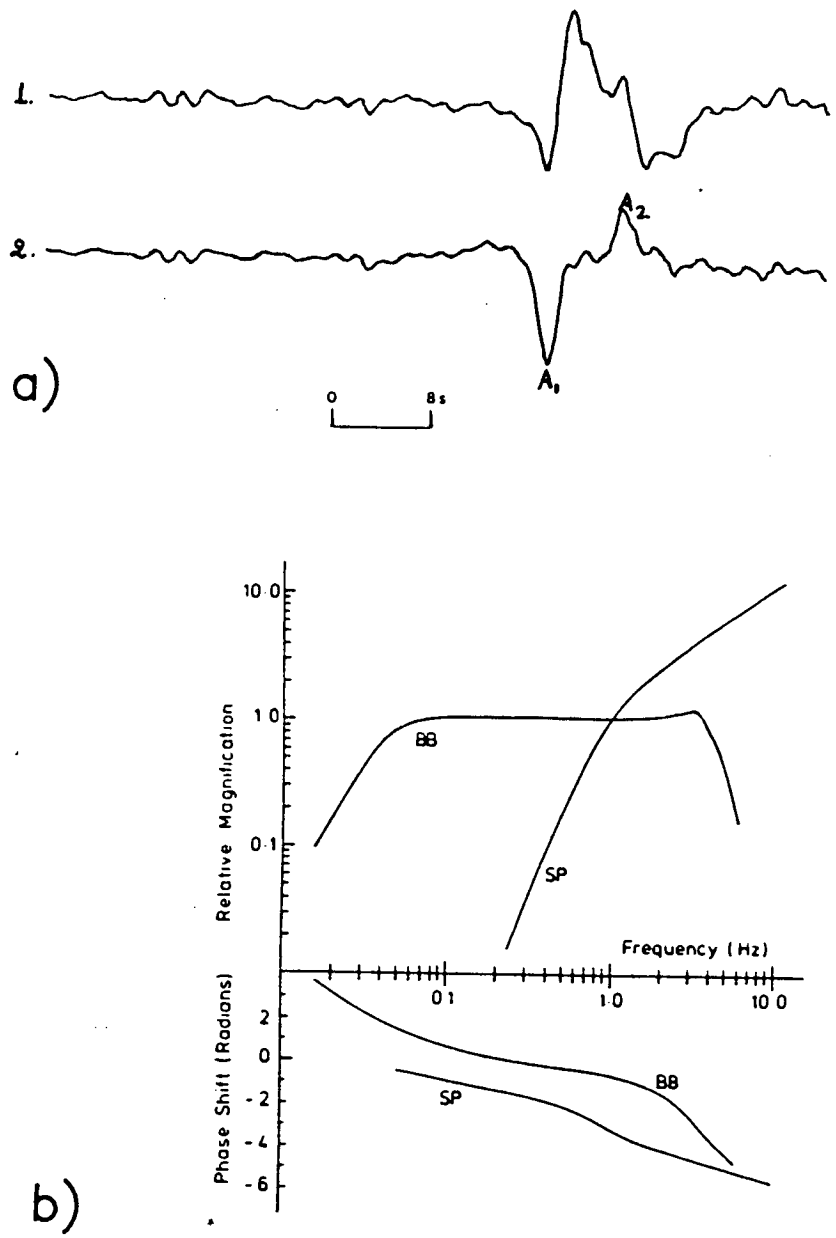

Figure 2.08. a) *(1)* Broadband *P*-wave seismograms recorded at WOL for the New Hebrides earthquake, January 9. *(2)* Seismogram *(1)* after removal of phase shifts due to the BB seismograph. The signal on the phaseless seismogram is now seen to consist of two pulses, the first and largest has negative polarity (A_1), the second (A_2) positive polarity. b) Relative magnification and phase shift for broadband and short-period seismographs.

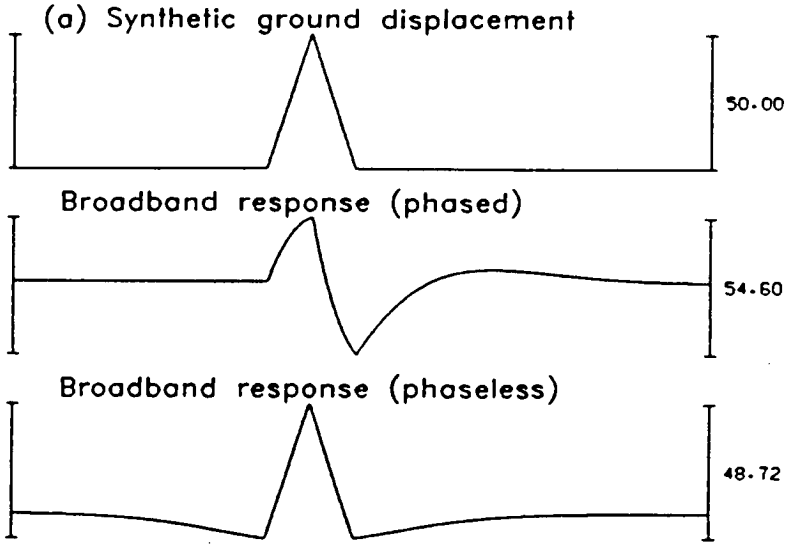

Figure 2.09. a) A synthetic triangular ground displacement and the response of the displacement (BBD) instrument to it. The upper trace is the ordinary "phased" response and the second is phaseless. A negative overshoot is seen in the upper trace, which would distort any later arrivals. The lower trace represents much more faithfully the input pulse as on a slightly distorted baseline. This is no longer causal, and a small, low frequency, negative precursor can be seen. b) *(Top trace)* Short-period seismogram recorded at COL for the 13 September 1986, Kalamata earthquake. *(Second and third traces from the top)* The response of the BBD instrument at COL to the same event, deconvolved from the SP. In the upper "phased" trace the positive overshoot from the negative direct *P*-wave interferes constructively with the reflected phases, distorting the waveform. This does not happen in the lower (phaseless) trace, which shows the negative direct *P* pulse more clearly. The two *bottom traces* represent the "phased" and "phaseless" velocity broadband records for the same event at the same station. Again, the phaseless record shows more clearly the true polarities of the interfering phases.

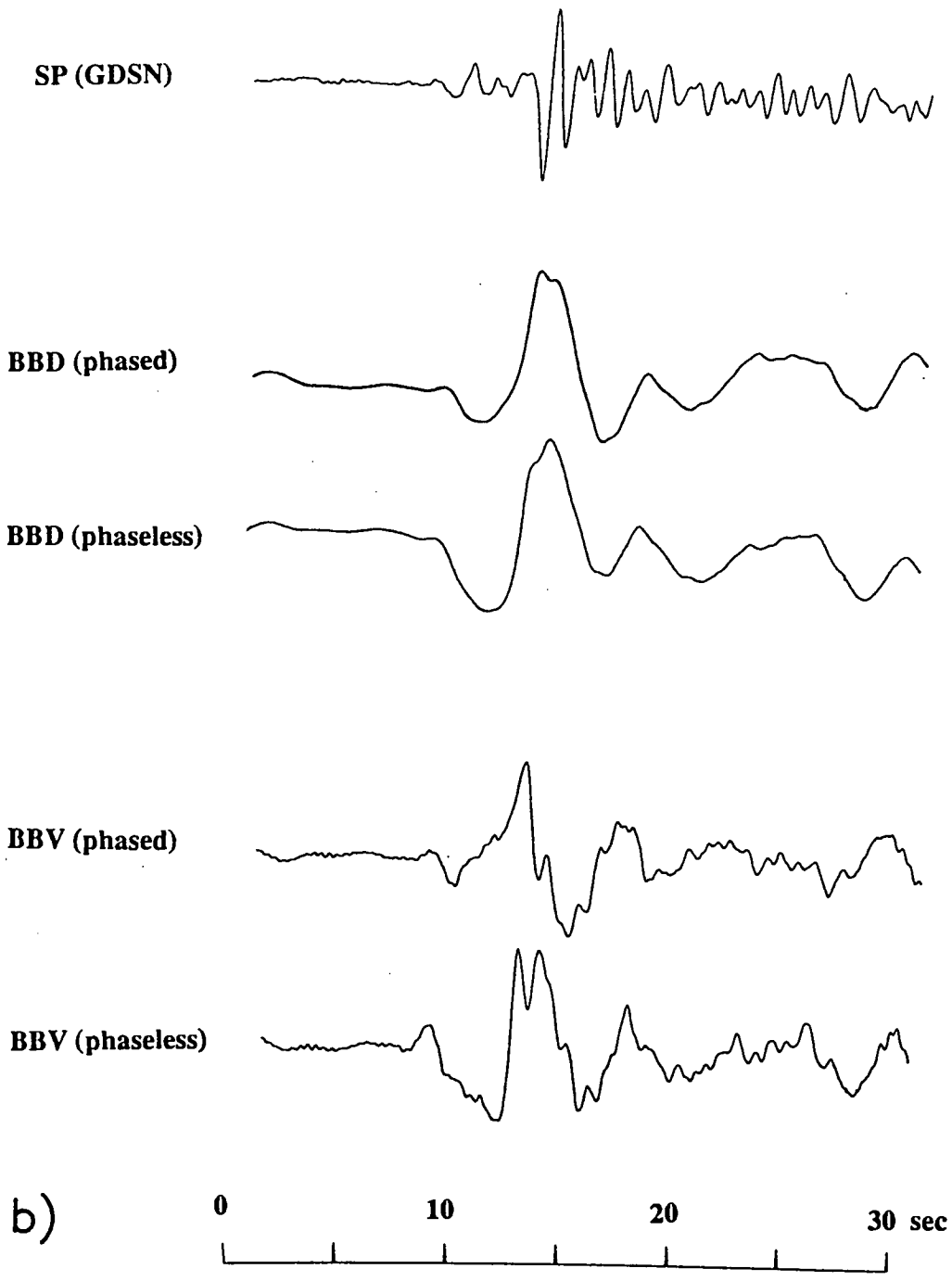

Figure 2.09. (continued).

It is now common to invert teleseismic waveforms to derive a set of point-source force-couples (i.e. moment tensor), their time histories, and to map the temporal and spatial distribution of earthquake slip.

The magnitude was the first quantitative measure of the strength of an earthquake. It is still widely used although its shortcomings are well known. It is also the most difficult parameter to relate to other important source characteristics such as strain energy release, fault offset, stress drop, source dimensions, moment and radiated seismic energy. These other parameters can be related, one to another, fairly easily, but their relationship to magnitude requires a spectral description of the seismic source. Such a description requires a complete time and space history of the faulting or stress release mechanism. For example, the magnitude is calculated from seismic-wave amplitudes at a given period whereas the seismic energy release involves integration over the whole spectrum. Aki (1966) introduced the concept of seismic moment (M_0) from dislocation theory as a measure of earthquake size directly related to the physics of the earthquake source. Moreover, it can be estimated easily from seismic records (e.g. Brune, 1970, 1971; Douglas *et al.*, 1972; Langston and Helmberger 1975) or, when possible, from geological observations of surface faulting etc. using the equation (2.1). The seismic moment is the size of the double couple at the earthquake source, arising from a propagating dislocation with conservation of the angular momentum.

Magnitude scales are found to be a strong function of wave frequency; in particular, M_S tends to an upper limit for great earthquakes. All instruments for recording earthquakes have response characteristics which sample only a limited range of the seismic energy spectrum about their natural frequency, f_0, or equivalent period, T_0. For the surface-wave magnitude scale, M_S, this natural period is about 20 s, and for the body-wave scale, m_b, it is about 1 s. These magnitude scales cannot pick up increases in energy release in frequency ranges outside the natural bandwidth of the seismographs. So as larger and larger events with longer and longer fault lengths and natural periods are recorded, a point is reached where an event, say twice as large in terms of energy as a previous one, produces no detected increase in the measured amplitude. However, recently, the moment magnitude, M_W, has been defined to provide a more uniform and open-ended magnitude scale. Kanamori (1977) has proposed the relation:

$$M_W = 2/3 \log_{10} M_0 - 10.7 \qquad (2.3)$$

where M_0 is the seismic moment of an earthquake in dyn cm. The moment magnitude has the advantage (as a measure of size) that it does not saturate at the top of the scale and has a sounder theoretical basis than M_S, which is a purely empirical measure.

2.4.1 Some relationships between earthquake source parameters

Aki's (1967) proposed scaling law for earthquakes assumes that stress drop is constant and independent of magnitude, and equivalently, that for circular faults, moment is proportional to the radius cubed. Stress drops for earthquakes throughout the world are found to lie between about 1 and 100 bar over 5 or 6 magnitude units (e.g. Kanamori and Anderson, 1975; McGarr *et al.*, 1981), and so are generally consistent with this scale-invariant hypothesis. Relationships between seismic moment and magnitude have been determined for earthquakes of all sizes, both globally and in particular areas. Kanamori and Anderson (1975) use a simple dislocation model to show that, theoretically, log (M_0) ~ M_S for small earthquakes (magnitude < 5), log (M_0) ~ 3 M_S for large (magnitude > 6.5), and log (M_0) ~ 1.5 M_S for the most common intermediate cases (Fig. 2.10). Ekström and Dziewonski (1988) carried out a global study of the M_0 - M_S relationship and found that, although the global relationship is well modelled by the theory, there are significant regional differences (Fig. 2.11). In areas of continental extension (e.g. Aegean, central Asia and North America), earthquakes have higher than average M_S relative to M_0, and those from mid-ocean ridges and fracture zones have lower M_S. Subduction zones show no particular trend. Attenuation is an important factor to consider, as surface waves are path dependent, but attenuation alone cannot explain the distribution of the observed variations. Possible explanations include source complexity in continental areas, leading to an underestimation of M_0, or the lack of an appropriate depth correction in the M_S scale.

2.5 GENERATION OF SYNTHETIC SEISMOGRAMS

Previous studies have shown that moderate-sized earthquakes associated with subduction processes in the Hellenic and in the Aleutian Islands subduction zones have shallow to intermediate focal depths and produce complex seismograms. In cases of shallow focal depths (< 10km) the surface reflections *pP* and *sP* interfere strongly with the direct *P*-wave, and in cases of complex seismograms such phases are difficult to identify. This leads to an appreciable trade-off between source parameters such as depth and seismic moment which is difficult to analyse with inversion techniques. In common with many other studies, source parameters are determined here by forward modelling, which allows a direct investigation of the sensitivity of the model to variations in the individual parameters.

The synthetic seismograms that are generated to carry out such forward modelling aim to reproduce the various characteristics, such as pulse duration and amplitude, of the

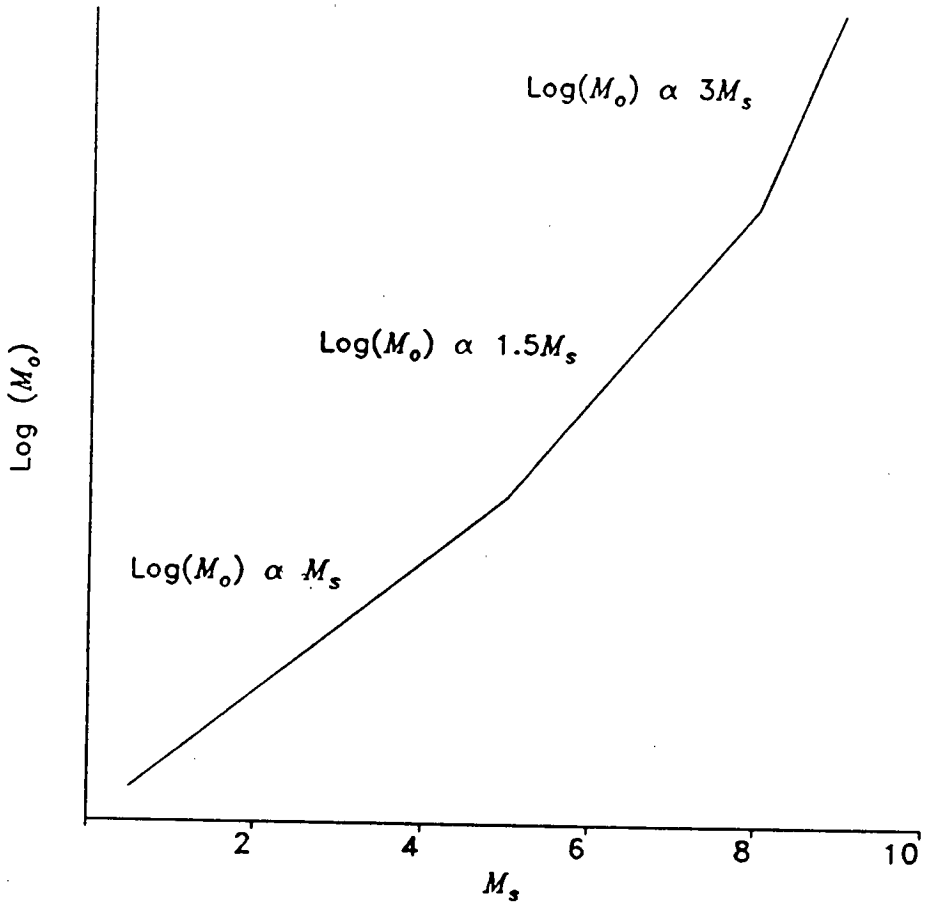

Figure 2.10: The relationship between seismic moment and magnitude over the full magnitude range. Kanamori & Anderson (1975) calculate these relationships theoretically, assuming a constant stress drop, based on the rise time, source dimension and excitation of 20 s period surface waves. Small earthquakes have short rise times and small dimensions, larger earthquakes have short rise times and larger dimensions, and great earthquakes have long rise times and large dimensions.

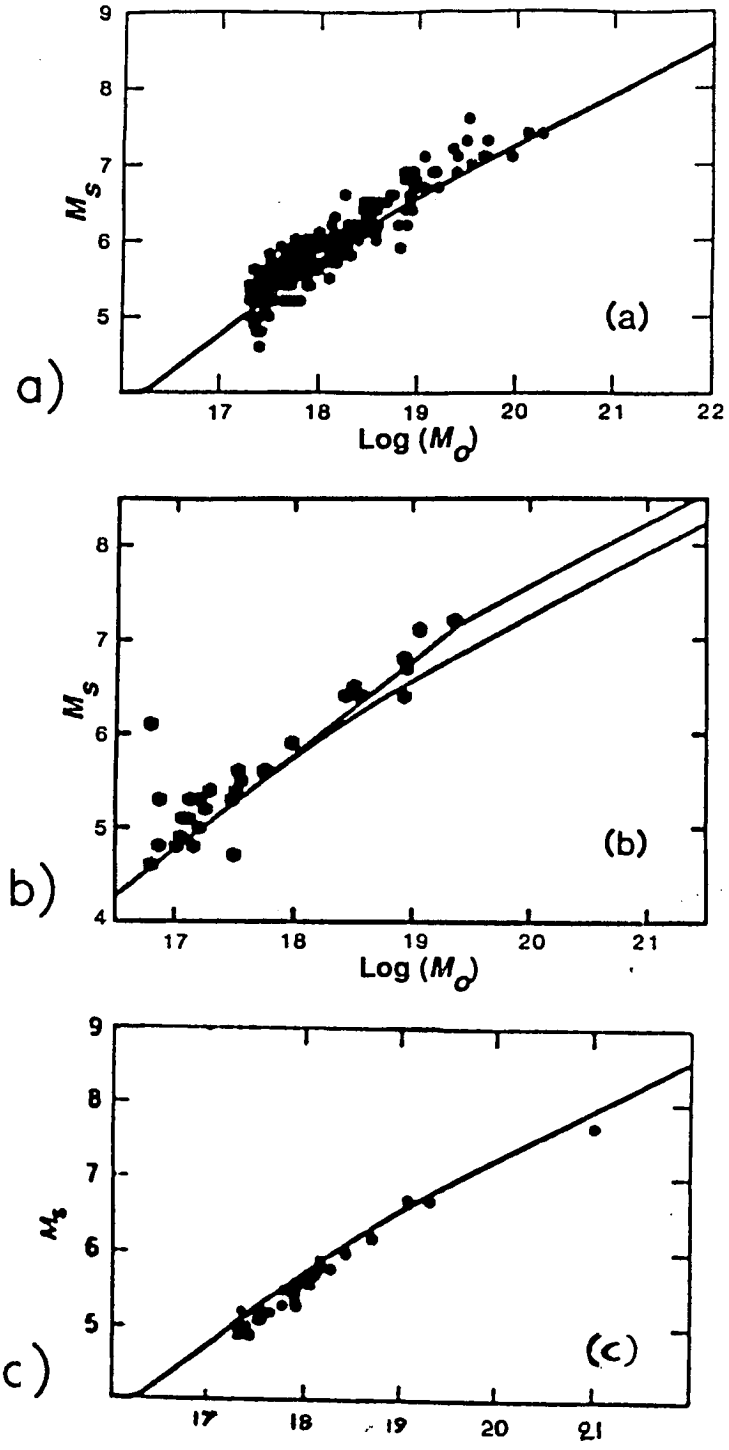

Figure 2.11. The relationship between seismic moment and magnitude. a) Continental earthquakes (including those from the Aegean) compared to the global relationship for all earthquakes (Ekström & Dziewonski, 1988). Most points plot above the line, implying that continental earthquakes have low M_0 or high M_S compared to the global average. b) Aegean earthquakes. The lower curve is the global average, as in (a), and the upper curve is a better approximation for continental earthquakes (Ekström & England, 1989). c) Distribution of M_0 - M_S observations for thrust-type earthquakes in the Andreanof Islands region of the Aleutian Islands (Ekström & England, 1989).

observed records. Nodal amplitudes at appropriate stations, amplitude ratios between direct and surface reflected phases, and variation in *P*-wave pulse duration among different stations are used to compare the synthetic and the observed seismograms, and thus to verify the fault plane solution obtained.

2.5.1 The model

The method used in this study to generate the synthetic seismograms is that of Hudson (1969a) and Douglas *et al.* (1972), which considers a finite two-dimensional Savage-type source (Savage, 1966). Broadband seismograms include wavelengths (~ 1 - 100 km) of the order of the spatial dimensions of the earthquake source for all except the larger earthquakes, and therefore a two-dimensional model should be used. This type of model has the advantage of enabling determination of the fault size and the amount of slip, and, if the earthquake breaks the surface, the length of the surface break can be estimated. It also allows the appearance of a fault break as a boundary condition of the modelling.

In the Savage model, the earthquake source is assumed to be a double couple of finite size. The fracture is assumed to initiate at the centre or focus of an ellipse and propagate outward at a constant rupture velocity until it reaches the boundary (Fig. 2.12a). Slip occurs instantaneously at each point as the rupture front passes (Fig. 2.12b). It is possible to use a more realistic finite-time for slip to occur at each point, but this requires a great amount of computing time with negligible differences to pulse shape (R. Abercrombie, personal communication). If the time for slip to occur at each point remains constant (e.g. it is instantaneous), the amplitude of the synthetic displacement pulse is proportional to the stress drop which does not relate to any time constants of the source function, therefore it has no effect on pulse duration. The final slip distribution is of the form:

$$\text{slip at a point} = (1 - (x^2 / r^2))^{1/2} \qquad (2.4)$$

where x is the distance of the point from the centre of the fault, and r that from the edge to the centre of the fault (Fig. 2.12c). This slip distribution has been reproduced experimentally (Archuleta and Brune, 1975). This kinematic model is relatively simple when compared to more recent dynamic models obtained by direct solution of dynamic rupture initiation and termination processes (e.g. Das 1985; Das and Kostrov 1987, 1988). The variable kinematic source parameters of the model are focal depth, source orientation (strike, dip, slip angle), fault dimensions, stress drop, rupture velocity and

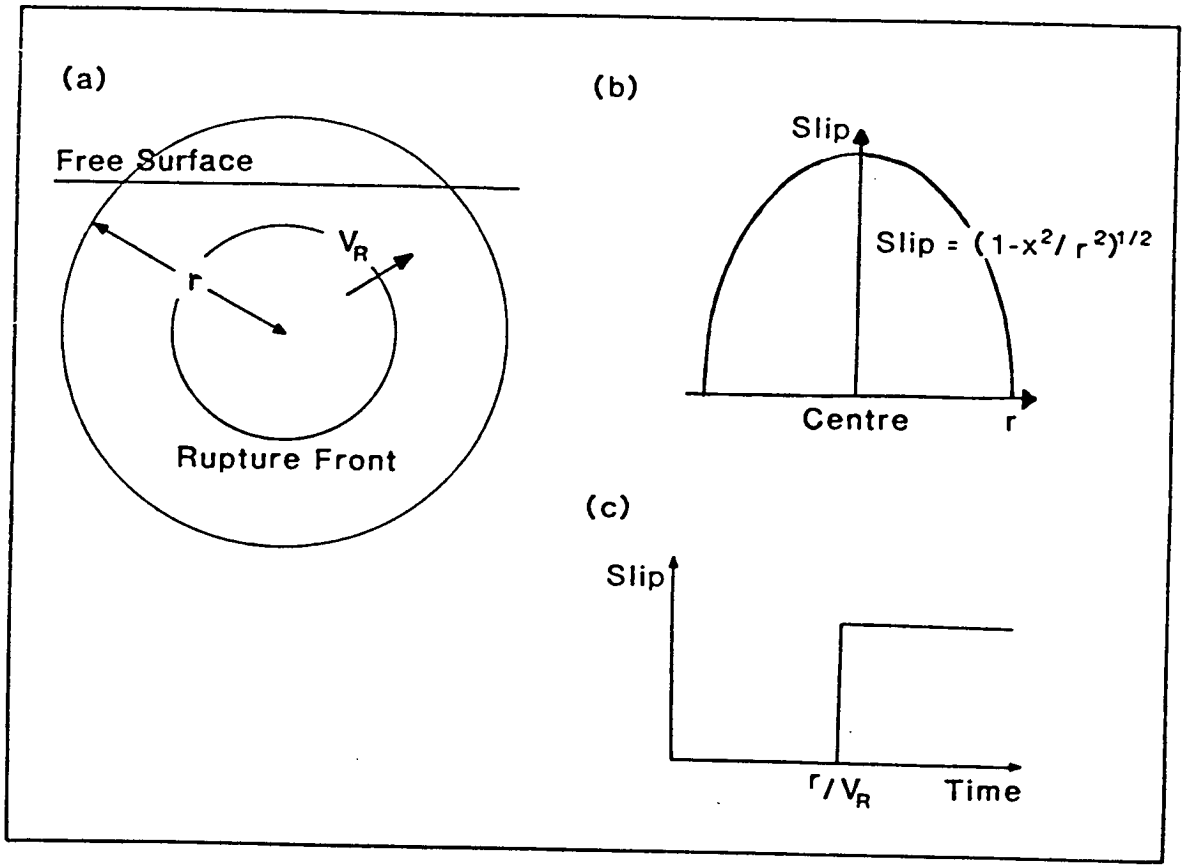

Figure 2.12. The two dimensional finite dislocation model (after Savage, 1966). Here only the example of a circular fault is shown. a) The rupture starts at the centre of a circle or focus of an ellipse and radiates outwards at a constant rupture velocity (v_r), until it reaches the edge of the ellipse, or the free surface. b) The final slip distribution. c) Slip occurs instantaneously at a point on the fault as the rupture front passes.

seismic moment. A homogeneous plane-layered velocity structure both near the source and the receiver is assumed. In addition, an average anelastic attenuation correction for the whole path is chosen to match the dominant period of the signal. The latter parameter is defined as the travel-time in seconds divided by the average quality factor Q, and it is denoted by t^*.

2.5.2 Radiation pattern and directivity

For a moving source, waves that leave the travelling rupture in opposite directions will have different amplitudes and pulse durations. Increase in the amplitude is accompanied by decrease in the pulse duration in order to preserve the area under the pulse, which represents the total slip at the source, and it is constant and equal for all stations. It follows from elementary kinematic considerations for a sound pressure wave at R in Fig. 2.13a, that the required radiation factor is:

$$(1 - M\cos\theta)^{-1} \qquad (2.5)$$

where M is the seismic Mach number (v_r / β), and β is the S-wave velocity. Thus the amplitude in the direction of rupture is larger than that away from the motion by a factor of $(1 + M)/(1 - M)$. The spectral amplitude ratio between two waves that leave the source OA in opposite azimuths θ and $\theta + \pi$ is called *directivity function*, $D(\theta)$, and it is independent of the source time function. Therefore, it provides an experimental measure of fault length and v_r from seismograms at a station or stations on a great circle path.

In addition, there is a frequency shift, similar but not identical, to the Doppler effect in acoustics, so that a moving point source, of frequency ω_0, is observed to emit frequency $\omega_0 / (1 - M\cos\theta)$. As a result waves generated at different parts of the fault interfere, either constructively or destructively, and this produces a deviation from the standard double couple radiation pattern (Fig. 2.13b). The greater the rupture velocity, the greater this deviation is.

In the two-dimensional Savage (1966)-type source model it is possible to use the finiteness of the rupture plane to determine the most likely fault plane of the solution determined. This essentially uses a directivity effect which has no variation in pulse length in the plane of the fault in the case of a circular fault with the rupture initiating at the centre. However, when the fault is assumed elliptical and the rupture starts at the focus of the ellipse, a frequency shift with azimuth can be obtained. Moreover, if the rupture starts at the upper focus of an elliptical fault plane and propagates downward, then the direct P-waves recorded at a station have smaller duration but greater amplitude than their free surface reflections pP and sP. The opposite happens when the rupture propagates upward.

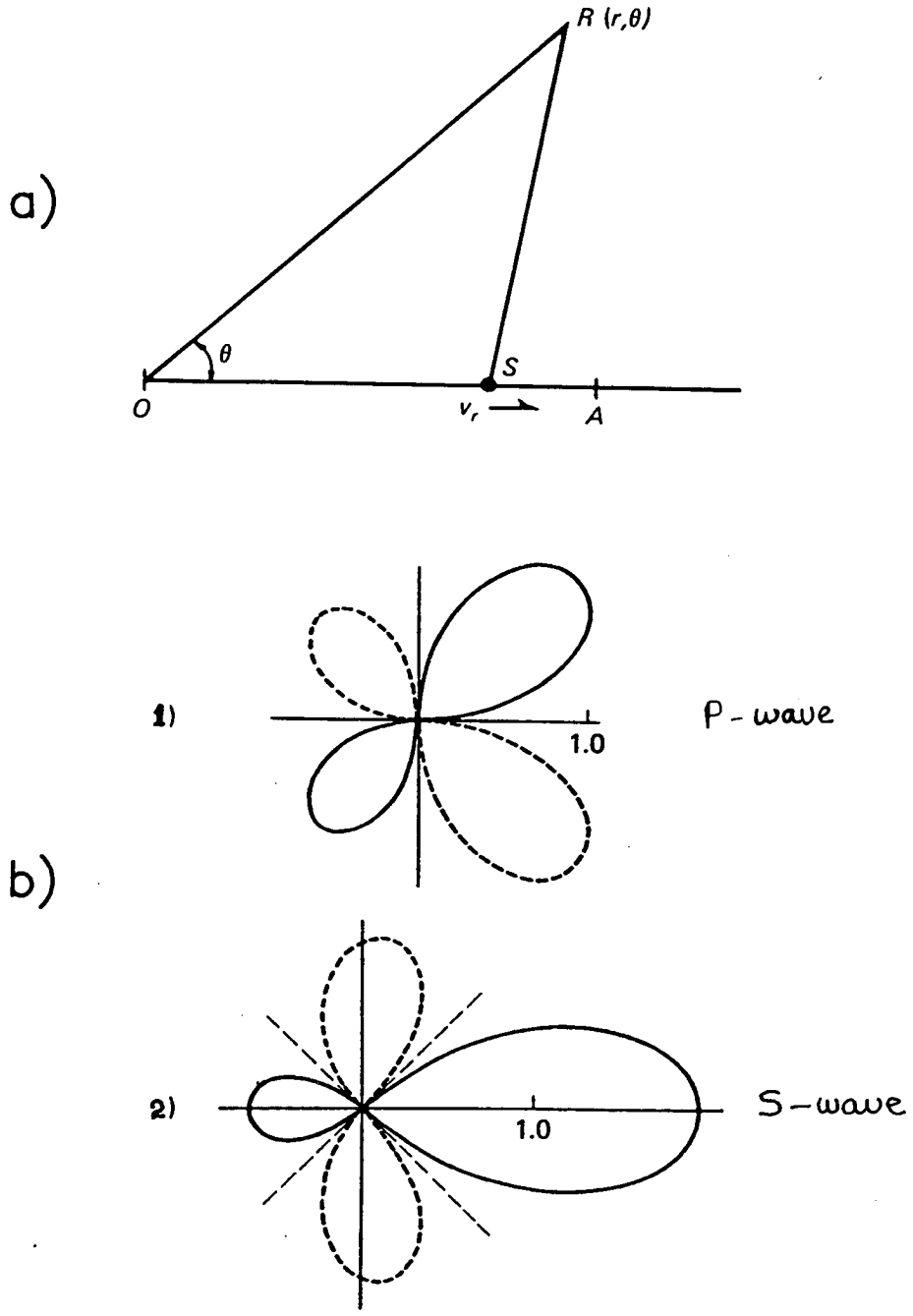

Figure 2.13. a) Moving point source and b) Radiation patterns of the *P*-(1) and *S*-waves(2) from sources with rupture propagation for: 1) $v_r / \beta = 0.5$; 2) $v_r / \beta = 0.9$, where v_r and β denote the rupture and shear wave velocities, respectively. Solid lines indicate positive and dashed lines negative values (from Hirosawa and Stauder, 1965).

Directivity effects, with or without frequency shift, are observed for some of the earthquakes studied and are presented in the following Chapters.

2.5.3 Resolution, errors, and the sensitivity of the model

The resolution of the modelling procedure in the estimation of source parameters is not easily defined. The estimation of realistic errors is very difficult and extremely model-dependent. This is partly due to the large number of sources of error, many of which it is unrealistic to quantify, and partly to the inevitable trade-off between the different modelling parameters which are very much dependent on one another. Radiation pattern, location errors, incorrect correction for attenuation and other path effects, heterogenities in the velocity structure of both the source and the receiver area, and the resolution of the model itself given the constraints of the available data are some of the main sources of error. Fault plane solutions for all the earthquakes studied here have been calculated using a high resolution method (RAMP, described above) so the errors in the radiation pattern are negligible compared with other sources of error. Most of the events presented in this study are sufficiently deep (15 - 200 km) to resolve depth phases (*pP*, *sP*) which can be seen on the broadband seismograms. As a result, depth is a well resolved parameter here, its constraints being within $\pm$ 2 km.

Figure 2.14 demonstrates the general effects on the synthetic seismograms of varying the different model parameters such as fault radius, rupture velocity, stress drop and depth. Altering the radius by $\pm$ 0.5 km significantly decreases the fit between the observed seismogram and the model, as does altering the rupture velocity by $\pm$ 0.2 km s^{-1}. The alteration of the depth by $\pm$ 1 km has the same effect.

Since stress drop is proportional to the pulse amplitude, and it is completely independent of the pulse duration, it is used to give an exact (peak-to-peak) amplitude fit of the *P* phases at each station. It is then possible to calculate the mean stress drop, over all stations, and its 95 % confidence limits, which are the errors quoted in Table 4.3 and Table 6.3. From this mean stress drop and its confidence limits, the mean seismic moment and its confidence limits can be calculated. Here the confidence limits represent the 95 % zone which is equal to:

$$\bar{x} \pm 1.96\,\sigma \qquad (2.6)$$

where σ is the standard deviation of the mean $\bar{x}$. Ideally, these values should include errors in radius, depth and rupture velocity since all affect the pulse amplitude as well as its duration. A total error of about a factor of 2 in seismic moment, and perhaps slightly more in stress drop is probably more realistic.

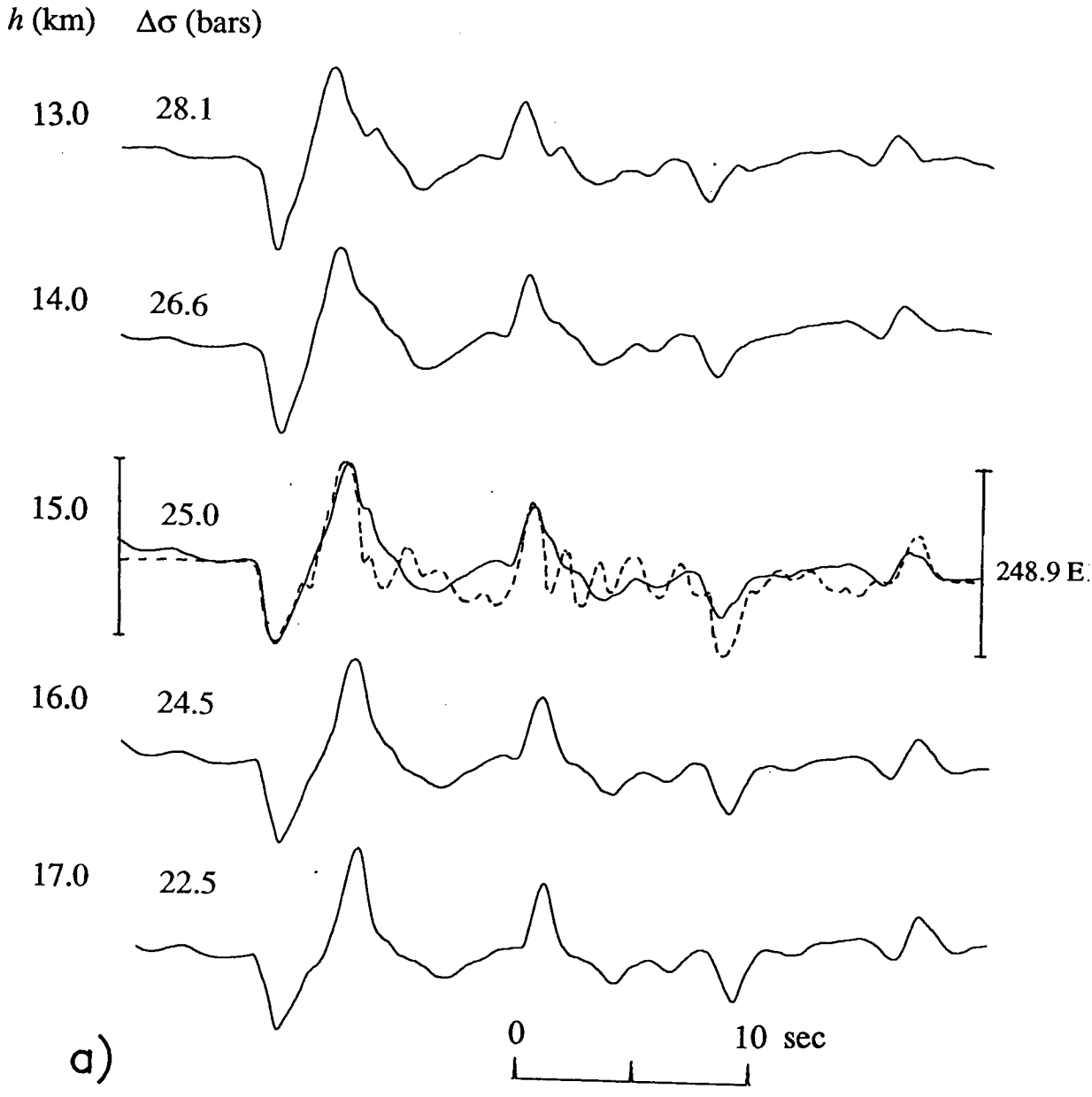

Figure 2.14. Models of the 3/5/80 Aleutian earthquake at SHIO (BBD) to show errors and resolution. All the models *(solid lines)* are scaled to fit the observed amplitudes using stress drop. a) Varying depth (4.0 km radius, 2.5 km/s rupture velocity). b) Varying radius (15.0 km depth, 2.5 km/s rupture velocity). c) Varying rupture velocity (15.0 km depth, 4.0 km radius).

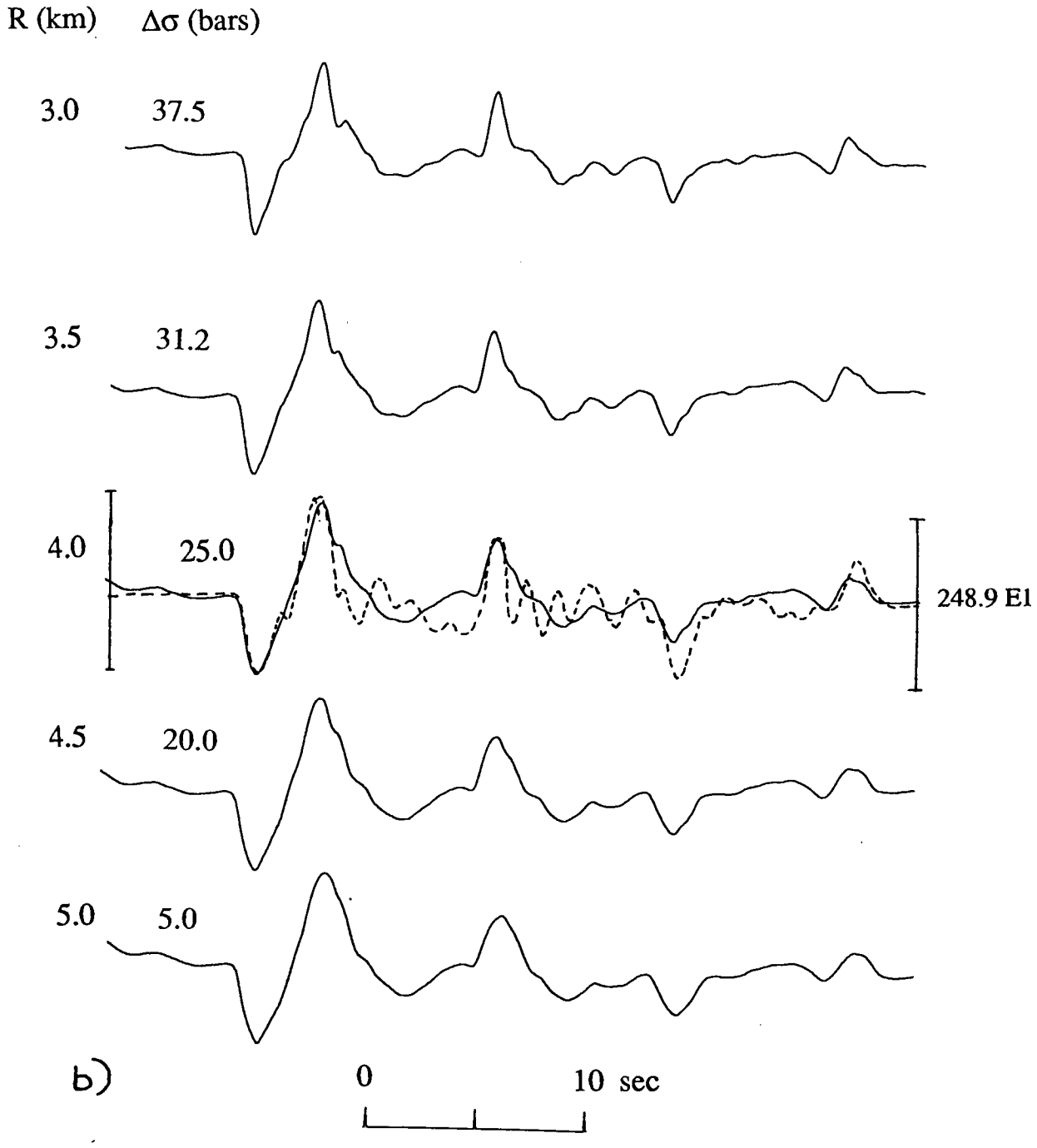

Figure 2.14. (continued).

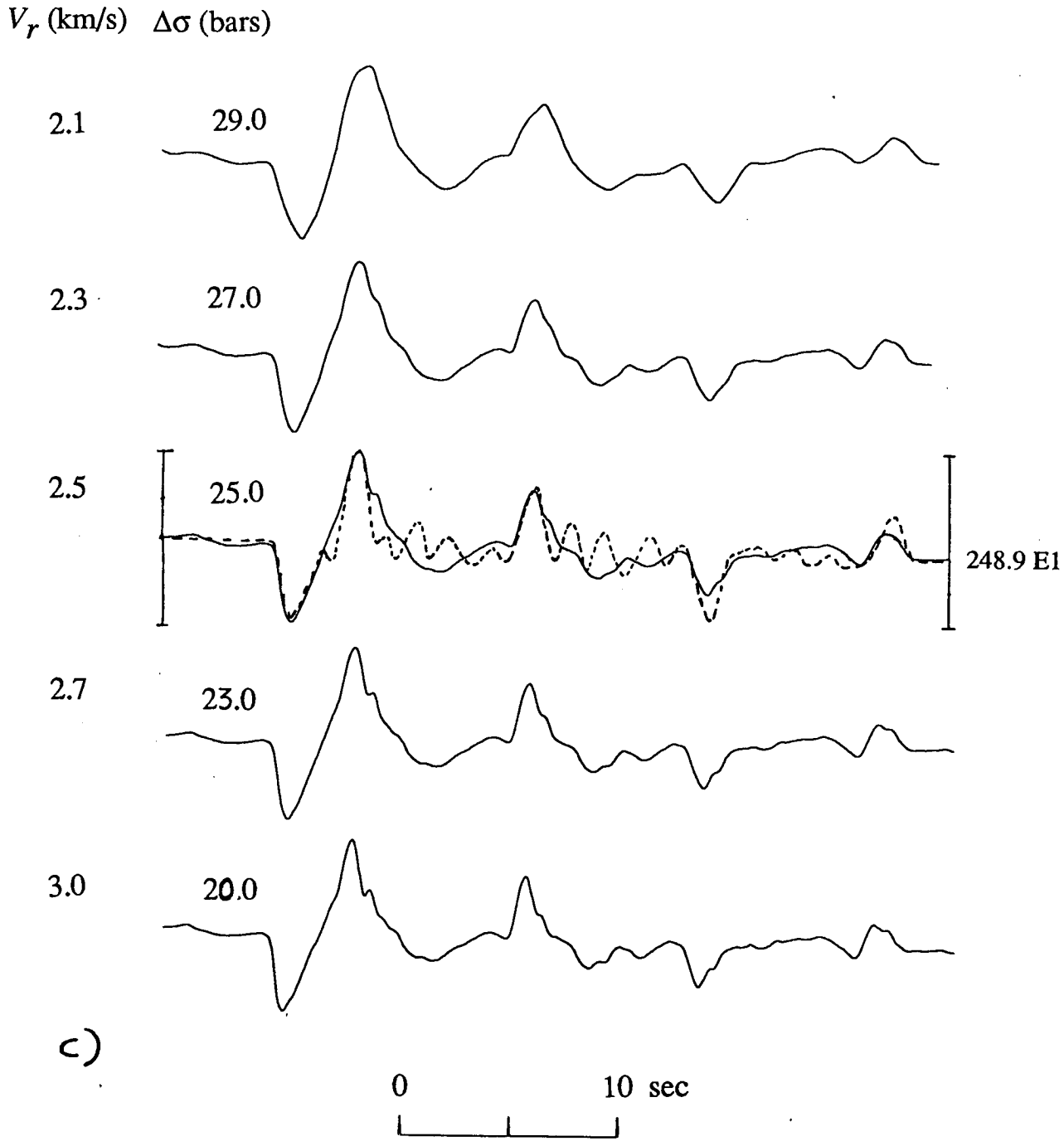

Figure 2.14. (continued).

a. Sensitivity analysis

The relative errors and the resolution of the modelling parameters are discussed in the sensitivity analysis by Abercrombie (1991). There, a quantitative analysis is carried out to investigate the relative sensitivity of the model to the different modelling parameters, and also a comparison is made of the modelling using deconvolved and long-period data. Each model parameter is varied in turn, whilst the others are held constant. The fit of the perturbed model to the observed is characterized in terms of both the peak-to-peak amplitude (A) and duration (T) of the P phases:

$$E_A = \frac{A_m - A_o}{A_o} \tag{2.7}$$

$$E_T = \frac{T_m - T_o}{T_o} \tag{2.8}$$

where E_A is the error in amplitude, E_T, that in the duration, and subscripts m and o indicate model and observed respectively.

$$RMS\ error = \sqrt{(E_A^2 + E_T^2)} \tag{2.9}$$

The results (Fig. 2.15) show clearly that, for broadband data, the parameters in order of increasing sensitivity are: depth, stress drop, radius and rupture velocity, and for long-period data, depth, stress drop, rupture velocity and radius. The more sensitive the model is to a parameter, the more reliably the parameter can be determined.

A similar sensitivity analysis is also carried out here in order to confirm that the above results are applicable and valid for the present study too. As is seen on Fig. 2.16, the two analyses give similar results, although the most sensitive parameter is here the rupture velocity. Perturbation of depth, rupture velocity, fault radius and stress drop values of the preferred model results in variation of peak-to-peak P-wave amplitude and duration. All four parameters are proportional to the amplitude and duration, except from the rupture velocity which is the only parameter inversely proportional to the duration. Decreasing the rupture velocity by 30 % increases the duration by 20 % and decreases the amplitude by 25 %. A similar increase in the duration can also be obtained if the fault radius only increases by 50 %. However, in the latter case an increase of 150 % in the amplitude is caused. To compensate for this, a decrease of approximately 165 % in stress drop would be required. An increase of 50 % in the fault radius also requires an increase of 40 % in the rupture velocity if the duration is to be kept constant. Both the above variations cause an increase in amplitude of 300 % which is cancelled out by a decrease in stress drop of 330 %. Therefore, although the model parameters are very much dependent on each other, the model is very sensitive to small variations of these parameters as shown in Fig.

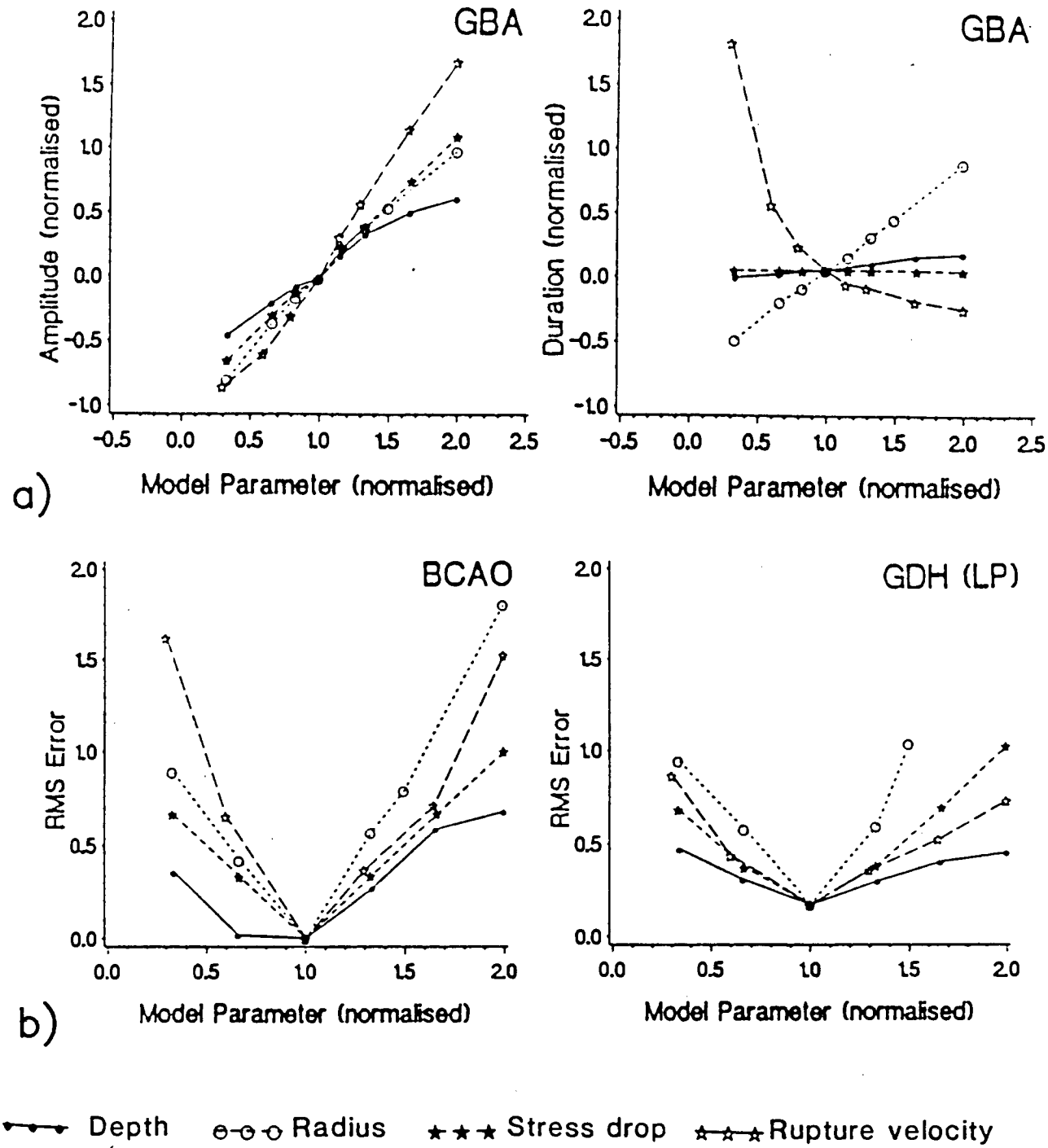

Figure 2.15. Sensitivity analysis of models for the 24 February 1981 earthquake (Greece) (Abercrombie, 1991). The models are perturbed by varying each of the model parameters in turn, and comparing the fit of the perturbed model to the amplitude and duration of the *P* phases. All analyses are of BBD data except where LP is specified: **a)** Error in amplitude and duration relative to the observed, plotted against the model parameters (normalised by dividing by the parameter value of the best model). **b)** RMS error in amplitude and duration combined, plotted against the normalised parameter values.

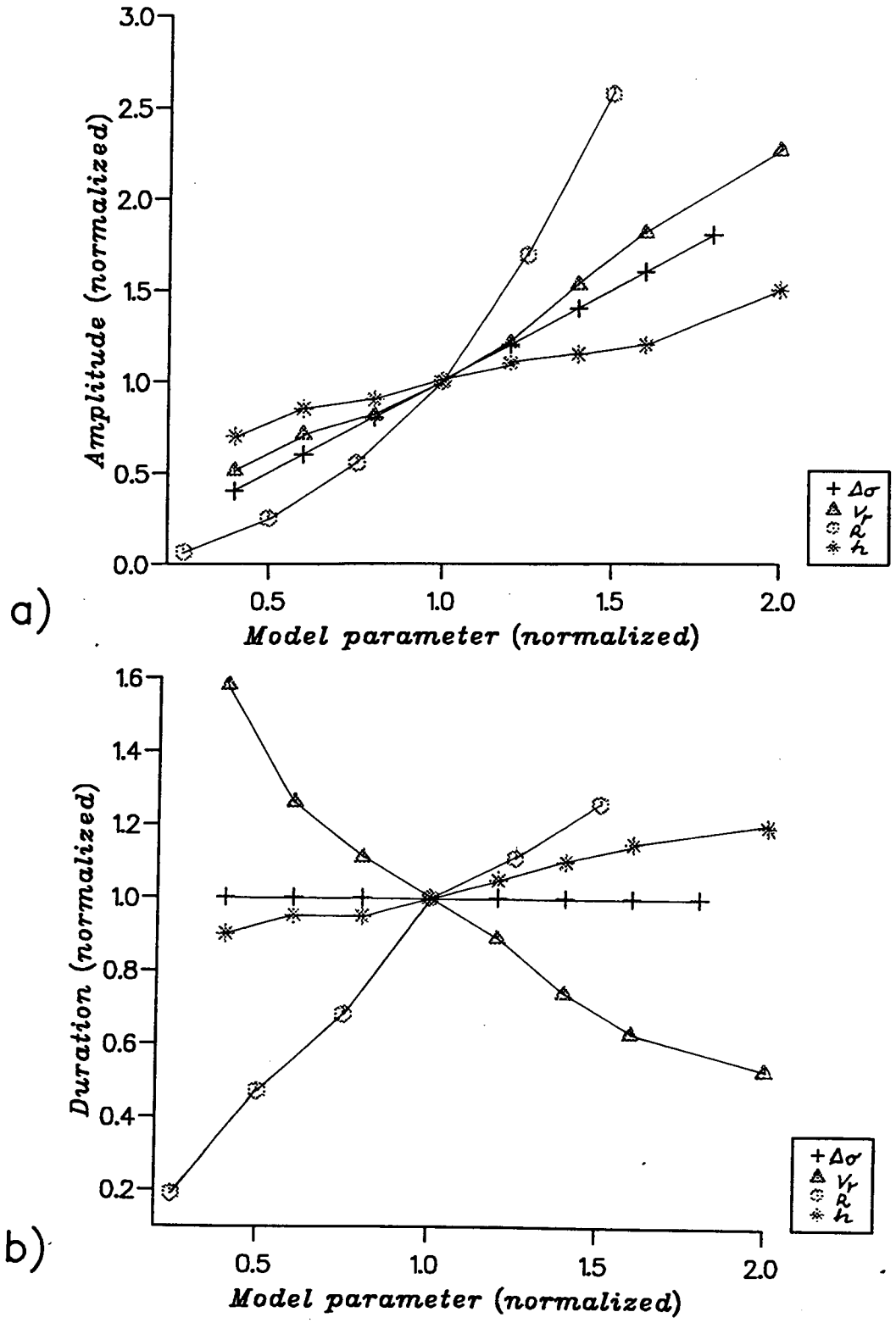

Figure 2.16. Sensitivity analysis of models for the 3 May 1980, Aleutian Islands earthquake. The models are perturbed by varying each of the model parameters in turn, and comparing the fit of the perturbed model to the amplitude and duration of the *P* phases. All analyses are of BBD data: a) Error in amplitude relative to the observed, plotted against the model parameters (normalised by dividing by the parameter value of the best model). b) Error in duration relative to the observed, plotted against the model parameters (normalised by dividing by the parameter value of the best model).

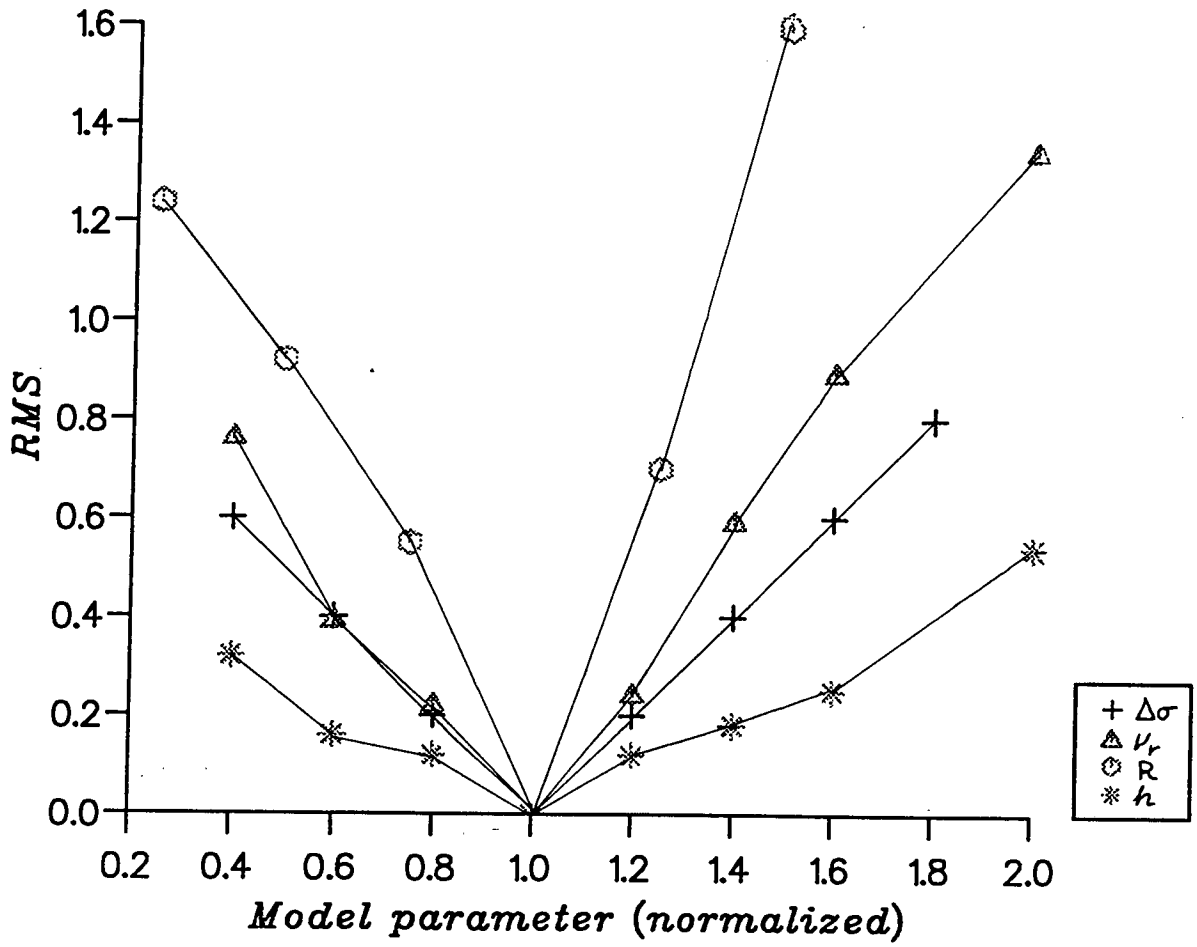

Figure 2.17. *RMS* error in amplitude and duration combined for the 3 May 1980, Aleutian earthquake, plotted against the normalised parameter values.

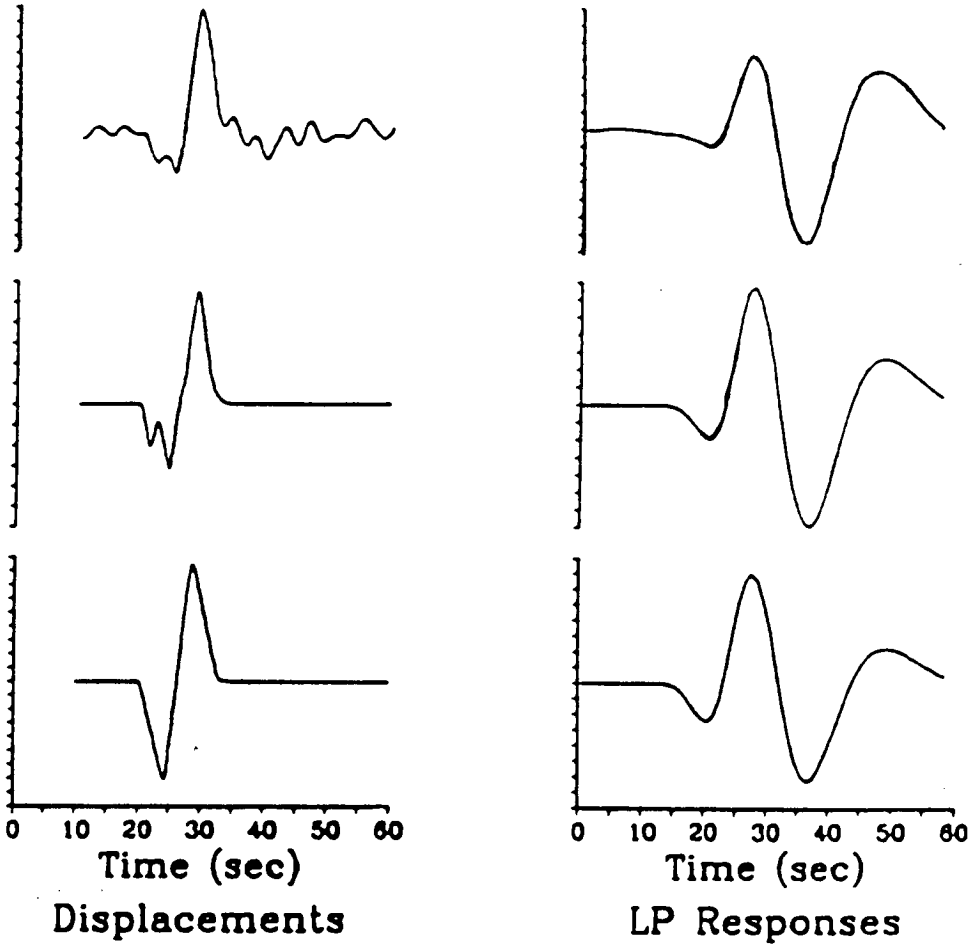

Figure 2.18. A comparison of broadband and conventional LP recordings from the North Yemen earthquake, 1982 (Choy & Kind, 1987). Three different broadband displacement pulses (*left column*) and the coresponding responses to convolution with the instrument response of a digital WWSSN seismograph (*right column*). *Top*: the *P*-wave data recorded at SLR. *Middle*: the synthetic BB displacement and LP records obtained using the preferred double event model of this earthquake. *Bottom*: the best synthetics obtained by modelling the source as a single event. The differences between these two models are clear in the BB displacement records, but they are not perceptible in the LP records.

2.17. In contrast with the low sensitivity of depth, in most cases of the modelling carried out in the present study, depth is one of the parameters that is well constrained, due to the greater focal depths of the events studied.

The long-period models are much less sensitive to variations in the model parameters than the broadband models (Choy and Kind (1987); Fig. 2.18), confirming the greater resolution attainable using broadband body-waves instead of long-period data alone. Therefore, the insensitivity of the model to the model parameters is not the main source of error in determining the source parameters.

2.6 SUMMARY

The relative amplitude method is used to determine the source orientations of the earthquakes studied in this thesis, since it puts tight constraints on the fault plane solutions and makes use of the additional information extracted from a seismogram. Even in cases of limited data, the compatible orientations occupy a small fraction of the total orientation space. Broadband seismograms (recovered from short-period records) are utilised because they better represent the displacement at the source than conventional SP or LP records. A two-dimensional finite dislocation model is used in the calculation of the synthetic seismograms, as it is a more realistic representation of the earthquake source than the point-source model, and is sensitive to the variations of the modelling parameters. Body-wave modelling is carried out in order to determine the earthquake source parameters.

CHAPTER 3

TECTONICS AND SEISMICITY OF THE HELLENIC SUBDUCTION ZONE

3.1 INTRODUCTION

The Aegean and the surrounding area is one of the most seismically active regions of the world. In particular the Aegean sedimentary basin is currently being formed by stretching of the continental lithosphere at strain rates (10^{-15} - 10^{-16} s^{-1}) amongst the highest in the world, and the seismicity associated with this subduction/extension process is the highest in Europe (Fig. 3.01). It remains one of the most important natural laboratories for the seismotectonics of distributed continental deformation.

The most prominent features of tectonic origin are, from south to north (Fig. 3.02): a) the *Mediterranean Ridge*, a compressional submarine accretionary prism which extends from the Ionian Sea to Cyprus and follows the trend of the Hellenic arc; b) the *Hellenic trench*, representing the contact point of the African and Eurasian plates with a maximum water depth of 5.0 km; c) the *Hellenic arc*, which consists of an outer *sedimentary arc*, including the island of Crete, and an inner *volcanic arc*, including the volcanoes of Methana, Santorini, Milos; and d) the *back-arc* Aegean area, which includes the Aegean sea, the mainland of Greece, Albania, south Yugoslavia, south Bulgaria and western Turkey.

In this chapter the pattern of the prevailing deformation in the greater Aegean area will be discussed and the associated seismicity will be described.

3.2 GEODYNAMIC MODELS

The Aegean area, like many areas of distributed continental deformation, does not appear to behave like a rigid plate, or even the rigid edge of a larger Eurasian plate (McKenzie, 1978). Various studies, summarized below, have been carried out in order to establish a dynamic model which explains the pattern of deformation observed in the greater Aegean area.

Makris (1976) used gravity and seismic data from Greece and adjacent areas to explain the high seismicity and tectonic activity of the area. Computed 2-D gravity models revealed that below the Aegean region a large "plume" of hot upper-mantle material is rising, causing strong attenuation of the crust. The hot "plume" extends to the

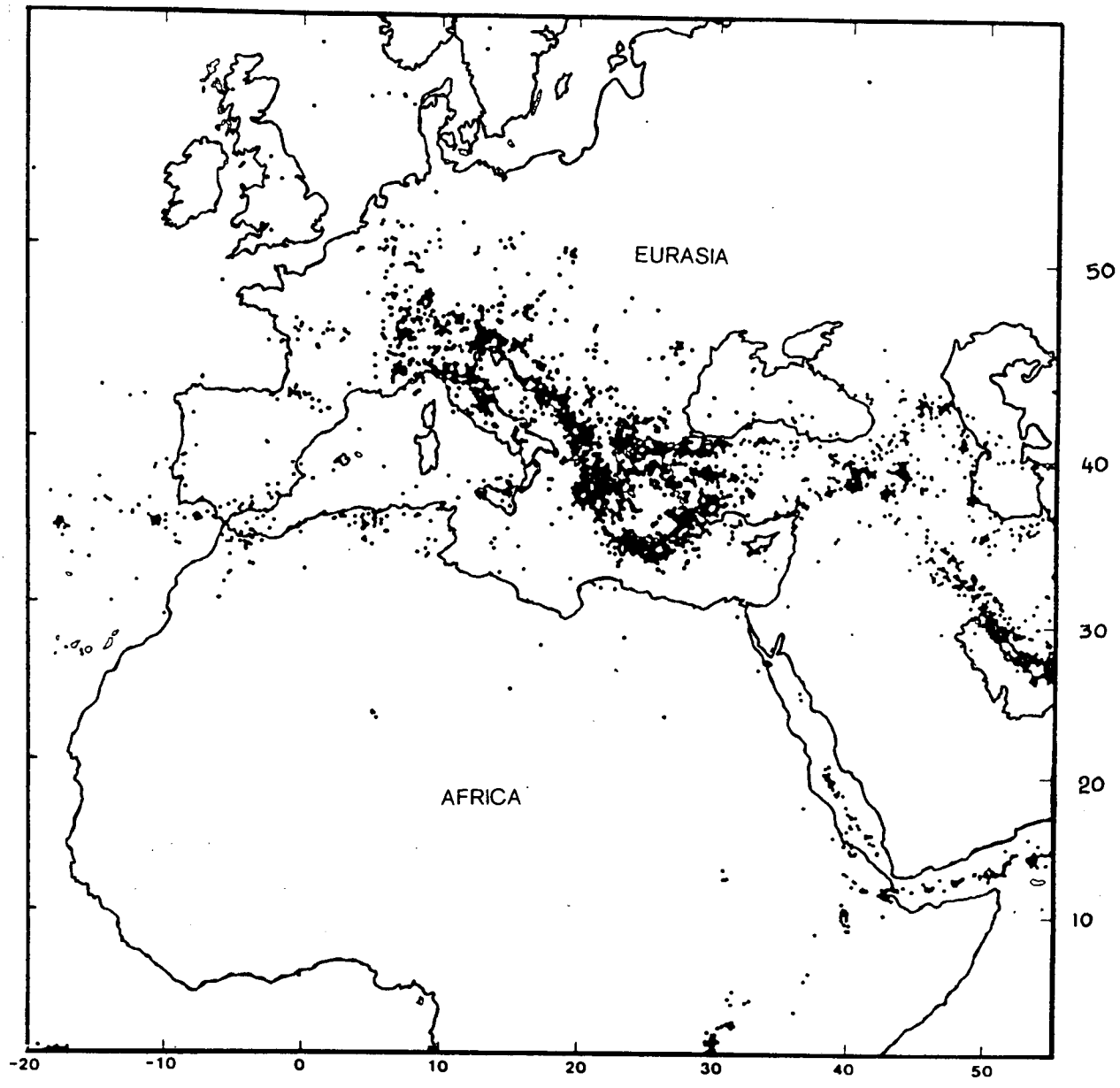

Figure 3.01. Map of earthquake epicentres associated with the African - Eurasian collision, as reported by the USGS from 1961 to 1983.

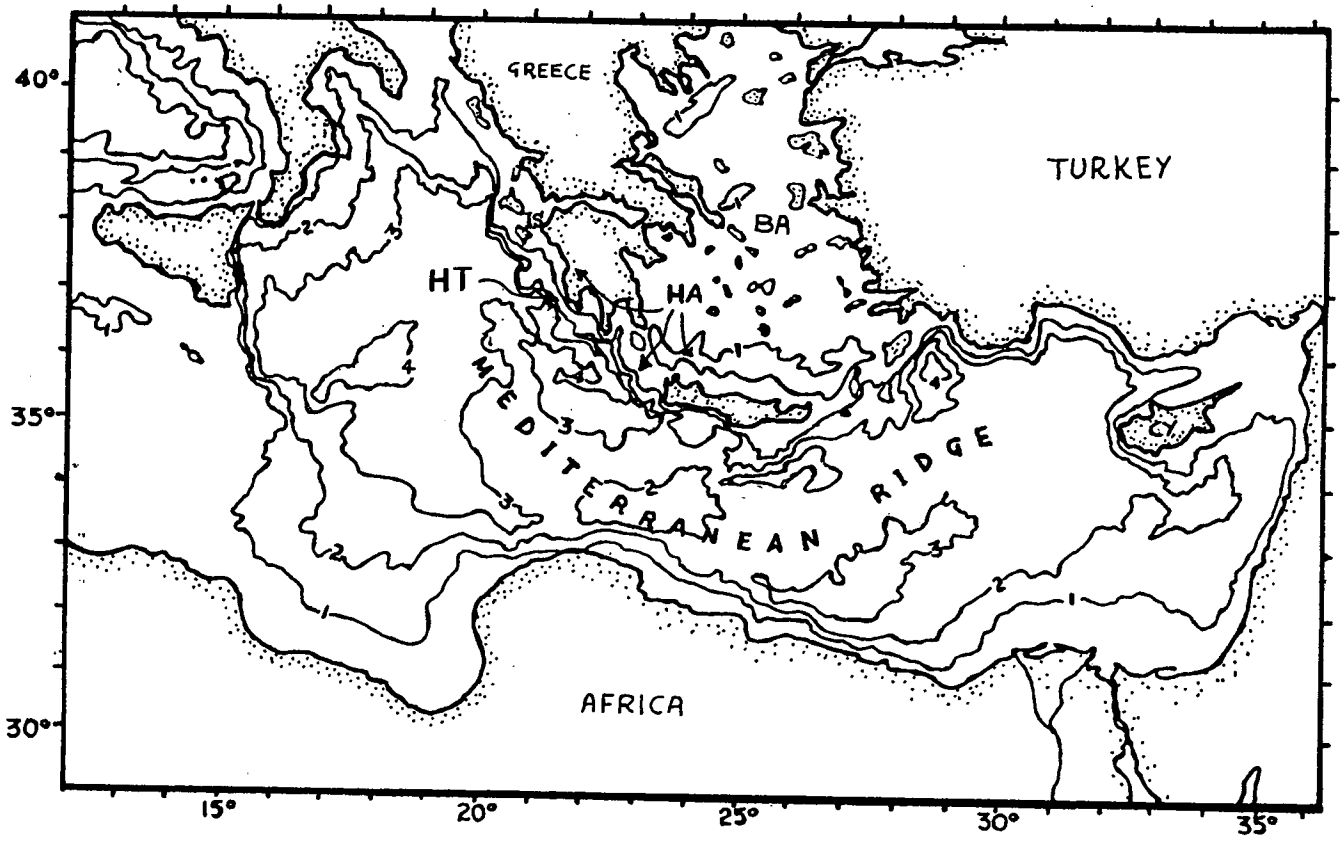

Figure 3.02. The main tectonic features of the Aegean and the surrounding area and the bathymetry of the eastern Mediterranean sea. HT is the Hellenic trench, HA is the Hellenic arc, BA is the back-arc region, IS is the Ionian sea, and and CY is Cyprus.

base of the lithosphere and has very probably been mobilized through compressional processes that forced the lithosphere to sink into asthenosphere. The above model is supported by:

1) high heat flow in the Aegean region;

2) low compressional-wave velocity of 7.7 km/sec in the upper mantle;

3) lower density than normal extending to the base of the lithosphere;

4) teleseismic *P*-wave travel-time residuals of the order of +2 sec for seismic events recorded at the Greek seismic stations;

5) volcanics in the Aegean area with a chemical composition which can be explained by assuming an assimilation of oceanic crust by the upper mantle;

6) deep seismicity (down to 200 km) which has been interpreted by various authors as a Benioff zone.

In a later study, Makris (1977) claims that the collision between the African and the Eurasian plate is of continent-continent or continent-subcontinent type. The deformation at the collision front is plastic and triggers fragmentation of minor irregular blocks that are subducted in the low *Q* upper mantle, causing intermediate seismicity.

McKenzie (1978) interpreted the deformation of the area as thinning due to a convection cell set up by a slab sinking under the Hellenic arc and a sinking blob of cold crust off western Greece and Albania. With the added knowledge of the available fault plane solutions, McKenzie (1978) interpreted the thin crust as being due to stretching rather than thinning. The Aegean has been stretched by up to a factor of 2 since the Miocene with extension taking place at the present day mainly to the north and east of the volcanic arc. This stretching can account for the high heat flow observed in the back-arc region. The Hellenic trench consists of a number of deep basins between Cephallonia and Rhodes, and it is considerably shallower than the trenches of the western Pacific. The maximum depth of the seismogenic part of the sinking slab is approximately 200 km, though seismic tomography has recently revealed that a cool but aseismic lithospheric slab penetrates deeper than this (Spakman, 1990; Ligdas *et al.*, 1990).

Le Pichon and Angelier (1979, 1981) also interpreted the geophysical observations of high heat flow and thin crust under the Aegean as being caused by crustal stretching. However, they modelled the deformation with a subducting slab, sinking vertically under the Hellenic arc instead of as a part of local convection cell (Fig. 3.03). They proposed that stretching has occurred in response to changing boundary conditions at the Hellenic arc rather than internal convection.

Wdowinski *et al.*, (1989) investigate the large-scale tectonics of back arc environments using a thin viscous sheet model. The model explains the deformation within continental lithosphere that is subjected to horizontal forces on its plate

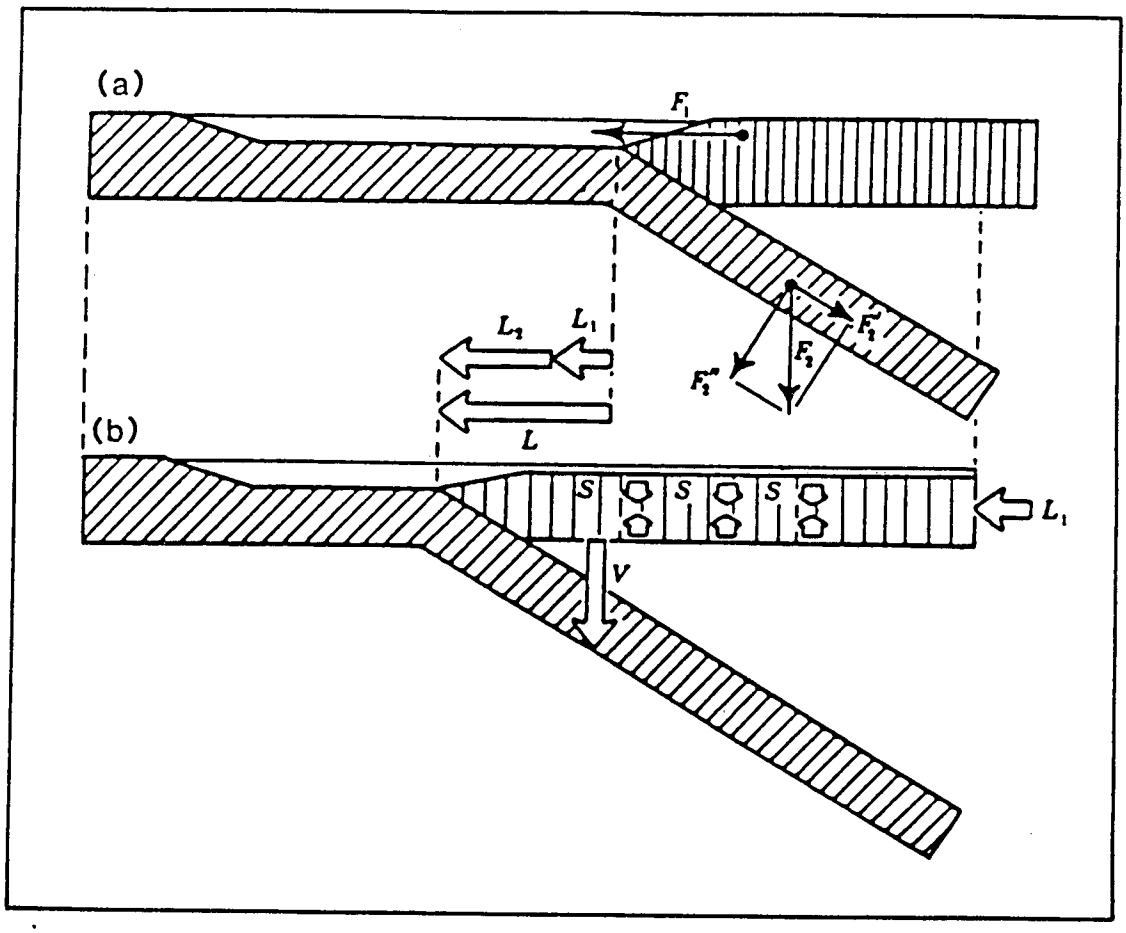

Figure 3.03. A section of the tectonic model of the Aegean by Le Pichon & Angelier (1981). This is a schematic north-south section of the Hellenic subduction zone with relative motions and gravitational forces. North is to the right of the figure. (a) F_1, outward component of the gravitational force acting on the Aegean region, due to its hydrostatic head with respect to adjacent Mediterranean sea crust. F_2, negative buoyancy force acting on the sinking slab, with components F_2' and F_2", parallel and perpendicular to the slab, respectively. (b) L_1, displacement of Eurasia relative to Africa; L_2, displacement of the Hellenic arc relative to Eurasia due to the Aegean expansion (L_2 is probably 3 or 4 times larger than L_1); L, total displacement of the Hellenic arc relative to Africa; S, subsidence of the Aegean region due to lithospheric thinning (double arrows), and subsequent transgressions; V, vertical motion of the sinking slab. The vertical disappearence of the sinking slab creates a trench rollback which allows the hinge point of the Hellenic arc to retreat.

boundaries, and to basal drag from the asthenospheric flow beneath. The shear tractions acting on the base of the deformable lithosphere are derived from a corner flow model that assumes a rigid subducting plate and a deformable overlying plate. The calculated shear tractions and the deformation within the overlying plate are interdependent so the corner flow and the thin viscous sheet models are solved simultaneously. Their model predicts that in an extensional environment a zone of compression can develop near the trench and that extensional strain rate can increase with distance from the trench. This is observed in the Aegean.

3.2.1 The age of subduction

A crucial problem for the evolution of the Hellenic arc is the age of the Aegean expansion - Hellenic subduction process. Angelier *et al.* (1982) claim that the subduction process started 13 my ago with an error of 3 to 5 my. The evidence for this was:

a) The position of the tip of the subducted slab relative to 2.7 my old volcanoes of the inner arc corresponds to that age, provided that the rate of underthrusting was constant.

b) Kinematic considerations while comparing the Africa-Europe and the Hellenic arc-Europe rotations, and taking into account the continuity between the northwestern extremity of the arc and mainland Europe.

c) Geological studies: the late Miocene extension of the Aegean basins does not differ markedly from the Plio-Quaternary normal faulting; i.e. stratigraphic analyses in southern Aegean clearly demonstrate that the intense normal faulting that resulted in the destruction of the early-middle Miocene landmass began at the end of the middle Miocene.

Jackson and McKenzie (1988), assuming that the convergence rate of the subduction has been constant in time, believe that the deepest seismically active portion of the sinking slab, which is 400 km long near Kos, began to be subducted only 5 my ago. This is in agreement with Mercier *et al.* (1976) and McKenzie (1978), and also with palaeomagnetic results (Kissel and Laj, 1988, Morris, 1990).

3.3 FAULTING AND DISTRIBUTED DEFORMATION IN THE AEGEAN AREA

Knowledge of the orientation and other seismogenic properties of faults in a region is of great importance not only for theoretical purposes (e.g. seismotectonics) but also for practical reasons (e.g. seismic risk). The determination of these properties, however, is a difficult task since detailed mapping of surface fault traces can be achieved only for a limited number of strong shallow earthquakes on land. For this reason, several other

indirect methods have been tried (fault plane solutions, geological and geomorphological methods, Landsat photographs, distribution of aftershock foci, etc.). Papazachos *et al.* (1984) used fault plane solutions of shallow earthquakes and information on surface fault traces in combination with other seismic, geomorphological and geological information, to determine the type of faulting in the Aegean area (Fig. 3.04). According to their results, a zone dominated by thrust faulting is formed parallel to the coast along western Albania and the westernmost part of central Greece. The central part of this zone is dominated by purely thrust faults dipping towards the continental side, with a slip vector trend normal to the coast. In the northern and southern parts of the zone the faults are dextral strike-slip with thrust components and the slip vector is parallel to the coast.

Along the convex side of the Hellenic arc the shallow thrust faults have an almost constant NW - SE strike and the slip vector plunges consistently to NE (Fig. 3.04). That is, the slip vector is almost normal to the coast in the western part and parallel to the coast in the eastern part. This slip motion is considered to be a result of the convergence of the African lithosphere with the Eurasian lithosphere at the Aegean.

In the southern part of the area (Crete) and just north of the thrust zone, a zone of normal faulting is formed (Papazachos *et al.*, 1984). The slip direction in this zone (SW - NE) is almost parallel to the slip direction in the thrust zone along the convex side of the Hellenic arc.

Further north, a zone of strike-slip faulting between central Peloponnese and southwestern Turkey (Peloponnese-Cyclades-Dodecanese-southwestern Turkey) is observed. The slip vector along this zone has the same trend as the slip vector in the thrust zone in the convex side of the Hellenic arc. This indicates that there is a relationship between this fracture zone and the subduction along the Hellenic arc. The relationship is probably due to the movement of the aseismic lithospheric block of southern Aegean southwestwards (Papazachos *et al.*, 1984).

Central Greece, western Turkey, southern Yugoslavia and southern Bulgaria are dominated by normal faulting with slip vectors orientated in an almost N-S direction.

In the northern Aegean and in the northwestern part of Anatolia a zone of dextral strike-slip faulting, with considerable thrust or normal component in some cases, is observed. This zone is clearly related to the nothern Aegean Trough and its east extension, the right-lateral strike-slip North Anatolian fault.

However, although some well defined features are recognised, the pattern of deformation in the Aegean and its surroundings is rather complicated.

The kinematics of the deformation in the greater Aegean area is controlled by three factors (Fig. 3.05a): the westward motion of Turkey relative to Europe; the continental collision between NW Greece-Albania and the Apulia-Adriatic platform in the west; and

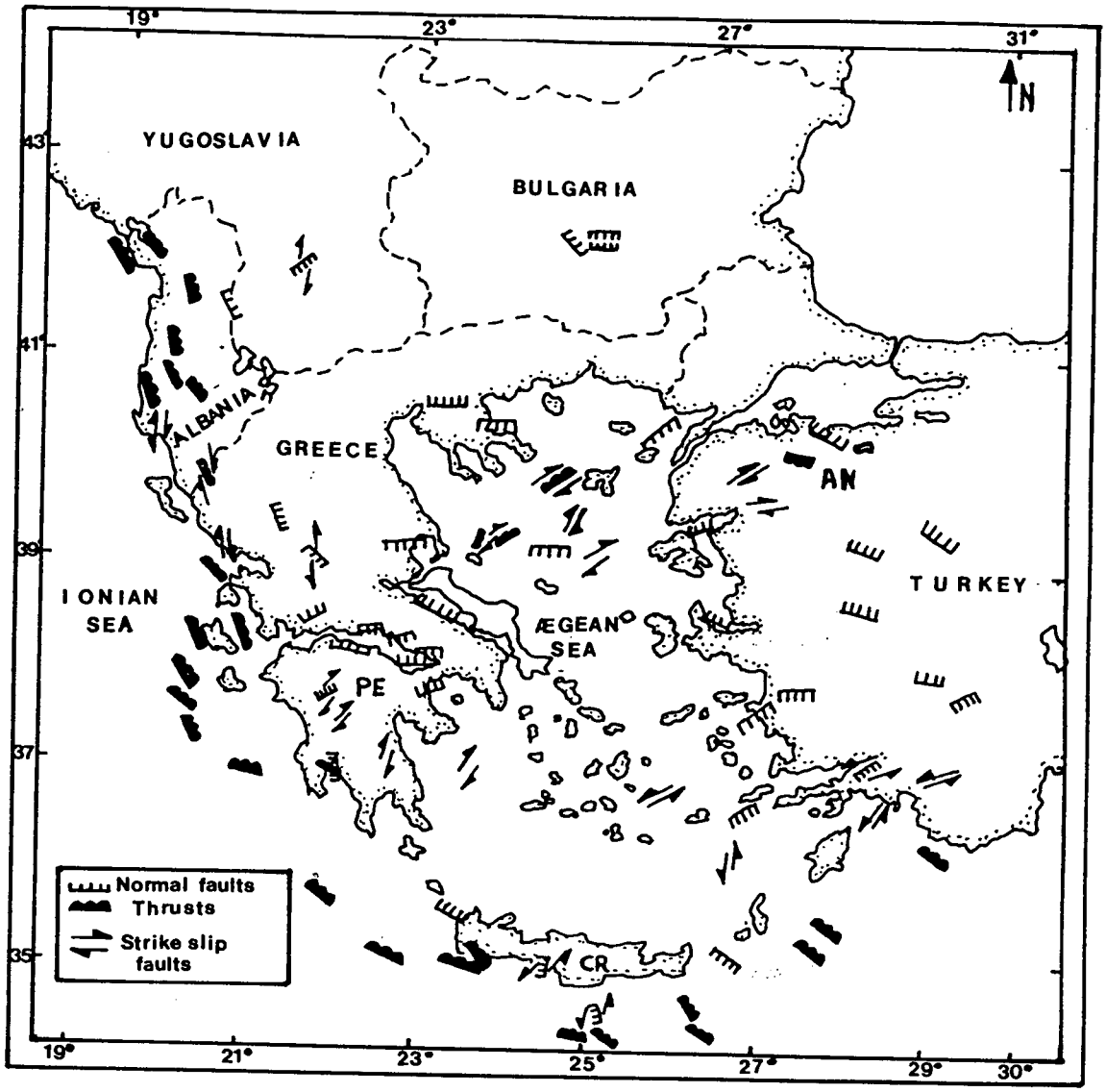

Figure 3.04. Type of faulting in the Aegean area (after Papazachos *et al.*, 1984). CR is Crete, PE is Peloponnese, and AN is Anatolia.

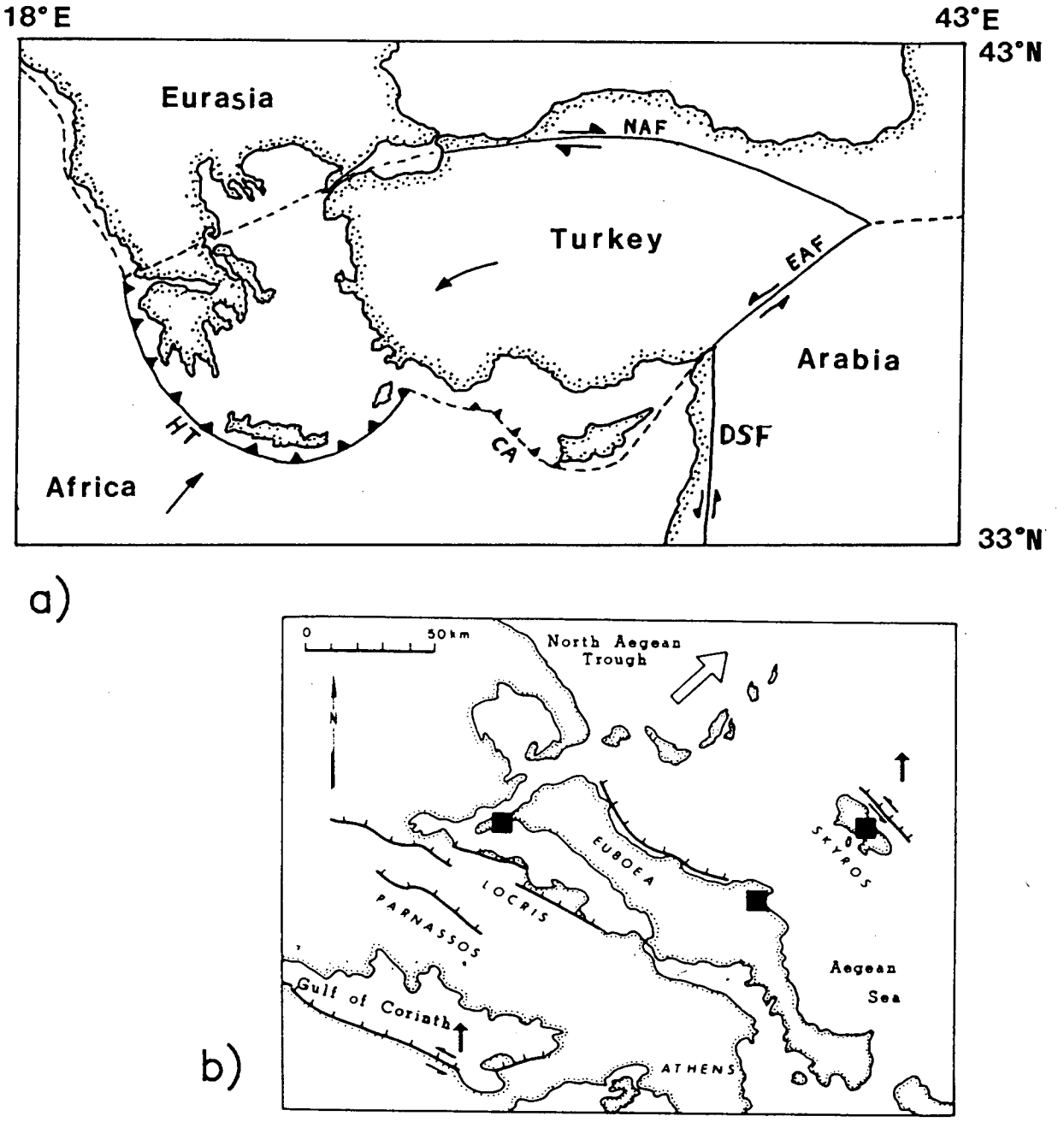

Figure 3.05. (From Jackson and McKenzie, 1988). a) Sketch-map showing the kinematics of deformation in the greater Aegean area. The dashed lines imply possible tectonic boundaries. HT is the Hellenic trench, NAF is the North Anatolian Fault, EAF is the East Anatolian Fault, DSF is the Dead Sea Fault, and CA is the Cyprus Arc. b) The main zone of distributed normal faulting in central Greece. Major active normal faults that dip NNE and dominate both topography and bathymetry are shown by heavy lines with ticks on their downthrown sides.

the presence of the Hellenic subduction zone to the south. As the right-lateral slip on the North Anatolian fault reaches the western Aegean, it becomes distributed on several parallel faults (Fig. 3.05b). The continental shortening in NW Greece and Albania does not allow the rotation of the western margin of the region to be rapid enough to accommodate this distributed E-W right-lateral shear, and thus leads to E-W shortening in the northern Aegean. This is compensated by N-S extension as the southern Aegean margin can move easily over the Hellenic subduction zone (Taymaz *et al.*, 1991). This stretching can be balanced by subduction and trench rollback at the Hellenic trench (Spence, 1987; Fig. 3.06).

3.4 THE SEISMICITY OF THE HELLENIC ARC

The Hellenic arc-trench system is a subduction zone of about 1000 km in length. At the northwestern end of the arc the seismically active zone runs into northwestern Greece, while at the eastern end the activity continues into Turkey. The distribution of focal mechanisms of shallow events, figure 3.07, shows the existence of thrust faulting along the coastal region of western Albania, as well as along the westernmost part of mainland Greece. The above-mentioned zone of thrust faulting is due to the collision of two continental lithospheres (Apulian - Eurasian). There is no evidence of subduction in this area.

Thrusting continues south, along the coastal regions of northwestern Greece, up to the island of Cephallonia. The most recent activity that struck this area of the Ionian islands was expressed by the January 17, 1983 sequence. The mainshock and the largest aftershock revealed dextral strike-slip movement (Scordilis *et al.*, 1985; Kiratzi and Langston, 1991; Chapter 4 of this thesis). This belt of dextral strike-slip faulting is considered as the westward termination of the Hellenic subduction zone.

A microearthquake study carried out in Peloponnese by Hatzfeld *et al.* (1989) showed that seismicity in that area is concentrated above 40 km and deeper earthquakes were not numerous. Seismicity under 30 km defines a flat zone at a depth between 40 and 70 km, starting from the trench to about 200 km towards the northeast (Fig. 3.08). Further northeast, the dip of the seismic zone abruptly changes to 45°. Fault plane solutions from the deeper events generally indicate T-axes plunging northeast, within the subducting slab. They interpret the seismicity deeper than 30 km as due to the superposition of two different factors: (a) the steep zone is due to the subduction of the lithospheric plate beneath the Aegean, and (b) the shallow flat zone located between the trench and Argolida is partly due to loading of the overriding Aegean plate.

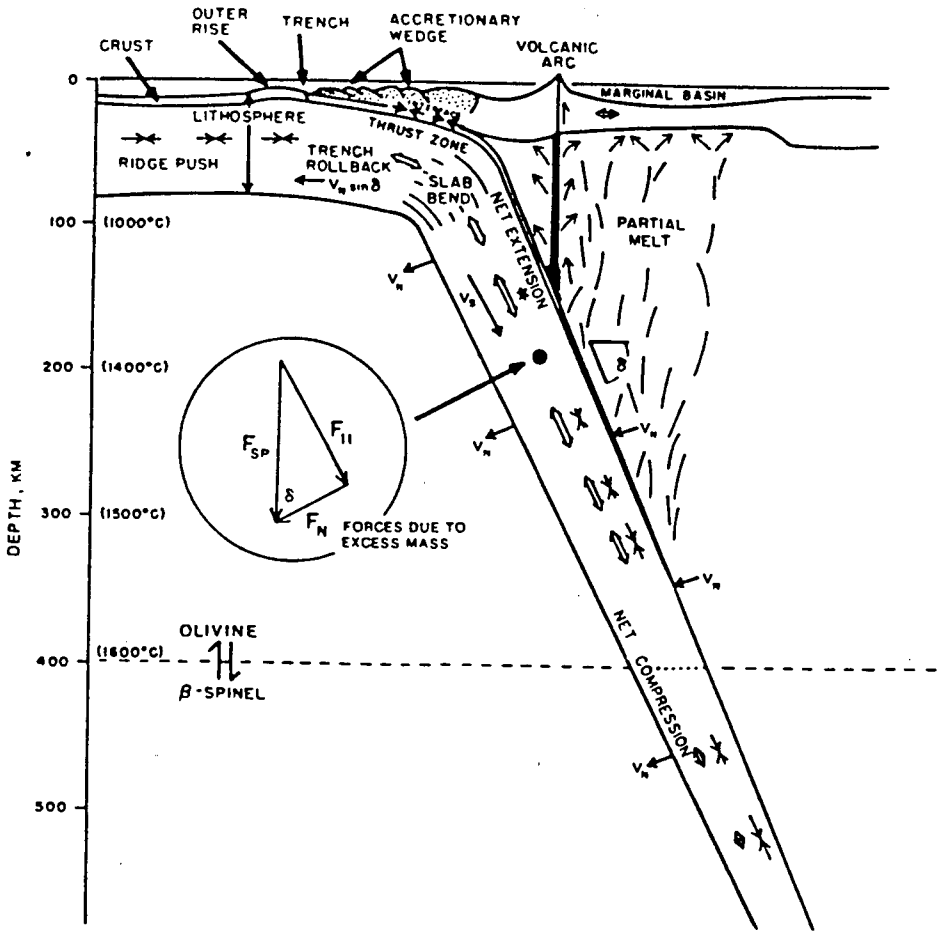

Figure 3.06. Schematic diagram of the role of slab pull force in establishing steady state conditions at a subduction zone. The greatest plate bending is at the slab bend zone, just downdip of the interface thrust zone. Unlabeled arrows within the plate show extension (open arrows) and compression (arrows meeting); the body force at a given depth point is the sum of plate push from above (F_{II}), plate pull from beneath (F_{SP}) and resistive forces (F_N). (from Spence, 1987).

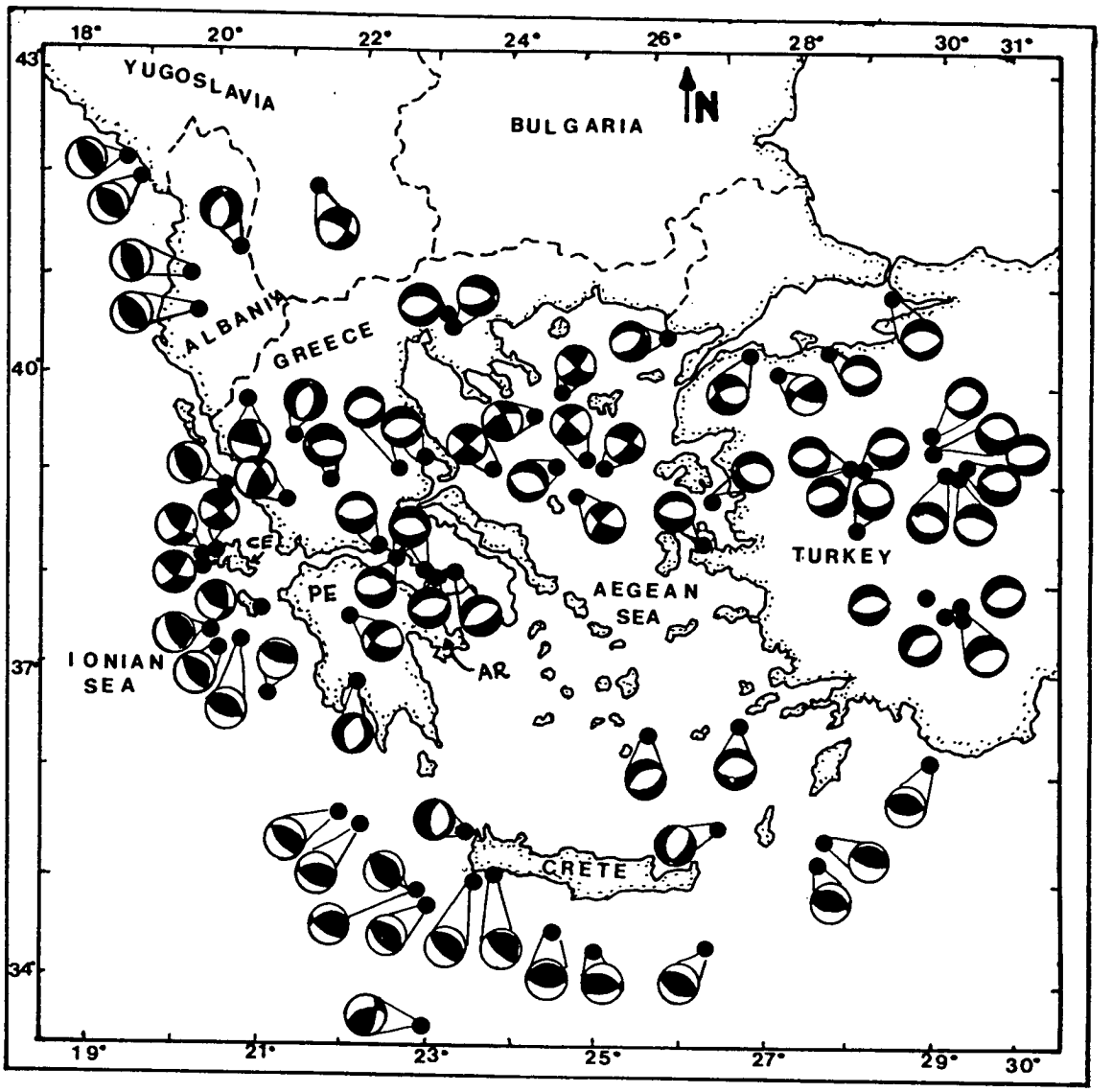

Figure 3.07. Fault plane solutions of the shallow earthquakes of the Aegean and the surrounding area. The data cover the period 1963 - 1986 for events with $M_S \geq 5.5$. The black quadrants denote compression and the blanc quadrants denote dilatation (after Papazachos *et al.*, 1991). CE is the Cephallonia island, PE is Peloponnese, and AR is Argolida.

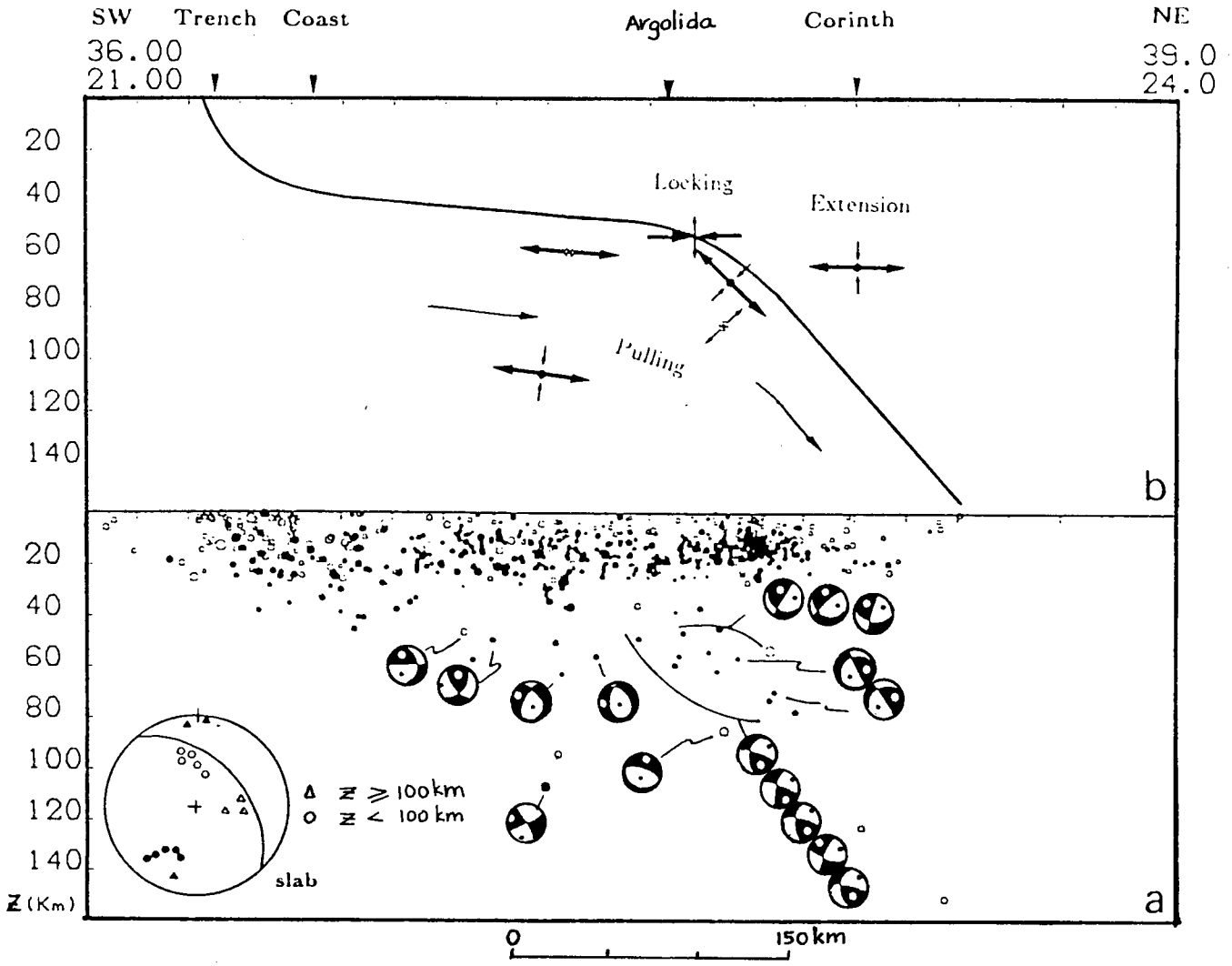

Figure 3.08. Cross-section across the Peloponnese striking NE-SW (Hatzfeld *et al.*, 1989). (a) *Data*: A shallow dipping slab is observed for the first 200 km, and a sudden dipping of the subduction beneath Argolida. Focal mechanisms are shown in section, using a back-hemisphere projection. (b) Interpretation: Only the P- and T-axes are represented here. When the axis is perpendicular to the cross-section it is a cross between a circle. Thick arrows are used for the assumed main driving force. Most of the focal mechanisms located within the slab show a T-axis plunging the same as the slab, and they are consistent with downdip slab pull due to a combination of gravity and the reaction of the underriding lithosphere, due to material displacement by trench rollback. This is also shown by the inset which represents the focal shere with the trace of the slab, the P-axes (black symbol), the T-axes (open symbol). Thrust faulting is observed where the dip changes abruptly, due to probable locking. Extension is obseved down to 70 km beneath the Gulf of Corinth.

Along the convex side of the Hellenic arc (Fig. 3.07), the distribution of focal mechanisms of shallow earthquakes reveals the existence of low angle thrust faulting, with the shallow dipping plane considered as the fault plane (McKenzie, 1978; Papazachos *et al.*, 1984). Papazachos *et al.* (1991) finds that the trend of the P-axis of these events is normal to the arc at its western part and tends to become parallel to the arc at its eastern part. They also show that the focal mechanisms of intermediate depth (> 40 km) earthquakes, that occurred in the southern Aegean area, indicate thrust faulting with considerable strike slip component.

The intermediate-depth seismic activity of the Hellenic arc can be separated into two zones (Fig. 3.09), which correspond to two parts of the Benioff zone (Papazachos, 1990). This dips from the convex side (eastern Mediterranean sea) to the concave side (Aegean sea) of the Hellenic arc. One part shows a low dip angle, approximately 23°, (Fig. 3.10), and includes earthquakes with focal depths between 70 km and 100 km. This part has a high seismicity and is situated below the inner slope of the sedimentary part of the Hellenic arc. Based on the fact that this part of the Benioff zone is a continuation of the seismic zone of shallow earthquakes along the Hellenic arc, and that both zones have the same seismicity, it is concluded (Papazachos, 1990) that they constitute a continuous seismic belt along which coupling occurs between the subducted and the overthrust lithospheres. The inner part of the Benioff zone shows low seismicity with earthquakes of focal depths between 100 km and 180 km. It dips at a mean angle of 38° (same figure) below the volcanic arc of the southern Aegean sea, and it is the result of the subduction of the front part of the eastern Mediterranean lithosphere without coupling with the Aegean lithosphere (Papazachos, 1990).

Another observation made by the same author is that the T-axes of both shallow and intermediate seismicity do not follow the direction of the Benioff zone (and hence the subducted slab). This disagrees with the results of Taymaz *et al.*, (1990), who state that several T-axes of events from the same area are aligned down the dip of the subducting slab, presumably representing the pull of the subducted lithosphere, as seen elsewhere in slabs with seismicity shallower than the 400 km spinel/perovskite phase change (Isacks and Molnar, 1971; Bott, 1982).

3.5 SOURCE PARAMETERS OF EARTHQUAKES IN THE HELLENIC ARC

Studies of the distribution of earthquake hypocentres have shown that the African slab beneath the Aegean has a broad amphitheatre-like shape (Papazachos and Comninakis, 1971; Makropoulos and Burton, 1984; Kondopoulou, Papadopoulos and Pavlidis, 1985) although most of the focal depths have not been obtained with high

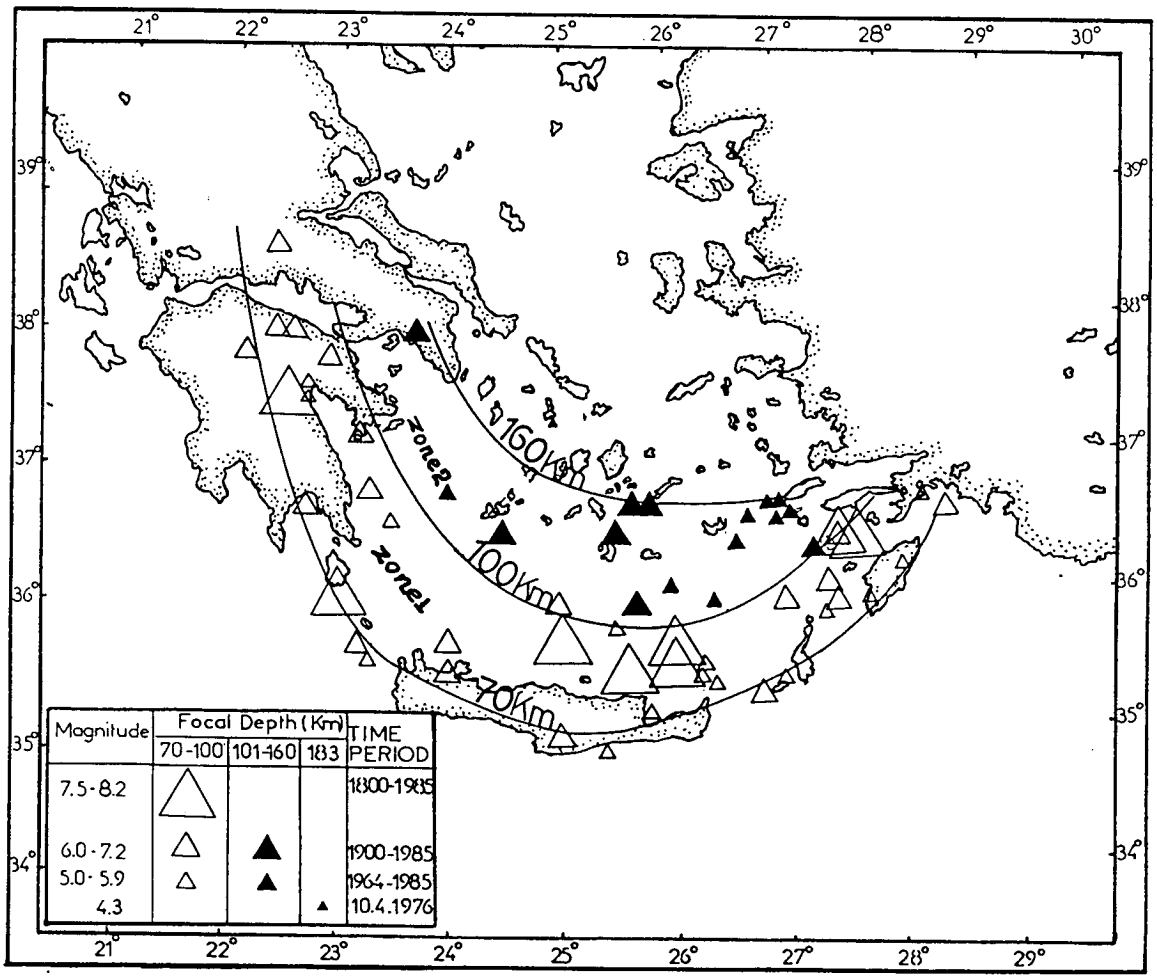

Figure 3.09. The two seismic zones (zone1, zone2) of intermediate-depth earthquakes in Greece (Papazachos, 1990). The volcanic arc is associated with the 150 km contour, as commonly observed in other subduction zones.

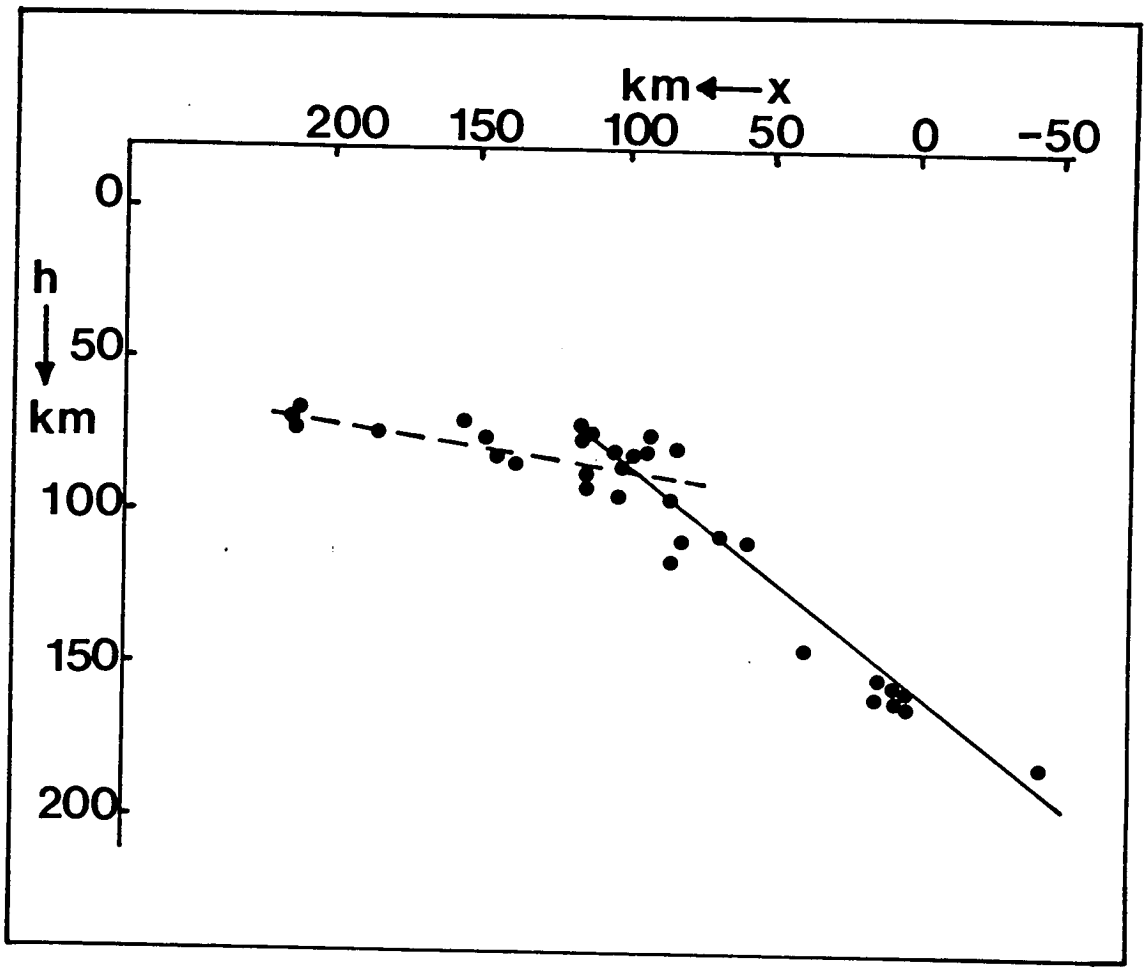

Figure 3.10. The two branches of the Benioff seismic zone in the southern Aegean as shown in a cross-section perpendicular to the Hellenic arc (Papazachos, 1990).

precision. The reported focal depths from the international agencies are usually overestimates, so additional work is needed to determine more accurately the location of earthquake hypocentres, i.e. whether they lie in the Aegean lithosphere or in the underthrusting African lithosphere. For this reason every effort is made in the present work to obtain reliable depths from modelling of the *P*-wave and its surface reflections.

A data set of precise and reliable fault plane solutions is the starting point of any study on the state of stress of subducting slabs. The precise knowledge of the inferred direction of maximum stress has been of primary importance, for example, in the analysis of the stress distribution connected with double seismic zones and with bent or disrupted Benioff zones. However, it is important to note that the direction of maximum stress (σ_1) is not necessarily equal to the *P*-axis in the focal sphere, unless σ_1 happens to be at 45° to the fault plane.

Fault plane solutions for some earthquakes in the Hellenic arc based on first motion polarities are available (Ritsema, 1974; McKenzie, 1972, 1978; Papazachos *et al.*, 1986), but their quality is not always sufficient for accurate studies, especially when using smaller events near the level of background noise. The main drawback of this method is that only one part of the seismogram (the *P*-wave arrival) is used. In the last few years various authors have published fault plane solutions for a number of earthquakes that have their epicentres in the Hellenic arc. Kiratzi and Langston (1989, 1991) determined the source parameters of two events using a body-wave (WWSSN LP) inversion technique. Taymaz *et al.* (1990), using Nabelek's (1984) inversion technique, obtained the focal depths and the fault plane solutions of fifteen events from the Hellenic arc near Crete. Their dataset consisted of WWSSN LP body-waves. Finally, Beisser *et al.* (1990), using BB data from the Grafenberg array and an one-station inversion method, calculated the source parameters of nine earthquakes from the same area.

The previous studies show a variety of different fault plane orientations and types. It is important to establish the degree to which the mechanisms of these events can be well constrained, because they strongly influence the views about the tectonics of the area.

An important parameter expressing the rate of deformation at a tectonic setting is the static seismic moment M_0. Jackson and McKenzie (1988) summed the seismic moment tensors determined by the Harvard group for shallow-focus earthquakes in the Hellenic trench for the time period 1912 to 1976, and concluded that most of the upper-crustal convergence in the Hellenic trench occurs aseismically, with the seismicity accounting for only about 10 per cent of the motion. The estimated moment rate was found to be 8.5×10^{18} Nm yr^{-1} and the rate of subduction 3.0 - 13.0 mm yr^{-1}.

Tselentis *et al.* (1988), using published moments of 45 events in the Hellenic arc between 1950 and 1981, calculated a moment rate of 34 x 10^{18} Nm yr^{-1}; the rate of subduction was found to be 11.3 mm yr^{-1}.

Main and Burton (1989) showed that the total seismic moment release rate for the period 1918 - 81 is only 7.29 x 10^{18} Nm yr^{-1}, and as a result claim that the slab must be sinking almost completely aseismically, except perhaps locally at relatively shallow depths in the underthrusting zone. Second order deformation caused by internal deformation at the slab may well be enough to explain almost all the deeper observed seismicity (Main and Burton, 1989).

Seismic moments seem to have been underestimated for earthquakes in the Aegean area, or M_S overestimated. In figure 3.11 (from Main and Burton, 1989) the relationship between surface-wave magnitude, M_S, and seismic moment, M_0, determined used body waves (a) and surface waves (b) is shown. The relationship is compared with reference lines for stress drops of 5 and 55 bar assuming a theoretical slope of B = 1.5 on the diagrams (Kanamori and Anderson, 1975). The body-wave seismic moments in (a) show a marked systematic difference from the surface-wave moments in (b). The size of the difference is $\delta A = 0.341$. This implies that the body-wave moments are systematically lower than the surface-wave moments for a given M_S by a factor of about 2.1. This is supported by field investigation of active faults in the back-arc Aegean area (Jackson and McKenzie, 1988). An alternative cause of the discrepancy could be that the earthquake surface-wave magnitudes calculated by the ISC for the Aegean are systematically too high by approximately 0.02 units. In some cases very shallow events can appear to have lower moments calculated from body-wave inversions because of interference from reflected *pP* and *sP* phases (Soufleris *et al.*, 1982). Another explanation is that some of the events presented in figure 3.11 are complex, caused by segmented faults with two or three elements separated by a few barriers (Main and Burton, 1989).

Kanamori and Anderson (1975) suggest that the average stress drop value for interplate earthquakes is 30 bar. Kiratzi *et al.* (1985) observed that the earthquakes in Greece are characterized by low stress drop values ranging between 1 to 10 bar. Abercrombie (1991) studied some earthquakes in the back-arc Aegean region and found that the average stress drop for events with $m_b > 5.5$ is 10 bar. Main and Burton (1990) propose two M_S - M_0 relationships for a constant stress drop dislocation model and M_0 in Nm :

$$\log M_0 = 1.5\, M_S + 9.198\ (\pm 0.317) \qquad (3.1)$$

$$\log M_0 = 1.5\, M_S + 8.823\ (\pm 0.248) \qquad (3.2)$$

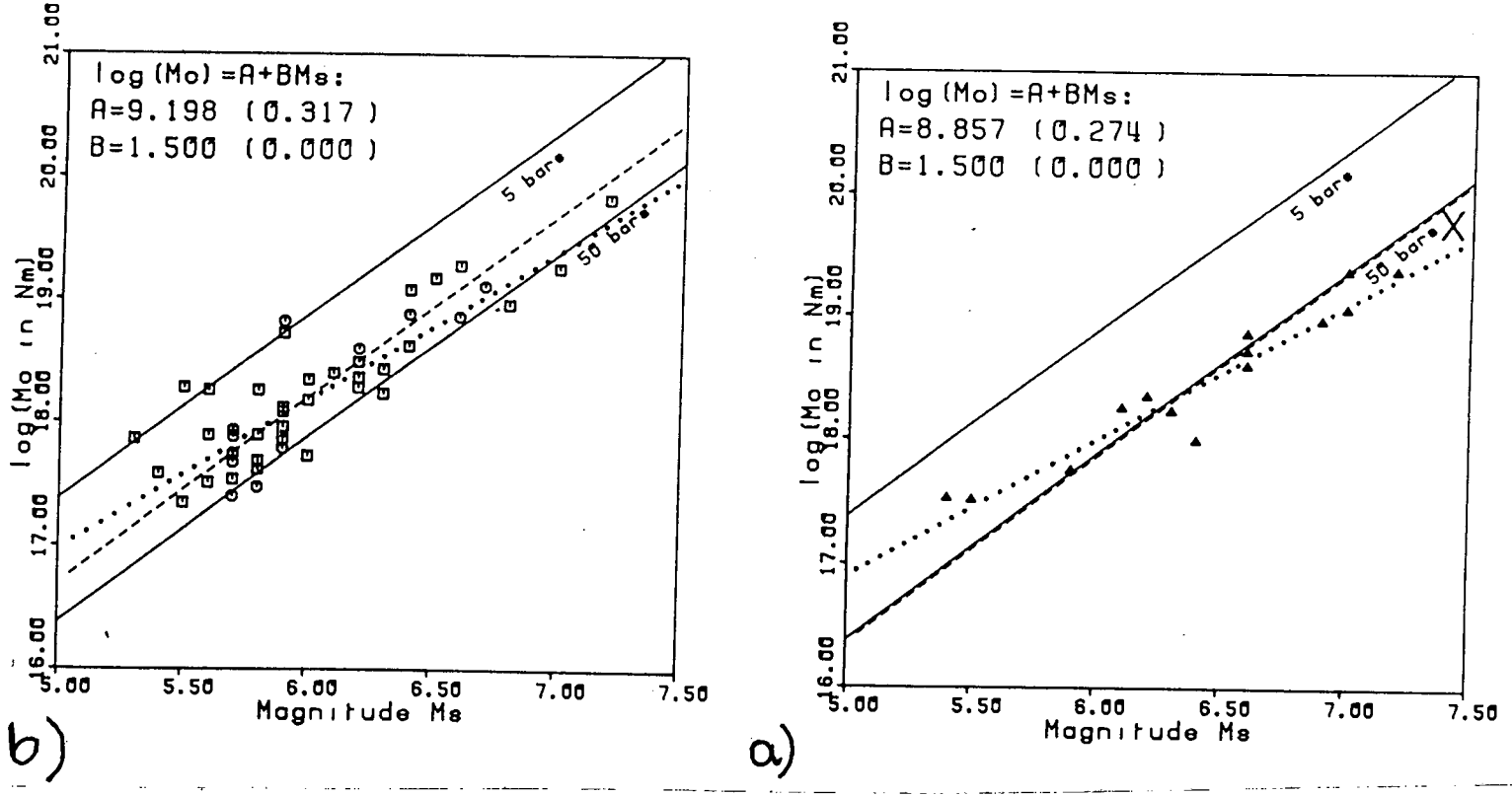

Figure 3.11. (From Main and Burton, 1989). Moment-magnitude plots for Aegean earthquakes. a) various published body-wave determinations, and b) combination of various surface-wave studies. The body-wave moments are systematically lower than the surface-wave moments for a given M_S by a factor of about 2.1. The dashed lines indicate the best fit to the data for B = 1.5. Dotted lines correspond to a least squaresfit allowing variable B. For this line, for the surface wave determinations, it is found that A = 10.970 ($\pm$ 0.632) and B = 1.206 ($\pm$ 0.105). For the body waves, A = 11.409 ($\pm$ 0.612) and B = 1.102 ($\pm$ 0.095).

based on surface and body wave moments respectively. The surface wave results imply stress drops of 25 (+25, -12) bar for the dislocation model, and body wave results imply higher stress drops of 55 (+55, -27) bar.

3.6 DATA USED IN THE PRESENT WORK

In order to study the source mechanisms and other parameters (e.g. depth, fault dimensions, rupture velocity, static seismic moment, stress drop) of recent earthquakes with epicentres in the Hellenic arc, digital seismograms from the GDSN were used.

The events consist of moderate-sized (m_b > 5.5), shallow- to moderate-depth earthquakes. They cover the time period from 1980 to present for which GDSN data are available. GDSN data were preferred because of their digital form, which is necessary when converting SP to produce BB records. During the time period mentioned above, seven earthquakes with magnitudes greater than 5.5, associated with the Hellenic arc have occurred. They were all recorded by a number of GDSN stations and they will be discussed individually in the following chapter.

3.7 SUMMARY

The distribution of deformation in the Hellenic subduction zone reflects the tectonic complexity of the area. Several dynamic models have been proposed in order to explain the pattern of deformation in the area, with a coupled subduction/stretching process being favoured as a general model. These models are based mainly on geological, geomorphological and seismological data from the area, augmented in recent years by satellite and palaeomagnetic data.

The study of the seismicity associated with the subduction reveals important information about the position and slope of the Benioff zone, the seismic energy and moment release in both the sinking and the overriding lithosphere, and the rate of convergence at the subduction boundary. Seismic tomography reveals the possibility of an aseismic extension to the Benioff zone.

The views about the tectonic regime of an area are strongly influenced by the focal mechanisms, focal depths, seismic moments, stress drops and other rupture characteristics of the earthquakes which occur in the area. Therefore it is important that the reliable estimations of these parameters are obtained. The present work aims to reliably evaluate those earthquakes associated with the subduction process, and for which high-quality digital data are available, so that methods based on analogue data or more routine inversions can be tested and calibrated.

CHAPTER 4

SOURCE PARAMETERS OF RECENT EARTHQUAKES IN THE HELLENIC ARC

4.1 INTRODUCTION

Between the years 1980 and 1986, seven earthquakes with magnitudes greater than 5.5 occurred in the Hellenic arc. Table 4.1 shows their origin time, location, depth and magnitude as reported in the ISC bulletins, and Fig. 4.01 shows the ISC location of their epicentres. Determination of the source parameters of these events is attempted in this chapter. Their fault plane solutions are calculated using the relative amplitude method, introduced by Pearce (1977, 1980), which enables the maximum source information to be extracted from the whole seismogram, even if the *P*-wave first motion polarity cannot be read unambiguously.

Forward body-wave modelling has proved to be a good means of determining the parameters associated with the seismic source, such as depth, source dimensions, rupture velocity, seismic moment and stress drop. To carry out such modelling of the Hellenic arc earthquakes, broadband seismograms are used. As mentioned in Chapter 2, when moderate-sized earthquakes are studied teleseismically, the matching of the broadband instrument response to the source duration, and the better resolution of the depth phases on the broadband records than on the long-period records, make their use a great advantage when compared to conventional (SP and LP) records.

For each earthquake the source parameters determined here are described and are followed by results obtained by others using different methods. A comparison, where appropriate, of the various results is attempted in the section 4.4 of this Chapter.

4.2 THE DATA

The data were taken from digitally recording stations of the GDSN. Most of the earthquakes presented in this Chapter were recorded by an adequate number of stations with sufficiently high signal-to-noise ratio to be studied by the methods described in Chapter 2. Some have either few or poorer quality recordings, so that only limited constraints can be placed on focal mechanisms and source parameters. First, both long- and short-period three-component seismograms are used to calculate the fault plane solutions of the earthquakes by the relative amplitude method, assuming a double

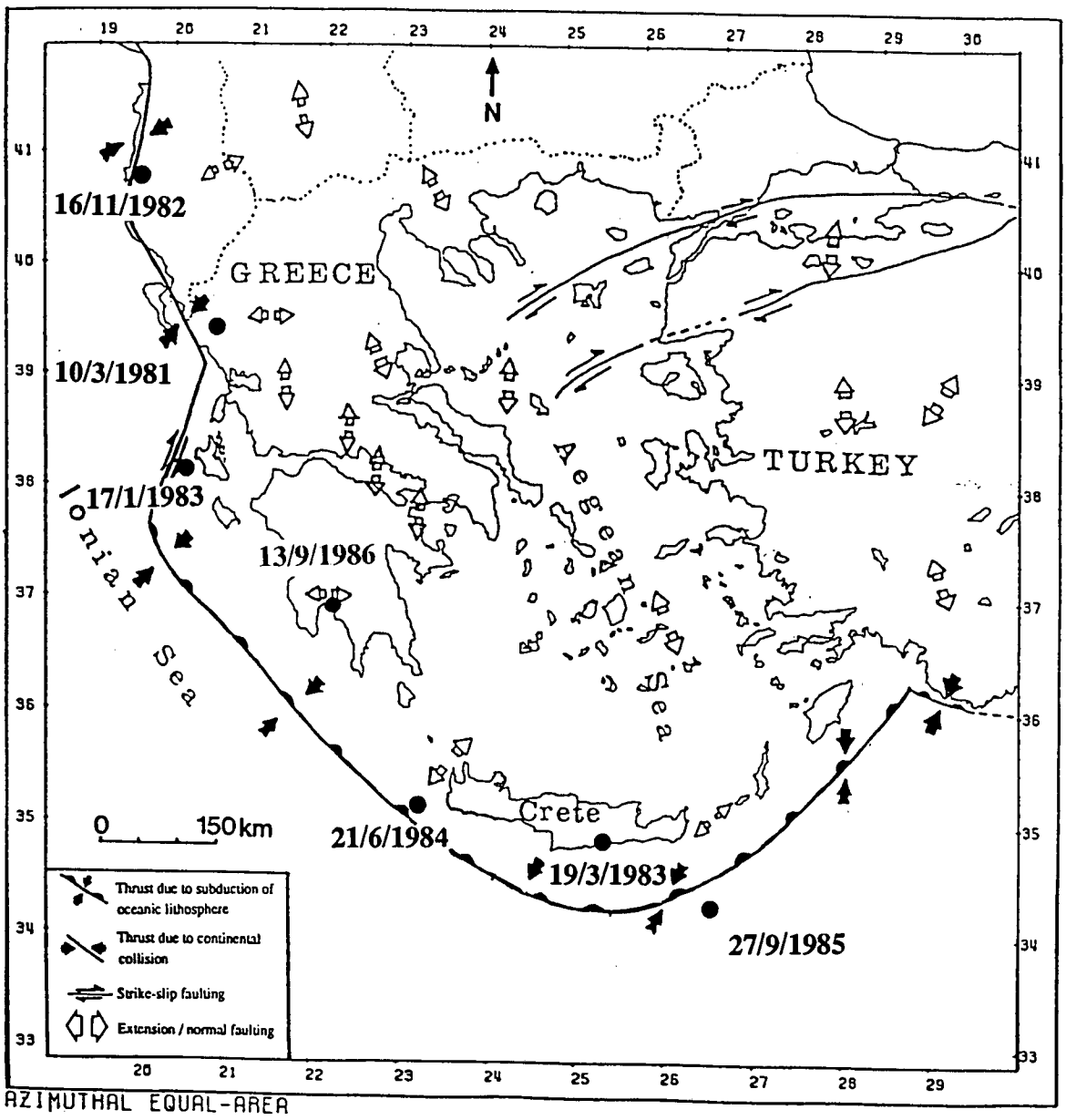

Figure 4.01. ISC locations of the seven earthquakes studied in this Chapter.

couple source mechanism (Pearce, 1977, 1979, 1980). Where possible, additional information is obtained from long-period (LP) World Wide Standard Seismograph Network (WWSSN) records in order to improve coverage of the focal sphere. Since all the events are shallow, only the polarities and amplitudes of the direct body waves (*P*, *SH*, *SV*) can be reliably used in the computation. The *p*P and *sP* surface reflections interfere with the direct *P*-waves in the case of events 3 and 7, and they are not identifiable for the other events.

Table 4.1 Published (ISC) source parameters for seven earthquakes in the Hellenic arc.

Event	Date	Time (h:m)	Lat (°)N	Lon (°)E	m_b	M_s	D (km)	M_o (x10^{18} Nm)
1	10 Mar 81	15:16	39.48	20.69	5.6	5.2	31	-
2	16 Nov 82	23:41	40.82	19.58	5.5	5.7	20	0.32
3	17 Jan 83	12:41	38.07	20.25	6.2	7.0	17	24.0
4	19 Mar 83	21:41	35.02	25.32	5.7	5.0	65	0.33
5	21 Jun 84	10:43	35.36	23.24	5.8	5.9	39	22.0
6	27 Sep 85	16:39	34.40	26.54	5.6	5.2	44	0.33
7	13 Sep 86	17:24	37.01	22.20	5.8	5.8	15	0.98

To obtain broadband seismograms, the instrument response of the GDSN SP records (in the frequency domain) is divided out and multiplied by the broadband (0.1-10.0 Hz) response. It has been shown (Abercrombie, 1991) and has been confirmed by this study (Chapter 2) that short-period data alone, with an instrument response centred on 1 s, are sufficiently broadband to yield reliable records by the deconvolution process described above, for events of magnitude ~ 6.0, with duration of up to a few seconds.

Observed BB records of displacement are then compared with synthetics generated by a source model. The method of Hudson (1969a, b) and Douglas *et al.* (1972) is used. This considers a finite two-dimensional Savage-type source (Savage, 1966) with a homogeneous plane-layered velocity structure near the source and the receiver, and an average anelastic attenuation for the whole path. The source model parameters are

adjusted by trial and error until the best possible fit to the waveforms around the focal sphere is obtained.

4.3 THE EARTHQUAKES

In this section the fault plane solutions and other source parameters obtained from studying the earthquakes listed in Table 4.1 are presented. The earthquakes are presented in chronological order, and are compared to published solutions obtained by alternative methods in the next section.

4.3.1 Event 1 - 10 March 1981, NW Greece

The data used to calculate the fault plane solution of the 10 March 1981 earthquake are shown in Fig. 4.02. They consist of four *P*-wave polarities and horizontal-component S-wave polarities from two GDSN stations. The vectorplot, in the same figure, shows the range of solutions compatible with these data according to the relative amplitude method. On these plots each vector represents an acceptable source orientation defined by its fault plane strike, σ, angle of dip, δ, and slip angle in the fault plane, ψ (Pearce, 1977). The constraints on the fault plane cannot be characterised as tight, but they do indicate a thrust mechanism. The magnitude of this event (m_b = 5.6) is close to the lower limit of the magnitude range that can be recorded teleseismically. The four top traces of Fig. 4.02 show the GDSN SP seismograms from the stations BCAO, KAAO, CHTO and SCP. Although the records show sufficient signal-to-noise ratio, their limited number and complexity do not allow for unambiguous body-wave modelling of the source function.

4.3.2 Event 2 - 16 November 1982, SW Albania

a. Source parameters

Figure 4.03 presents the LP *S*-wave seismograms (lower traces) used to calculate the fault plane solution for the earthquake of 16 November 1982 (Albania). The solutions obtained are shown on a vectorplot. The solutions suggest a strike slip mechanism with a dip-slip component and they are also shown on an equal area projection of the lower focal hemisphere (Fig. 4.04). SP records from three stations (BCAO, SCP, COL) are only available for this earthquake because of its small size (m_b = 5.5). These are shown in the top half of Fig. 4.03. Because the SP records are few and have a low signal-to-noise ratio, body-wave modelling has not been successful for this event.

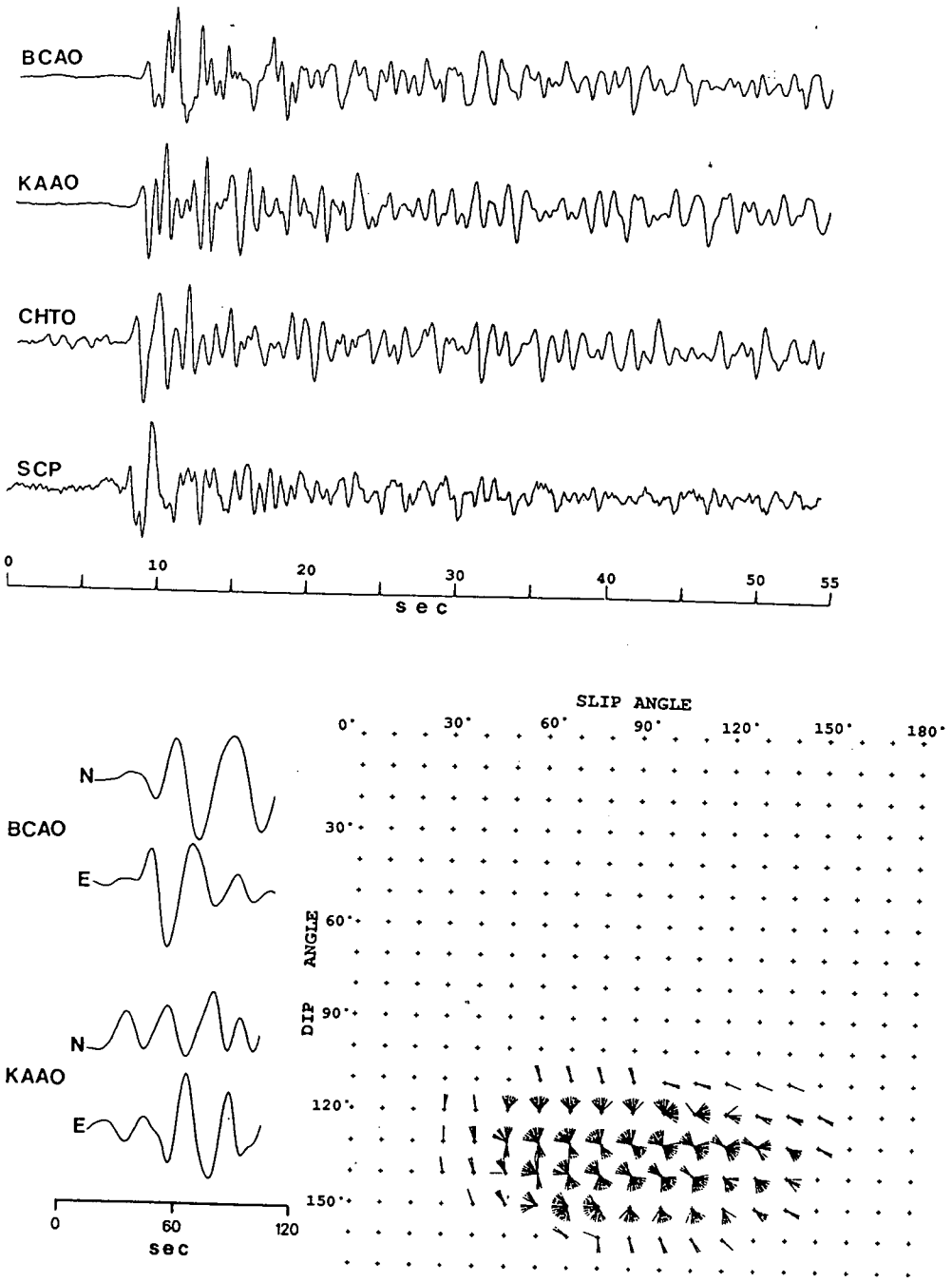

Figure 4.02. Data used to calculate the fault plane solution of event 1. The four top traces represent the available GDSN SP seismograms. The horizontal components (N, E) are GDSN LP *S*-wave seismograms. The compatible solutions obtained for this event are shown on the vectorplot.

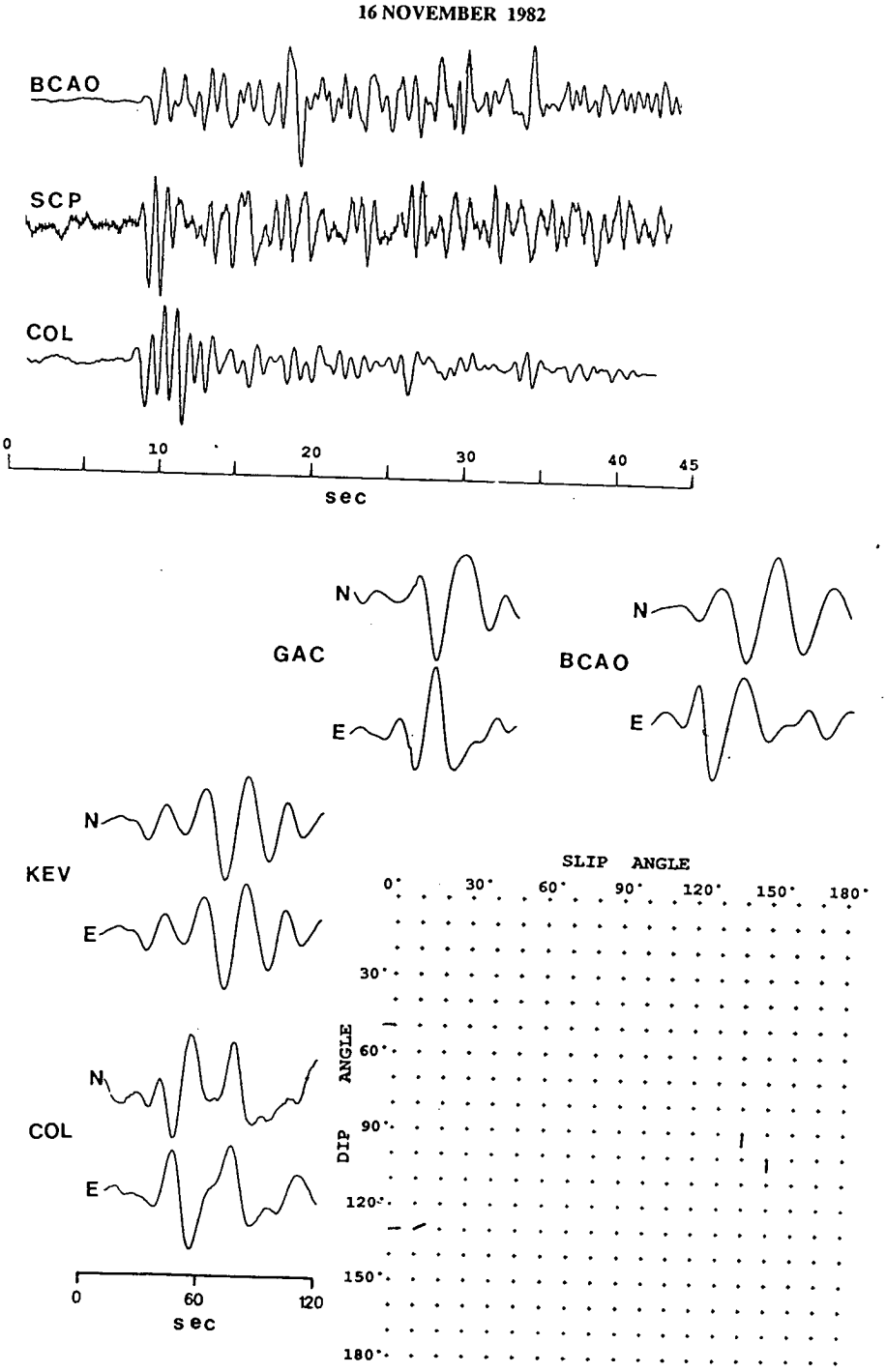

Figure 4.03. Data used to calculate the fault plane solution of event 2. The four top traces represent the available GDSN SP seismograms. The horizontal components (N, E) are GDSN LP *S*-wave seismograms. The compatible solutions obtained for this event are shown on the vectorplot.

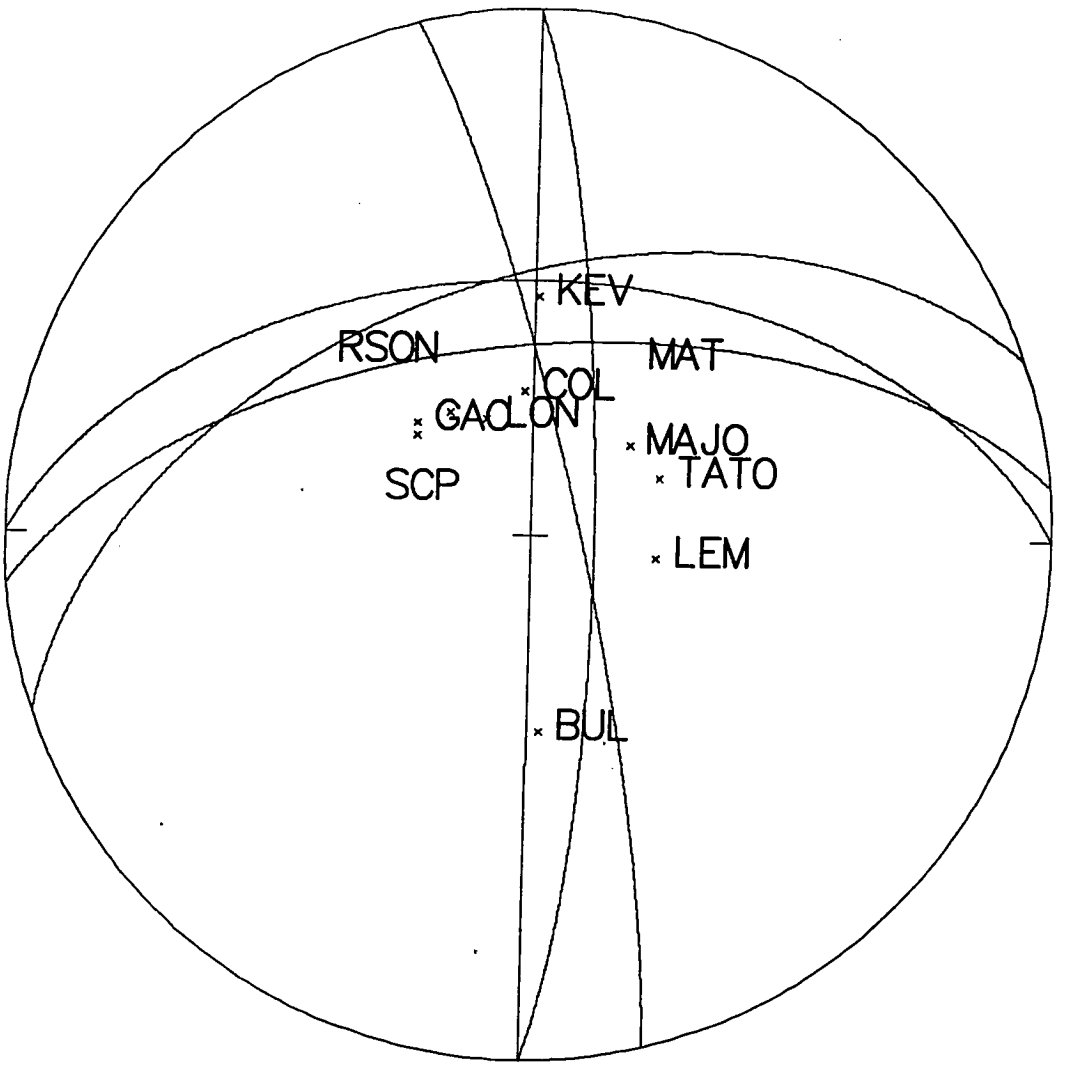

Figure 4.04. The compatible fault plane solutions obtained for event 2 plotted on an equal area projection of the lower focal hemisphere.

b. Other work

There is a CMT fault plane solution (Dziewonski *et al.*, 1983a) for this event reported in the ISC bulletins, which has a strike of 297°, dip of 35°, and rake of 54°. The centroid depth is estimated to be 10 km.

4.3.3 Event 3 - 17 January 1983, Ionian Islands

The Ionian islands, located at the northwestern part of the Hellenic arc, have been the site of intense seismic activity in historical times and in this century. The subduction zone at its north-west end has no clear bathymetric expression, so the actively deforming zone is mainly defined by the location of large earthquakes and the stress orientation by their focal mechanisms. The most recent strong event occurred on the 17th January 1983 and had surface wave magnitude $M_S = 7.0$.

a. Source parameters

The event was well recorded by both WWSSN and GDSN stations. The large surface-wave magnitude compared to a body-wave magnitude of 6.2 is consistent with a shallow depth. To determine the fault plane solution, seismograms from stations of the two global seismic networks with epicentral distances in the range of 30° - 90° are used. The polarities of the *P*-, *SV*- and *SH*-waves together with their amplitudes are inserted in the calculation (Fig. 4.05a). The solutions which are compatible with these observations are plotted on a vectorplot (Fig. 4.05b). They show a near-vertical dip slip thrust fault with a strike slip component with a strike of 305 ± 5°, a dip of 95 ± 5° and a slip angle in the fault plane of 130 ± 5°. The errors on σ, δ and ψ are overestimates since the number of solutions is less than the number suggested by the combination of the above errors, and this is clearly shown on the vectorplot. The fault plane solution convention used here differs from the more common convention given by Aki and Richards (1980), in that the slip angle of convention used here refers to slip of the footwall rather than the hanging wall (see Pearce, 1977). Here, the strike varies between 0° and 360°, the dip between 0° and 180°, and the slip angle between 0° and 180°.

A solution with $\sigma = 307.5°$, $\delta = 96.0°$ and $\psi = 130.0°$ is used in the calculation of synthetic seismograms for event 3, since it produces the best match between synthetic and observed waveforms.

Plotted around the focal sphere, in Fig. 4.06, are the BB displacement pulses (middle solid traces), deconvolved from the GDSN SP records (top traces). Six SP GDSN stations at suitable epicentral distances have clearly recorded the event with a high signal-to-noise ratio. However, because the event is larger, its longer source signal duration yields

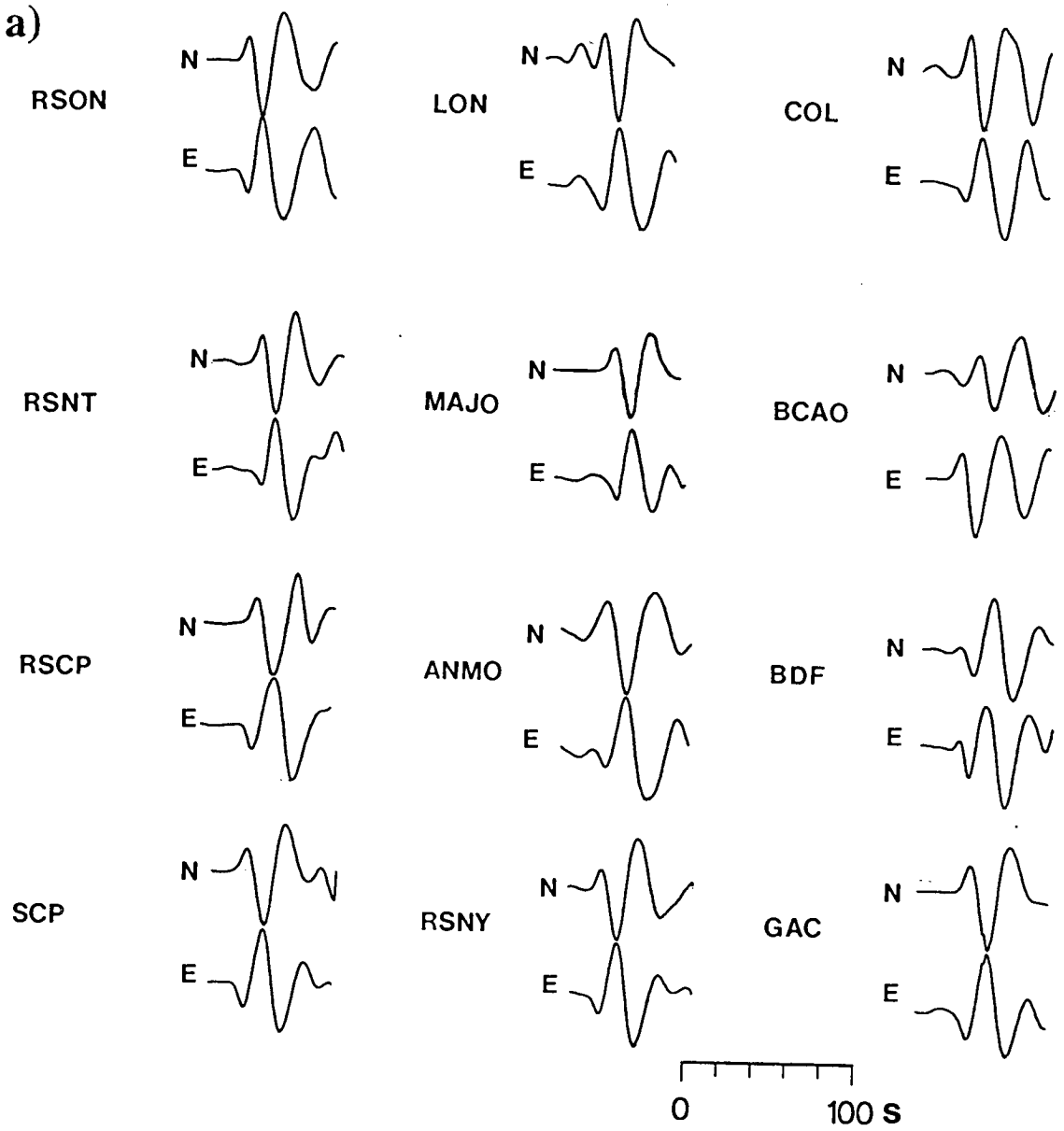

Figure 4.05. (a) Part of data used to calculate the fault plane solution for event 3. (b), (c) vectorplot and focal mechanism as in Figure 4.04 (b,c) for event 3.

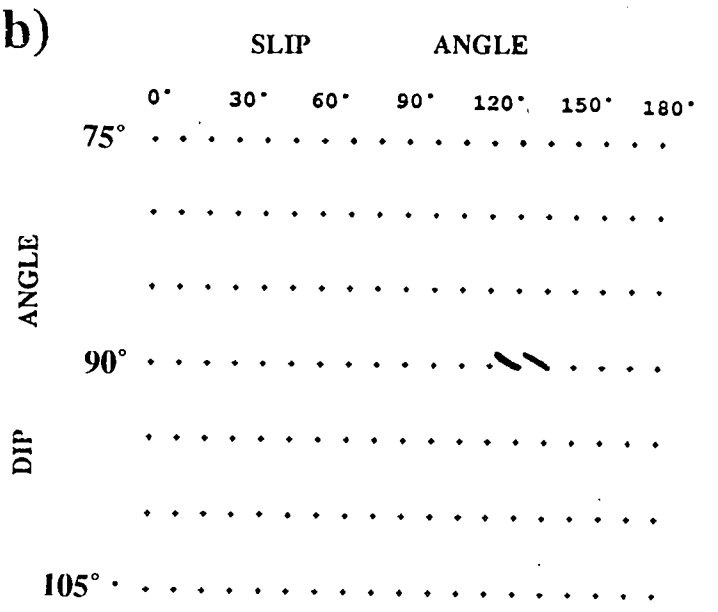

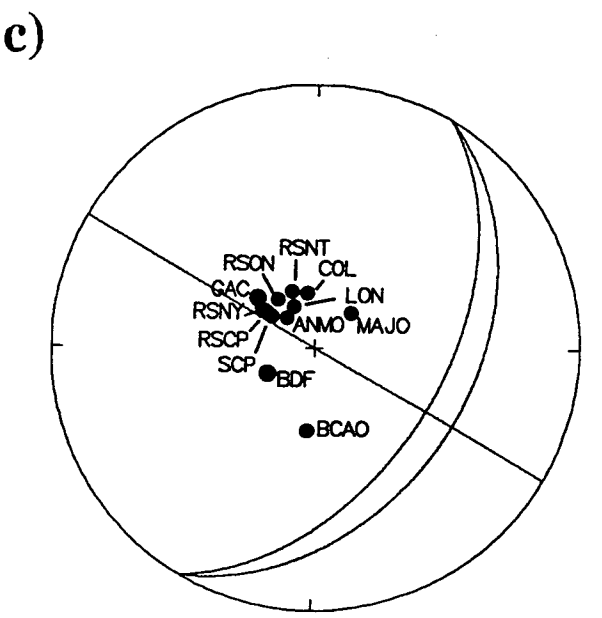

Figure 4.05. (continued).

complex waveforms on short-period records, making it impossible to identify the polarities of *P*-waves. This problem does not occur on the BB records where the wider frequency response, which includes the dominant signal frequency, allows a better representation of the true pulse at the source. The velocity structure model used to calculate the synthetic seismograms is given in Table 4.2a and it is based on the studies of Makris (1978a, b).

Table 4.2a. Crustal model for event 3.

V_p (km s^{-1})	V_s (km s^{-1})	Density (g cm^{-3})	Thickness (km)
1.5	0.0	1.0	2.0
3.5	2.0	2.2	1.0
6.0	3.4	2.8	17.0
6.2	3.5	2.9	9.0
7.7	4.7	3.3	Halfspace

The event is shallow, therefore the depth phases are likely to interfere. A good agreement is obtained between the synthetic (dashed lines in Fig. 4. 06) and the observed BB pulses, assuming a circular fault with a radius of 10 km, a rupture velocity of 2.4 km s^{-1}, and an attenuation factor (t^*) of 0.6 s. The latter parameter is defined as the travel-time in seconds divided by the average quality factor Q, and it is denoted by t^*. The hypocentral depth obtained is 8 km. The mean stress drop over all the stations used in the modelling is 31 bar. In the Savage-type model of the source, the slip is instantaneous, so the stress drop does not relate to any time constants of the source function. In an elastic medium the stress drop is, therefore, proportional only to the pulse amplitude, and is independent of the pulse duration, which is controlled mainly by the fault area and rupture velocity. The stress drop is used in the modelling mainly to give an exact (peak-to-peak) amplitude fit of the main *P* phases at each station. The calculated seismic moment is 5.70 x 10^{18} Nm (Table 4.3). These values are corrected for the surface break of 12 $\pm$ 2 km, which results from the difference in length between the assumed fault radius (10 km) and the estimated depth (8 $\pm$ 1 km). No verification of this predicted surface break can be made at this stage, because it lies on the Ionian Sea floor.

b. Other work

The CMT fault plane solution (Dziewonski *et al.*, 1983) gives a dip-slip mechanism with a small strike slip component for this event ($\phi = 34°$, $\delta = 14°$, $\lambda = 153°$). The static

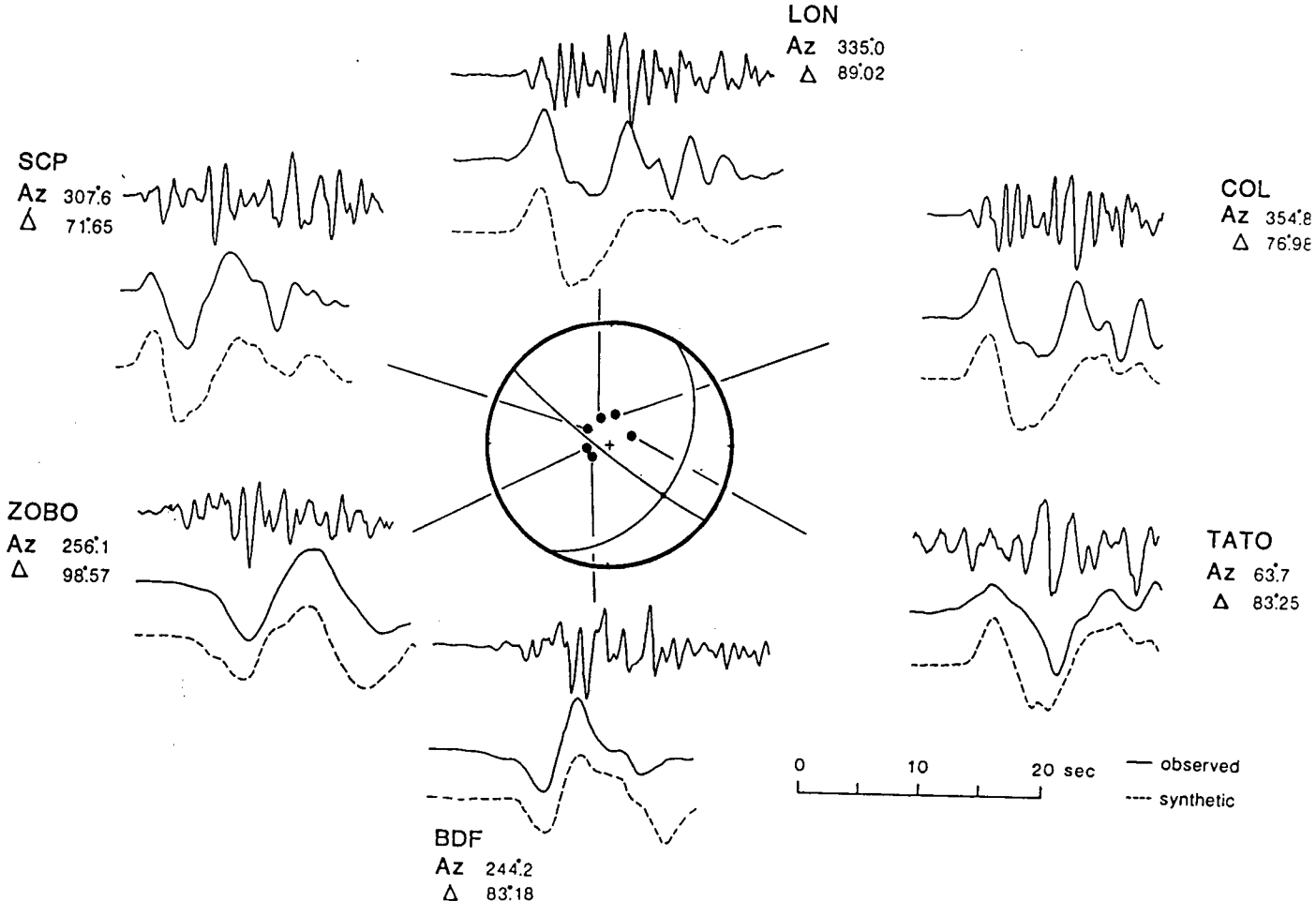

Figure 4.06. GDSN SP *P*-wave displacement seismograms (top solid lines), BB converted from SP (middle solid lines) and BB synthetics (dashed lines) are plotted about the focal sphere for event 3.

seismic moment calculated is 24.0 x 10^{18} Nm and the focal depth 10 km. On the other hand, Scordilis *et al.* (1985), using first motion polarities from a local network, found a strike-slip focal mechanism with a small thrust component (ϕ = 40°, δ = 45°, λ = 168°) and a depth of 9 km.

The solution determined by Anderson and Jackson (1987) using first motion polarities read from WWSSN seismograms, gives almost pure dip-slip (ϕ = 135°, δ = 83°, λ = 90°). The seismic moment is found to be 23.5 x 10^{18} Nm. Kiratzi and Langston (1991), using a moment tensor body-wave inversion technique, obtained a strike-slip mechanism with a dip-slip component (ϕ = 60°, δ = 47°, λ = 74°). A value of 7.3 x 10^{18} Nm is obtained for the seismic moment.

4.3.4 Event 4 - 19 March 1983, SW Crete

a. Source parameters

Figure 4.07a shows the data used to obtain the fault plane solution. Despite the fact that the reported depth (~ 65 km) is sufficient in theory to resolve surface reflections on long-period records (ISC catalogues, PDE bulletins, Beisser *et al.*, 1990), no surface reflections were detectable on the available GDSN records. Figure 4.07b shows the two source orientations found here to be compatible with the data displayed on a vectorplot according to the relative amplitude method. Both the fault plane solutions show a thrust mechanism with σ = 120°, 80° (± 5°), δ = 150°, 150° (± 4°) and ψ = 70°, 120° (± 6°) respectively.

In figure 4.08, SP, BB and calculated synthetic BB displacement seismograms for this event are plotted about the focal sphere as solid and dashed lines respectively. The lack of depth phases at the GDSN stations KEV, LON, SCP, COL and MAJO is apparent on the SP as well as the BB records. However, this is because these stations lie close to the null vector on the upper focal hemisphere. By contrast, LP data from the WWSSN stations at LEM and BUL, which are well away from the null vector, display phases which can be identified as *pP* (with a time delay of about 15 s, consistent with a depth of approximately 65 km).

A fault plane solution with a strike of 120°, dip of 150° and slip angle in the fault plane of 70° is found to give the best fit to the data. The four-layer crustal model used is based on the studies of Makris (1978a, b) and is described in Table 4.2b. In addition, the effect of velocity structure beneath the receiver is added and an average anelastic attenuation for the path was chosen to match the dominant period of the signal. Here t^* was set to 0.6 s.

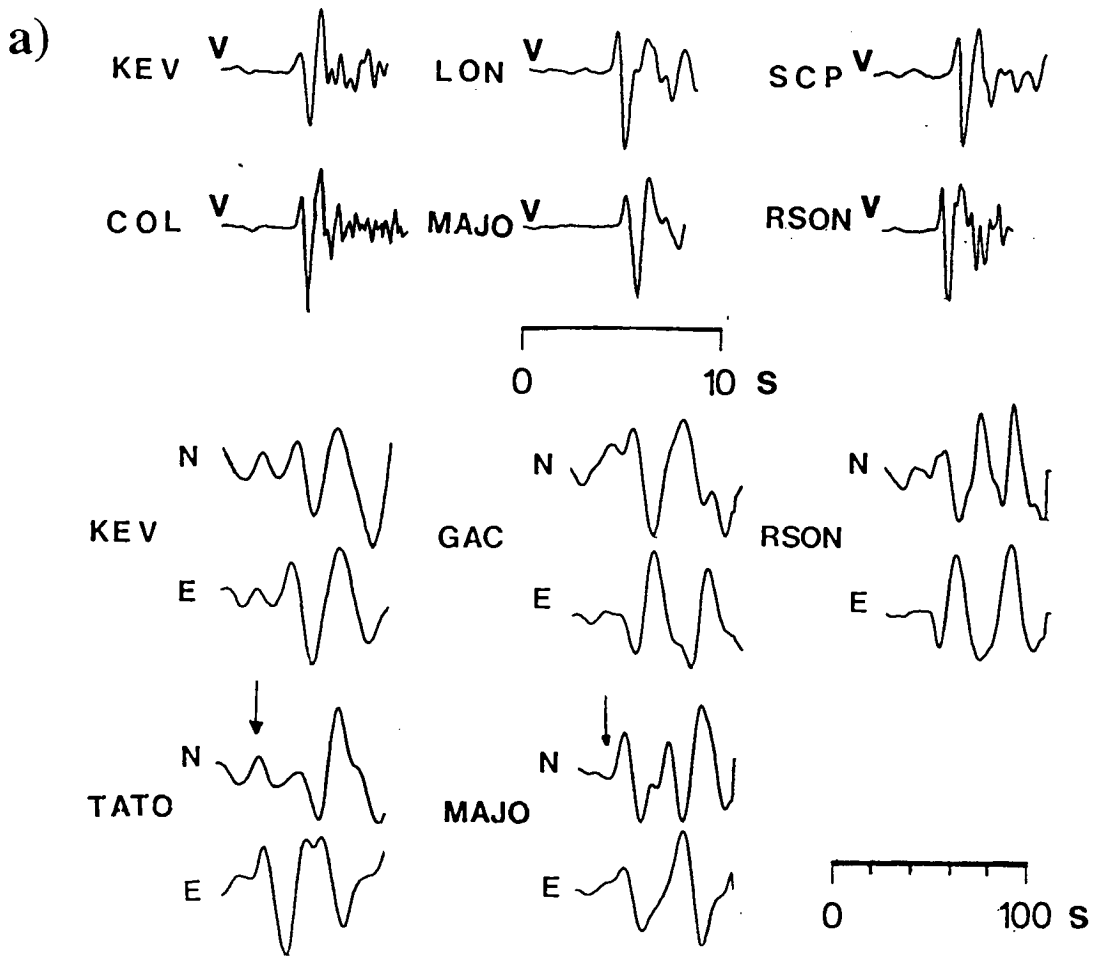

Figure 4.07. (a) Data used to obtain the fault plane solution for event 4. The vertical (V) components are SP GDSN *P*-waves and the horizontal components (N, E) are LP GDSN *S*-waves.

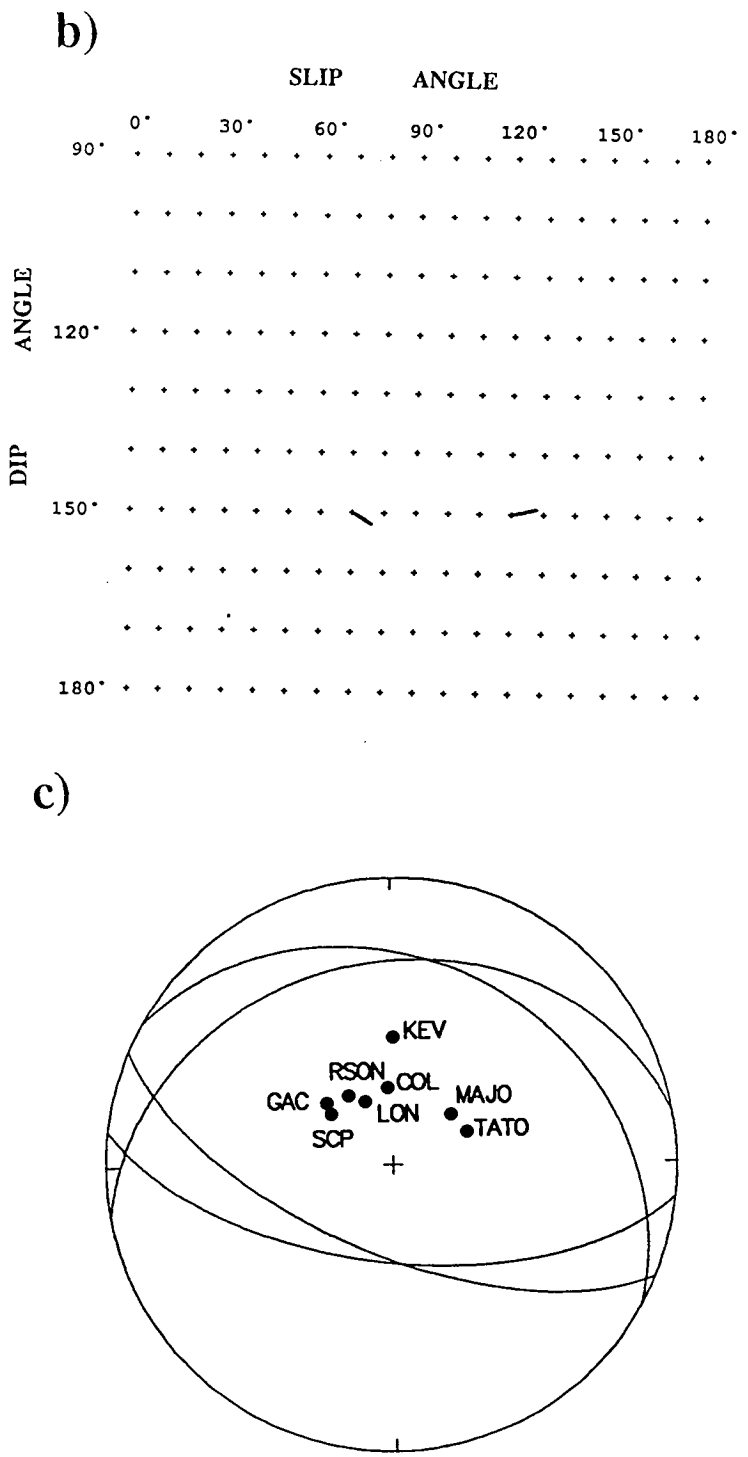

Figure 4.07. (b) The two compatible solutions for the same event plotted on a vectorplot. (c) The fault plane solutions shown in (b) now plotted on an equal area projection of the lower focal hemisphere.

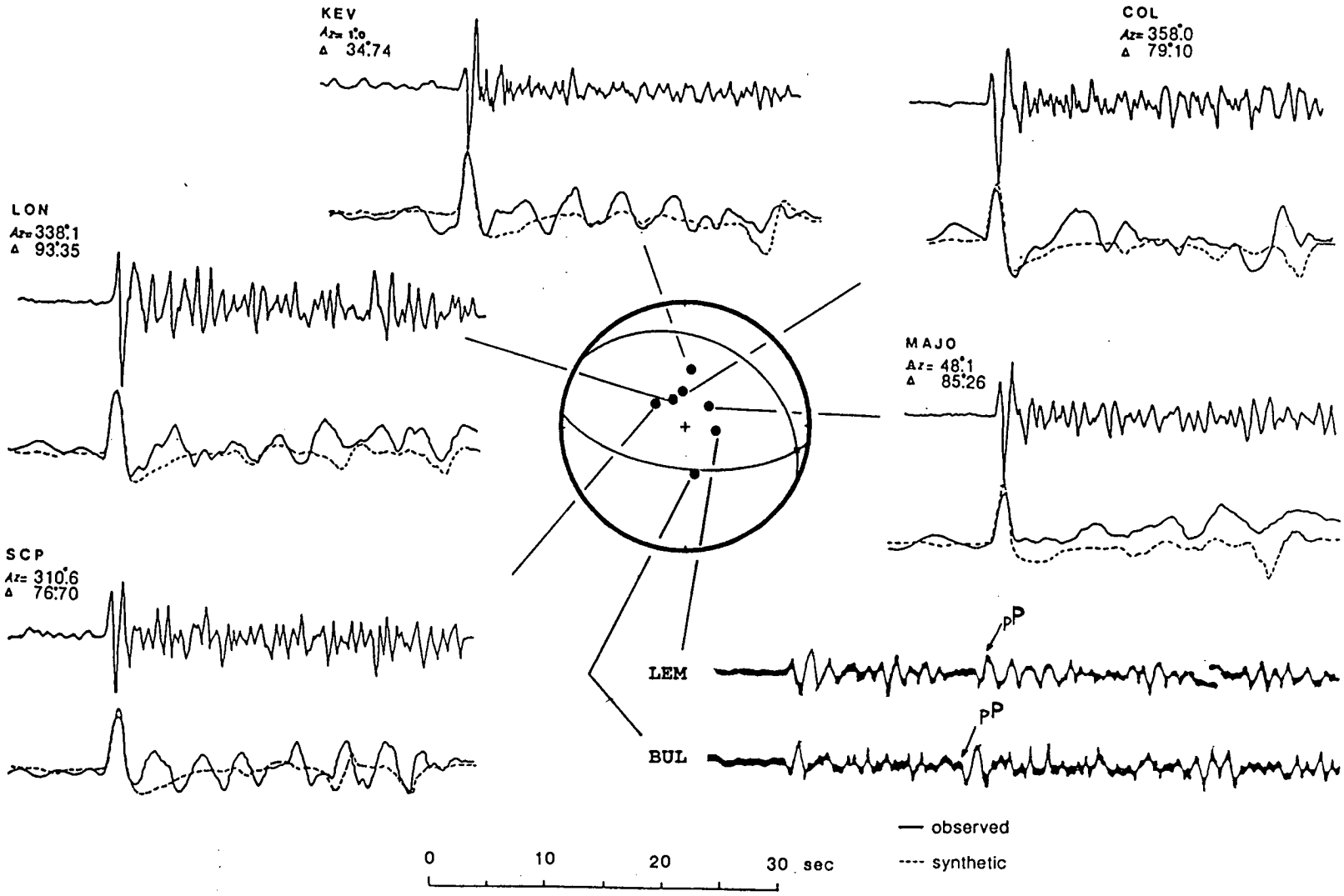

Figure 4.08. *P*-wave displacement seismograms for event 4. The GDSN SP data (top) and their BB conversion (bottom) are plotted as solid lines; the synthetic BB displacements are plotted as dashed lines. WWSSN LP data are shown for the stations LEM and BUL.

A satisfactory fit is obtained for a circular fault with a radius of 2.5 km. A rupture velocity of 2.1 km s^{-1} is assumed and the average stress drop used over all the stations is 25 bar. The calculated static moment is 0.15 x 10^{18} Nm.

Table 4.2b. Crustal model for event 4.

V_p (km s^{-1})	V_s (km s^{-1})	Density (g cm^{-3})	Thickness (km)
4.0	2.1	2.2	1.5
6.1	3.4	2.8	18.0
6.5	3.6	2.9	12.0
7.7	4.7	3.3	50.0
7.8	4.8	3.4	Halfspace

b. Other work

The CMT solution (Dziewonski *et al.*, 1983) has a strike of 358°, a dip of 39° and a rake of 131°. The focal depth is 65 km and the seismic moment 0.33 x 10^{18} Nm. Taymaz *et al.* (1990) studied this event using an inversion technique with WWSSN LP *P*- and *SH*- waves. According to their fault plane solution one of the nodal planes has a strike of 44°, a dip of 51° and the rake is 139°. The focus is found to be 67 km deep. The estimated seismic moment is 0.30 x 10^{18} Nm. Beisser *et al.* (1990), deploying an one-station inversion technique which uses BB Grafenberg array data, found that a solution with ϕ = 17°, δ = 51° and λ = 124° produced synthetic seismograms that match the observed data. The focal depth is 70 km and the seismic moment is 0.10 x 10^{18} Nm.

4.3.5 Event 5 - 21 June 1984, NW of Crete

a. Source parameters

The earthquake of the 21 June 1984 was located west of Crete and had a body-wave magnitude of 5.8. LP *S*-wave polarities, and relative polarities, from six GDSN stations are the input data for the fault plane solution calculation (Fig. 4.09). The acceptable solutions occupy a large fraction of the total vectorplot area (same figure), due to inadequate coverage of the focal hemisphere with stations that recorded the event.

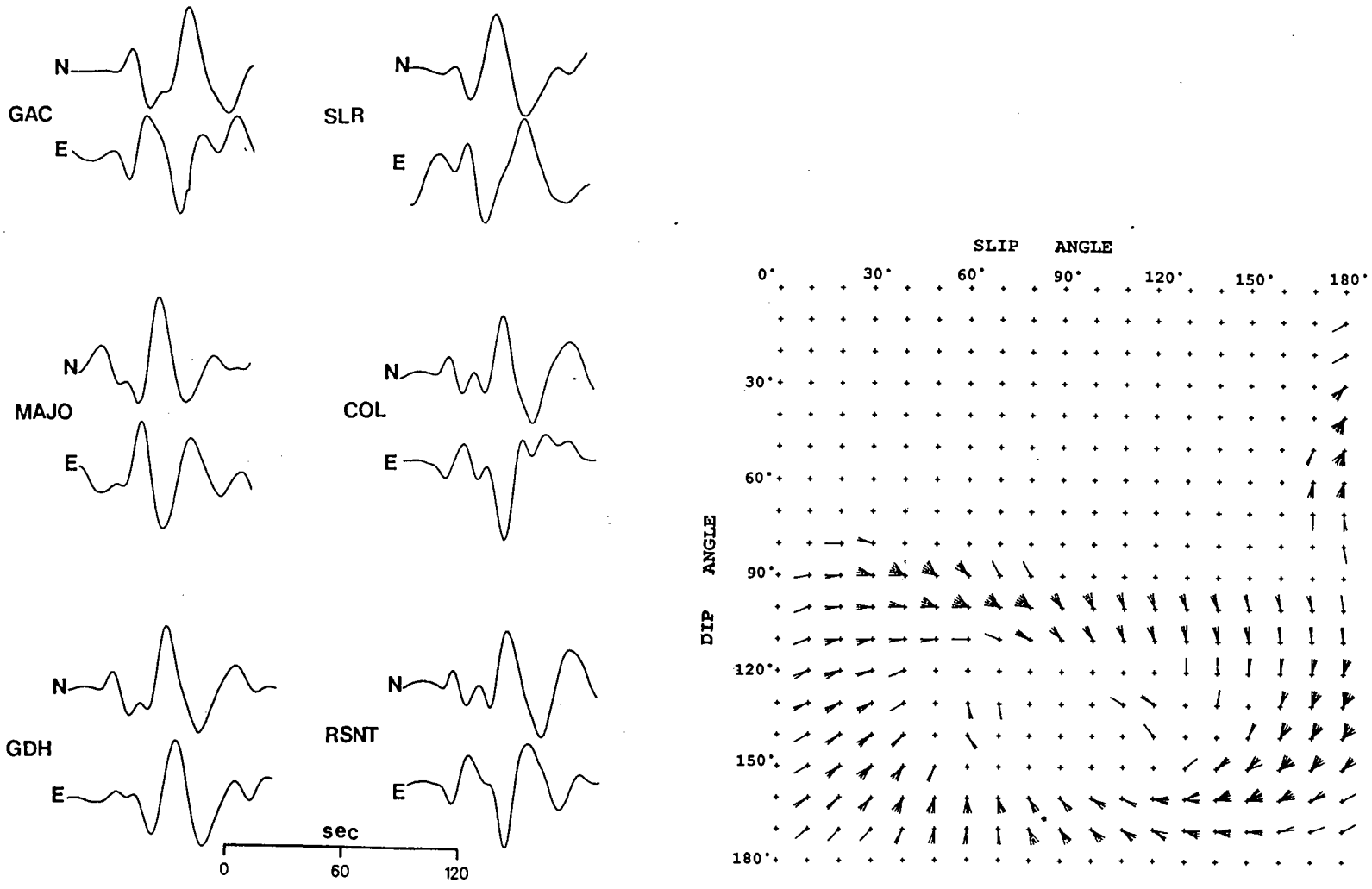

Figure 4.09. LP *S*-wave seismograms (horizontal components) from six GDSN stations used to calculate the fault plane solution of event 5. The vectorplot with the acceptable solutions is shown at the bottom-right part of the figure.

However, most of the solutions lie in the area of low angle thrust mechanisms, suggesting that such a mechanism is more probable for this event.

This earthquake was recorded by 10 GDSN stations at epicentral distances 30° - 90°. Figure 4.10 shows the SP seismograms recorded at three GDSN stations (LON, MAJO, CHTO) and their BB conversions, both displacement and velocity. The positive onset of the *P*-waves is apparent on the BB records, although on the BB velocity record small precursors seem to precede the main event. This is observed at all stations. Furthermore, the complexity of the seismograms (same figure), both SP and BB, do not allow any clear identification of surface reflections, so that body-wave modelling has so far proved to be impossible.

b. Other work

The CMT solution (Dziewonski *et al.*, 1985a) has a strike of 79°, a dip of 7° and a rake of - 128°. The focal depth is 34 km and the seismic moment 0.22 x 10^{18} Nm. According to the fault plane solution determined by Taymaz *et al.* (1990) one of the nodal planes has a strike of 110°, a dip of 72° and the rake is 83°. The focal depth was found to be 39 km. The estimated seismic moment is 1.2 x 10^{18} Nm. Beisser *et al.* (1990) found that a solution with $\phi = 50°$, $\delta = 80°$ and $\lambda = 110°$ produced synthetic seismograms that match the observed data. The focal depth is 50 km and the seismic moment is 0.38 x 10^{18} Nm.

4.3.3 Event 6 - 27 September 1985, southeast of Crete

a. Source parameters

Figure 4.11 shows the range of acceptable fault plane solutions obtained using the relative amplitude method. Although only SP *P*-wave polarities from 5 GDSN stations were available for this event, they place a strong constraint on the source orientation; this is shown schematically by the shaded areas in Fig. 4.10, where the solid lines represent the two nodal planes estimated by Dziewonski *et al.* (1986). There is a disagreement between the fault plane solutions obtained by the two methods. SP records at two GDSN stations (RSON and RSNT) have recorded the *P*-wave first motion as a dilatation. This is confirmed by the deconvolved BB records, where the negative polarities are more obvious. However, the CMT solution predicts compression at these sites, and furthermore, BB displacement synthetics computed using this solution do not show any similarity to the observed records (same figure). This implies that the CMT solution is incorrect in this case.

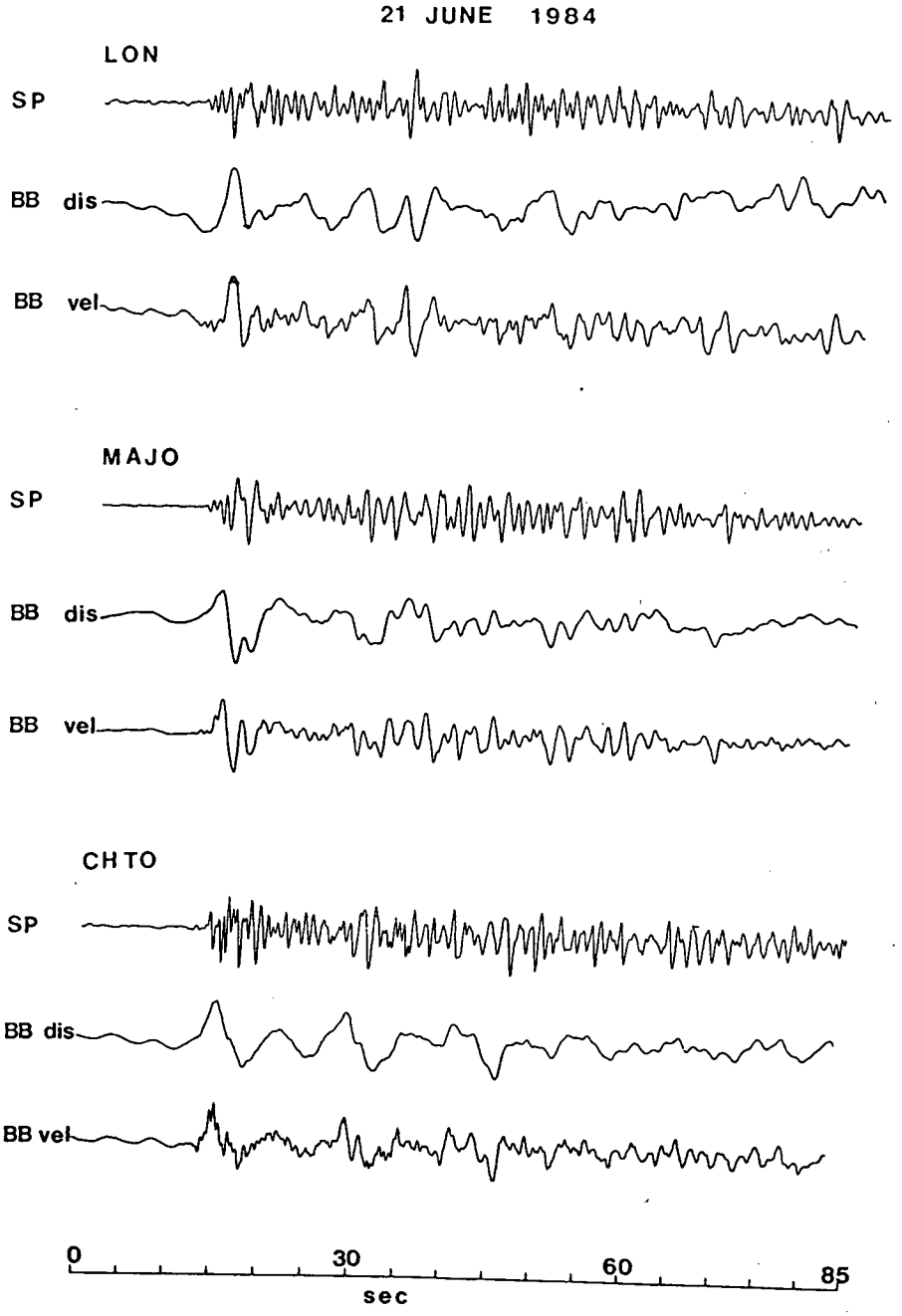

Figure 4.10. SP seismograms for event 5 (top trace), recorded at three GDSN stations, and their broadband conversions. The middle trace represents the broadband displacement record and the bottom trace is the broadband velocity record.

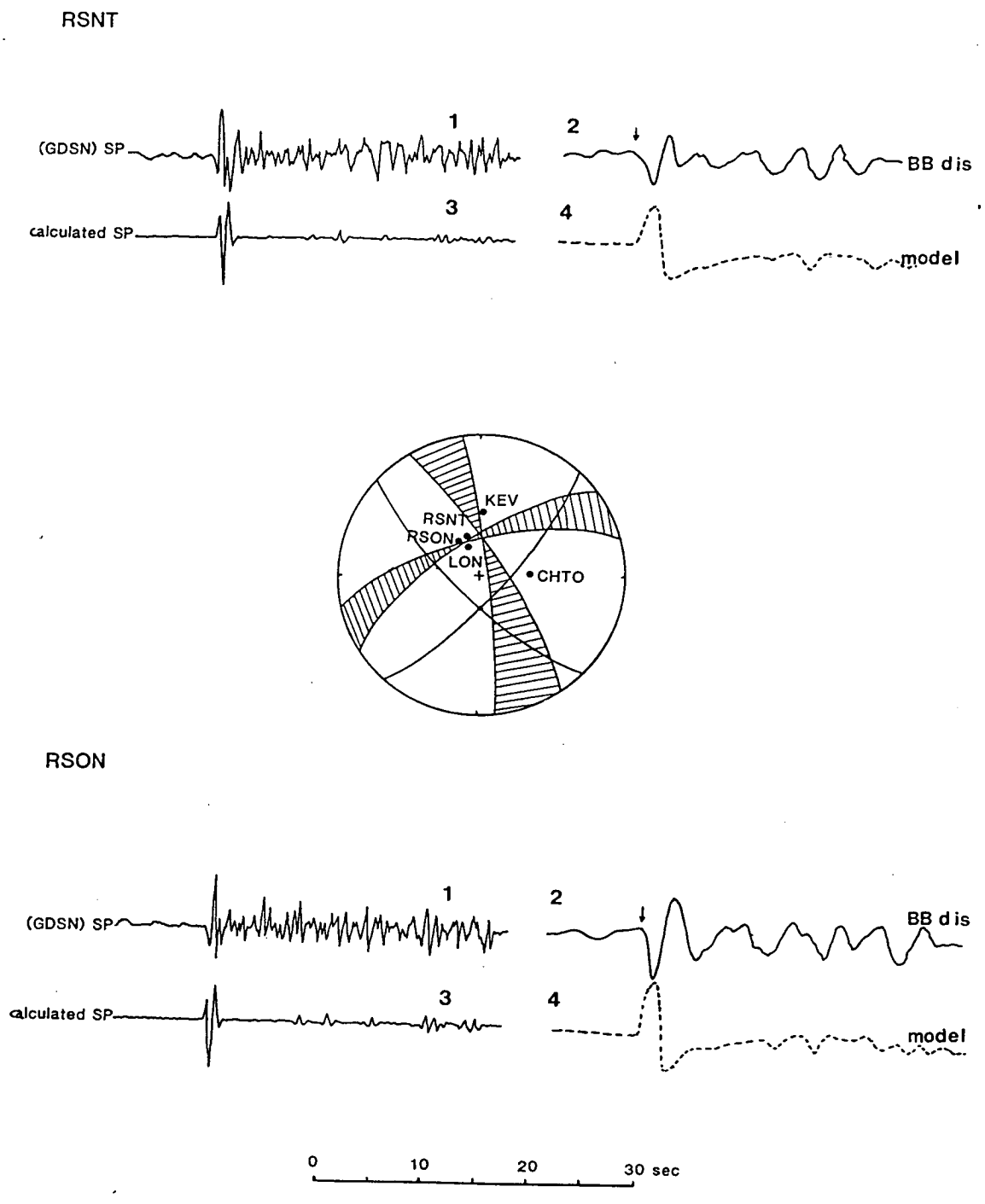

Figure 4.11. Allowed fault plane solutions schematically plotted on an equal area projection of the lower focal hemisphere, calculated using RAMP, for event 6 (shaded areas). On the same projection the two thicker lines represent the two nodal planes of the CMT solution for the same event. For the stations RSON (lower diagram) and RSNT (upper diagram) the following *P*-wave data are shown: (1) GDSN SP, (2) BB converted from SP, (3) synthetic SP using the CMT fault plane solution, (4) synthetic BB using the CMT fault plane solution.

b. Other work

The CMT fault plane solution (Dziewonski *et al.*, 1986) gives a strike-slip mechanism ($\phi = 135°$, $\delta = 76°$, $\lambda = 13°$). The static seismic moment calculated was 0.33 x 10^{18} Nm and the focal depth 44 km.

The solution determined by Taymaz *et al.* (1990) is also a strike-slip mechanism ($\phi = 125°$, $\delta = 77°$, $\lambda = 9°$). The seismic moment was found to be 0.55 x 10^{18} Nm.

4.3.7 Event 7 - 13 September 1986, Kalamata, SW Peloponnese

The 13 September 1986 earthquake, which destroyed a large part of the city of Kalamata, SW Peloponnese, is the first shallow event, in this area of the overriding continental crust of the Aegean, to be well recorded teleseismically and to have produced clear surface faulting. Because of the low seismicity no focal mechanisms were previously available for this region.

a. Source parameters

Figure 4.12 shows the data used to calculate the fault plane solution of the event using the RAMP method. SP *P*-wave onsets were not clear as a small precursor seems to precede the main shock (Fig. 4.14). However, on the BB records all the *P*-wave onsets clearly show negative polarities (Fig. 4.14) which are inserted in the computation together with the relative polarities of the two horizontal components (*SH*, *SV*) of the *S*-waves. All the solutions that are compatible which the data plotted on the vectorplot are shown in Fig. 4.13. They give a normal fault which strikes at a NNE direction and has an average dip of 45°.

Seven SP GDSN stations at epicentral distances 30° - 90° have recorded the event. The larger magnitude of this earthquake results in a longer signal duration. Consequently, the SP seismograms seem to be complex and the identification of any polarities of direct *P*-waves is not possible. The top traces in figure 4.14 are the SP recordings at the stations LON, COL, GDH, MAJO, CHTO, BCAO and TATO. Their signal-to-noise ratio is high enough to give BB records of displacement which are shown immediately below. It can be seen on the BB recordings from BCAO and CHTO that there seems to be a small precursor of the same polarity preceding the main onset. The shape of the pulse suggests that the direct *P*-waves interfere with their surface reflections (*pP*, *sP*), which in turn suggests a shallow focal depth.

The fault plane solution with a strike, σ, 196°, dip, δ, 44°, and slip in the fault plane, ψ, 94° was used to calculate the synthetic seismograms which are represented by the third

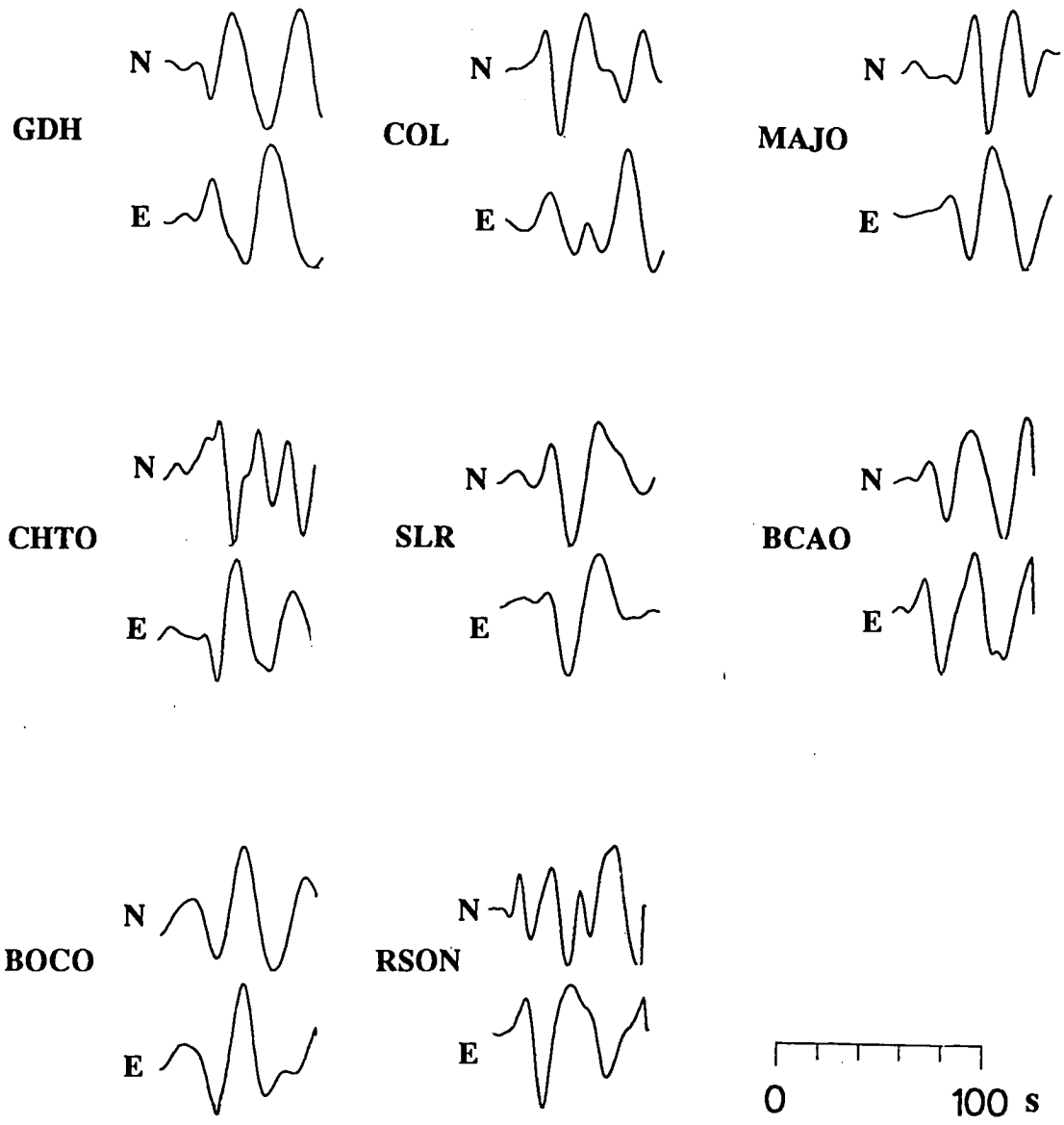

Figure 4.12. Part of data used to calculate the fault plane solution for event 7. They consist of LP, *SH*- (NS, EW) waves from 8 GDSN stations.

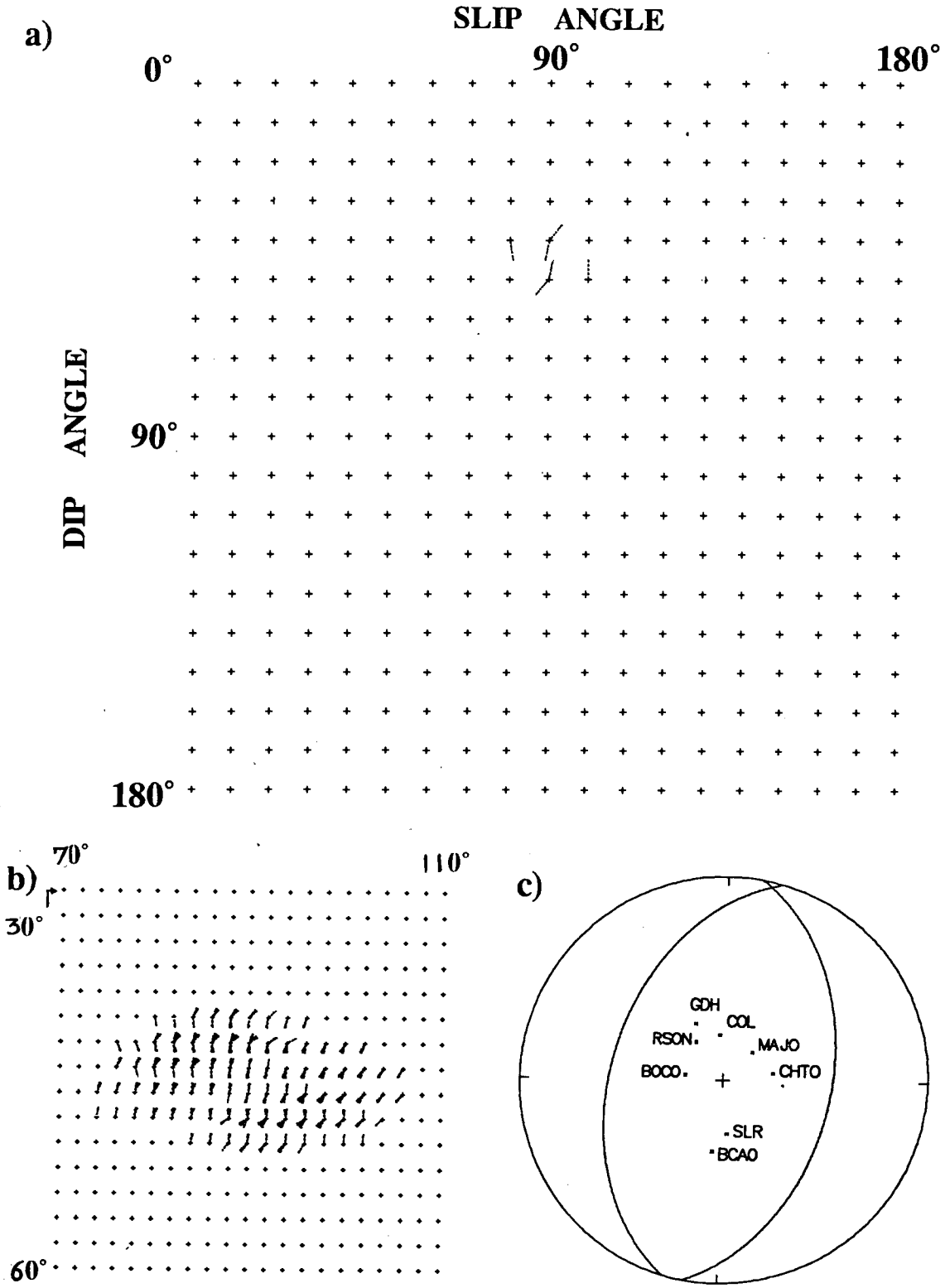

Figure 4.13. (a) The solutions compatible with the data obtained for event 7 plotted on the vector plot. (b) Part of the vector plot (dip = 30° - 60°, slip = 70° - 110°, interval = 2°). (c) The solution used in modelling is plotted on an equal area projection of the lower focal hemisphere.

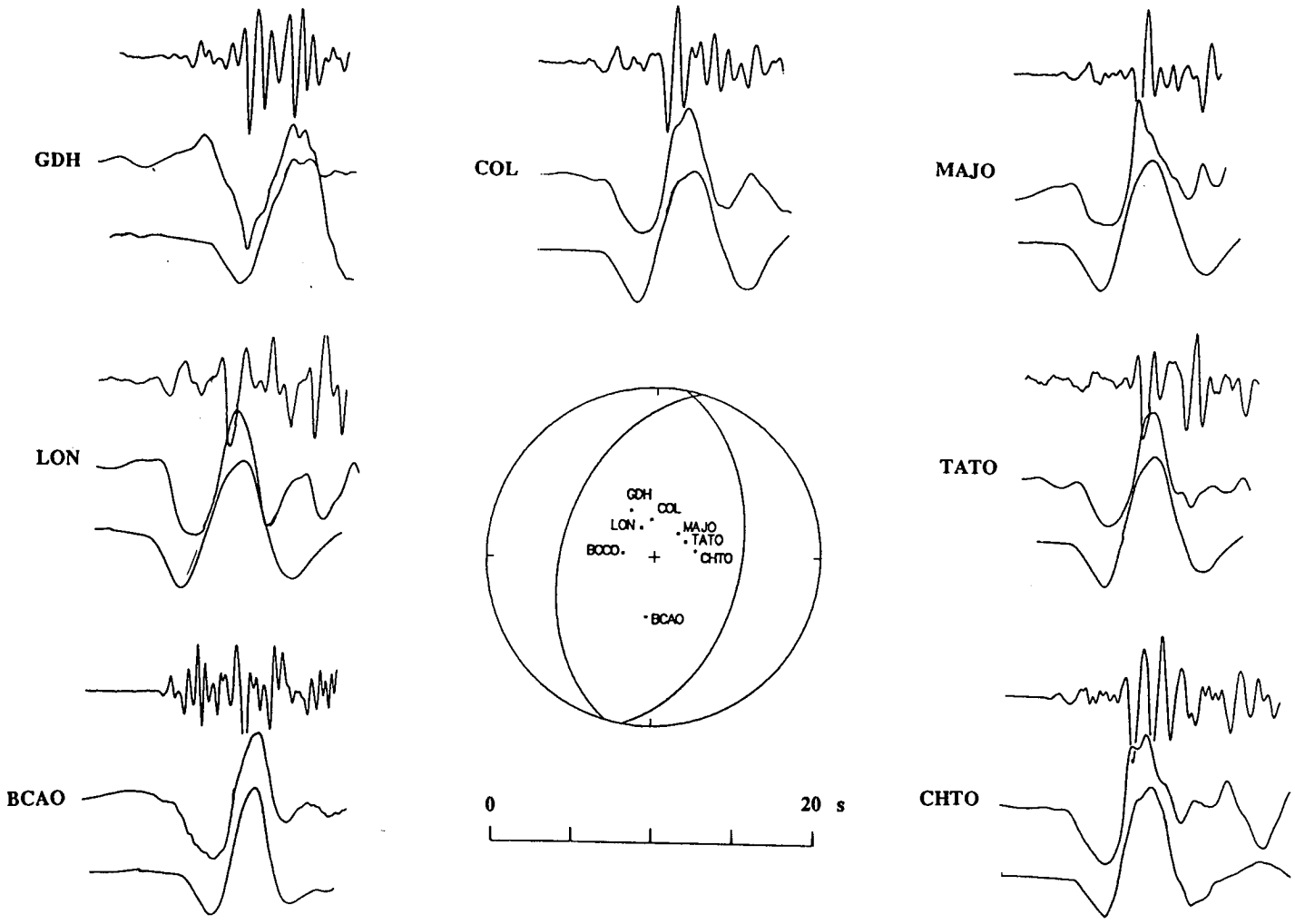

Figure 4.14. GDSN SP *P*-wave displacement seismograms (top lines), BB converted from SP (middle lines) and BB synthetics (bottom lines) are plotted about the focal sphere for event 7.

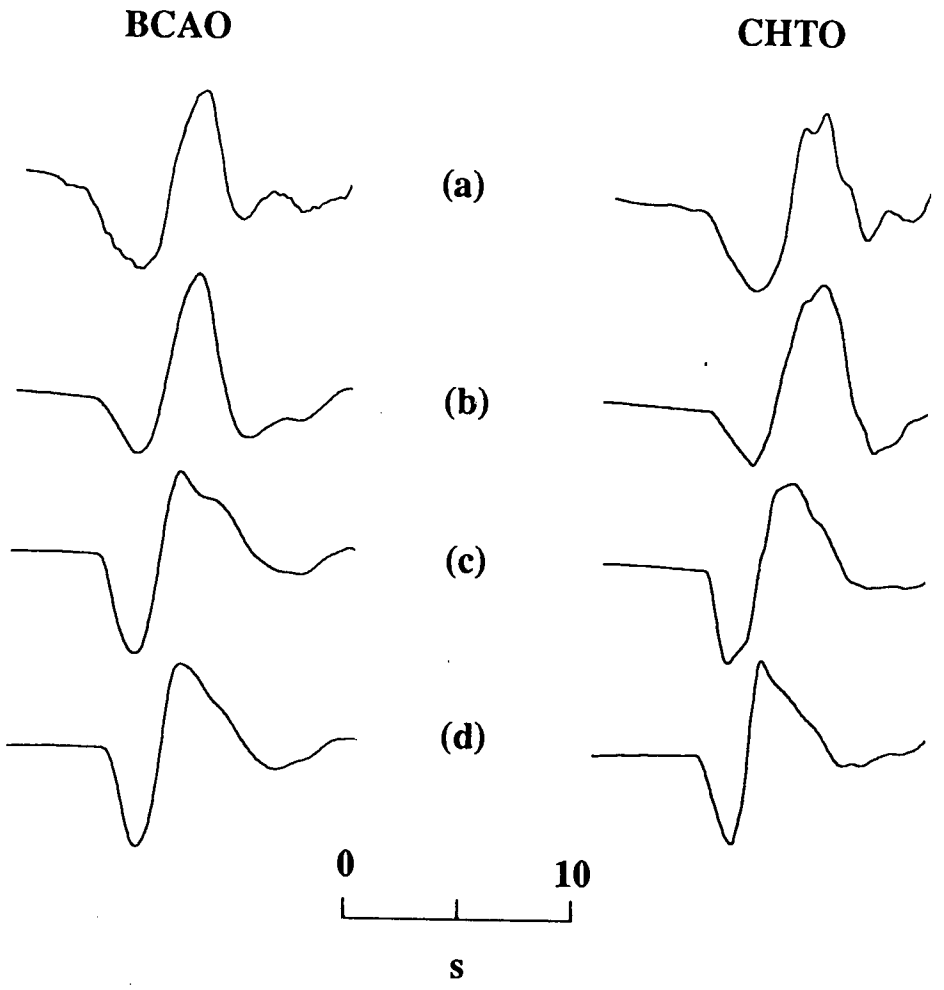

Figure 4.15. Observed and synthetic seismograms generated for event 7: (a) observed BB seismograms at BCAO and CHTO, (b) synthetic trace using an elliptical rupture model where the rupture initiates at the focus of the ellipse, (c) the rupture initiates at the centre of the ellipse, and (d) the rupture model is a circle with the rupture initiating at its centre. The preferred model is (b).

trace from the top on Fig. 4.12. The crustal structure in the epicentral area is given in Table 4.2c.

Table 4.2c. Crustal model for event 7.

V_P (km s^{-1})	V_S (km s^{-1})	Density (g cm^{-3})	Thickness (km)
5.8	3.2	2.2	10.0
6.1	3.4	2.8	20.0
7.9	4.8	3.4	Halfspace

The rupture is assumed to initiate at the focus of an ellipse with a major axis of 11 km and a minor axis of 3 km and propagate upwards. To produce the best fit between the observed and the synthetic seismograms the ellipse was required to be placed on the fault plane with its major axis at an angle of 45° from the strike. In Fig. 4.15 the synthetic seismograms produced using a circular fault and ellipses in different orientations are shown for comparison. The depth is found to be 5.5 $\pm$ 0.5 km. The stress drop varies with azimuth from 15 to 50 bar giving a mean stress drop of 37 bar. Station GDH is not taken into account in this calculation because of its exceptionally high *P*-wave amplitudes (~ 17000 nm), which required a stress drop value greater than 100 bar to be reproduced on the synthetics. The calculated seismic moment is 1.02 x 10^{18} Nm. A rupture velocity of 3.1 km s^{-1} is assumed. Because of the upward rupture propagation at the source and the shallow focal depth, no possible directivity effects, such as azimuthal pulse duration and amplitude variation, can be resolved on the broadband records. The attenuation operation factor t^* varies between 0.2 and 0.6 s with the azimuth of the recording stations. In analogy with the Cephalonia event, these values are corrected for surface break of about 9 km which results from the difference in length the assumed major axis of the elliptical fault plane (11 km) and the estimated focal depth of the earthquake.

b. Other work

Papazachos *et al.* (1988), using SP and LP data from the national (Greek) and regional network, suggest a normal fault mechanism for this event, with ϕ = 200°, δ = 50° and λ = - 85°. The length and the width of the fault are found to be 15 and 11 km respectively. The focal depth is 8 km, the estimated seismic moment is 0.6 x 10^{18} Nm, and the average stress drop is equal to 5 bar.

Lyon-Caen *et al.* (1988), by body-wave modelling of WWSSN LP data, determine a fault plane solution with ϕ = 201°, δ = 45° and λ = 283°. The seismic moment is found to

be 7 ± 2.5 x 10^{17} Nm and the centroid depth 5 ± 3km. The average fault length is 8 km, and the fault width along dip is 14 km (as shown by the aftershock distribution). They observed complexity of the initial rupture on teleseismic WWSSN and GDSN SP records which is expressed as a small arrival about 3.5 s before the main event, suggesting that the rupture propagation was not smooth. They suggest that the main shock initiated in a zone more to the north, defined by the aftershock seismicity, 3 - 4 s before the rupture front reached the main fault plane. There, most of the energy was released and the rupture presumably propagated southwards (Fig. 4.16).

4.4 DISCUSSION

For moderate-sized earthquakes, such as the events presented above, it is essential to model the seismic source using broadband data so that the frequency range where most of the energy is contained is included in the bandpass, if detailed rupture characteristics are to be determined. When BB records for events 3 and 7 are compared with the SP seismograms, it can be seen clearly that the polarity of the direct *P*-wave can be identified only on the BB records. This enables the determination of the source mechanism to be better constrained. Moreover, the shape of the pulse produced by the interference of the direct and the surface reflected waves, in cases of events 3 and 7, is apparent on the BB seismograms and can be modelled in order to obtain the rupture characteristics of the source.

Table 4.3. Source parameters for event 3, 4, and 7.

Event	σ (°)	δ (°)	ψ (°)	D (km)	M_o (x 10^{18} Nm)	$\Delta\sigma$ (bar)	R (km)	Vr (km s^{-1})
3	*307*	*96*	*130*	8.0	5.71± 0.62	31 ±14	10.0	2.4
4	*120*	*150*	*70*	65.0	0.16±0.09	25.4±5.9	2.5	2.1
7	*196*	*44*	*94*	5.5	1.02±0.70	37 ±27	11.0	3.1
							x 3.0	

A comparison is made now between the source parameters of the seven earthquakes obtained here (Table 4.3) with those calculated by other studies. Firstly, the differences and similarities between the fault plane solutions determined here using the different methods are discussed. In Fig. 4.17 the fault plane solutions of recent (1970 - present),

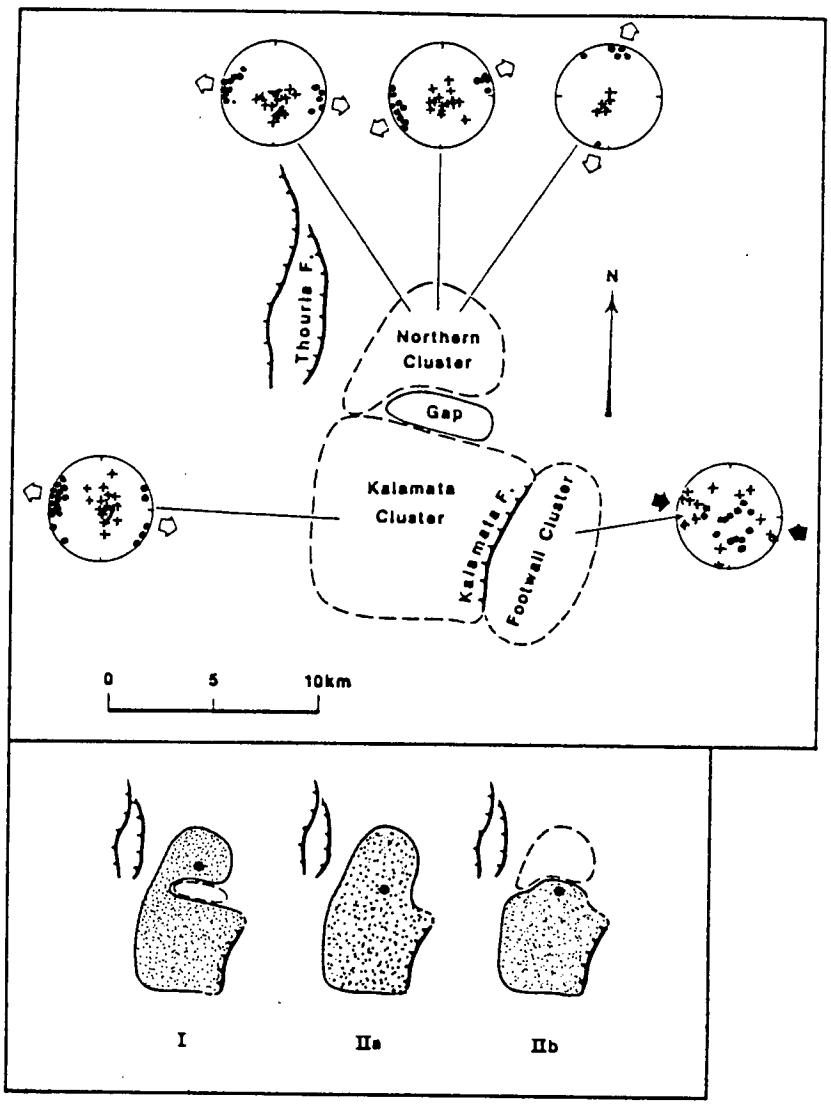

Figure 4.16. (From Lyon-Caen et al., 1988) Aftershock distribution with respect to fault geometry. (*Top*) The Kalamata cluster is related to the downward extension of the Kalamata fault. The northern cluster and the gap of aftershocks are within the relay zone between Kalamata and Thouria faults. P (pluses) and T (dots) axes for all focal mechanisms are plotted for each cluster. Open arrows indicate mean direction of extension; solid arrows indicate mean direction of compression. (*Bottom*) Earthquake rupture propagation. Sketches illustrate three possible scenarios. The location of the main shock with an asterisk, within the northern cluster for I, within the gap for IIa and IIb. The rupture area is in grey in each case.

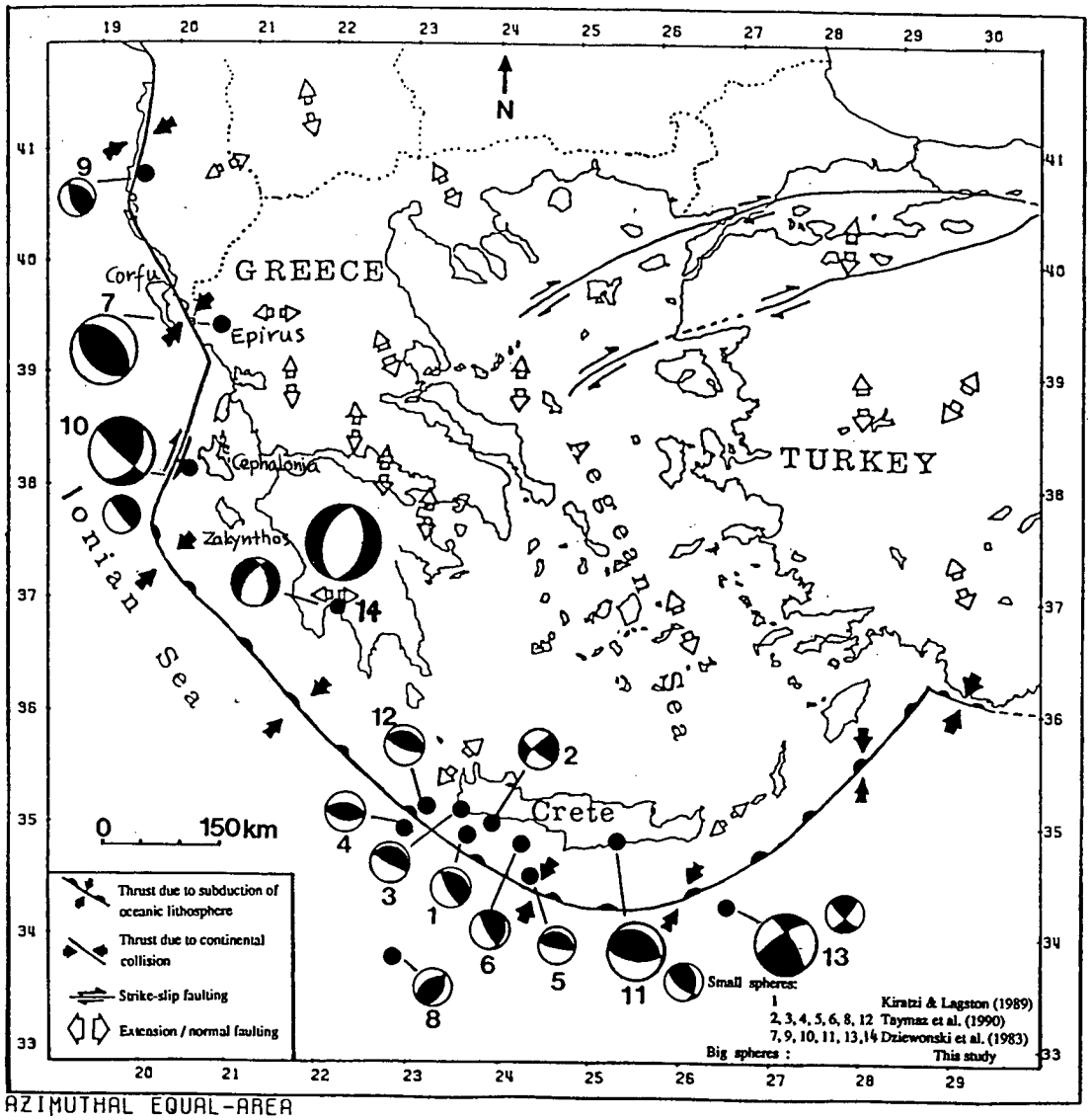

Event numbers							
This figure	7	9	10	11	12	13	14
This study	1	2	3	4	5	6	7

Figure 4.17. Main seismotectonic features of the Hellenic arc and the Aegean sea. Earthquakes with epicentres on the arc and $m_b > 5.5$ for the time period 1970 until the present are shown numbered according to table 4.4, together with fault plane solutions according to the references cited in that table. The larger focal sphere projections, events 7, 9, 10, 11, 13, 14, represent computed results of this study.

moderate-sized earthquakes (Table 4.4) from the Hellenic arc are shown, including results from the present study.

The fault plane solution of the 10 March 1981 (event 1) earthquake, although not well constrained due to limited data, is indicative of a thrust mechanism. However, there is no published fault plane solution for this event to be compared with the one obtained here.

The earthquake of 16 November 1982 (event 2) has a strike-slip mechanisms with a small thrust component. The CMT solution gives a thrust mechanism with a very small strike slip component. There is a big difference in the strike and dip of the two nodal planes.

The solution obtained here for event 3 (17 January 1983), gives an almost vertical dip-slip fault with a strike-slip component. This compares with the CMT solution (Dziewonski *et al.*, 1983), which gives dip-slip with a very small strike-slip component, and with the solution obtained using first-motion polarities read from WWSSN seismograms (Anderson and Jackson, 1987), which gives almost pure dip-slip. Scordilis *et al.* (1985) and Kiratzi and Langston (1991) have found a fault plane solution with a strike-slip dextral fault with a small thrust component. This solution supports the existence of a transform fault that connects the northwestern edge of the Hellenic arc with the compressional zone, which is produced by the collision of the Apulian plate with the Eurasian plate, along the Adriatic-north Ionian coast. Another two earthquakes that occurred in almost the same area (17 September 1972, 23 March 1983) have fault plane solutions that show a right-lateral strike slip motion (Anderson and Jackson, 1987, Kiratzi and Langston, 1991, respectively). This right-lateral strike-slip fault probably terminates the Hellenic subduction zone (Fig. 4.17). Dewey and Sengör (1979) believe in the existence of a right-lateral transform fault between Cephalonia and Zakynthos at the northward termination of the Hellenic arc, also suggested by the observed offset in seismicity in that region. However, Kissel and Laj (1988) believe that the geographical extension of the arc has been underestimated by different models (e.g., Le Pichon and Angelier, 1979), since palaeomagnetic evidence from Corfu and Epirus, more to the north, show that they have undergone significant rotation.

For event 4 (19 March 1983), a thrust mechanism was obtained here. The solutions determined using the centroid (CMT) method (Dziewonski *et al.*, 1983), the inversion of WWSSN LP *P*- and *SH*-waves (Taymaz *et al.*, 1990), and the method of one-station inversion (Beisser *et al.*, 1990) are similar with regard to the type of mechanism but they differ in the strike of the two nodal planes. The focus, because of its depth being greater than the depth of Moho (~ 34 km), is located in the subducted African lithosphere.

Table 4.4. Earthquakes along the Hellenic arc with $m_b \geq 5.5$ for the time period between 1970 and present.

Event	Date	Time	Lat(°N)	Long(°E)	m_b	Reference	Event number in this study
1	4May72	21:39	35.1	23.6	5.9	1	
2	29Nov73	10:57	35.1	23.8	5.7	2	
3	18Aug77	9:27	35.2	23.5	5.5	2	
4	11Sep77	23:19	34.9	23.0	5.8	2	
5	15May79	6:59	34.6	24.5	5.5	2	
6	15Jun79	11:34	34.9	24.2	5.5	2	
7	10Mar81	15:16	39.3	20.7	5.6	4	1
8	17Aug82	22:22	33.7	22.9	6.0	2	
9	16Nov82	23:41	40.8	19.6	5.5	3	2
10	17Jun83	12:41	38.1	20.2	6.2	4	3
11	19Mar83	21:41	35.0	25.3	5.7	4	4
12	21Jun84	10:43	35.3	23.3	5.8	2	5
13	27Sep85	16:39	34.4	26.5	5.6	4	6
14	13Sep85	17:24	37.0	22.2	5.8	4	7

Fault plane solutions from:

1: Kiratzi and Langston (1989)
2: Taymaz et al. (1990)
3: Dziewonski et al. (1983)
4: This study

The fault plane solution for event 5 (21 June 84) is not well constrained. The azimuthal coverage of the focal sphere of the stations available was not adequate to produce a well determined solution. However, most of the acceptable solutions obtained lie in the area of the vectorplot that indicates a thrust mechanism. The CMT solution suggests an almost vertical normal fault. The solution given by Taymaz *et al.* (1990) implies an almost vertical reverse fault. Beisser *et al.* (1990) agree with the latter solution, but with difference in strike of the fault plane of about 60°.

For event 6, although only first motions from a small number of stations were used, the range of acceptable solutions is well defined and occupies a small fraction of the whole orientation space. There is a significant difference between my solution and the CMT solution in that both nodal planes dip in the opposite sense. This highlights an advantage in the accuracy of the relative amplitude method over the CMT method when targeting specific suitable events. The solution determined by Taymaz *et al.* (1990) is similar to the CMT solution.

The 13 September 1986 earthquake (event 7) has a normal fault mechanism and all solutions obtained by different methods are similar. It is the only event, from all those examined here, that has produced a surface break whose direction and length could be measured. Papazachos *et al.* (1988) believe that the Kalamata earthquake was produced by a listric normal fault striking in a NNE-SSW direction and dipping WNW and the recent ground ruptures extend for 15 -18 km, following approximately the entire fault scarp. The dip angle of the fault decreases with depth, since the dip of the fault plane measured at the surface is about 70°, while the fault plane solution shows that the dip is 40° at depth. The T-axis is almost horizontal and trends in a E-W direction, which is the direction of the narrow extensional field observed behind the compressional zone in the western part of the Hellenic arc. Lyon-Caen *et al.* (1988) claim that the existence of active E-W extension in this region (Fig. 4.18) implies a recent change in the tectonic regime, and consequently a change in boundary conditions at the subduction zone, probably in response to the incoming margin of Africa.

The source model used to calculate the synthetics is highly sensitive to variations in the model parameters (Abercrombie, 1991; Chapter 2 of this thesis). The focal depth, the source region seismic wave velocities, the layer thicknesses and densities can all be perturbed from their initial values in order to maximise the waveform match between theoretical and observed seismograms by trial and error. The crustal structure velocity model used in the modelling was in all cases based on the studies of Makris (1978a, b). When appropriate, a sea-water layer was added based on the bathymetry. It is acknowledged that a flat, multi-layered crustal structure is not a realistic approximation

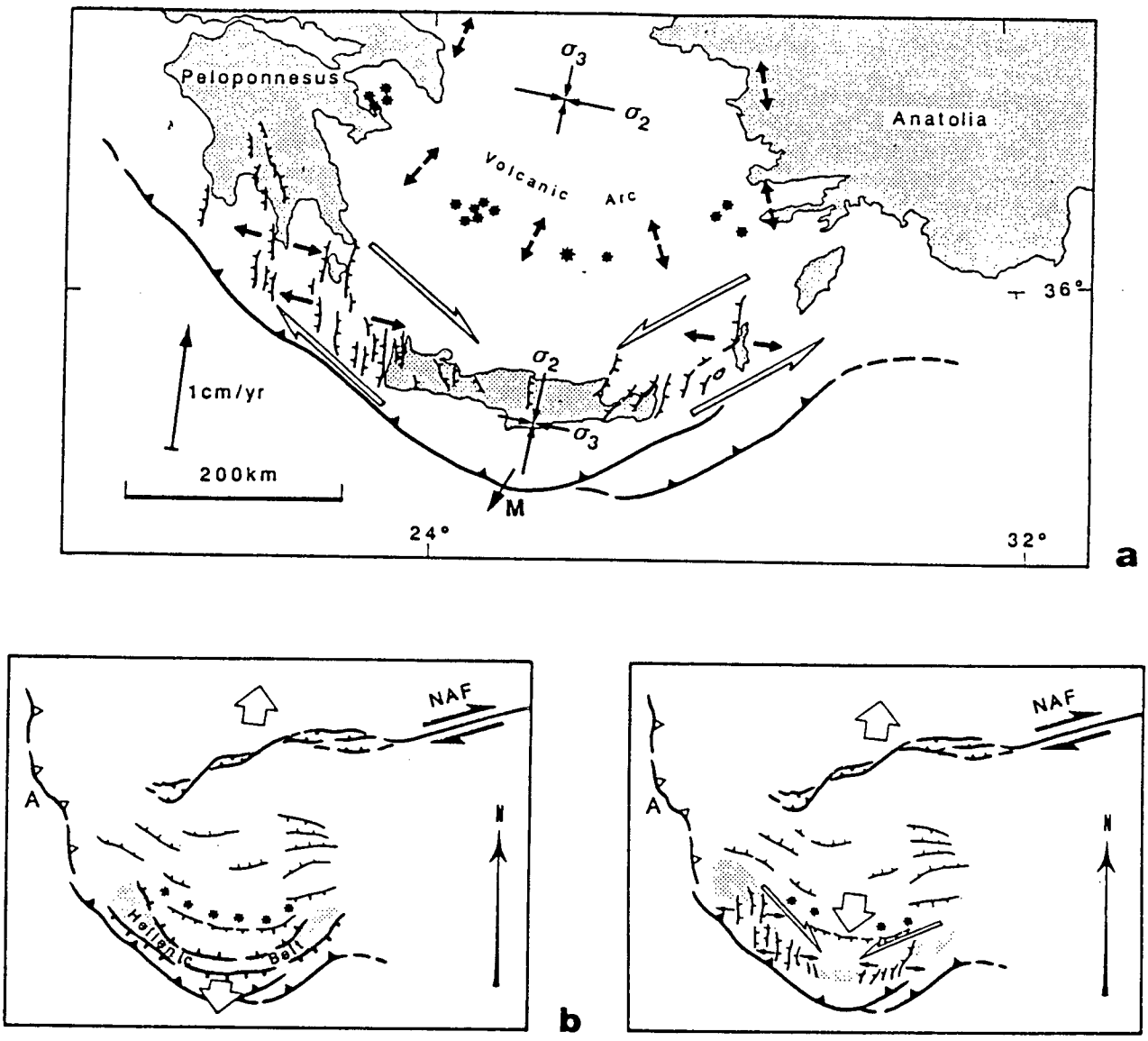

Figure 4.18. (a) Sketch map of fault kinematics in the Hellenic arc. Small solid arrows show direction of local extension. *En echelon* N-S normal faulting implies right-lateral motion between Peloponnese and western Crete and left-lateral motion Between Anatolia and eastern Crete (open arrows). Average direction of active extension (σ_3) is about N-S at the north of the volcanic arc and about E-W in the Hellenic arc, near the subduction zone. (b) Outline of the evolution of normal faulting in the Aegean region from late Miocene-Pliocene (?) (left) to Pliocene-Quaternary (right). Large open arrows represent the bulk Aegean extension. NAF is the North Anatolian fault, A is the collision with the Apulia.

for velocity structures near plate boundaries and it may not be appropriate for all recording stations. However, no systematic effects were observed on the expected dissimilarities between observed and synthetic seismograms.

For two of the events presented here (3, 4) a two-dimensional circular rupture model, with the rupture initiating at the centre of the circle, was assumed in the calculation of the synthetics and it produced waveforms that matched well the observed data. An elliptical rupture model with rupture initiating at the focus of the ellipse and propagating upwards was needed to obtain a good fit between the observed and the synthetic seismograms for event 7.

As the fault size increases with magnitude, the fault radius or the major axis of the ellipse was found to range between 2.5 and 11.0 km. However, in order to obtain the source duration of the *P*-wave seen on the observed seismograms the rupture velocity had to be increased and for the events studied it varied between 2.1 and 3.1 km s^{-1}. This is towards the upper end of the rupture propagation velocities (0.6 - 0.9 β) proposed by Madariaga (1976), which can reach *P*-wave velocity values because of diffraction effects, proposed by Das and Kostrov (1988).

The attenuation factor (t^*) did not show significant azimuthal variation. It had an average value of 0.6 s. The stress drop used (around 30 bar) is typical for interplate earthquakes (Kanamori and Anderson, 1975). This compares with relatively low intraplate stress drop of ~15 bar reported for shallow earthquakes in the Aegean back-arc region by Abercrombie (1991), using the same technique.

Seismic moments were found to be systematically lower than those estimated by others (Dziewonski *et al.*, 1983). Kiratzi *et al.* (1985), Tselentis *et al.* (1988), and Main and Burton (1990) have produced relations between surface wave magnitude M_S and seismic moment for earthquakes from the whole Aegean area. In all cases the scalar moments obtained here are towards the lower limits of their calculations. This is probably due to the differences in frequencies of the waves used by the other methods. The CMT method uses very long period waves and Main and Burton (1990) have used surface waves with a period range of 30 - 50 s. Kiratzi *et al.* (1985) and Tselentis *et al.* (1988) have used published moments which have been calculated using surface waves. Many recent studies comparing moment as a function of bandwidth (e.g., Silver and Jordan, 1983; Boatwright and Choy, 1986), have found that moment is a frequency-dependent quantity; it generally increases with increasing period. Moments obtained from long-period body waves (Christensen and Ruff, 1986), and very-long period Rayleigh waves (Monfret and Romanowicz, 1986), progressively increase in size. Variations in frequency-dependent moment far exceeding a factor of 4 have been observed by Silver and Jordan (1983) in the frequency range 1.0-10.0 mHz for great earthquakes. Therefore,

the discrepancy between moments obtained here using intermediate-period body waves, and those using longer-period waves is consistent with the conclusions of those studies.

4.5 SUMMARY & CONCLUSIONS

Seven recent moderate-sized earthquakes associated with the Hellenic subduction zone have been studied. Their fault plane solutions were determined using the relative amplitude method and were well constrained in most cases. For those events with fewer data the constraints on the solutions were poorer, although sufficiently good to indicate the source mechanism. Thrust mechanisms, obtained for most of the events examined, agree with the general compressional stress regime of the subduction zone. However, strike slip components are present in the cases of events associated with transform faults that are suggested by geological, morphological and seismic data. One of the events (event 7) has a normal fault type of mechanism which is in agreement with the active E-W extension regime at the epicentral area.

Focal depth, source dimensions, rupture velocity, stress drop and static seismic moment were obtained by forward body-wave modelling for three of the events. Focal depth was well constrained due to identifiable surface reflections of the direct *P*-waves on the BB records. Fault radius increases with magnitude and for the events studied ranges between 2.5 - 11.0 km. Stress drop is typical for interplate earthquakes (~ 30 bar). The rupture velocity assumed in the modelling, ranging from 2.1 to 3.1 km s^{-1}, lies close to the upper limit determined by the shear wave velocity. Seismic moments obtained from modelling the *P*-wave pulse are lower than those calculated using longer period waves. This is reasonable as moment is considered to be a frequency-dependent parameter. Finally, this Chapter highlights the importance of analysing earthquakes individually in order to gain information about the seismotectonic stress regime of a specific area.

CHAPTER 5

TECTONICS AND SEISMICITY OF THE ALEUTIAN ISLANDS SUBDUCTION ZONE

5.1 INTRODUCTION

Earthquakes from the Aleutian Island arc were chosen to be studied using the same methods as for those in the Hellenic arc, in order to apply the same methods and compare results from two similar tectonic environments.

The Aleutian arc is one of the world's longest island arc systems and is one of the most seismically active areas in the world. In this area of the North Pacific ocean, the Pacific lithospheric plate is subducting under the North American plate in a N-NW direction. The convergence is oblique at the eastern part of the arc and progressively takes the form of transform motion toward the western part. The main features of tectonic origin, typical of island arcs, are present here, and are from south to north (Fig. 5.01): a) *The Aleutian trench*, having a maximum water depth of about 7 km and its steepest side arcward, b) *The Aleutian terrace*, a geomorphological broad forearc region, and c) *The Aleutian island arc* or *volcanic arc*. The latter two areas comprise the *Aleutian ridge*. Submarine *transverse canyons* cut through the Aleutian terrace and trench and trend nearly at right angles to the slip direction of the oceanic lithosphere of the Pacific plate. Five major blocks can be identified along the length of the arc: *Near block, Buldir Block, Rat block, Delarof block* and *Andreanof block*. There exist three well documented north-trending fracture zones in the *outer ridge* or *rise*, in the north Pacific. These are the *Amlia fracture zone* (173°W), the *Adak fracture zone* (177°W), and the *Rat fracture zone* (178°E). Pronounced topographic disturbances are present on the northward extension of each of these fracture zones.

In this Chapter, the subduction process and the evolution of the Aleutian arc, together with proposed geodynamic models are described briefly. The associated seismicity, its distribution along the arc and in the Benioff zone, is outlined. The relationship between the seismicity and the deformation pattern of the area is discussed. Finally, some characteristics of earthquake source parameters for the arc are presented.

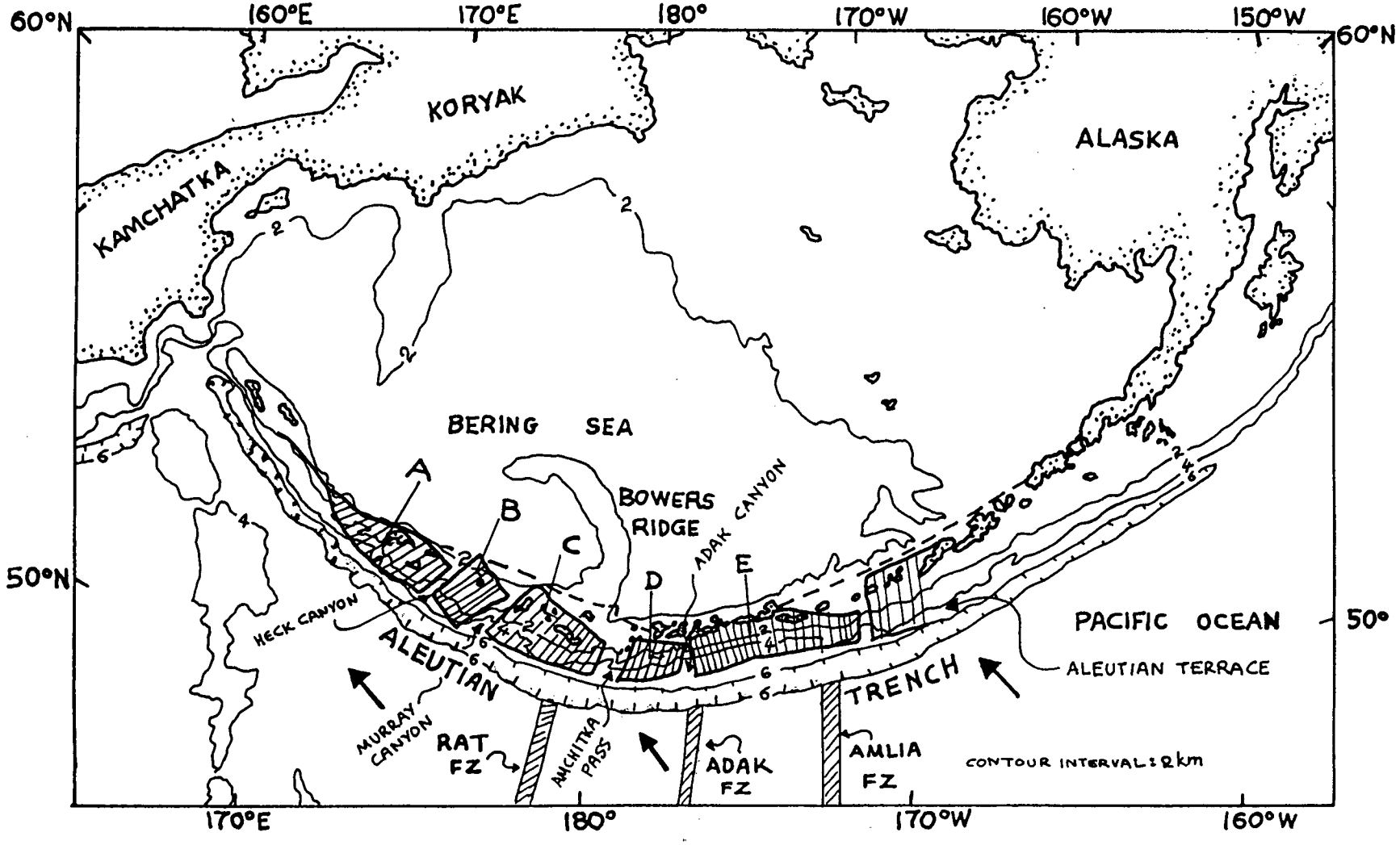

Figure 5.01. Main tectonic features of the Aleutian Islands subduction zone. A: Near block, B: Buldir block, C: Rat block, D: Delarof block, E: Andreanof block, FZ: fracture zone.

5.2 GEODYNAMIC MODELS

In a study of crustal and upper mantle structure of the central Aleutian arc (Grow, 1973), seven reflection profiles of the trench and terrace were presented. Although some of the observations and conclusions presented in that study are unique to the area, the major structural elements and processes can be applicable to convergence boundaries in general (Fig. 5.02). The main zone of deformation is of compressional type and prevails in a narrow region (0.5 - 1.0 km wide) at the northern extremity of undisturbed trench sediments. In this region the initial form of deformation appears to be thrusting rather than folding. Reflection, refraction and gravity data indicate that the Aleutian terrace, which is about 50 km wide, has 7 to 8 km of sediment near its axis. This is a near-maximum value for island arc systems. The ridge separating the trench and the terrace is composed of uplifted deformed sediments. The dip of the Benioff zone beneath the north slope of the terrace is less than 20° and may be as low as 5° to 10°. The absence of earthquakes beneath the terrace and the presence of very shallow earthquakes beneath the southern edge of the Aleutian ridge favour the shallower limit.

The gravity data (Grow, 1973) over the trench and the terrace suggest that the wedge of low-density deformed sediments, which have accreted north of the trench axis, may be between 30 and 70 km wide, depending on the dip of the Benioff zone. On the basis of the gravity data over the Aleutian arc, a density contrast of +0.05 g per cc between the descending lithosphere and the surrounding lithosphere (for an 80 km thick plate) appears most reasonable, and its contribution over the outer trench slope eliminated the classical gravity problem of artificially thinning the oceanic crust in that region. Moreover, a high-temperature, low- density region is necessary beneath the volcanic region and above the descending lithosphere in order to balance the gravity model.

A characteristic feature of the arc is the presence of transverse submarine canyons which cut through the Aleutian terrace and ridge and trend nearly at right angles to the slip direction of the oceanic lithosphere. Their cross sections are generally asymmetric, being steepest on their southeast slopes. These canyons were first described by Gates and Gibson (1956) who gave convincing arguments for their having a tectonic rather than erosional origin: they are not connected to a land mass large enough to erode them, are consistently asymmetrical in cross section, and lie subparallel to each other at an angle to the direction of maximum slope. The well-developed morphology of the blocks and terrace canyons (Fig. 5.03) suggests that the character of underthrusting has been regularly repeated over a long period of time (Spence, 1977). This implies that the pressure overloads that diffuse downslab episodically are highly repeatable and that the process of induced partial melt concentration is also repeatable. The narrowness of the Aleutian volcanic arc suggests that the depth from which volcanic magma arises has not

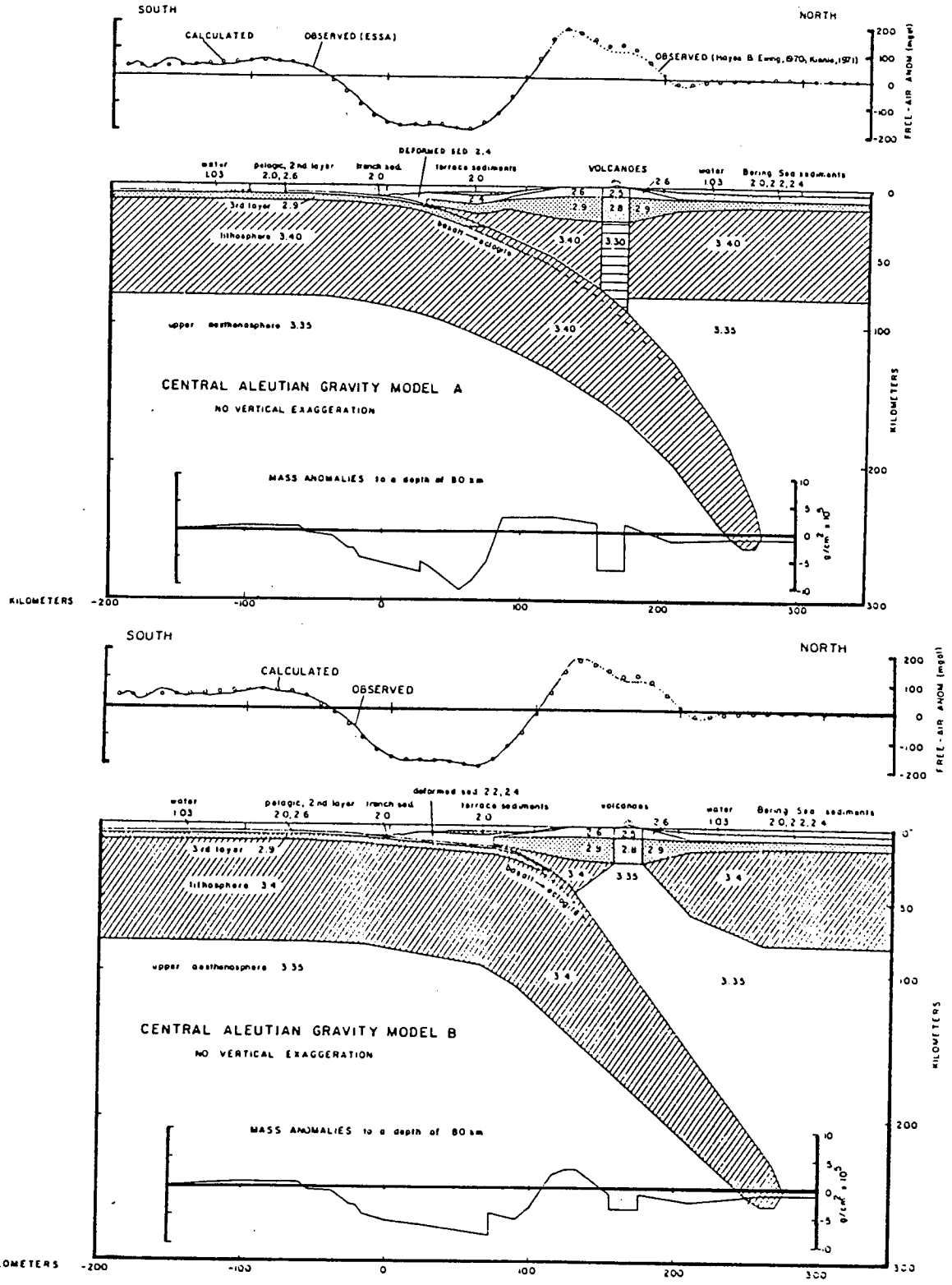

Figure 5.02. Two dimensional gravity models (A, B) for crust and upper mantle, central Aleutian arc (Grow, 1973). Both models are compatible with the data.

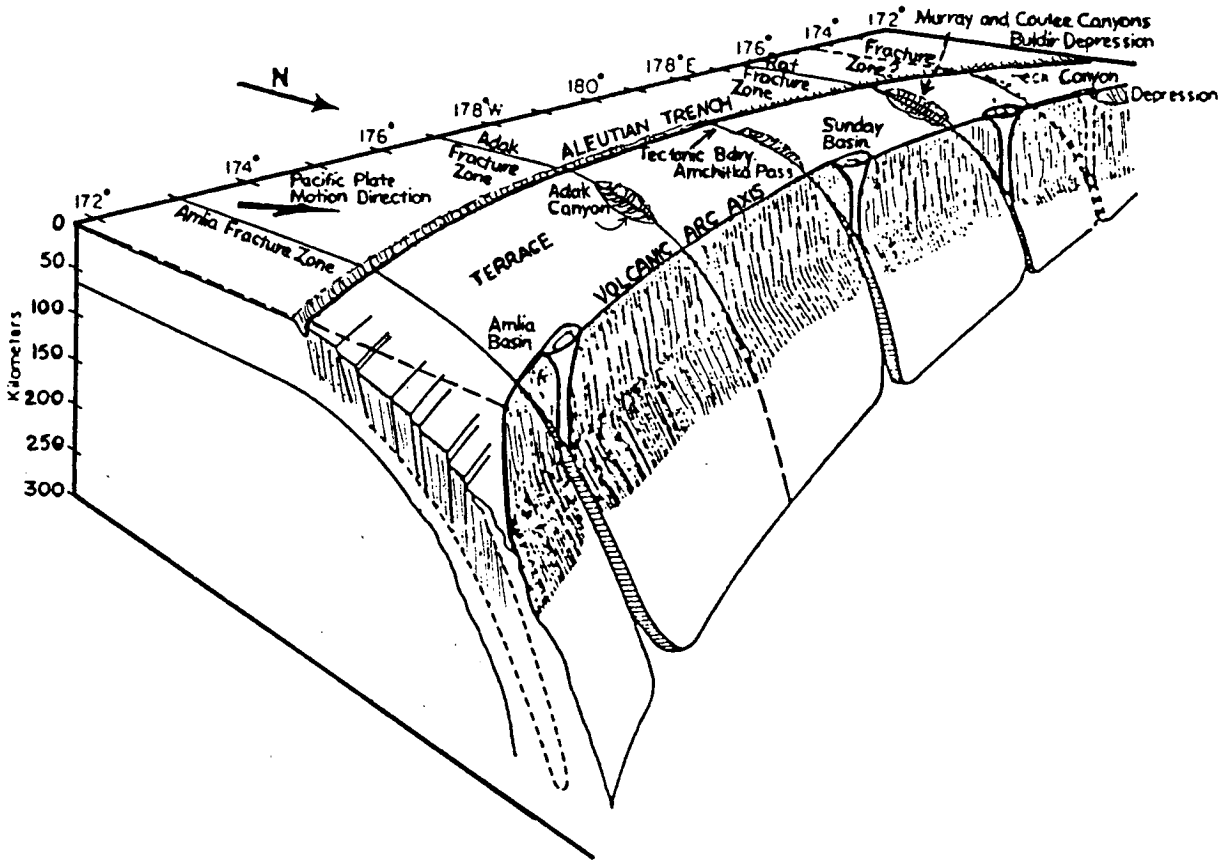

Figure 5.03. Schematic diagram of laterally segmented subducting Pacific plate, showing north Pacific plate fracture zones, canyons of the Aleutian terrace, major depressions on the volcanic arc axis, and the inferred magmatic source zone for the Aleutian volcanic arc. The depth of the subducted plate decreases westward as the Pacific plate motion becomes more transcurrent to the Aleutian arc (from Spence, 1977).

changed significantly and thus is consistent with the suggested repeatable character of the Aleutian arc underthrusting. If the direction of the subduction were to change, then the mechanics of the underthrusting would change and this would lead to a slight subparallel immigration of the volcanic arc axis. Transverse canyons are generally absent in the Aleutian arc east of 177°W. The easternmost is the Adak canyon. LaForge and Engdahl (1979) believe that the Aleutian transverse canyons are block-fault structures caused by lateral extension of the overriding lithosphere.

Davies and House (1979), based mostly on local network data, state that even though there is considerable variation in tectonic style, the shape of the Benioff zone and its location relative to the active volcanoes do not vary much along the length of the Aleutian arc. The volcanic arc is approximately colinear with the 95 km depth contour of the Benioff zone. In contrast to the consistency of the Benioff zone along the entire arc, the main thrust zone gradually widens to its maximum of about 400 km in south central Alaska. This widening of the thrust zone (and hence of the interface between the underthrusting and the overthrusting lithospheric plates) may allow the accumulation of more strain energy which results in the occurrence of larger earthquakes in the eastern Aleutian arc than in the central Aleutian arc.

A combined location and velocity inversion technique was applied to travel-time data from well recorded central Aleutian earthquakes by Engdahl and Gubbins (1987). Results indicated a steep dipping slab with a thickness of 80 to 100 km and a downdip length of about 400 km, well below the deepest seismic activity (Fig. 5.04). The slab is characterized by seismic velocities as much as 11 % higher than the surrounding mantle in its upper portions and 4 to 6 % higher at depth. A sharp velocity gradient and lower velocities occur directly beneath the volcanic arc, near the top of the slab. The velocity anomaly spreads out and falls off very slowly with depth. This is probably due to lack of resolution and/or deficiencies of their method.

Geist *et al.* (1988) propose that the arc massif between approximately 170°E and 170°W is broken into five blocks which since late Miocene or early Pliocene have moved to the west and rotated clockwise with respect to the rest of the North American plate (Fig. 5.05). The rotation away from the plate to the north caused the formation of several summit basins along the arc. Transverse canyons are formed along block boundaries due to the left lateral shear between blocks, as well as extensional stresses caused by differential rotation of adjacent blocks and the curved geometry of the arc. As a result, the spacing between blocks must increase and the arc must extend in the along-arc direction.

Ekström and Engdahl (1989) suggest that part of the overriding plate which is in contact with the subducting plate is weakly coupled to the rest

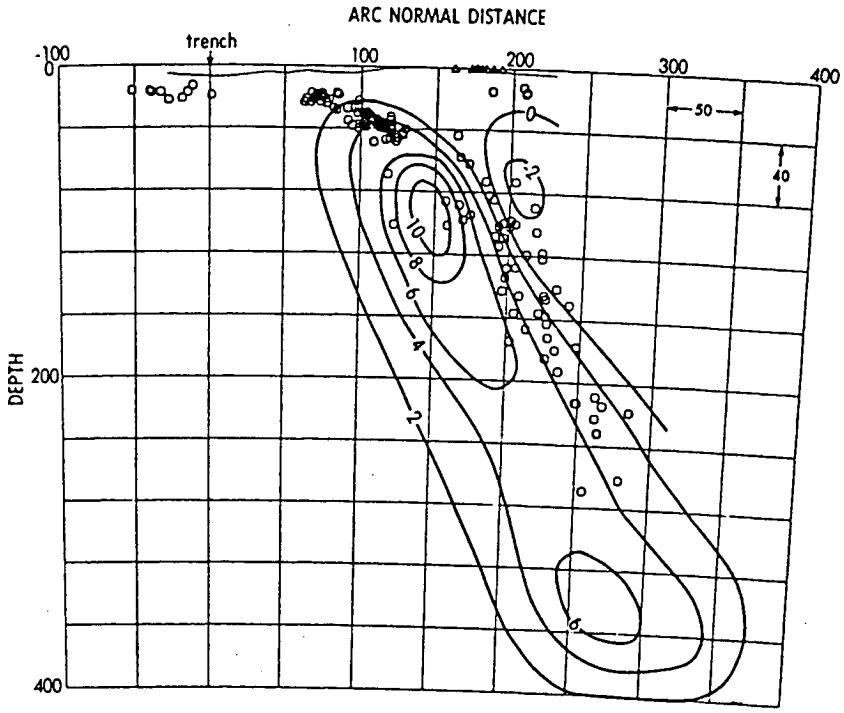

Figure 5.04. Cross section of velocity change contours of the inversion results for the central Aleutian subduction zone (from Engdahl and Gubbins, 1987).

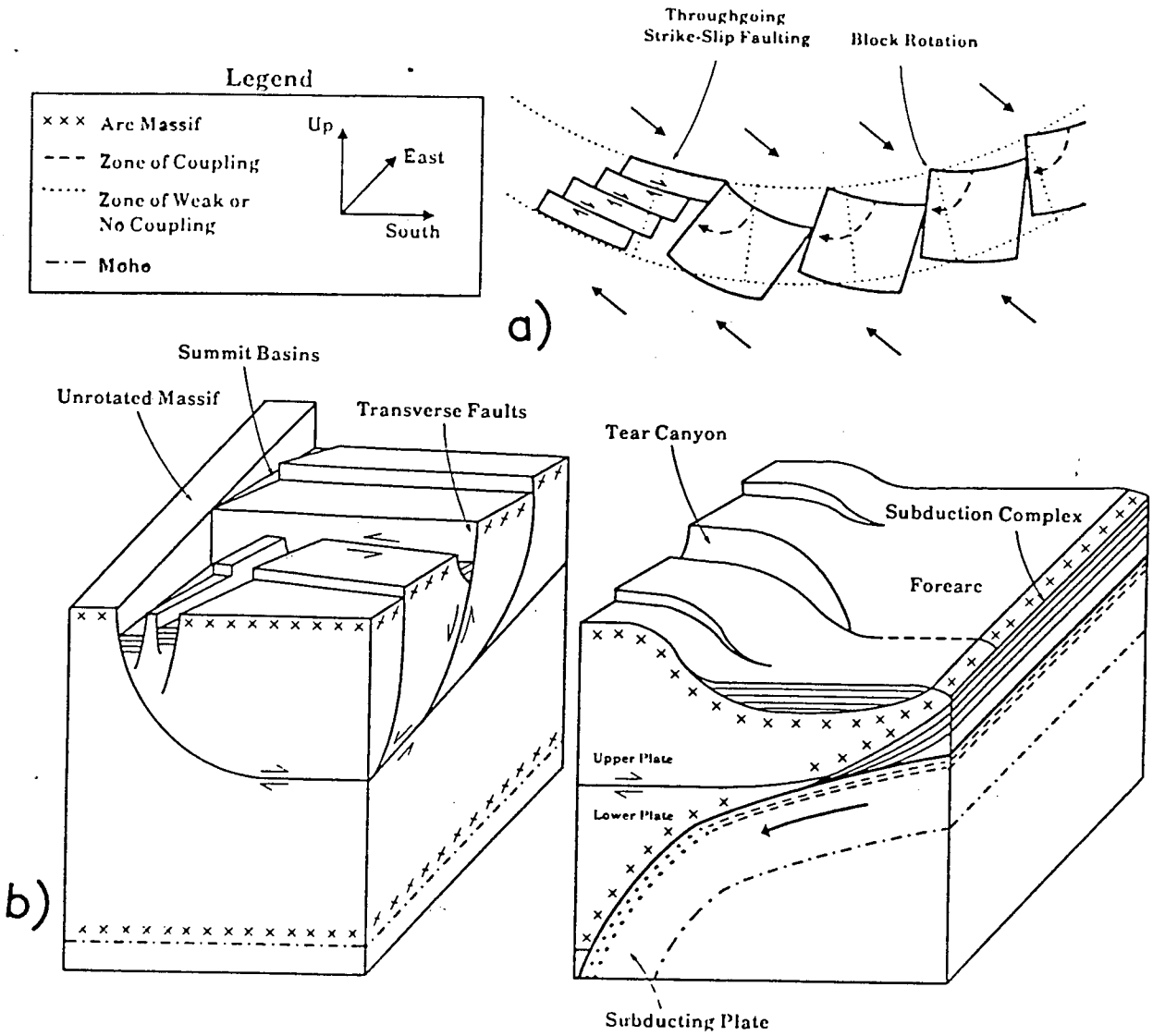

Figure 5.05. a) Rotation of blocks along an arc with a constant orientation of forces. The obliquity of the force field with respect to the arc increases to the left, as does the magnitude of the shear couple and the amount of block rotation. Increasing amounts of rotation in the direction of block translation creates geometric gaps between blocks that are interpreted to correspond to transverse canyons. Block rotation continues until the arc parallel shear stress reaches a critical point where throughgoing strike-slip faults are prevalent. b) Schematic, exploded block diagram illustrating a possible configuration for faulting related to block rotation. In addition to the blocks rotating about a vertical axis trenchward and eventually over the accretionary complex, the blocks are rotating about a horizontal axis from down-to-the-west displacement on transverse faults. The detachment fault shown extending from the summit basins to the subduction complex is one possible explanation for how rotational deformation is accounted for at depth. Arc-normal basal shear across the detachment is intended only to present rotational movement of blocks in the upper plate and not horizontal movement of the lower plate transmitted by the subducting lithosphere (from Geist *et al.*, 1988).

of the overriding plate north of the volcanic arc, and can be dragged along the arc with a velocity of approximately half the along-arc projection of the relative plate motion.

Boyd and Creager (1991) analysed teleseismic travel time data to image the structure of the Aleutian subduction zone. They constructed theoretical residual spheres by tracing rays through three-dimensional thermal models of the subducting slab assuming a pressure independent thermal coefficient of velocity. Assuming a constant dip, a slab penetration depth of 600 km fits the central Aleutian events best (Fig. 5.06). This is at least 300 km below the deepest earthquake. In the western Aleutian arc, where the relative plate motion becomes transform, seismicity ceases at less than 100 km depth and volcanism is no longer active, it has been previously assumed that no slab exists. However, a slab-like, high-velocity zone was imaged by the study of Boyd and Creager (1991). Their model suggests that material which is subducted obliquely in the central Aleutians is subsequently transported laterally at depth along the Aleutian arc towards the west. The lack of volcanic activity in the western Aleutians is apparently related to this lateral transport of the slab, perhaps indicating that the slab is dehydrated and incapable of producing the volatiles necessary for arc magmatism (Creager and Boyd, 1991).

5.3 EVOLUTION OF THE ARC AND SUBDUCTION RATES

The Aleutian arc originated when the north Pacific subduction zone of the Kula plate shifted southward from the Beringian continental margin to the present offshore position of the arc (Fig. 5.07). Subduction at the Beringian continental margin seems to have ended in earliest Tertiary time, suggested by the 50 - 55 my age for the oldest rocks found on the Aleutian Islands. By middle Eocene, voluminous magmatic growth built the bulk of the arc and started to diminish by at least 40 Ma. The decrease in magmatism at this time coincides with a change in the motion of the Pacific plate, 43 Ma, and the contemporaneous abandonment of the Kula-Pacific spreading centre, 43 - 45 Ma (Engebertson *et al.*, 1986, Lonsdale and Smith, 1986). The new plate configuration resulted in a marked decrease in the rate of subduction from as much as 200 km my^{-1} for the Kula plate prior to 43 Ma, to 58 - 70 km my^{-1} for the Pacific plate (rates from Engebertson *et al.*, 1986, at 173°W).

The Oligocene and Miocene history of the arc was marked by the intrusion of plutons accompanied by uplift and warming of the crestal region (Marlow *et al.*, 1973, Citron *et al.*, 1980). Tectonic sinking of the ridge along with localized extensional deformation of the crestal region characterizes the late Cenozoic history of the arc (Fig. 5.07). Regional subsidence has been attributed to subduction of segments of the inactive Kula ridge beginning at about 10 Ma (Engebretson *et al.*, 1986, Lonsdale and Smith, 1986), and the

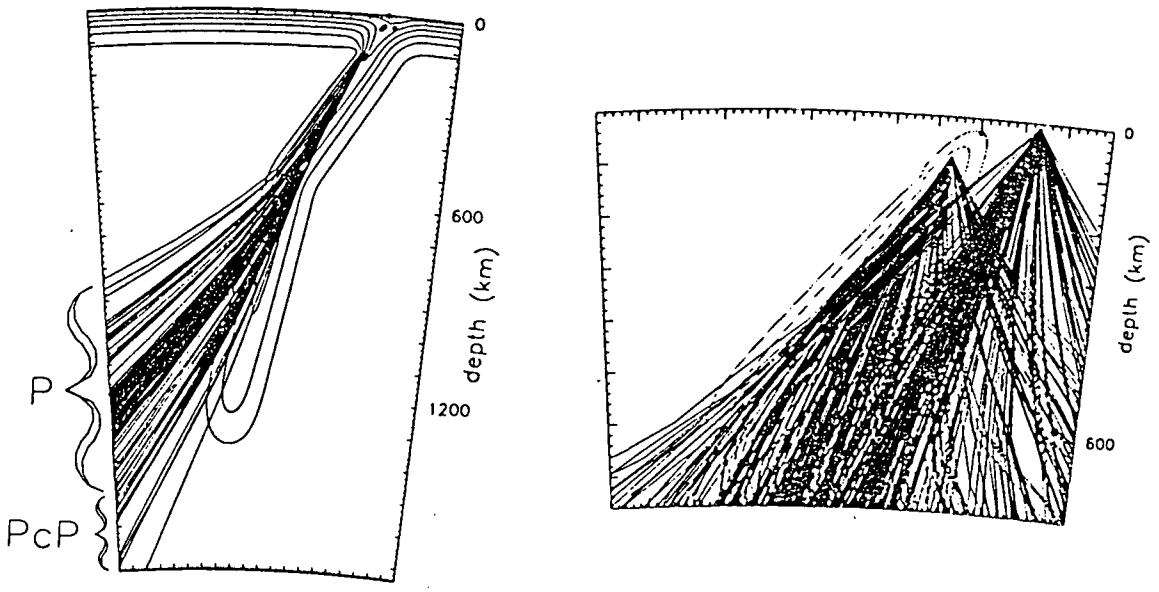

Figure 5.06. Cross sections of slab models for the central (left) and the western (right) Aleutians, showing paths of rays for three earthquakes propagating to various stations. Left diagram shows isotherms of the potential temperature model contoured at 200°C intervals. Right diagram shows P-wave velocity anomaly contoured at 0.1 km s^{-1} intervals. Ray paths are projected onto the plane through a geocentric rotation about the arc pole. For the central Aleutians only *P* and *PcP* rays to the dense set of European stations are shown. In the western Aleutians *P* rays to all stations are shown. The difference in ray sampling between events provides the resolution of slab geometry (Boyd and Greager, 1991).

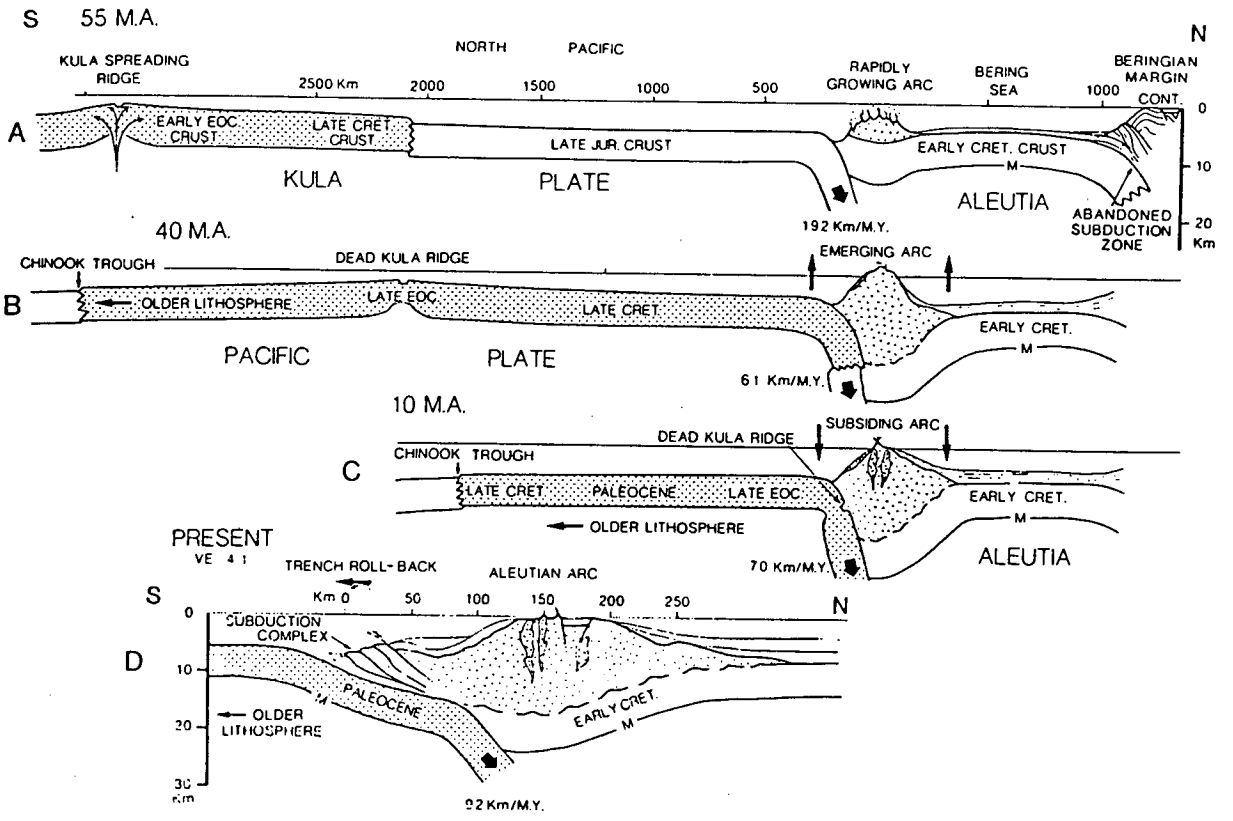

Figure 5.07. Schematic diagram illustrating the tectonic history of the Aleutian arc (taken from Scholl *et al.*, 1987). Linear convergence velocities are from Engebretson *et al.*, 1986, at 173°E. a) At 55 Ma, active spreading at the Kula ridge between the Pacific and Kula plates, initial subduction at the Aleutian arc, and cessation of subduction at the Beringian margin occurred contemporaneously. b) By at least 40 Ma, spreading at the Kula ridge has ceased and the Aleutian arc underwent regional uplift attributed to the subduction of more buoyant Pacific lithosphere of the former Kula plate. c) At roughly 10 Ma, subduction of the dead Kula ridge initiated regional subsidence of the arc as increasingly older lithosphere was subducted. d) Starting at about 5 Ma to the present, the subduction complex and the forearc region formed, owing to an abrupt increase in trench floor turbidite sedimentation. Accelerated block rotation of the Aleutian massif begun approximately this time.

consequential underthrusting of increasingly older and denser oceanic lithosphere beneath the arc. Summit basins began to form in late Miocene to early Pliocene time and were filled with sediments derived from ridge crest material and late Cenozoic volcanism (Geist *et al.*, 1987). The latest Cenozoic episode, starting 5 Ma, coincided with an increase in the rate of subduction of the Pacific plate to approximately 87 km/my at a more northerly azimuth (Engebretson *et al.*, 1986).

5.4 SEISMICITY OF THE ALEUTIAN ARC

The Aleutian arc has been the site of several of the world's great earthquakes. Figure 5.08 shows the distribution of seismicity along the entire length of the Aleutian Islands subduction zone for the last twenty years. Specific rupture zones and gaps have been studied in detail by many authors and are shown in figure 5.09 (from Davison and Scholz, 1985).

As in most subduction zones, the seismicity of the Aleutian arc occurs in four distinct seismotectonic regimes based on the location of earthquakes and their focal mechanisms (Taber *et al.*, 1989). These regimes are:

1) *The trench and outer rise.* The total number of events near the trench and outer rise is small compared to the other parts of the subduction zone. In the central Aleutian area this regime is limited to a zone of about 10 km landward and up to 90 km oceanward of the trench axis. It is spatially separated from the main thrust zone by an approximately 35 km-wide aseismic region coincident with the location of the accretionary prism (Engdahl *et al.*, 1989). The focal depths of trench and outer rise earthquakes are subcrustal ranging from 13 to 22 km beneath the ocean surface (Engdahl *et al.*, 1989). Focal mechanisms for these earthquakes are characterised by normal faulting with the extensional axis perpendicular to the trench. These events are apparently caused by the tensile stresses generated in the Pacific plate as it bends underneath the plate margin. The limited depth range of seismicity implies that the bending strength of the lithosphere is exceeded in only a narrow region which puts an upper limit on the location of the neutral surface within the lithosphere. The earthquake of 3 May 1980 (event 8) belongs to this zone and it is examined in the next Chapter.

2) *The main thrust zone.* Most of the strain generated by plate convergence is released along the main thrust zone during great earthquakes. Engdahl *et al.* (1989) have shown that between 172° and 179°W, the main thrust zone extends arcward 45 to 130 km from the trench axis and from 15 to 50 km in depth. They believe that the apparent thickness of this interplate thrust earthquake zone is no more than 15 to 20 km, and the spatial distribution of earthquakes is non-uniform. Focal mechanisms for earthquakes in

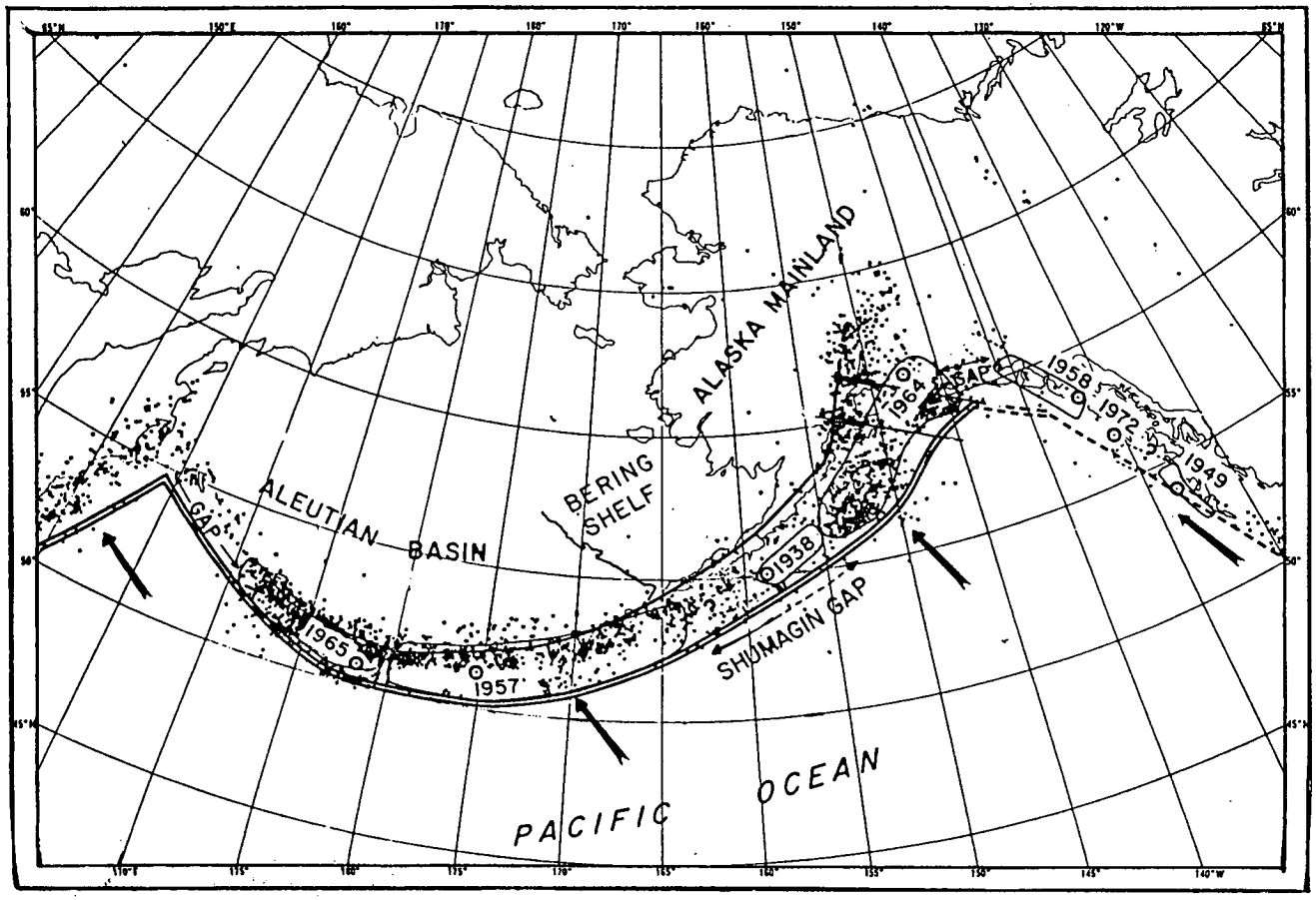

Figure 5.08. Seismicity of the Aleutian arc and adjacent areas. The single heavy line marks the trend of the active volcanoes and is approximately colinear with the 95 km depth contour of the Benioff zone below the volcanoes. The double heavy line shows the location of the Aleutian trench and (in the far west) part of the Kamchatka trench. The arrows show the direction of the relative motion between the Pacific and North American plates.

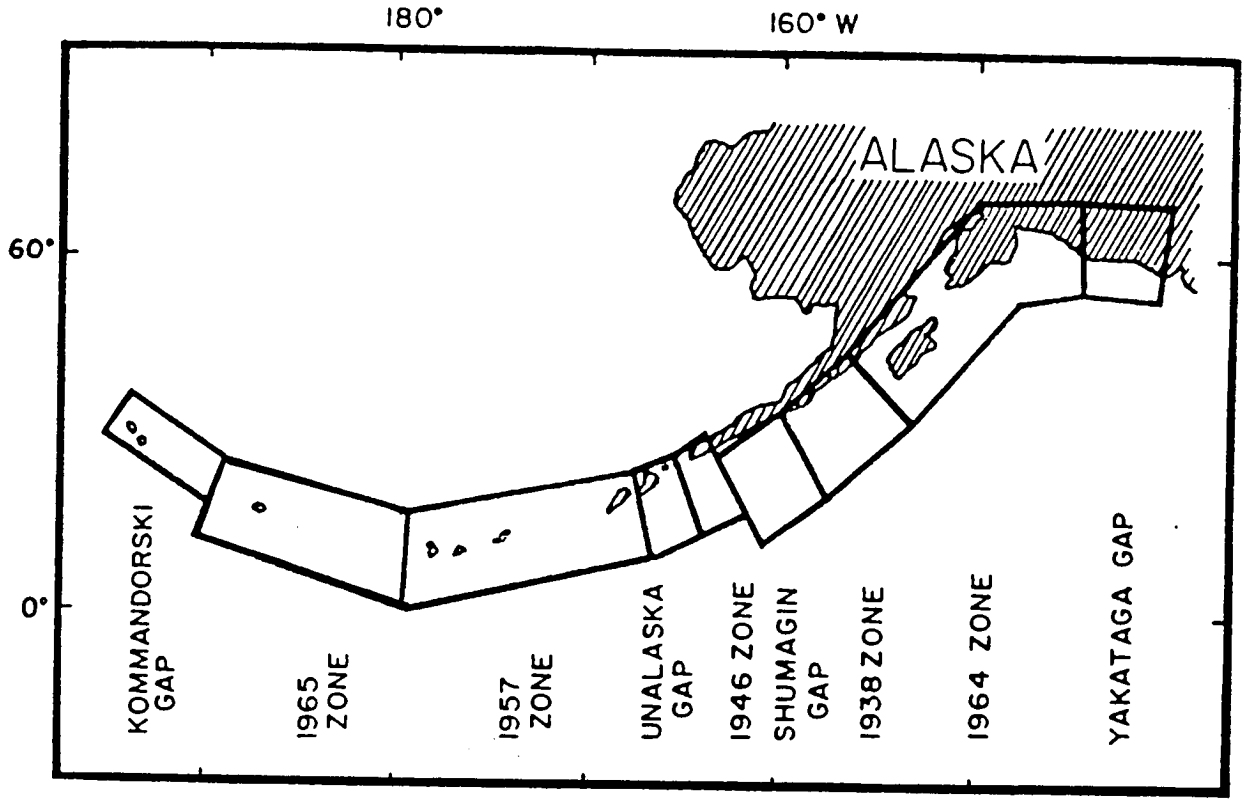

Figure 5.09. Seismic rupture zones and gaps (Davidson and Scholz, 1985).

this zone are consistent with thrusting along the plate interface. Most of the earthquakes that are presented in the next Chapter belong to this zone.

3) *The Benioff zone.* Earthquakes at depths greater than 50 km are less numerous than those in the main thrust zone. A zone of sparse seismicity separates events in the main thrust zone from those in the Benioff zone. In the central Aleutian area, the Benioff zone dips at an angle of about 60° arcward and earthquakes occur up to a maximum depth of 300 km. One earthquake from this zone is studied in the next Chapter.

4) *The upper plate.* Earthquakes in the overriding plate are concentrated at shallow crustal depths, usually near the volcanic arc. Focal mechanisms for these events suggest right-lateral strike-slip on near-vertical faults parallel to the arc.

5.4.1 Double Benioff zone

Engdahl and Scholz (1977) have shown that in the central Aleutians the Benioff zone below a depth of 100 km consists of two thin subzones of earthquakes about 25 km apart that merge at a depth of 175 km. Focal mechanisms in the upper zone indicate consistently downdip compression, while those of the lower zone show downdip tension. They suggest that these two subzones reflect the stresses in the elastic core of the lithosphere due to unbending. House and Jacob (1983) have studied the subduction zone beneath the 1500 km segment of the eastern Aleutian arc using teleseismic data. The principal result of that study was that hypocentres of intermediate-depth earthquakes appear to define a weakly developed double seismic zone at depths between 70 and 170 km. The two bands of the double seismic zone are at their shallowest depth 30 km apart and approach each other with increasing depth. Focal mechanisms indicate that the upper seismic zone is dominated by downdip P-axes and the lower one by downdip T-axes. These inplate stresses are consistent either with models of unbending of the subducting slab as it enters the mantle (Engdahl and Scholz, 1977, Fig. 5.10), or thermal changes (House and Jacob, 1982, Fig. 5.11), or of stresses due to slab pull (Spence, 1987, Fig. 3.06).

5.4.2 Slip partitioning and arc parallel strike slip faulting

Slip partitioning and arc-parallel strike-slip faulting has been previously primarily observed in subduction zones where the overriding lithosphere is of continental type (Fitch, 1972). Jarrard (1986) reviewed the evidence for arc-parallel strike-slip faulting for different areas of subduction and found very little direct evidence (earthquake mechanisms or mapped faults) for this type of deformation when the overriding crust is

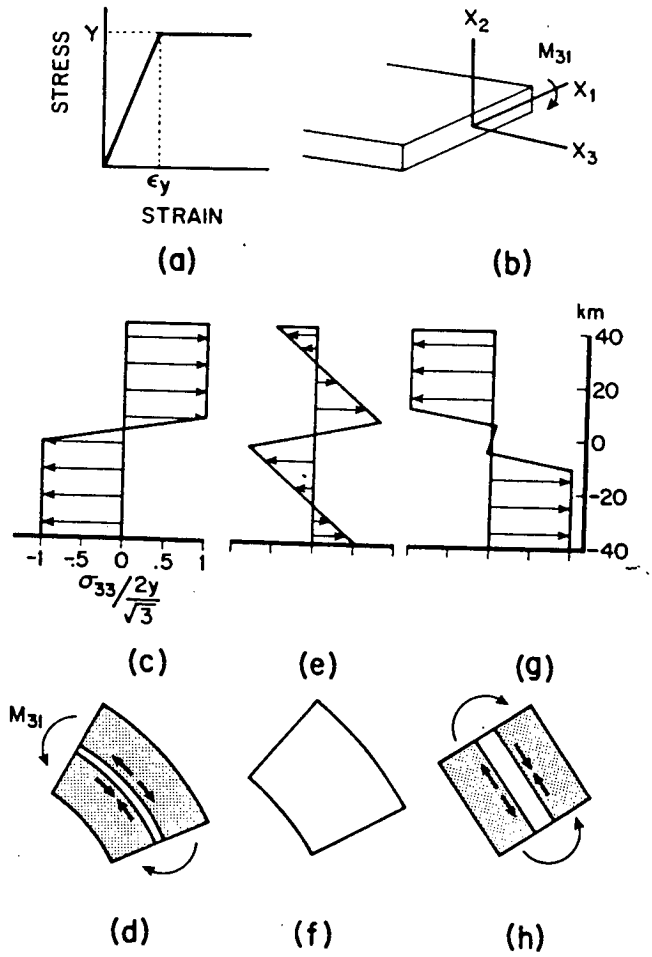

Figure 5.10. Models of the bending plate (Engdahl and Scholz, 1977). a) Assumed rheology, b) geometry of the model, c) stresses (σ_{33}), and d) plate configuration in the region of maximum bending, radius of curvature r = 150 km, e_Y = 3 %. Stresses are normalized to the yield stresses ($2/3^{-2}$) Y. The stippled region has yielded. e) Stresses and f) the same after a reverse moment has been applied to unbend the plate.

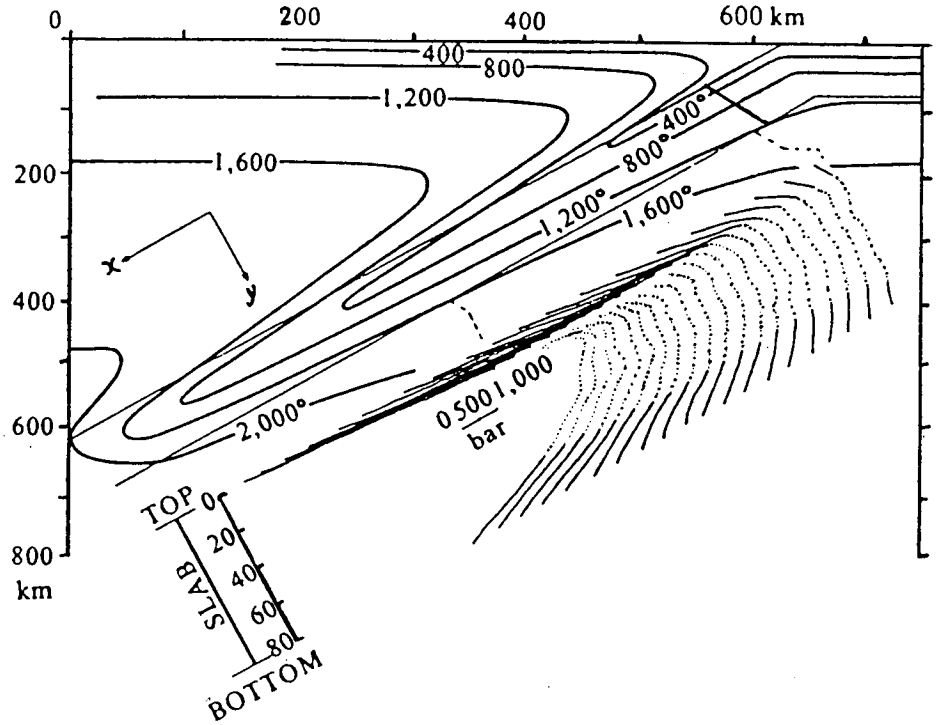

Figure 5.11. Thermal model of the descending lithospheric slab and cumulative thermoelastic stresses obtained from it (House and Jacob, 1982). Isotherms (in °C) are derived from numerical modelling of an 80 km thick slab that dips at 45° and subducts at a rate of 80 mm yr^{-1}. The coordinate system used appears in the inset, upper left; $y = 0$ at the centre of the slab; the z axis points out the page (along the strike of the slab); Cumulative thermoelastic stresses calculated for the 80 km thick slab model (no relaxation) are inset in the lower right. Each successively deeper profile is the sum of the stresses of the previous profile, plus the increment of stresses developed between the profiles. Tensional stresses are indicated by the dotted portions; compressional by the solid lines. Note that cumulative tensional stresses of > 2 kbar are reached only ~ 20 km inside the slab from where cumulative compressional stresses of 6 kbar have developed. Horizontal exaggeration of approximately 1.7.

oceanic, probably because oceanic lithosphere is stronger compared to continental lithosphere. Thus, if slip partitioning is occurring in such regions, the mechanism is probably aseismic. Jarrard (1986) found systematic discrepancies between the observed slip directions and the relative direction of plate motions, correlating well with the sense (dextral or sinistral) of the obliquety of convergence. Because of the limited data used by Jarrard (1986) for the Aleutian subduction zone, it is not possible to examine any variation of the observations along the arc. However, with the large number of focal mechanisms available today this could be easily attempted.

Ekström and Engdahl (1989) have observed that there is a deviation of the slip vectors on the main thrust zone from those predicted from large scale plate motions, and that several large earthquakes have occurred in the overriding plate, close to the volcanic line, which have strikes consistent with along-arc right-lateral shearing. These two observations suggest that there is a partitioning in strain between the slip on the main thrust zone and internal deformation of the arc massif. Figure 5.12 shows the slip vector azimuths for thrust type earthquakes along the Aleutian arc from 165°E to 150°W (Ekström and Engdahl, 1989). The data derived from the Harvard CMT catalogue (Dziewonski *et al.*, 1989) using all events with depth less than 50 km and one nodal plane correlating with the strike and dip of the subducting Pacific plate. The slip vectors west of approximately 160°W show an increasing deficiency in along-arc motion, up to approximately 170°E, where the seismicity is lower and plate motion is roughly parallel to the plate boundary. East of 160°W a group of earthquakes have slip vectors which are oriented more to the west than predicted. A simple model of strain partitioning is proposed (Ekström and Engdahl, 1989), in which the relative plate motion between the North American and the Pacific plate is accommodated by slip on the main thrust zone and strike-slip motions on a vertical plane coincident with the volcanic arc.

5.5 SOURCE PARAMETERS

5.5.1 Depth

The structure of the outer rise and trench part of the subduction zone is typically oceanic with a thin crust and very little sediment on the sea floor. As a result the sharp sea bottom velocity contrast is expected to produce strong reflections of *pP*. Also the phase *pwP* and its multiples is frequently recorded and add to the accurate determination of the focal depth. Earthquakes near the volcanic arc and above the plate interface occur at depths beneath the sediment basement interface which also can be estimated by the use of surface reflections of the direct *P*-waves.

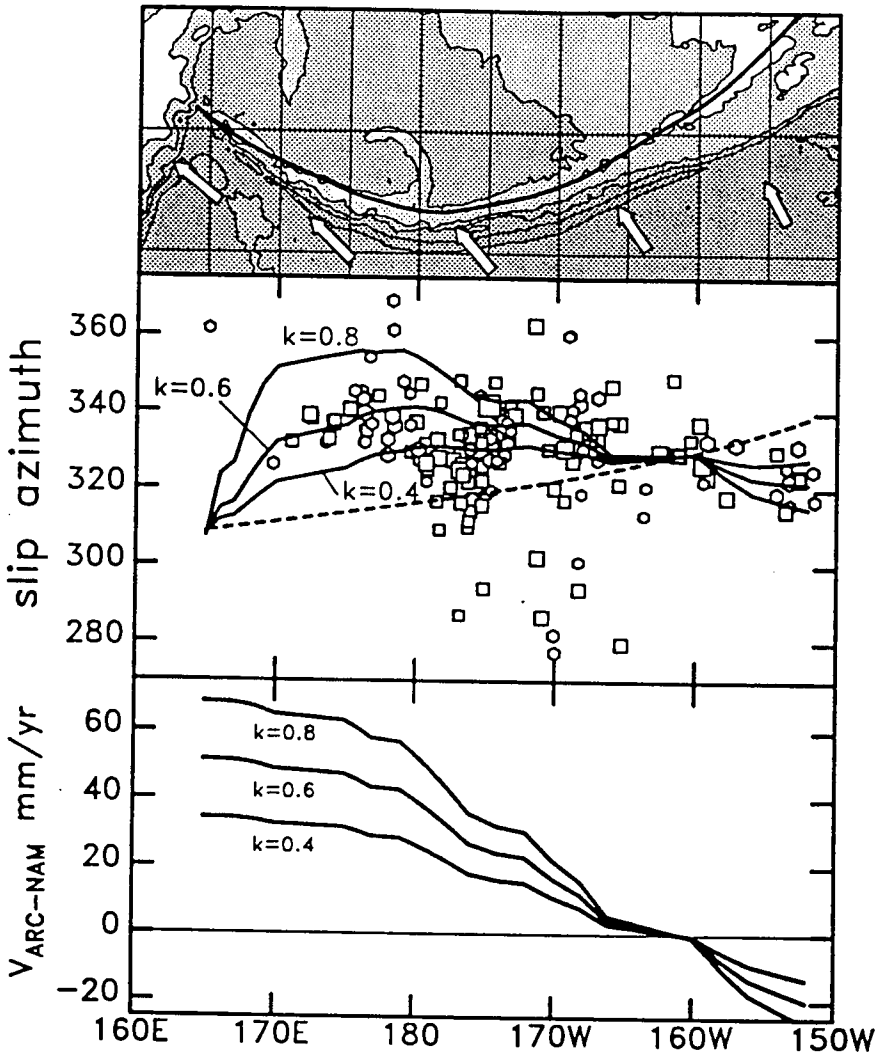

Figure 5.12. (*Top*) A map of the Aleutian arc. The arrows show the relative motion azimuths predicted by the model (RM2) of Minster and Jordan, 1978. The heavy solid line follows the locations of volcanoes along the arc. (*Middle*) Horizontal slip azimuths for thrust zone events which have one nodal plane which roughly coincides with the orientation of the main thrust zone. Events deeper than 30 km are indicated by squares, and shallower events by hexagons. The dashed line corresponds to the relative motion azimuth predicted from RM2. The solid lines correspond to the relative motion azimuths between the Pacific plate and the arc massif when a fraction of the along arc relative motion is postulated to occur on a vertical plane parallel to the volcanic line shown in the upper panel. (*Bottom*) The predicted magnitude of strike slip motion occurring within the overriding plate (from Ekström and Engdahl, 1989). [k is a proportionality factor between the magnitude of the overall relative plate motion with azimuth Φ ($V_{PAC-NAM}$) and the magnitude of strike slip motion on a vertical plane with strike Θ ($V_{ARC-NAM}$)].

Events deeper than 50 km in the central Aleutians, which apparently occur in the downgoing plate, are infrequent and usually of low magnitude (Engdahl and Billington, 1986). The estimation of their focal depth represents a special problem as ray paths of depth phases to receiving stations are widely separated and sample different deep structure than the paths of *P*-waves which travel down the plate. In this case, only phases with similar propagation paths should be compared for the determination of the focal depth.

5.5.2 Focal mechanisms

As mentioned in section 5.4.1, trench and outer rise earthquakes are characterized by normal faulting, the Benioff zone earthquakes vary from downdip compression in an upper plate to downdip tension in a lower plane, and earthquakes located in the overriding plate show evidence for arc parallel extension. Events in the main thrust zone have focal mechanisms that are expected to reflect the large scale motions associated with the plate convergence. However, it was found by Ekström and Engdahl (1989) who determined focal mechanisms using the CMT method, that the majority of the events in this zone have focal mechanisms which correspond to a relative motion vector which is more normal to the trench than that predicted by the large scale plate motions. The average difference is 10° - 15°. Deeper thrust plane events (h > 30 km) show greater scatter than shallow (h < 30 km) events. Ekström and Engdahl (1989) give three possible explanations for this discrepancy, the third being the more plausible: a) The focal mechanisms are systematically biased, probably due to heterogeneous subduction zone velocity structure, b) errors in the direction of plate convergence, and c) large, primary aseismic, deformation occurs away from the interplate contact zone in the overriding plate, causing partitioning of the relative plate motion.

In the present work, described in the next Chapter, seven moderate-sized, shallow-to-intermediate depth earthquakes with epicentres located on different parts of the arc are chosen and studied in detail.

5.5.3 Moment release

The Aleutian Islands subduction zone is one of the three zones in the world where more than 90 % of the total moment release is taken up by one great earthquake per 80 years. Such large events rupture the whole length of the arc, releasing the strain and resulting in a lack of moderate-sized events (Peterson and Seno, 1984). In figure 5.13 the pattern of accumulative moment release, between 1900 and 1980, in the

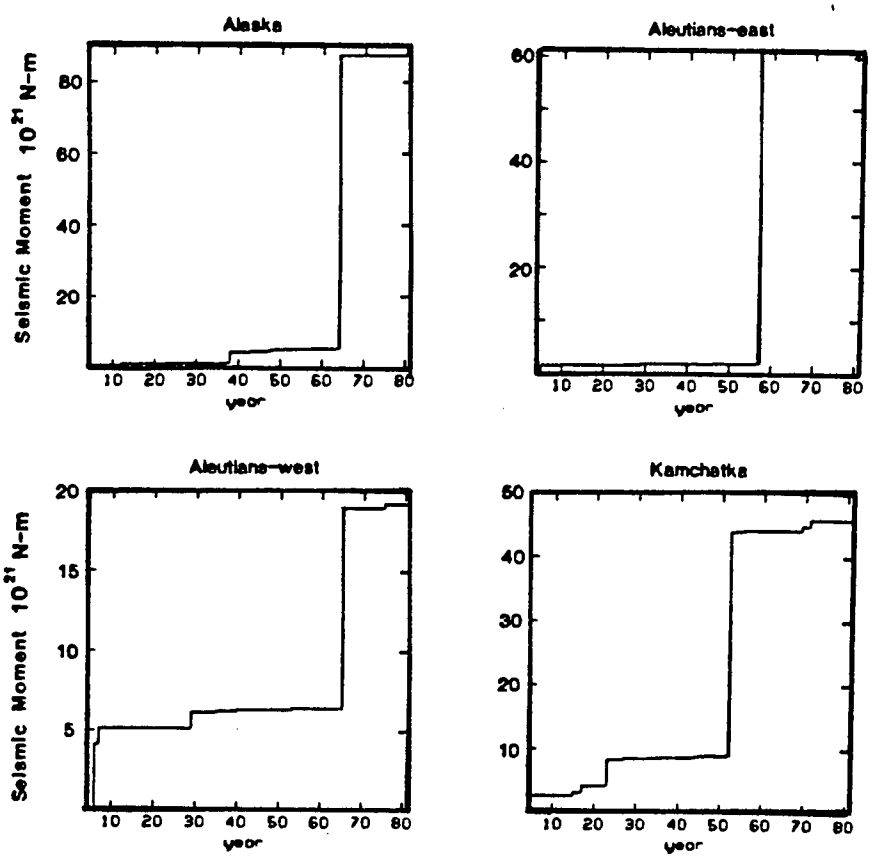

Figure 5.13. Seismic moment release for the Aleutian arc and adjacent areas (Alaska, Kamchatka). The vertical axis shows the accumulated seismic moment release since 1900 in units of 10^{21} Nm. Note the differing vertical scales which show that the amount of seismic moment release varies by several orders of magnitude (from Peterson and Seno, 1984).

Aleutians (east and west), Alaska and Kamchatka subduction zones is shown. In the eastern Aleutians the 1957 earthquake takes up more than 90 % of the total moment release in this zone.

Most zones in which the Pacific plate is subducting show a remarkable linear decrease of moment release with age (Peterson and Seno, 1984). One of the exceptions is the western Aleutians where the moment release rate is less than expected from the general trend. This is probably due to lower relative velocity (32 mm yr^{-1}) normal to the trench when compared with the relative velocity (79 mm yr^{-1}) averaged over the whole zone (Peterson and Seno, 1984).

5.6 SUMMARY

The Aleutian Islands subduction zone is a typical island arc system. However, extra features, such as transverse canyons and fracture zones, play an important role in the distribution of deformation in the area. Several models have been suggested, explaining the geodynamics of the area based on gravity, seismic, palaeomagnetic and tomographic results.

The pattern of seismicity defines the areas where most of the strain associated with the convergence of the two plates is released. Focal mechanisms of earthquakes in the main thrust zone correspond to a relative motion vector which is different from the predicted large scale relative plate motion. This suggests that primary aseismic deformation takes place away from the plate interface, in the upper plate, causing partitioning of the relative plate motion.

A well-formed double Benioff zone is described and proposed by many authors, revealed by the variation in the type of focal mechanisms with depth. Downdip axes of compression are documented for the upper part of the Benioff zone, whereas downdip axes of tension characterize the lower part of the same zone.

The detailed study of the source mechanisms of the Aleutian arc earthquakes is presented in the following Chapter.

CHAPTER 6

SOURCE PARAMETERS OF RECENT EARTHQUAKES IN THE ALEUTIAN ISLANDS SUBDUCTION ZONE

6.1 INTRODUCTION

Fifty seven moderate-sized ($5.5 < m_b < 6.5$) earthquakes occurred during the time period between 1980 and 1986 along the entire length of the Aleutian Islands subduction zone. A sample of seven earthquakes was selected for study using the methods described in Chapter 2, representing different parts of the arc and at different depths, and including one event in the Kamchatka peninsula. The criteria upon which the selection of the events was made were the size, the number of stations that recorded the event, and the quality of the available recordings. Table 6.1 shows their origin time, location, depth, magnitude and moment as reported in the ISC bulletins. The reported moment is the Harvard CMT solution. The ISC epicentre location of the seven earthquakes are also shown in Fig. 6.01.

In this Chapter each earthquake is examined individually by forward modelling. Firstly, the calculation of their fault plane solution is determined by the RAMP method. Hence, knowing the focal mechanism and assuming a simple kinematic source model, synthetic BB displacement seismograms are generated. These are then compared with the observed BB records of displacement in order to determine the source dimensions, focal depth, the rupture velocity, the mean stress drop and the static seismic moment for each event. Finally, in the discussion section of this Chapter, the source parameters obtained are interpreted in relation to the prevailing tectonic processes of the area, and compared to results obtained by other authors using different methods and data.

6.2 THE DATA, PROCESSING AND MODELLING

About 20 GDSN stations are located at teleseismic distances (30° - 90°) suitable to record Aleutian earthquakes. Most of the earthquakes presented in this Chapter were recorded by an adequate number of stations (~ 10) with sufficiently high signal-to-noise ratio to be studied by the methods described in Chapter 2. First, both long- and short-period three-component seismograms are used to calculate fault plane solutions by the relative amplitude method, assuming a double couple source mechanism (Pearce, 1977, 1979, 1980). Broadband records retrieved from the SP seismograms are also used to provide extra information about the polarities and the relative amplitudes of the surface

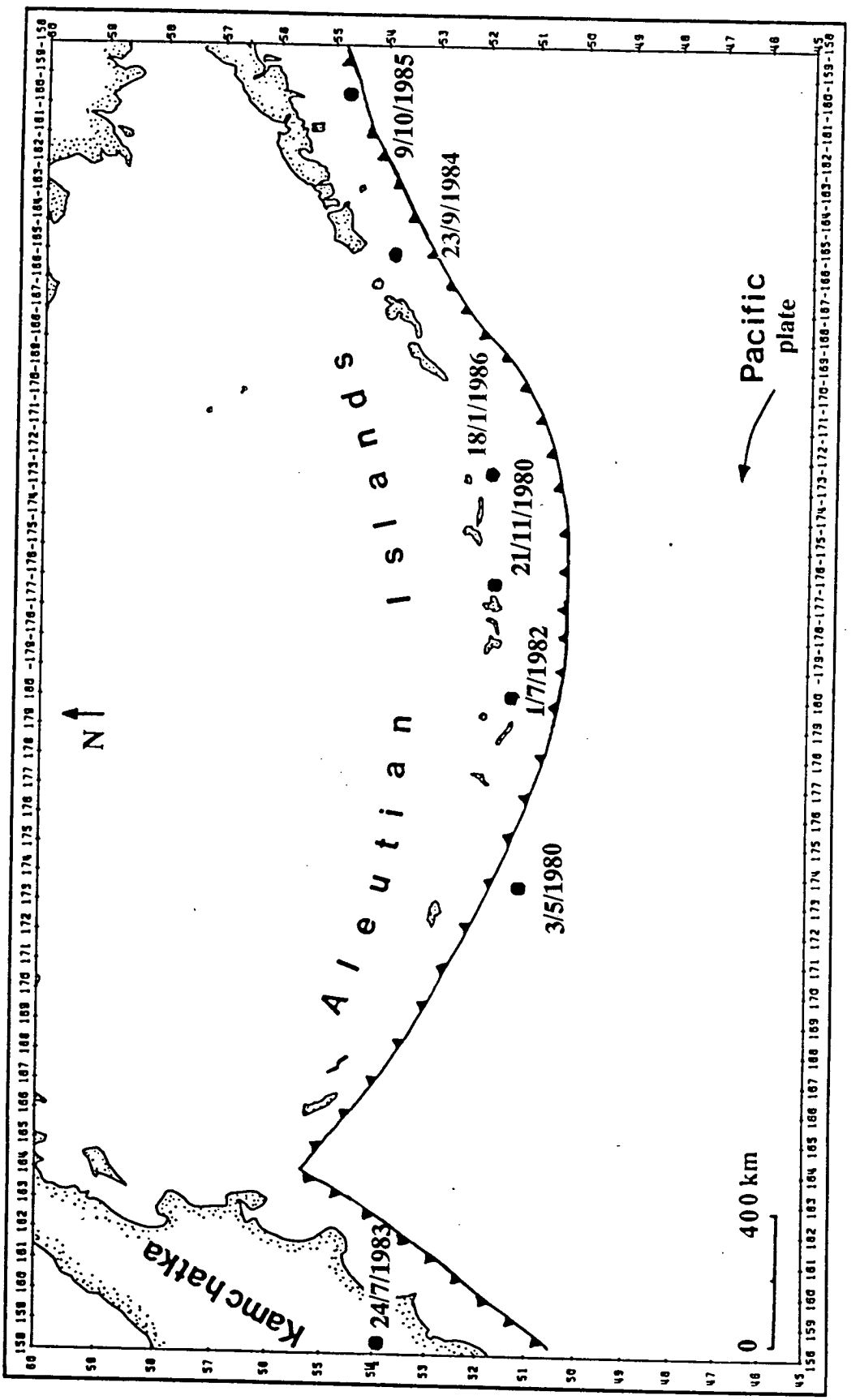

Figure 6.01. ISC locations of the seven earthquakes studied in this Chapter.

reflections (*pP*, *sP*) of the direct *P*- and *S*-waves and to allow forward modelling of the source function and average attenuation coefficient. The depth of the selected events, as found here, varies from 15 to 185 km. For the deeper ones the surface reflections of the *P*- and *S*-waves (*pP* and *sP*) together with the polarities and amplitudes of the direct body waves (*P*, *SH*, *SV*) could be reliably used in the computation of the focal mechanism.

Table 6.1. Published (ISC) source parameters for seven earthquakes in the Aleutian arc.

Event	Date	Time (h:m)	Lat (°)N	Long (°)	m_b	M_s	D (km)	M_o (x 10^{18} Nm)
8	03 May 80	09:30	51.21	173.61E	5.6	5.8	38	-
9	21 Nov 80	14:56	51.78	176.16W	5.7	5.7	58	1.31
10	01 Jul 82	07:41	51.39	179.94W	6.3	5.5	51	0.69
11	24 Jul 83	23:07	53.91	158.36E	6.1	-	190	2.35
12	23 Sep 84	17:06	53.58	165.46W	5.7	5.5	6	0.82
13	09 Oct 85	09:33	54.73	159.65W	6.5	6.1	30	8.67
14	18 Jan 86	01:58	51.54	173.11W	5.8	5.2	13	0.24

In order to obtain broadband seismograms the instrument response of the GDSN SP records is divided out (in the frequency domain) and the result is multiplied by the broadband (0.05 - 10.0 Hz) response. The results of Chapters 2 and 4 showed that short-period data alone, with an instrument response centred on a period of 1 s, are nevertheless sufficiently broadband to yield reliable records by the deconvolution process described above, for events of magnitude ~ 6.0, with a source duration of up to a few seconds.

Observed BB records of displacement (deconvolved from the SP records) are then compared with synthetics generated by a source model, using the method of Hudson (1969a, b) and Douglas *et al.* (1972). The kinematic source model is a finite two-dimensional Savage-type source (Savage, 1966) (Chapter 2). The Aleutian crustal and upper mantle structure, especially at the central area of the arc, is well known. This reduces the number of unknown parameters of the source model used. The rest of the model parameters (i.e. focal depth, source dimensions, rupture velocity) can then be determined by trial and error until the best possible fit to the waveforms around the focal sphere is obtained.

6.3 THE EARTHQUAKES

In this section the fault plane solutions and other source parameters (source dimensions, rupture velocity, stress drop, seismic moment) obtained from studying the earthquakes listed in Table 6.1 are presented. The earthquakes are presented in chronological order, and are in the next section compared when possible, to published solutions obtained by alternative methods. To avoid confusion with the Hellenic arc earthquakes (7 events), the first Aleutian event is given the number 8.

6.3.1 Event 8 - 3 May 1980, western Aleutians

This earthquake is located in the western part of the arc, close to Murray canyon (Fig. 5.01). Good SP recordings, were obtained at five GDSN stations, namely KONO, GRFO, ANMO, CHTO, and SHIO. They all show negative *P*-wave polarities. Using also information from LP records, namely polarities and relative amplitudes of *S*-waves, and additional *P* polarities (Fig. 6.02), a fault plane solution was calculated. The vectorplot and the equal area projection of the lower focal hemisphere indicate a normal fault mechanism with a small strike slip component (Fig. 6.03). One of the nodal planes dips at 60° to the SW. The direction of the T-axis is subparallel to the direction of the subduction at the area. Source finiteness is observed and the fault plane ($\sigma = 150° \pm 5°$, $\delta = 60° \pm 2°$ and $\psi = 64° \pm 2°$) reproduces the essential features of the seismograms successfully. The other nodal plane ($\sigma = 14°$, $\delta = 39°$, $\psi = 127°$) when used in the modelling produces synthetics that do not much the observed records. It can be seen in Fig. 6.04, that the negative *P*-wave pulses together with the polarities and amplitudes of the surface reflections (*pP*, *sP*) are generated by the model and are in good agreement with the observed ones at all the stations. In addition, the first sea surface reflection, which is observed at about 12 s after the direct *P*-wave, and its multiple reverberations at an interval of 8 s, are also predicted by the model. The time interval between the sea water reverberations implies a water depth of 6 km at the epicentral location. This is in agreement with the bathymetry of the area, which is a good independent check on the validity of the model used. The velocity structure in the hypocentral area was inferred from the studies of Grow (1973) and Engdahl and Billington (1986), and is given in Table 6.2a. Because the velocity structure is well known in this area, the number of unknown parameters inserted in the model is correspondingly reduced.

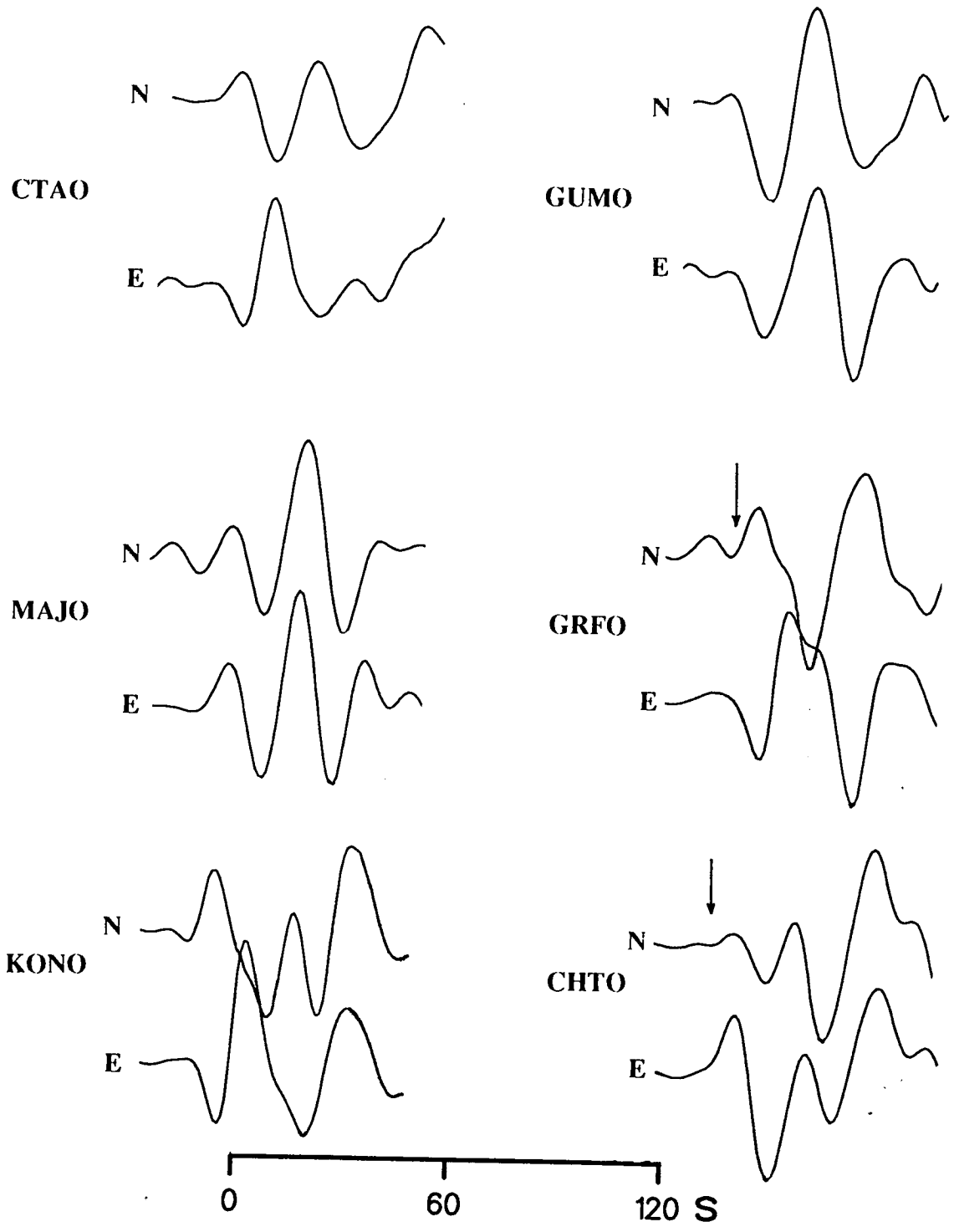

Figure 6.02. Long period *S*-waves used in the calculation of the fault plane solution for event 8. At the stations GUMO, MAJO, and CHTO the horizontal components (N, E) are of the same polarity, whereas at the rest of the stations the polarities are opposite.

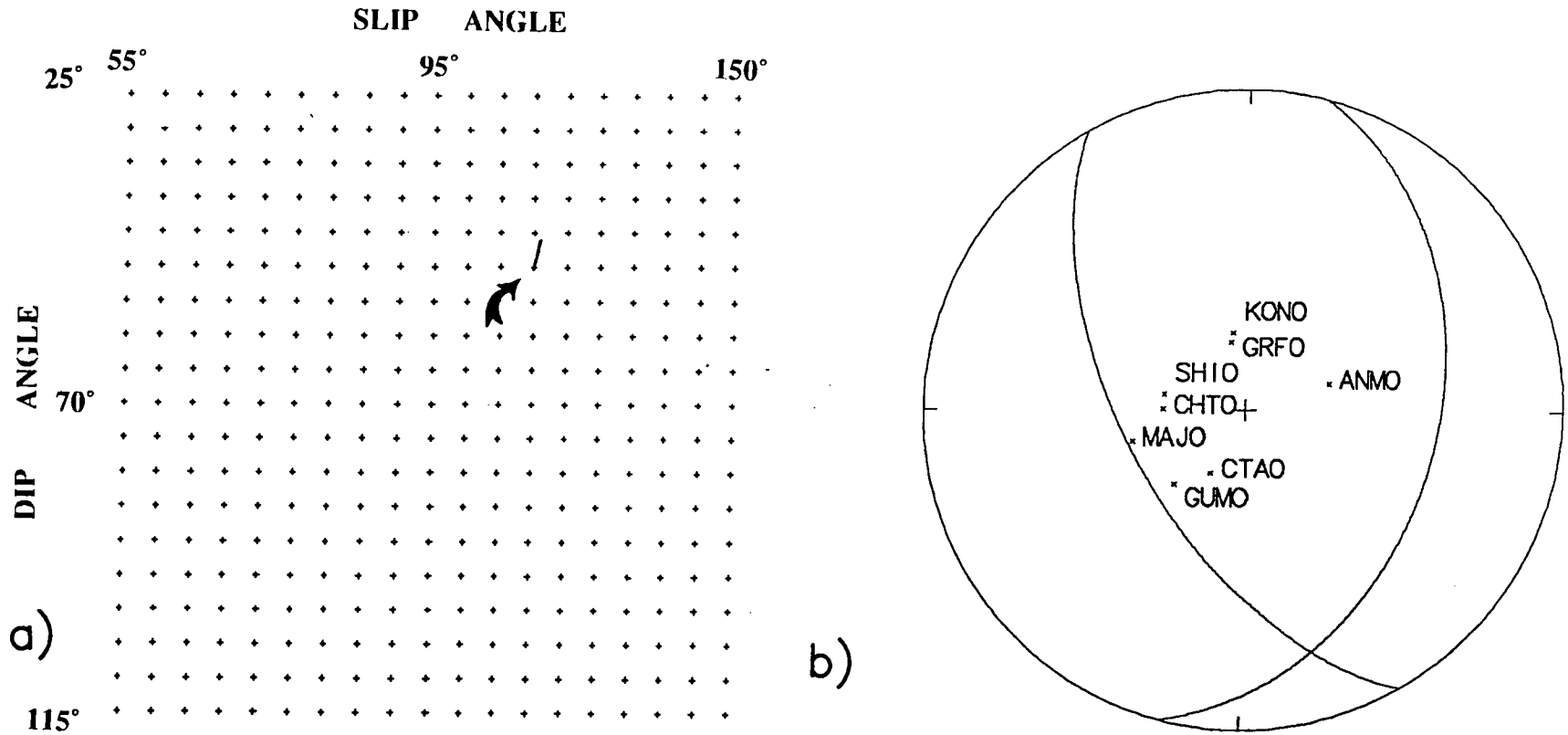

Figure 6.03. (a) The compatible solution obtained for event 8 is shown on the vectorplot, and (b) on the equal area projection of the lower focal hemisphere.

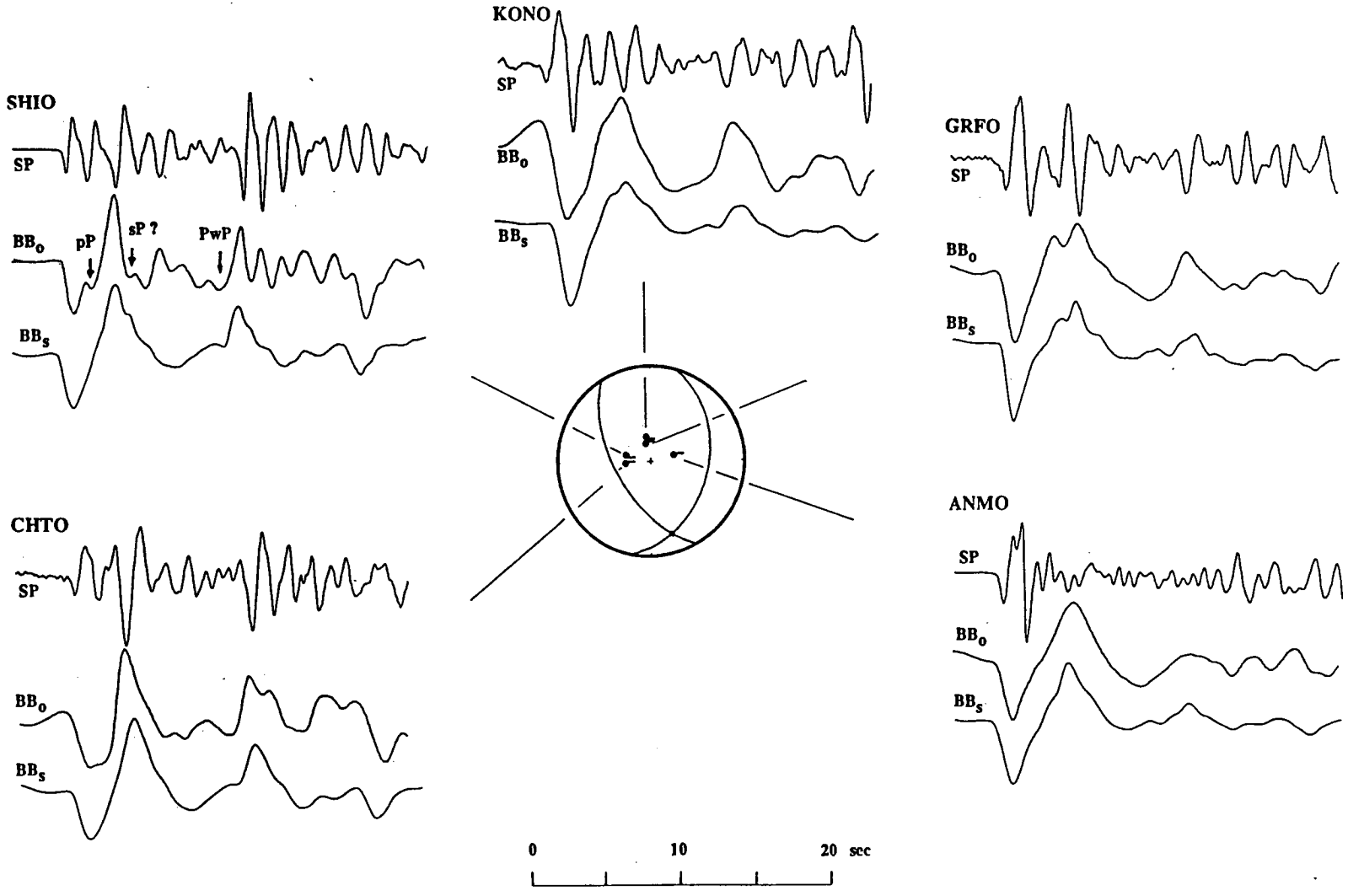

Figure 6.04. GDSN SP *P*-wave displacement seismograms (top solid lines), BB converted from SP (middle solid lines) and BB synthetics are plotted about the focal sphere for event 8.

Table 6.2a. Crustal model for event 8.

V_p (km s^{-1})	V_s (km s^{-1})	Density (g cm^{-3})	Thickness (km)
1.5	0.0	1.0	6.0
4.0	2.5	2.0	1.0
5.0	3.1	2.2	1.0
6.3	3.5	2.8	10.0
8.1	4.7	3.4	Halfspace

The time interval between the *pP*- and the direct *P*-wave, better observed at SHIO, implies a focal depth of 15 ± 1 km. The source rupture model is represented by a circular fault with a radius of 4.0 km, where the rupture initiates at the centre of the circle and propagates outward at a constant velocity of 2.5 km s^{-1}. The mean stress drop over the five stations used in modelling is 23.0 bar. The calculated mean seismic moment is 0.35 x 10^{18} Nm. The attenuation factor (t^*) is assumed to be 0.2 s for all stations.

6.3.2 Event 9 - 21 November 1980, central Aleutians

a. Source parameters

Figure 6.05 shows the data used to calculate the fault plane solution. Five GDSN stations (ANMO, MAJO, KAAO, CTAO, CHTO) have recorded the event well. All the SP seismograms from these stations show a positive *P*-wave polarity. Additional information was obtained from the LP records at the same stations and also from another two GDSN stations (TATO, JAS). The *S*-wave polarities and relative amplitudes from the NS and EW components were inserted in the calculation. As a result the solution is very well constrained ($\sigma = 239° \pm 5°$, $\delta = 132° \pm 2°$, and $\psi = 92° \pm 2°$). This solution (Fig. 6.06) is also plotted on an equal area projection of the lower focal hemisphere (Fig. 6.06). The mechanism is a pure thrust.

In order to distinguish which nodal plane is the fault plane, synthetic seismograms were generated using both the planes (Fig. 6.07) for two of the stations (ANMO and CHTO). The *pP*-wave is greater in amplitude than the *sP*-wave at ANMO, whereas the opposite is observed at CHTO. As a result, the nodal plane, which dips to the NW, is designated the fault plane because it predicts the duration and amplitude of the surface reflections (*pP* and *sP*) at both stations due to source finiteness. Therefore, the strike of the fault plane is 62°, its dip is 138° and its slip angle is 80°. The direct *P*-wave pulse

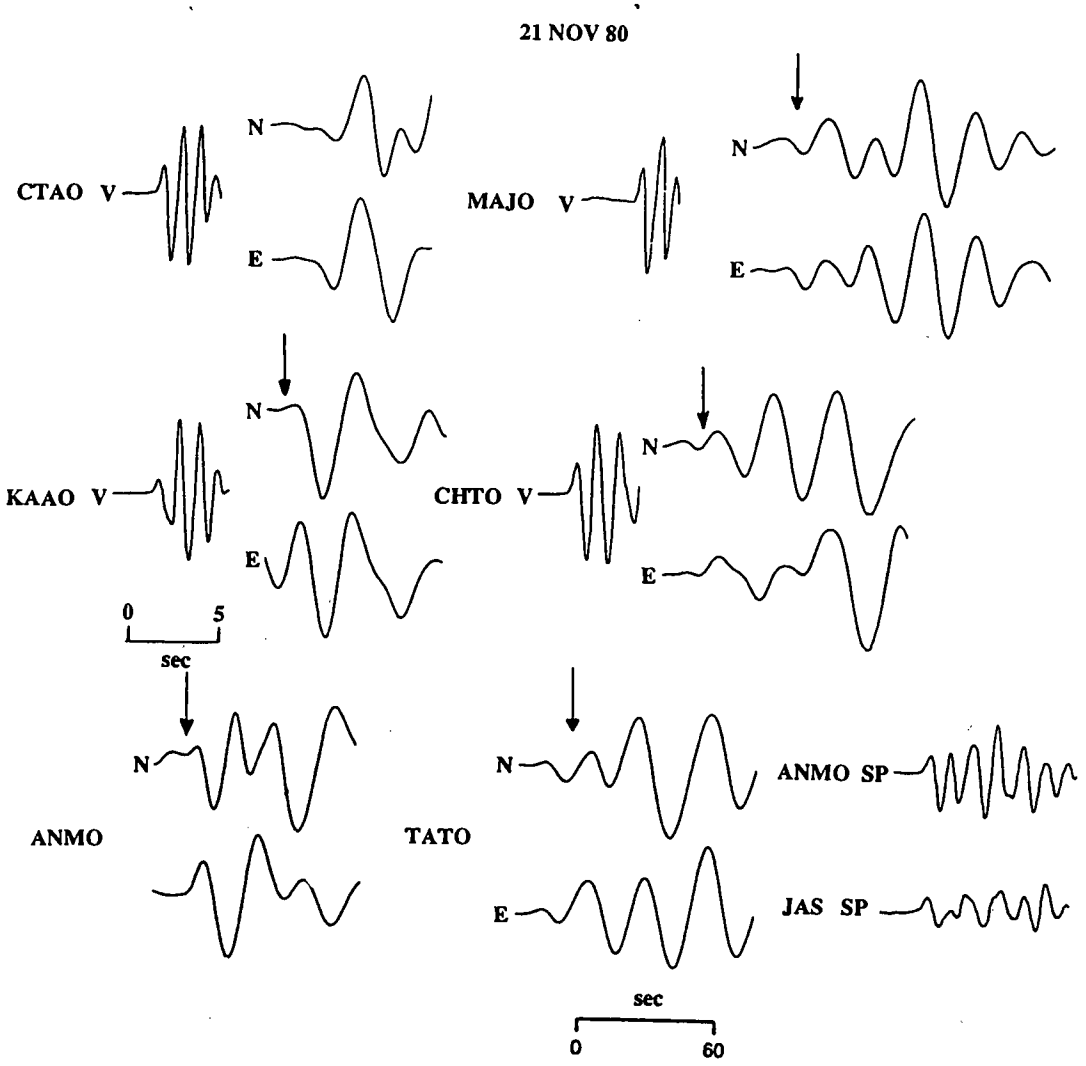

Figure 6.05. Data used to obtain the fault plane solution for event 9. The vertical (V) components are SP GDSN *P*-waves and the horizontal components (N, E) are LP GDSN *S*-waves.

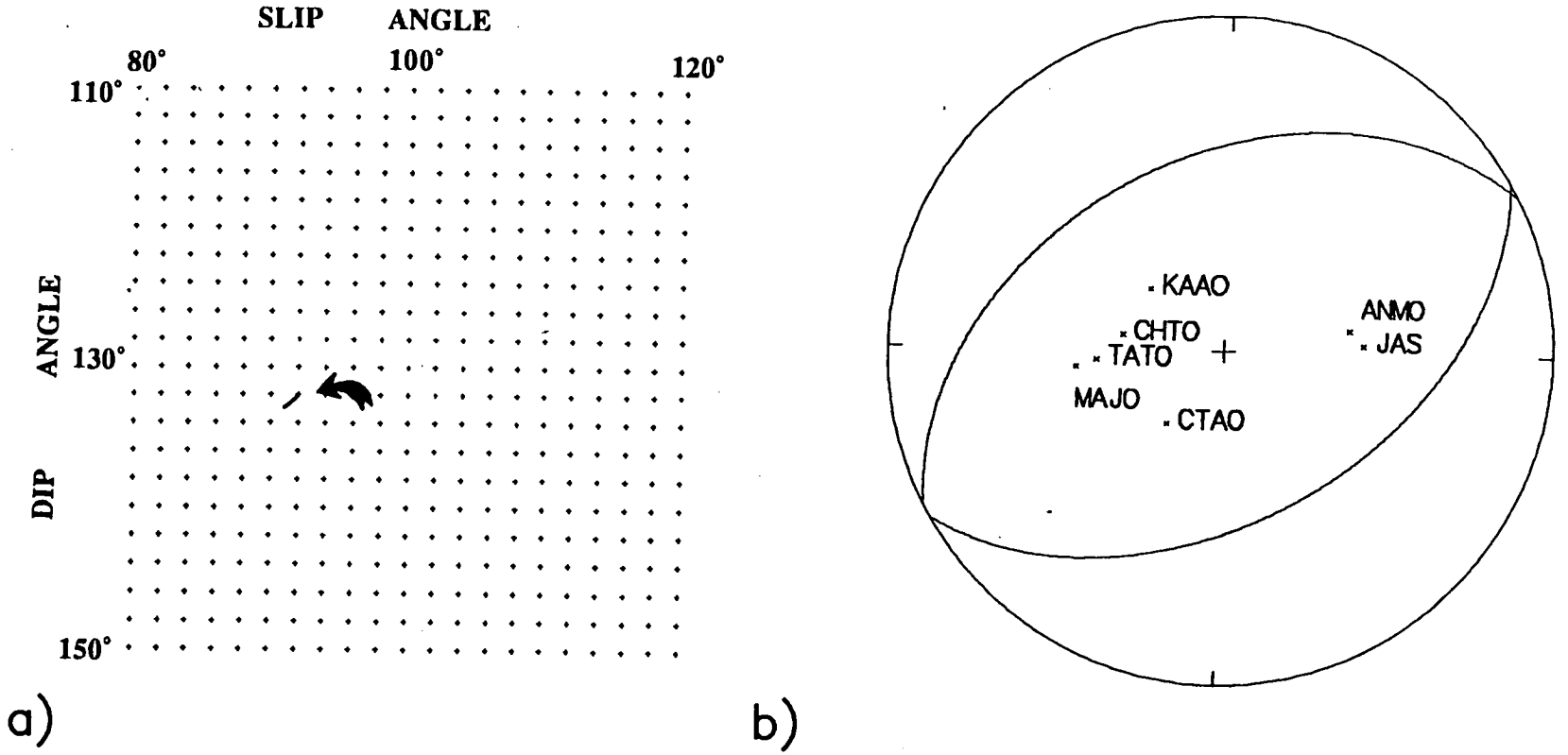

Figure 6.06. (a) The compatible solution for event 9 plotted on a vectorplot. (b) The fault plane solution shown in (a) now plotted on an equal area projection of the lower focal hemisphere.

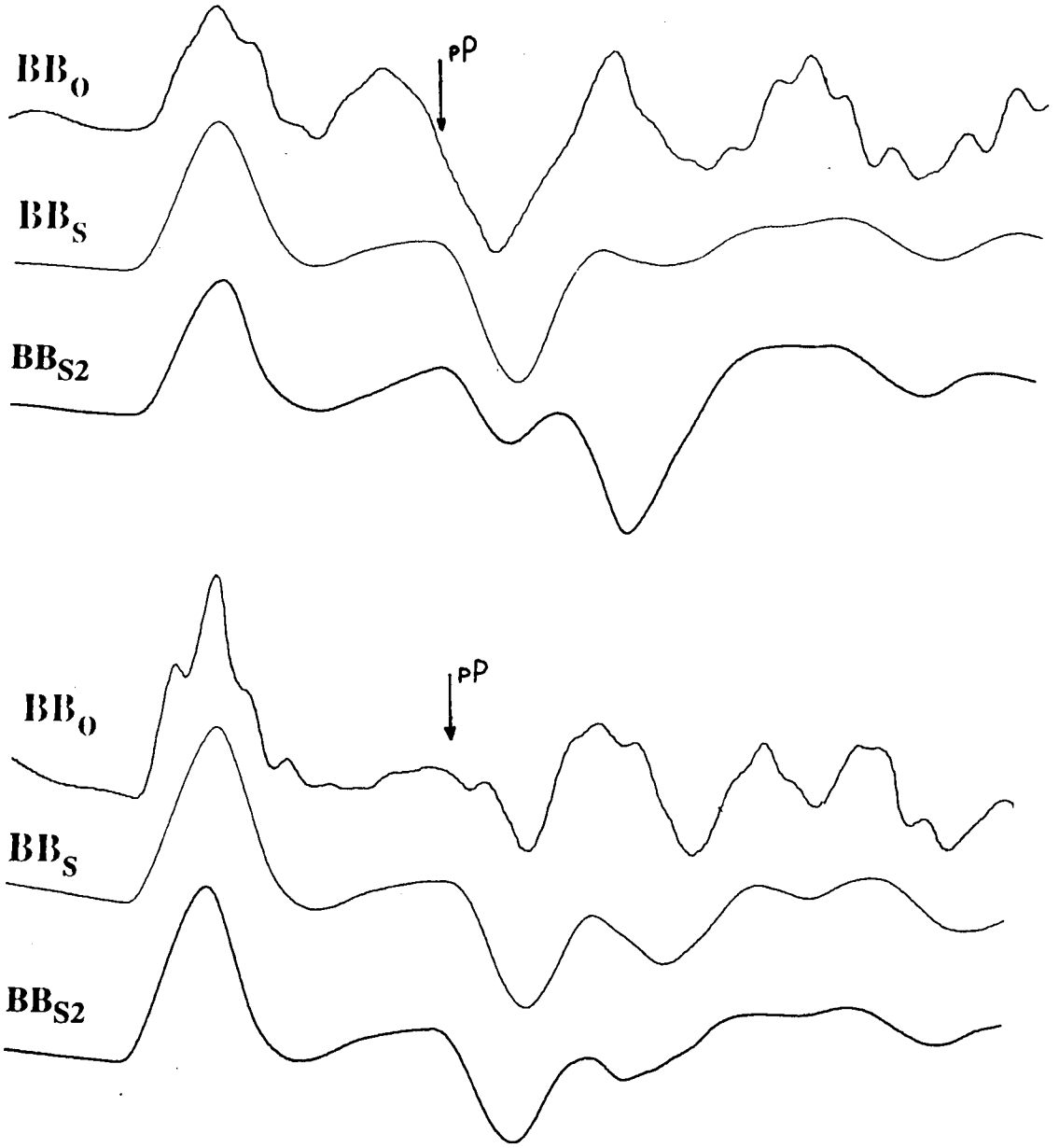

Figure 6.07. Broadband seismograms at stations ANMO and CHTO for event 9. The top trace is the observed BB record. The second trace is the synthetic waveform generated using the fault plane solution with $\sigma = 62°$, $\delta = 138°$, and $\psi = 80°$, and is the preferred model. The synthetic seismogram, generated using the other nodal plane ($\sigma = 239°$, $\delta = 132°$, $\psi = 92°$) as the fault plane, is represented by the third trace.

consists of three separate sub-pulses, probably corresponding to three sub-events, which are identifiable on all BB records (Fig. 6.08). In the modelling carried out here, they are considered as one pulse whose duration is the sum of the durations of the individual sub-pulses. The crustal structure in this area of the central Aleutians has been studied in detail by several authors (e.g. Grow (1973), Endgahl and Billington, 1986). Table 6.2b shows the crustal model in the epicentral area used in the modelling. A satisfactory fit between the observed and the synthetic seismograms is obtained using a circular fault with a radius of 7 km (Fig. 6.08). The rupture velocity is given a value of 2.1 km s^{-1} in order to match the observed duration of the *P*-wave pulse. The time difference between the arrival of the *pP*- and *P*-phase implies a focal depth of 35 $\pm$ 2 km. This suggests that the hypocentre is situated in the main thrust zone. The small amplitudes of the body waves observed require low values of stress drop. The mean stress drop was found to be 23 bar and the mean seismic moment 1.73 x 10^{18} Nm. The attenuation factor (t^*) varies between 0.2 and 0.6 s for different stations.

Table 6.2b. Crustal model for event 9.

V_p (km s^{-1})	V_s (km s^{-1})	Density (g cm^{-3})	Thickness (km)
1.5	0.0	1.0	0.5
4.5	2.0	2.3	2.0
5.5	2.5	2.5	5.5
6.6	4.0	2.8	15.0
7.8	4.2	3.1	20.0
8.1	4.7	3.4	Halfspace

b. Other work

A fault plane solution for this event was determined by Engdahl and Kind (1986) using the inversion technique described by Sipkin (1982) that fits GDSN long period data to theoretical sources. They suggest a thrust mechanism with one nodal plane having a strike of 50°, dip of 64° and rake 82°. Their estimated seismic moment is 1.20 x 10^{18} Nm and the focal depth is 37.0 km. The CMT solution for the same event (Ekström and Engdahl, 1989) has $\phi = 258°$, $\delta = 26°$ and $\lambda = 11°$, places the source at a depth of 40 km with a seismic moment of a value of 1.31 x 10^{18} Nm.

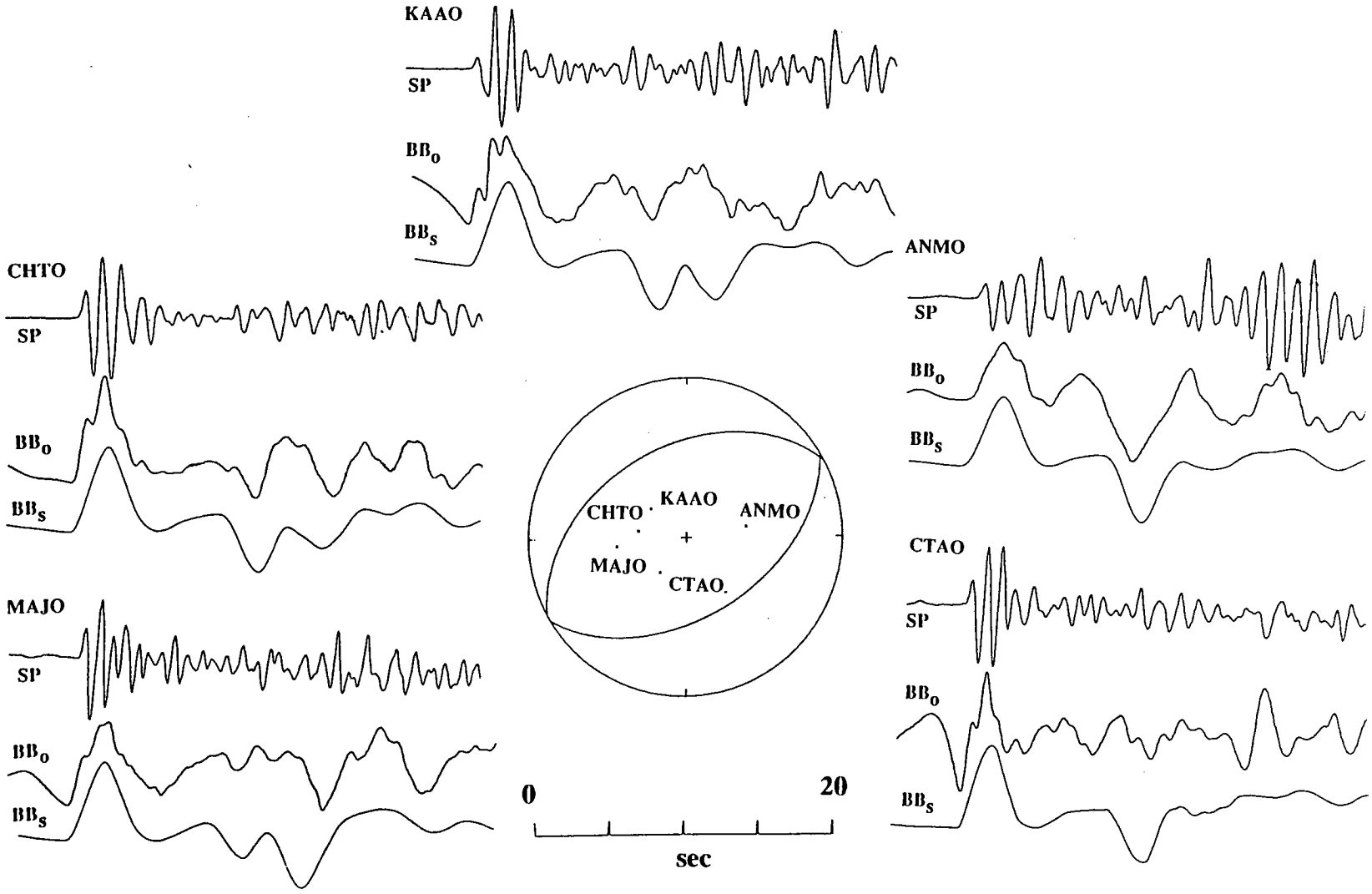

Figure 6.08. *P*-wave displacement seismograms for event 9. The GDSN SP data (*top*) and their BB conversion (*middle*) are plotted together with the synthetic BB displacements (*bottom*) for five GDSN stations.

6.3.3 Event 10 - 1 July 1982, central Aleutians

This earthquake also occurred in the central part of the arc, and has a body-wave magnitude of 6.3. Its surface-wave magnitude is considerably smaller (M_S = 5.5); this alone suggests a deep source.

a. Source parameters

SP seismograms (Fig. 6.09) show positive *P*-wave polarity recorded at eleven GDSN stations. These data, together with *S*-wave polarities (or relative polarities) and relative amplitudes of NS and EW components from four GDSN stations were used in the computation of the focal mechanism. The solution is well constrained and has $\sigma = 15° \pm 5°$, $\delta = 150° \pm 2°$, and $\psi = 120°$ (+2°, -10°). All the possible combinations of the values above are shown on the 2° interval vectorplot of Fig. 6.10. Source finiteness is observed for this event. Therefore, the plane with $\sigma = 20°$, $\delta = 152°$, and $\psi = 110°$ is designated to be the fault plane as it produced synthetic seismograms with the essential features of the observed records. This is plotted on the equal area projection of the lower hemisphere of Fig. 6.10. It should be noticed that the nodal character of the *P*-wave observed at ALQ and ANMO, as well as the null vector character of the same wave at MAJO, GRFO and BER are predicted by the above fault plane solution, even though this information was not inserted in the computation of this solution. It is difficult to identify the surface reflections of the direct *P*- and *S*-waves on the SP as well as on the BB records (Fig. 6.11). Assuming that the negative polarity phase, observable at ANMO and LON approximately 10 s after the *P* onset, is the *pP*, and the additional negative polarity phase observed at BER approximately 15 s after the *P* onset is the *sP*, then the depth of the event is 36.5 ± 1.5 km. The crustal structure at the source is given in Table 6.2c. The *P*-wave pulse duration shows a small variation with azimuth on the observed waveforms, possibly implying a directivity effect. The same variation of duration could be caused by variation in the attenuation factor (t^*) along the different ray propagation paths from the source to the recording stations. The quality of the data is not adequate to distinguish between these two possible causes. It is assumed that the source is circular, with a radius of 3.5 km and t^* ranges between 0.2 - 1.0 s for different stations producing the small differences in the *P*-wave duration observed at different stations. The model rupture velocity is 2.5 km s^{-1}, the mean stress drop over all stations is 28.3 bar and the mean seismic moment 0.27 x 10^{18} Nm.

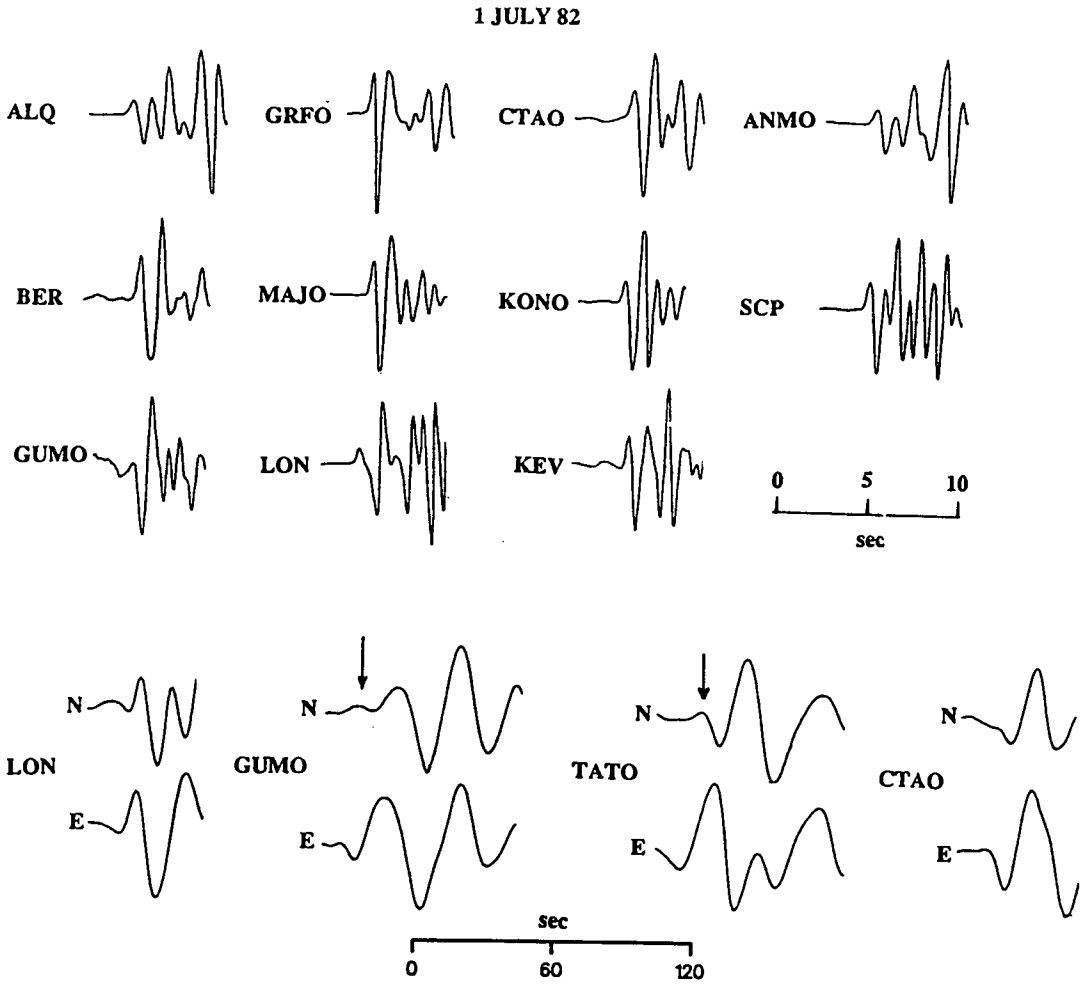

Figure 6.09. Eleven SP *P*-wave polarities and LP *S*-wave seismograms (horizontal components) from four GDSN stations used to calculate the fault plane solution of event 10.

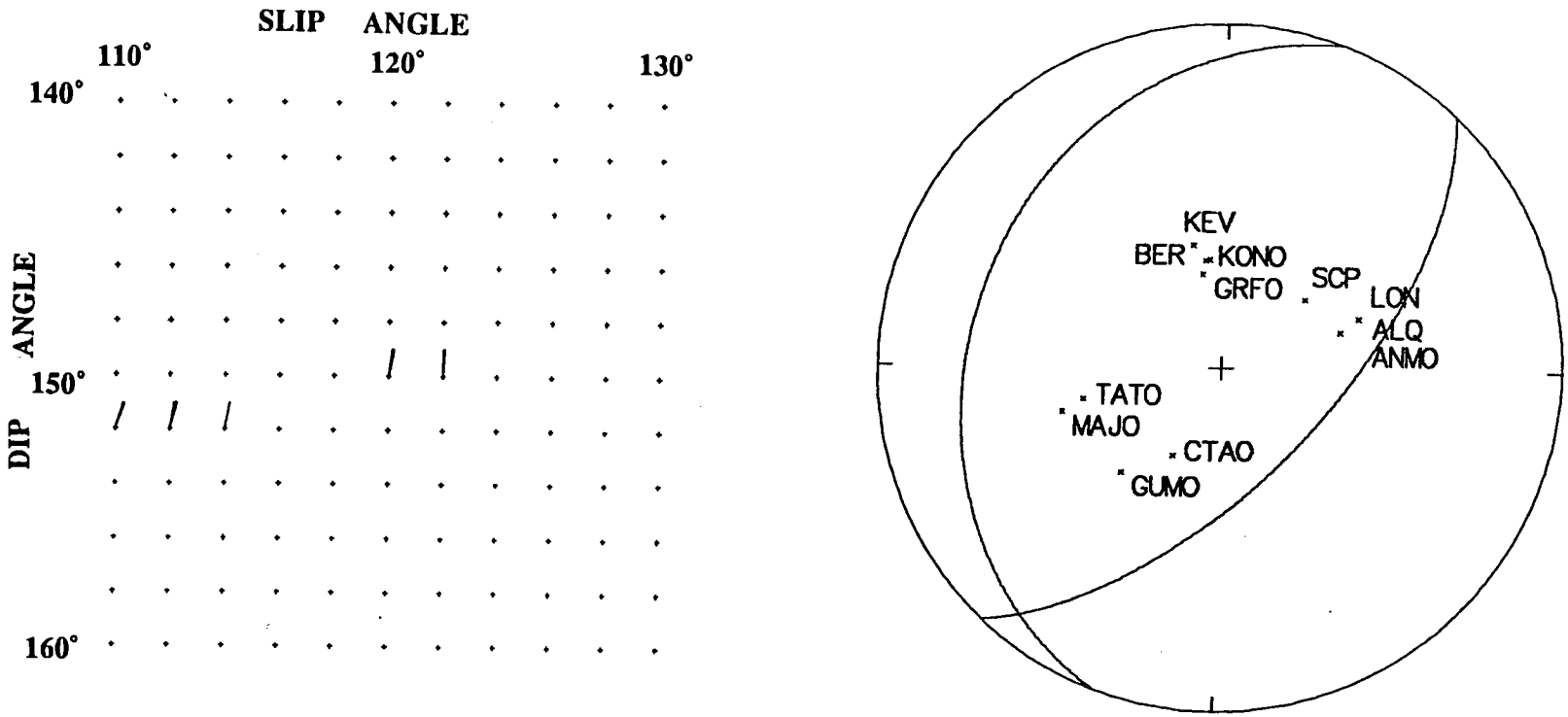

Figure 6.10. The vectorplot with the acceptable solutions obtained for event 10 is shown on the left. The fault plane solution used in the body-wave modelling is plotted on an equal area projection of the lower focal hemisphere.

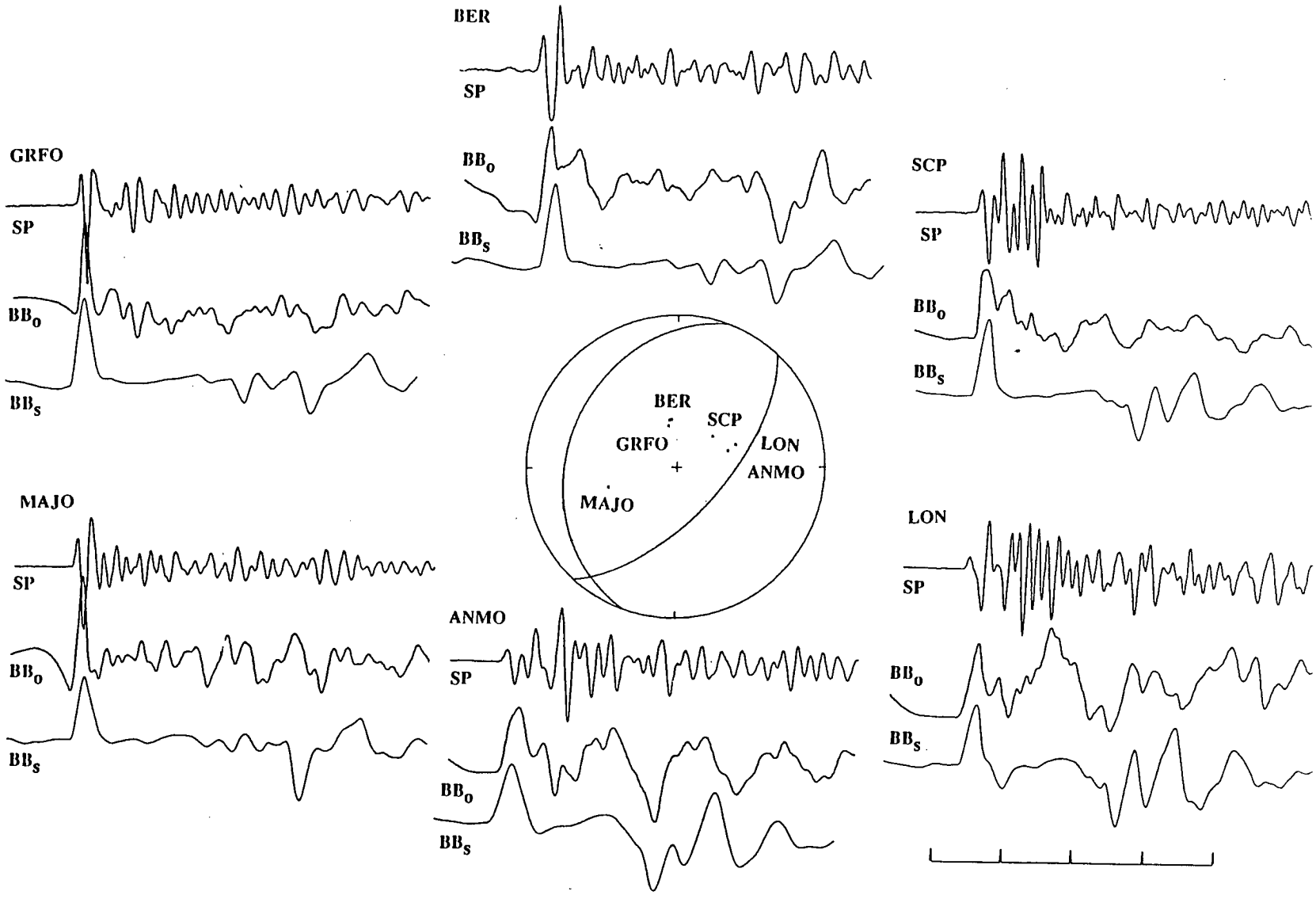

Figure 6.11. SP seismograms for event 10 (*top trace*), recorded at six GDSN stations, and their broadband conversion (BB_0, *middle trace*). The *third trace* represents the synthetic broadband displacement record.

Table 6.2c. Crustal model for event 10.

V_p (km s^{-1})	V_s (km s^{-1})	Density (g cm^{-3})	Thickness (km)
1.5	0.0	1.0	0.5
3.5	2.0	2.3	2.0
5.3	2.6	2.5	3.0
6.3	3.1	2.7	8.0
6.5	3.8	2.8	40.0
8.1	4.7	3.4	Halfspace

b. Other work

The CMT solution (Dziewonski *et al.*, 1983a) predicts a thrust mechanism with ϕ = 251°, δ = 32° and λ = 93°. The source is located at a depth of 49.5 km and the estimated seismic moment is 0.69 x 10^{18} Nm.

6.3.4 Event 11 - 24 July 1983, Kamchatka

a. Source parameters

This is the deepest event studied. It is located within the part of the Pacific plate that is subducting under Kamchatka peninsula. The earthquake is clearly recorded at most stations on SP and LP seismographs. SP *P*-wave polarities (Fig. 6.14) and LP *S*-waves (Fig. 6.12) were used in the determination of the fault plane solution. In this case two acceptable solutions were obtained [σ = 170°, 190° (± 5°), δ = 140°, 160° (± 5°), and ψ = 140°, 160°(± 5°) respectively], and are plotted on a vectorplot and an equal area projection of the lower focal hemisphere (Fig. 6.13). These solutions suggest an almost vertical dip-slip mechanism, with a small strike-slip component.

The SP seismograms are very simple (Fig. 6.14). On the BB records, retrieved from SP, the *P*-wave onset and the *pP* and *sP* phases are clearly shown. The *pP*-wave comes at about 42.5 ± 0.2 s after the *P*-wave onset, and it is clearer on the BB waveforms. This time interval suggests a focal depth of 183.5 ± 0.5 km. The *sP* phase cannot be identified on any SP seismogram, but becomes apparent on the BB records. This underlines one of the advantages of the broadband deconvolution technique.

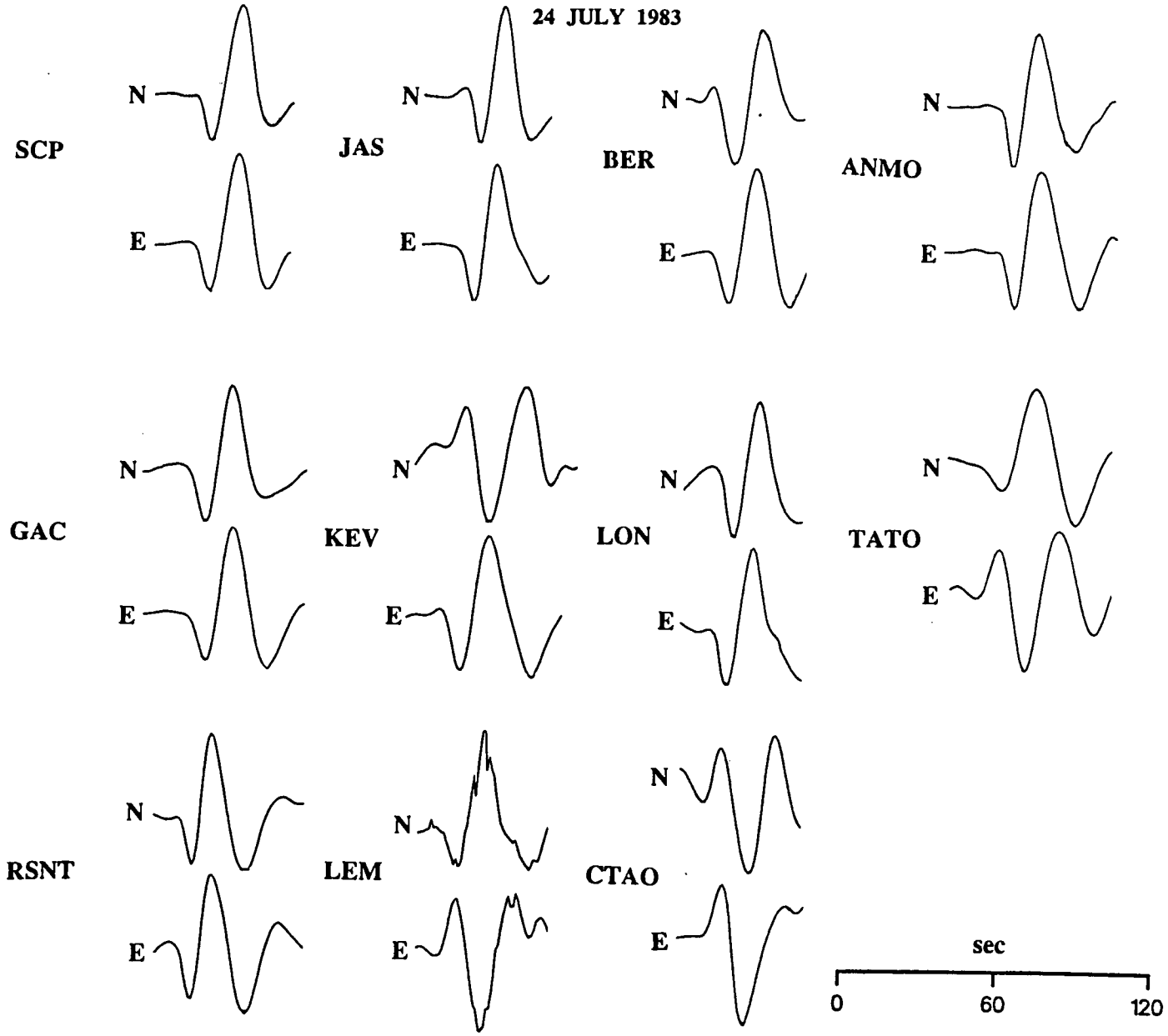

Figure 6.12. LP *S*-wave polarities of the horizontal components (N, E) from 11 GDSN stations used in the computation of the fault plane solution of event 11. At all stations, except KEV, LEM, and TATO, the NS components have the same polarities as the EW ones.

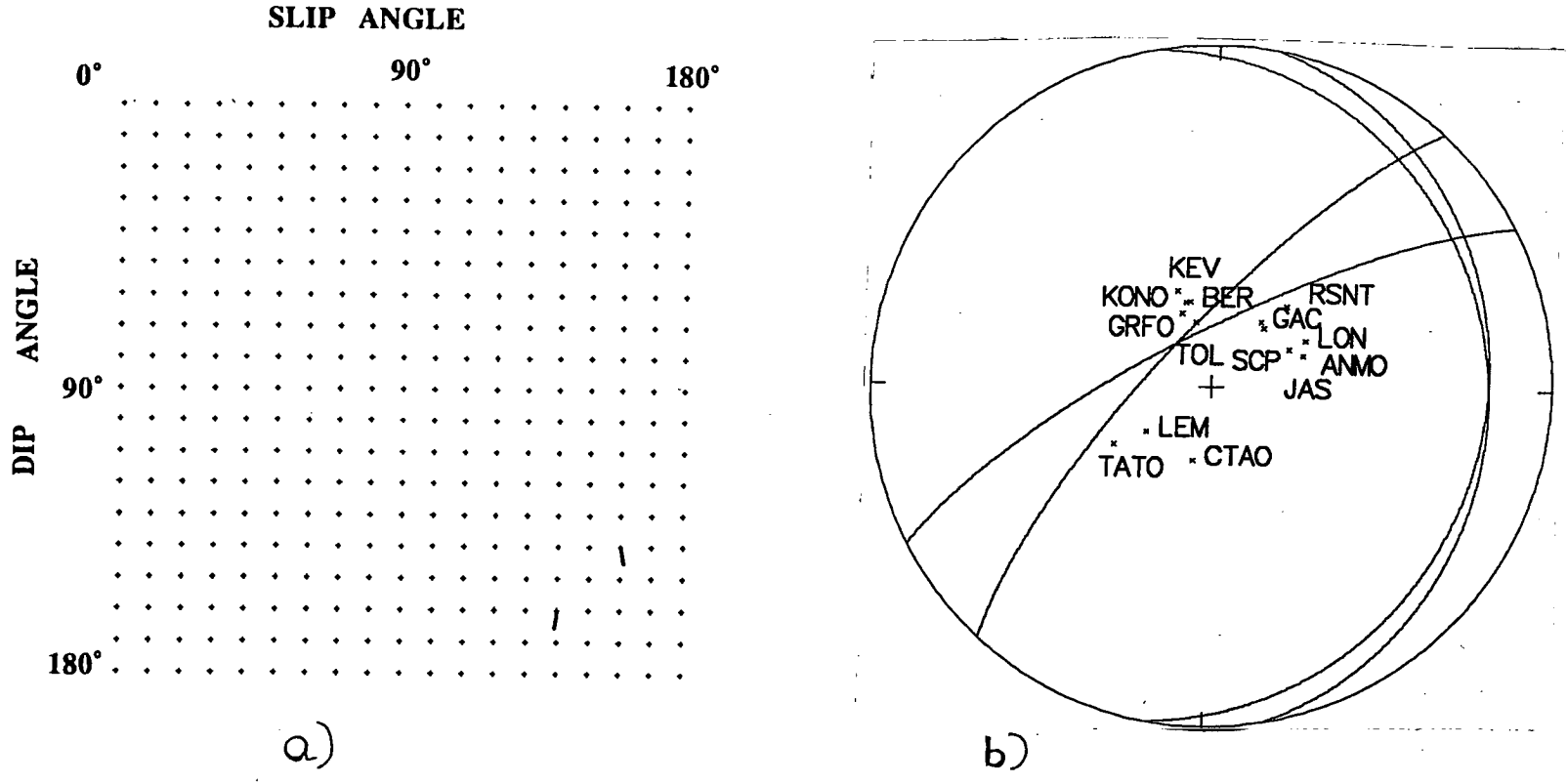

Figure 6.13. The two solutions compatible with the data obtained for event 11 are plotted on the vectorplot(a), and on an equal area projection of the lower focal hemisphere (b).

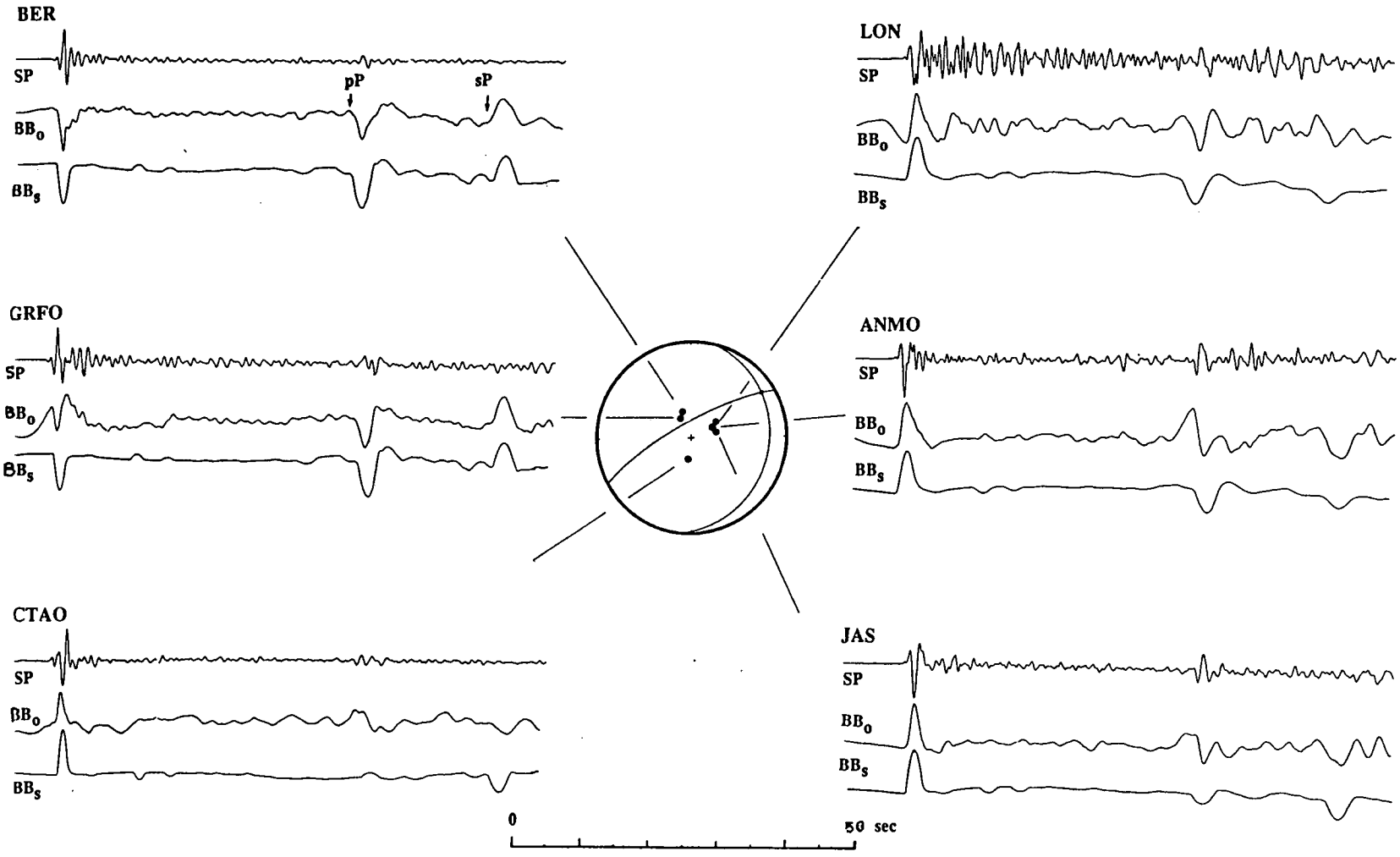

Figure 6.14. GDSN SP *P*-wave displacement seismograms (top lines), BB converted from SP (middle lines) and BB synthetics (bottom lines) are plotted around the focal sphere for event 11.

The duration of the *P*-wave pulse varies between 2.5 and 3.5 s amongst the available recording stations (Fig. 6.14). This is suggestive of a directivity effect and it is in the plane of the fault. Therefore in the body-wave modelling the source is assumed to be elliptical in order to reproduce synthetics which showed the same directivity effects. It is seen that on the observed seismograms at GRFO and BER the duration of the *pP* phase is much greater than the duration of the direct *P*-wave. This implies that the rupture starts at the upper focus of the ellipse and propagates downward. The fault plane has $\sigma = 62°$, $\delta = 103°$ and $\psi = 74°$. To obtain the duration variation of the direct *P*-wave at different stations, as well as the amplitude and duration ratio between *P*, *pP* and *sP* phases at BER and GRFO, the angle between the strike of the fault plane and the major axis of the ellipse is found to be 150°. The major axis of the ellipse is 5.5 km and the minor axis is 2.5 km. The rupture velocity used is 4.5 km s^{-1} which is 0.95 β. The assumed velocity structure at the source is given in Table 6.2d. The attenuation correction factor (t^*) is assumed to be 0.2 s and the mean stress drop is 213.3 bar. The seismic moment is found to be 2.33 x 10^{18} Nm.

Table 6.2d. Crustal model for event 11.

V_p (km s^{-1})	V_s (km s^{-1})	Density (g cm^{-3})	Thickness (km)
3.5	2.0	2.3	0.8
5.5	3.1	2.5	6.0
6.6	3.8	2.8	22.0
7.8	4.5	3.1	10.0
8.1	4.7	3.3	200.0
8.1	4.7	3.4	Halfspace

b. Other work

The CMT solution for this event (Dziewonski *et al.*, 1984) gives a vertical dip-slip mechanism with a small strike slip component. One of the nodal planes has a strike of 315°, dip of 11° and rake of 7°. The focal depth is 177.4 km and the seismic moment 2.35 x 10^{18} Nm.

6.3.5 Event 12 - 23 September 1984, eastern Aleutians

a. Source parameters

SP *P*-wave polarities from 6 GDSN stations (CHTO, CTAO, GRFO, KONO, SCP, ANTO), all showing positive onset, and *S*-wave (NS, EW) polarities from 7 GDSN stations (Fig. 6.15) were used in the calculation of the focal mechanism. Clear negative onsets of *S*-waves (both NS and EW) at stations CHTO and CTAO, and positive onsets of the same waves observed at ANTO , resulted in a well constrained solution ($\sigma = 350° \pm 5°$, $\delta = 140° \pm 4°$, and $\psi = 116° \pm 6°$). This solution, shown on the vectorplot and on the equal area projection of the lower focal hemisphere of Fig. 6.16, indicates a thrust mechanism with a small strike-slip component.

Broadband records were retrieved from SP ones recorded at MAJO, SCP, and CHTO (Fig. 6.17). It was not possible to obtain BB records for the stations GRFO and KONO. No reflected phases *pP* and *sP* are identifiable on any of the BB seismograms. Moreover, the duration of the direct *P*-wave appears to be too large for an event of this size (m_b = 5.7). The small size of this event is also supported by the relatively low amplitudes observed on the SP as well as on the BB seismograms. The most likely interpretation is that the surface reflections are interfering constructively with the direct *P*-wave in the first 8 s of the waveform. On the SP records at GRFO and SCP recurring phases, repeatedly observed at an interval of approximately 6.5 s, are possibly multiple sea surface reflections. The time interval between these phases, marked *pwP* on the diagram 6.17, suggests a water depth of approximately 2 km, which agrees with the bathymetry at the epicentral region. No body-wave modelling was carried out for this event as the BB records were too complex to be reproduced using a simple source model.

b. Other work

A pure thrust mechanism is proposed by the CMT solution (Dziewonski et al., 1985b), where the strike of one nodal plane is 244°, the dip is 32° and the rake is 92°. The depth is 46 km and the seismic moment is 0.82×10^{18} Nm.

6.3.6 Event 13 - 9 October 1985, eastern Aleutians - Alaska

a. Source parameters

Fig. 6.18 shows the data used to calculate the fault plane solution for event 13. All the SP records have positive *P*-wave onsets, apart from ANMO, which is unclear. At this

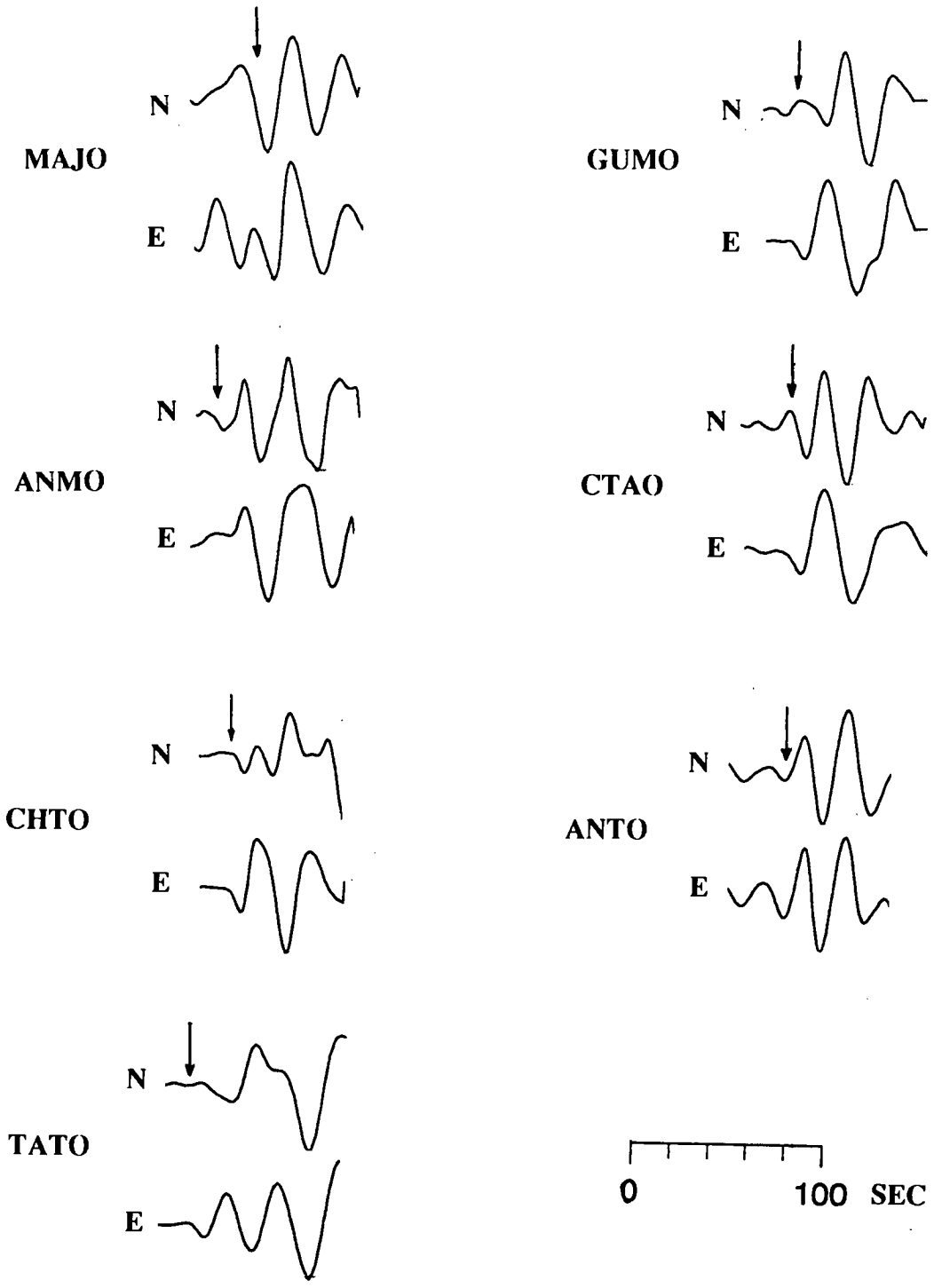

Figure 6.15. LP *S*-wave seismograms recorded at seven GDSN stations that were used in the fault plane determination of event 12.

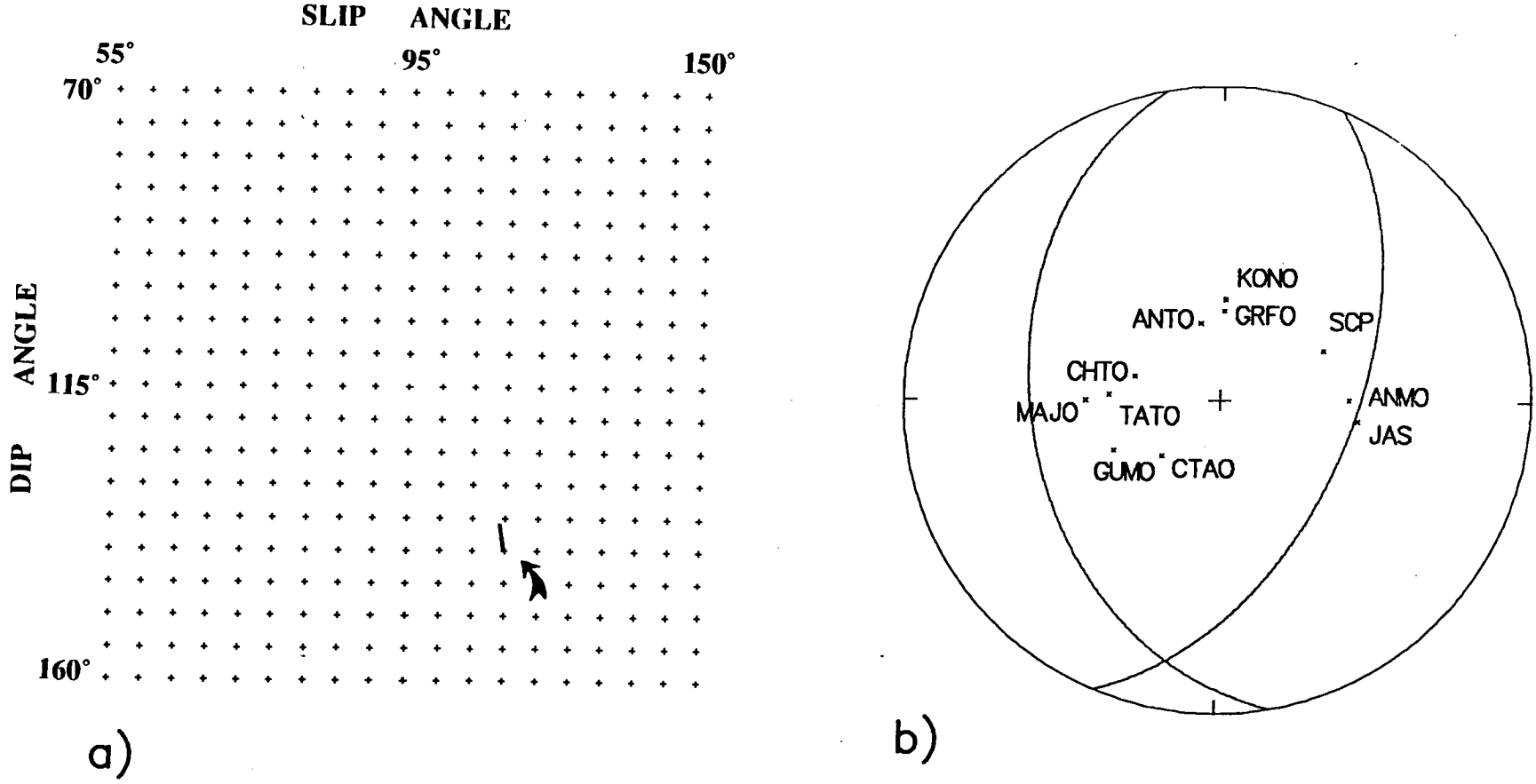

Figure 6.16. The fault plane solution determined for the 23 September 1984 (event 12) earthquake shown on the vectorplot (a), and on the equal area projection of the lower focal hemisphere (b).

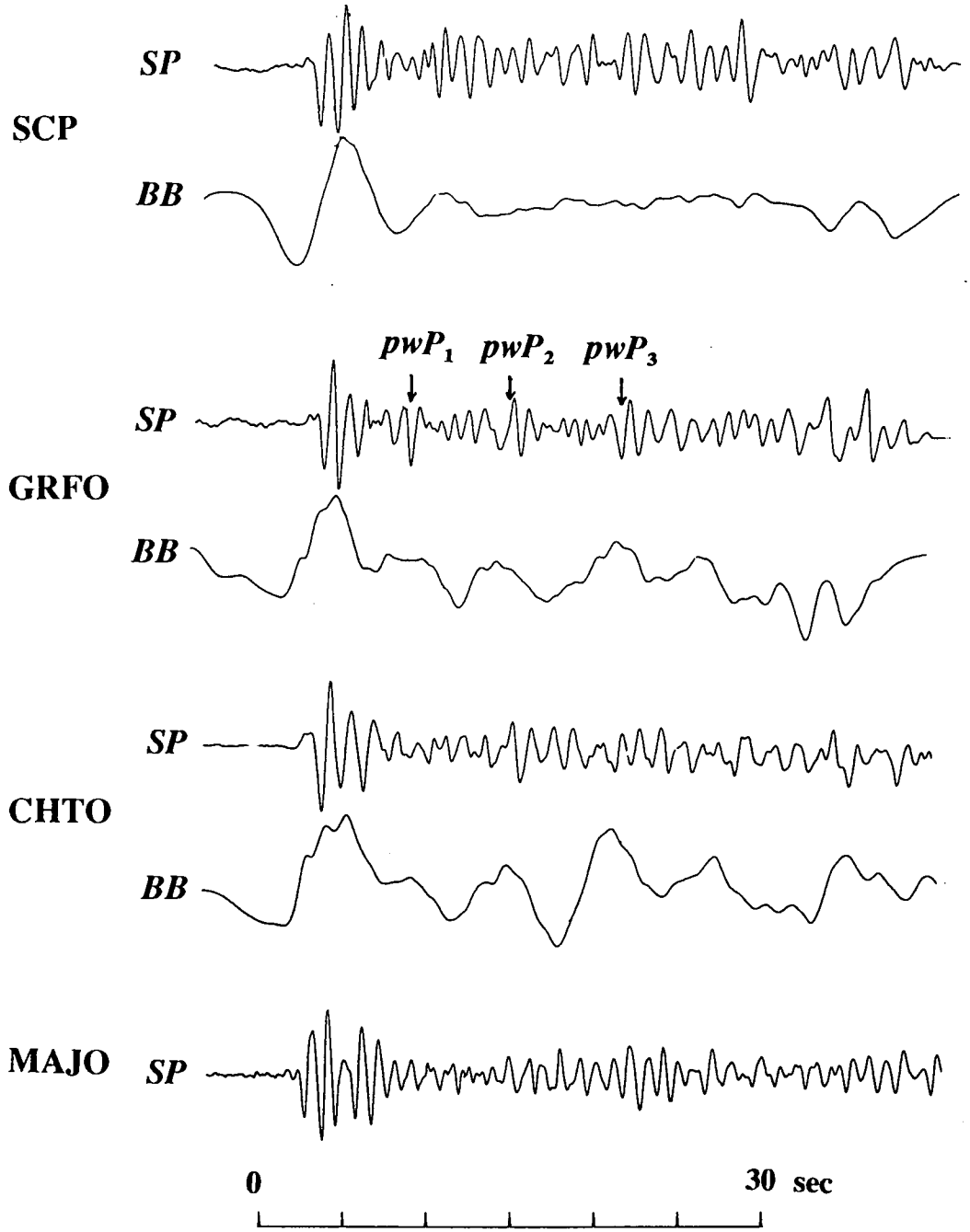

Figure 6.17. SP seismograms of event 12 recorded at SCP, GRFO, CHTO, and MAJO. Broadband displacement seismograms were retrieved for three of these stations and are plotted underneath the SP records.

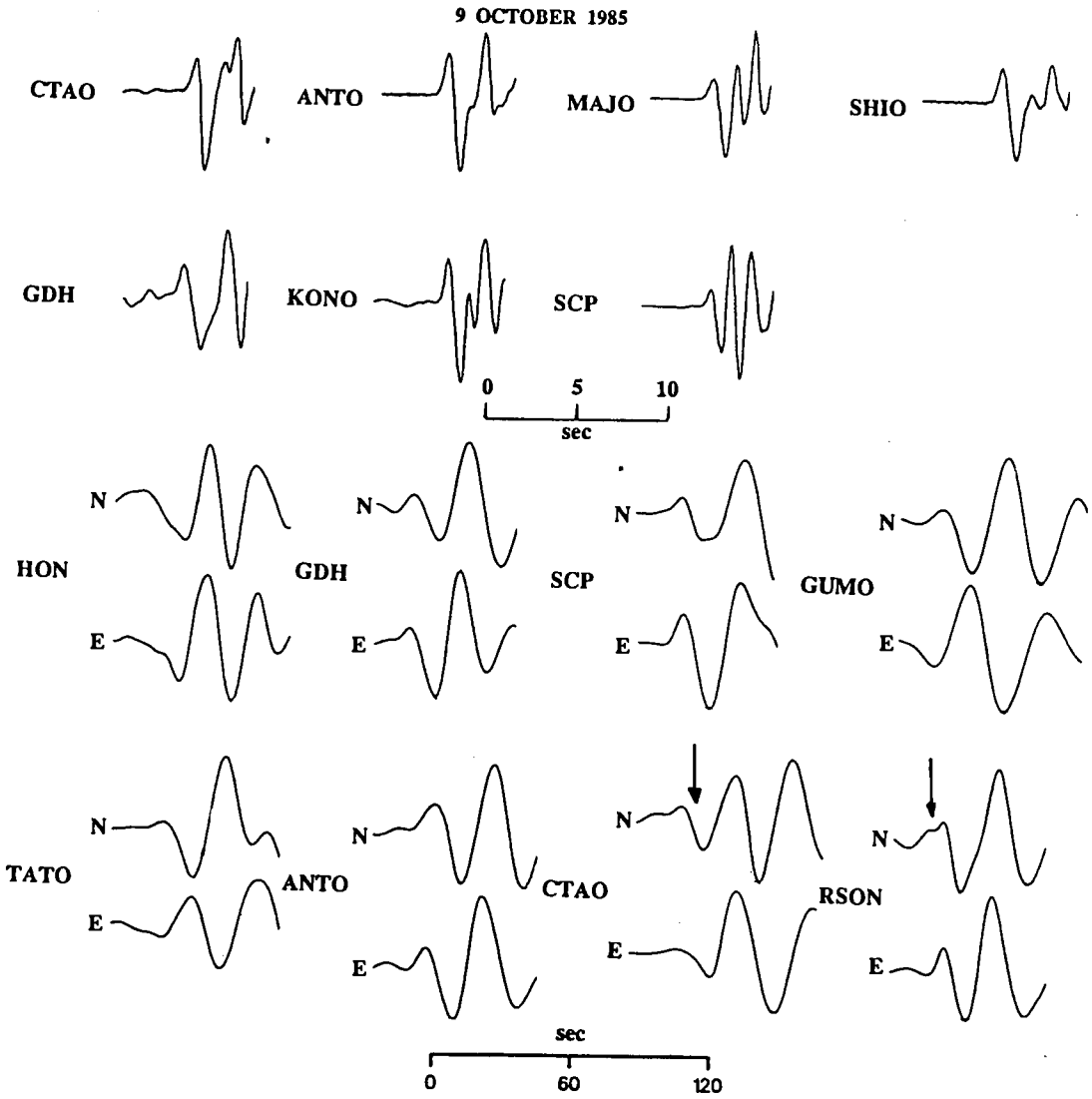

Figure 6.18. Data used to obtain the fault plane solution for event 13. The seven top traces are SP GDSN *P*-waves and the following horizontal components (N, E) are LP GDSN *S*-waves. At GUMO and TATO the NS and EW *S*-wave components are of opposite polarity.

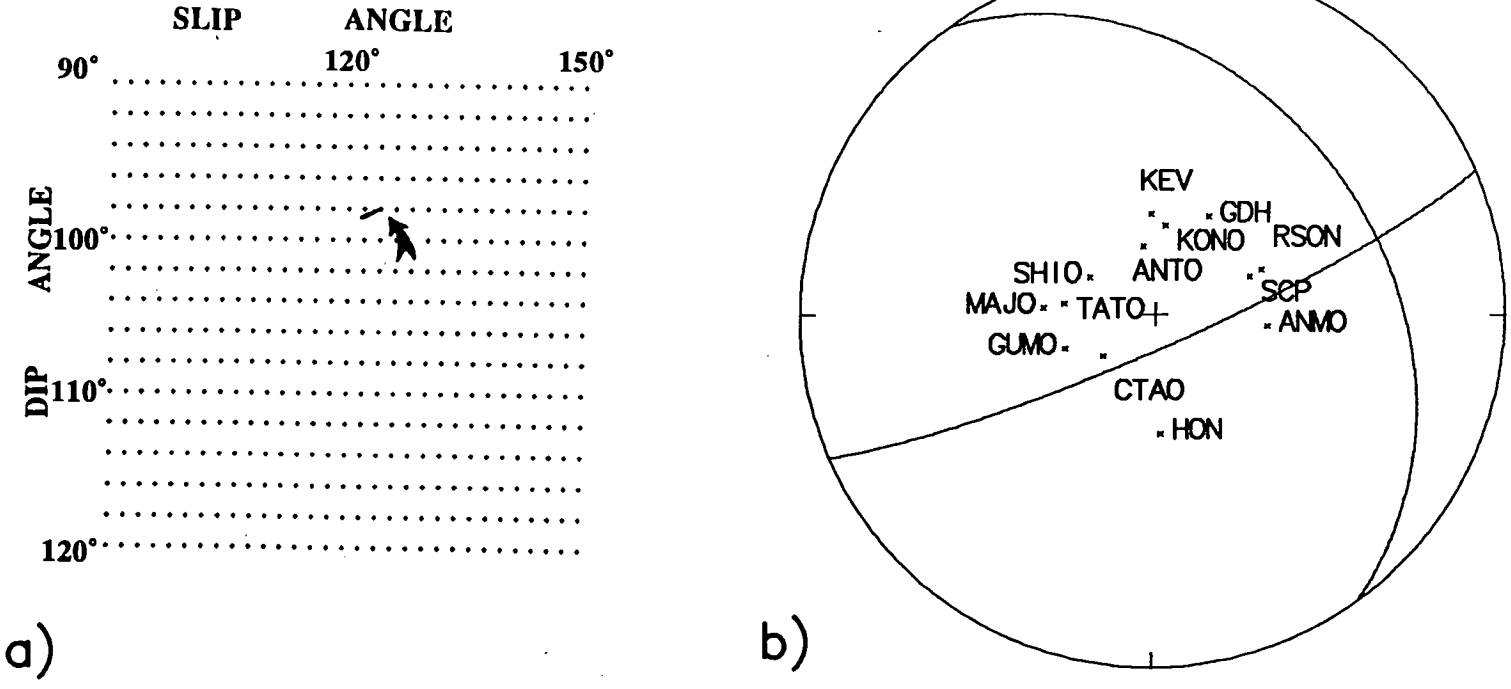

Figure 6.19. (a) The source mechanism obtained for event 13 is shown on the vectorplot, and (b) on the equal area projection of the lower focal hemisphere.

station the *P*-wave pulse seems to be nodal with very small amplitude (Fig. 6.20). The additional information from the *S*-waves recorded at seven GDSN stations constrained the fault plane solution to an almost vertical dip slip with a strike slip component (σ = 246° ± 5°, δ = 98° ± 2°, ψ = 124° ± 2°). The mechanism is shown on the vectorplot (Fig. 6.19a) and on the equal area projection of the lower focal hemisphere (Fig. 6.19b).

The synthetic seismograms generated for seven stations are shown in Fig. 6.20. Apart from ANMO, all stations show positive *P*-wave onset. The *pP* phase, having negative polarity, is apparent on all BB seismograms. Therefore, the estimation of the focal depth was made taking into account the time difference between the arrival times of *pP*- and *P*-wave. This gives a source depth of 41 ± 1 km. The above fault plane solution predicts the nodal character of the *P*-wave at ANMO, having a negative polarity, although its amplitude on the model is not as small as on the observed record. The crustal structure at the source is given in Table 6.2e. The model rupture starts at the centre of a circle with a radius of 8 km and propagates outward at a constant velocity of 3.2 km s^{-1}. The mean stress drop for all seven stations is 46.0 bar and the seismic moment is found to be 5.38 x 10^{18} Nm. t^* is assumed to be 0.2 s for all stations.

Table 6.2e. Crustal model for event 13.

V_p (km s^{-1})	V_s (km s^{-1})	Density (g cm^{-3})	Thickness (km)
1.5	0.0	1.0	6.5
5.2	3.0	2.1	1.5
6.3	3.6	2.8	10.0
6.6	3.8	3.1	35.0
8.1	4.7	3.4	Halfspace

b. Other work

The CMT (Dziewonski *et al.*, 1986b) solution (ϕ = 246°, δ = 16°, λ = 99°) yields an almost vertical dip-slip mechanism. The focal depth is 31.8 km and the seismic moment is 8.67 x 10^{18} Nm.

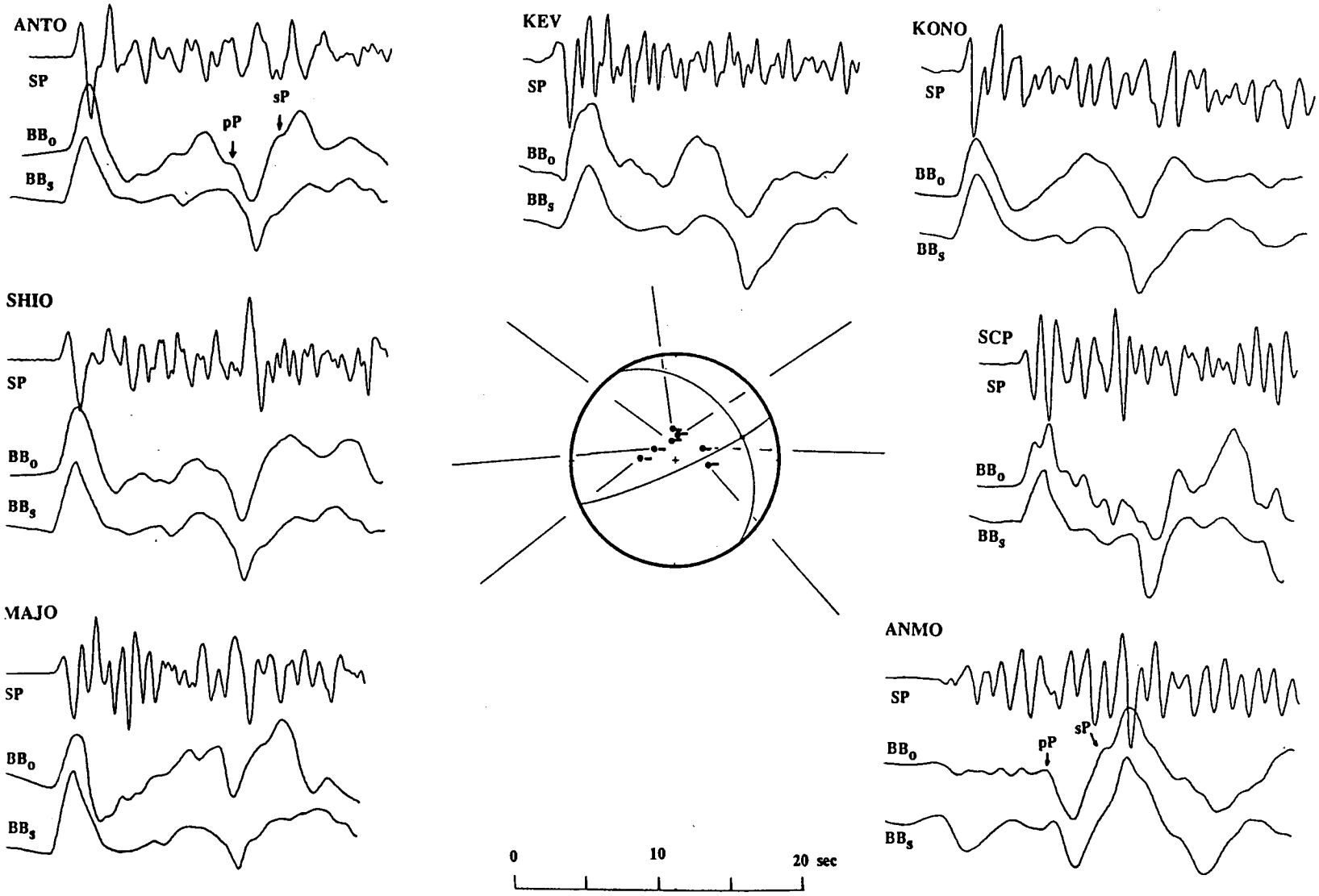

Figure 6.20. Plotted around the focal hemisphere are the SP seismograms (top) recorded at seven GDSN stations for event 13. Their broadband conversions (BB_O) are plotted immediately beneath. The synthetic seismograms (BB_S) that were generated using a source model are represented by the bottom traces. As it can be seen they match well the observed records.

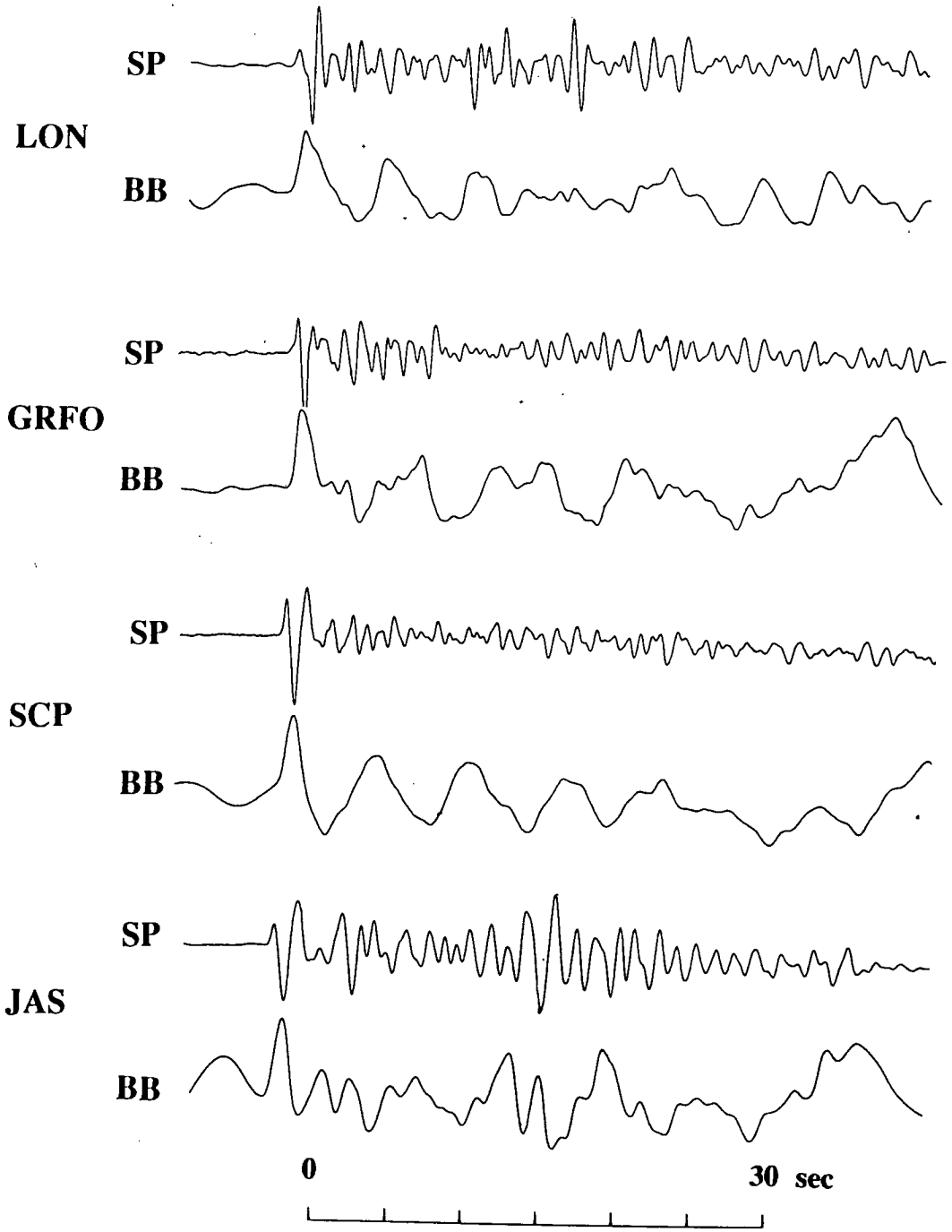

Figure 6.21. SP seismograms (top traces) of event 14 recorded at LON, GRFO, SCP and JAS. Broadband displacement seismograms were retrieved from the SP records and are plotted underneath.

6.3.7 Event 14 - 18 January 1986, central Aleutians

a. Source parameters

Another moderate-sized earthquake of the central Aleutians is the event of 18 January 1986. Four SP records from an equivalent number of stations were deconvolved to produce BB waveforms and they all show positive *P*-wave onsets (Fig. 6.21). In addition seven stations have recorded clearly *S*-wave pulses both on the NS and EW seismograph components (Fig. 6.22). NS and EW *S*-wave polarities are of the same sign at all stations apart from at CTAO where the NS component has negative polarity and the EW component has positive polarity. However, it was the ratio of the amplitudes of the horizontal components of the *S*-waves observed at KONO, CHTO, CTAO and ANTO that constrained the focal mechanism. The acceptable solution obtained has a strike of 110° ± 5°, a dip of 140° ± 5°, and a slip angle on the fault plane of 150° ± 5°, and is shown on the vectorplot and on the equal area projection of Fig. 6.23. This implies an almost vertical dip-slip mechanism with a considerable strike-slip component. Body-wave modelling was not successful as the BB records showed too much complexity and it was also impossible to identify unambiguously any reflected seismic phases on them.

b. Other work

The CMT solution (Dziewonski *et al.*, 1987a) suggests a thrust mechanism for this earthquake with the maximum stress axis at an EW direction, subparallel to the arc at the epicentral area ($\phi = 22°$, $\delta = 45°$ and $\lambda = 108°$). The hypocentral depth found is 35.8 km and the static seismic moment estimated is 0.24×10^{18} Nm.

6.4 DISCUSSION

In this section the source parameters determined for the above earthquakes are interpreted in relation to the tectonic environment in which each event has occurred, and compared to results obtained by other studies.

6.4.1 Focal mechanisms

Table 6.3 summarizes the source parameters determined here for the seven Aleutian earthquakes.

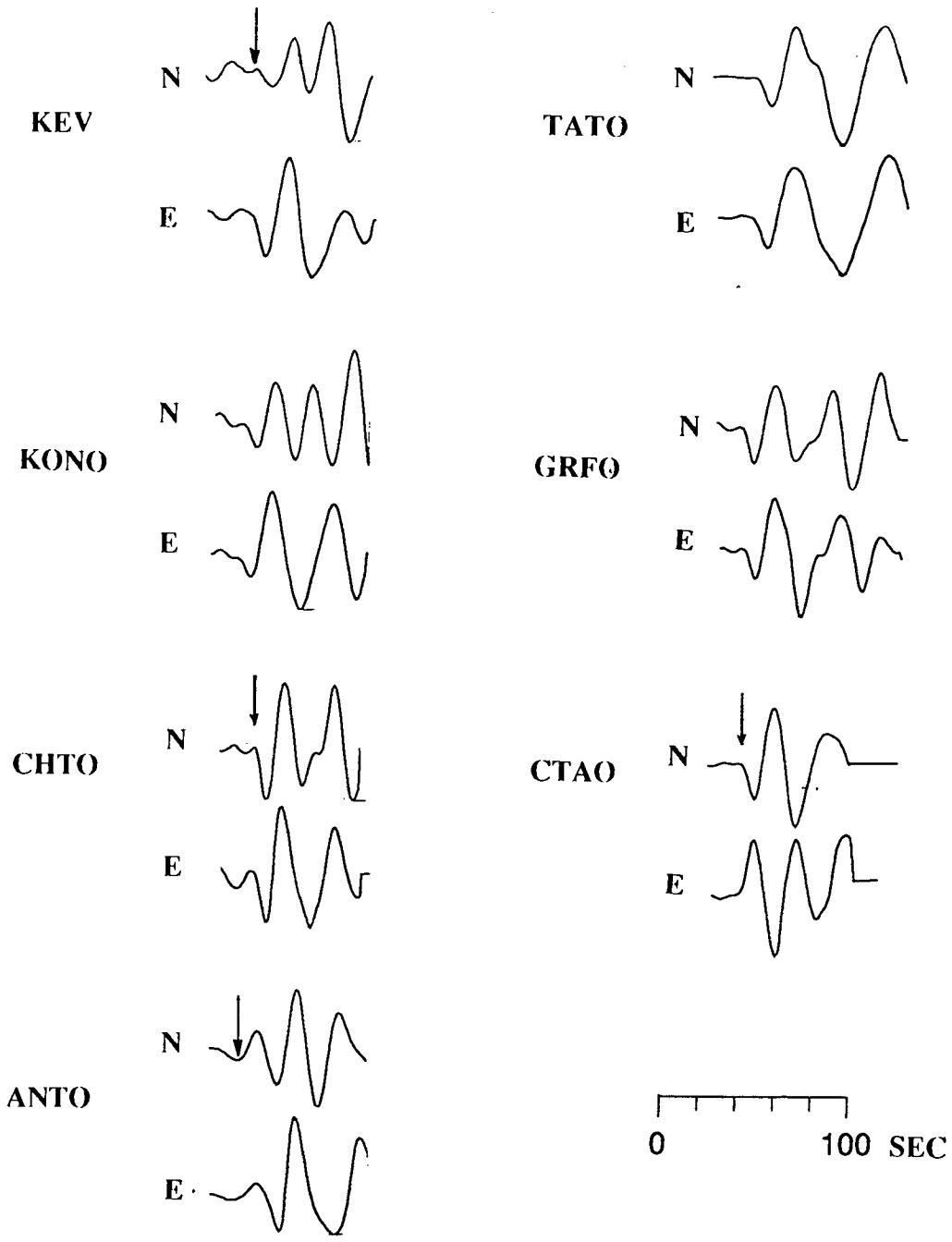

Figure 6.22. LP *S*-wave seismograms (NS and EW components) recorded at seven GDSN stations that were used in the fault plane determination of the 18 January 1986 earthquake (event 14).

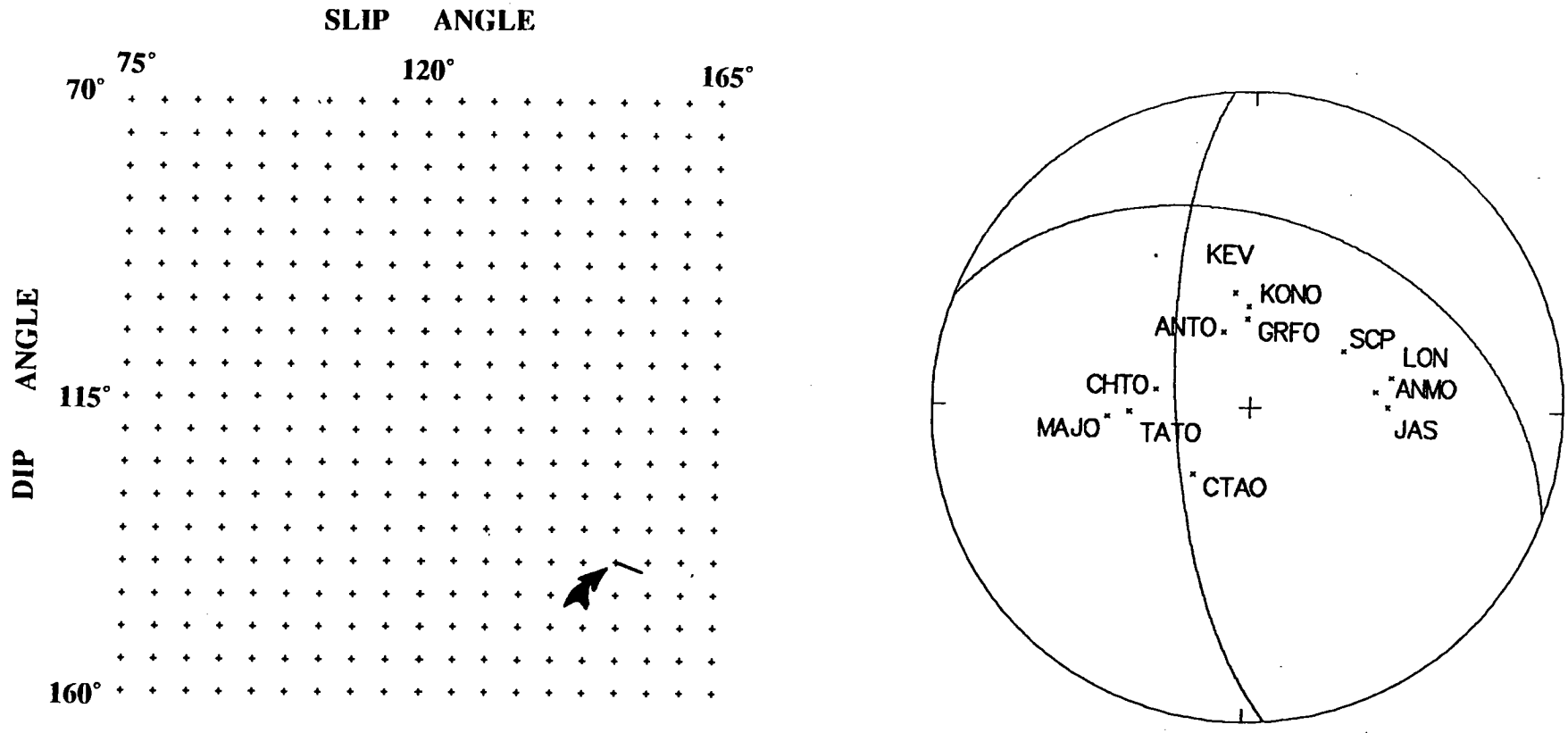

Figure 6.23. The source mechanism determined for event 14 is shown on the vectorplot (*left*) and on the equal area projection of the lower focal hemisphere (*right*).

Table 6.3. Source parameters for events 8, 9, 10, 11, and 13.

Event	σ (°)	δ (°)	ψ (°)	D (km)	M_0 (x 10^{18} Nm)	$\Delta\sigma$ (bar)	R (km)	V_r (km s^{-1})
8	*150*	*60*	*64*	15.0	0.35±0.17	23.0± 8.6	4.0	2.5
9	*62*	*138*	*80*	35.0	1.73±1.0	23.0±13.2	7.0	2.1
10	*20*	*152*	*110*	36.5	2.7±0.1	28.3±16.4	3.5	2.5
11	*62*	*103*	*74*	183.5	2.33±1.8	213.3±165.1	5.5 x 2.5	4.5
13	*246*	*98*	*124*	41.0	5.38±2.1	46.0±19.7	8.0	3.2

The focal mechanisms for all seven events studied were obtained. The data were generally sufficient to constrain the number of compatible solutions to one (at a search increment of ± 5°). It is worth noting that the fault plane solutions obtained predict all nodal and null-vector characteristics of the observed *P* phases, even though this information was not inserted in the computation. All the solutions calculated, apart from event 8 which has a normal fault mechanism, show pure (event 9) or have a large component of thrust-type mechanism. Events 10, 11, and 12, combine a thrust-type mechanism with a small strike-slip component, whereas events 13 and 14 have a larger strike-slip component. The larger spheres of Fig. 6.24 represent the fault plane solutions obtained for the events here using the relative amplitude method, whereas the smaller spheres represent results obtained by different studies and are plotted where available, for comparison.

Starting from the west is event 11 (24 July 1983) which has its epicentre in the Kamchatka peninsula. Its focal depth, well determined from body-wave modelling, places the source at 183.5 ± 0.5 km deep within the subducting Pacific plate. An almost pure vertical dip-slip mechanism with a small right-lateral strike-slip component was resolved for this event. The direction of the *P*-axis is parallel to the direction of the subduction and is consistent with down-dip compression. If the double Benioff zone theory applies to this Benioff zone (i.e. Engdahl and Scholz, 1977; House and Jacob, 1982), then the mechanism of this event is a typical example of the upper zone earthquakes, because such earthquakes result from the unbending stresses of the upper lithosphere after the initial tension associated with incipient subduction (Spence, 1987). The CMT solution is similar to the one obtained here.

Moving to the east, the first event associated with the Aleutian arc is the earthquake of 3 May 1980. This event occurred at a depth of 15 ± 1 km beneath the ocean surface.

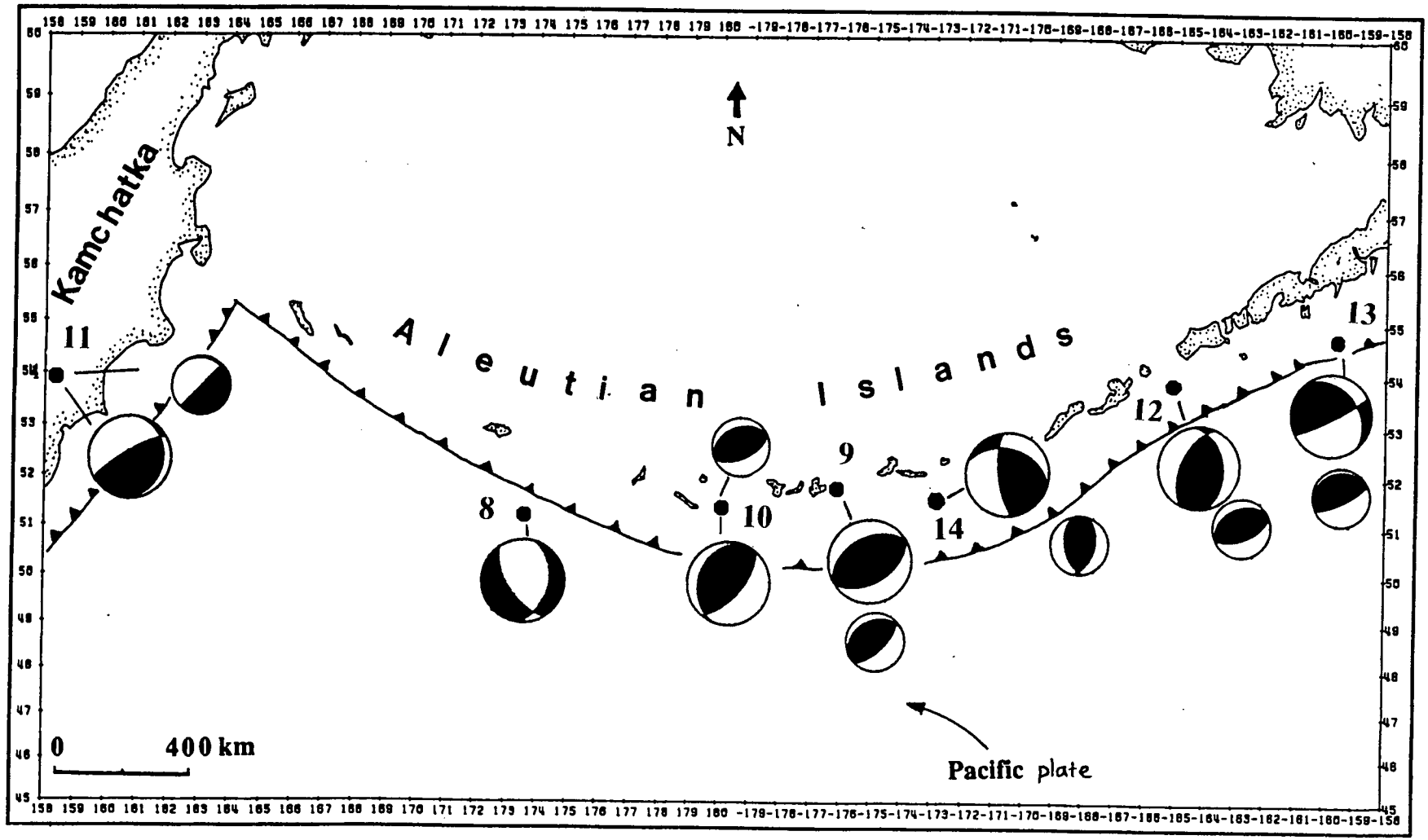

Figure 6.24. The fault plane solutions of the seven Aleutian earthquakes that were determined in this Chapter are represented by the larger spheres of this figure. Black quadrants indicate compression. Source mechanisms for the same events found by others are also plotted for comparison (small spheres). They are all CMT solutions apart from event 9, which is given by Engdahl and Kind (1986).

The depth of the trench at that area can be calculated using the time interval between successive sea surface reflection phases (pwP_1, pwP_2, etc.), and the value determined (7 km) agrees with the bathymetry. The event belongs to the trench earthquake group, which is characterized by normal faulting with the tensional axis perpendicular to the trench. The hypothesis is then that the event was triggered by tensile stresses generated within the subducting plate as it bends laterally underneath the North American plate boundary margin. Seismicity studies (i.e. Engdahl *et al.*, 1989) have shown that the depth range of earthquakes generated in this zone is small and implies that the bending strength of the lithosphere is exceeded in only a narrow region. No other solution is available for this event.

Most subduction zone earthquakes occur within the main thrust zone where most of the energy is released as a result of the plate convergence. The (pure) thrust mechanism of event 10 (1 July 1982), its focal depth (~ 40 km), and its distance from the trench (~ 45 km) suggest that this event occurred due to bending in the lower part of the main thrust zone. The *P*-axis of the mechanism determined trends NW-SE, parallel to the direction of subduction. The CMT solution also predicts a thrust mechanism, with the *P*-axis perpendicular to the trench.

Another event that belongs to the main thrust zone is that of 21 November 1980 (event 9). Its epicentre is located in the Adak Island region of the central Aleutian Islands, which is the most seismically active part of the arc. The focal mechanism is also pure thrust with a *P*-axis perpendicular to the arc. A similar fault plane solution is given by CMT but with a shallower dipping fault plane. For slab earthquakes that occur away from the trench, toward the direction of the arc, the seismograms become more complex (Engdahl and Kind, 1986). One explanation is that the number of overlying reflecting boundaries increases as the focal depth increases. This produces multiple reflected phases that complicate the *P*-wave coda and constructively or destructively interfere to cause a pulse broadening. Another possible cause of the increased complexity with depth along the dipping seismic zone is the influence of the subducting plate itself, as modelled by Spencer and Engdahl (1983). If the bottom and the top of the plate are rather sharp interfaces, they may give rise to reverberations of the direct *P*-wave and its reflections within the down-going plate. This complexity is noticeable on all records of event 9 (Fig. 6.08).

Event 14 (18 January 1986), in the eastern part of the Adak Island region has also its hypocentre in the main thrust zone, provided that the focal depth of 35.5 km, as given by CMT, is correct. However, the focal depth as reported in the ISC bulletins is 13 km, determined in this case from the time difference between *pP*- and *P*-wave onsets. Unfortunately no surface reflections were observed on the seismograms used here so that

the estimation of focal depth from body-wave modelling was not possible. One of the nodal planes in the fault plane solution determined here is almost vertical ($\delta = 81°$) and trends roughly NS, and the other nodal plane, having a smaller dip angle ($\delta = 60°$), trends WNW-ESE. If the focal depth is assumed to be 13 km, the event must have occurred in the overriding lithosphere. Earthquakes from this area are characterized by right-lateral strike-slip on near-vertical faults parallel to the arc. The near-vertical plane, however, in the solution calculated here, is perpendicular to the arc. However, it is perhaps more probable that this event is deeper (35 km) and belongs to the subducting plate for the following reasons: First the strike of the fault plane (approximately NS) is parallel to the strike of the Amlia fracture zone (Fig. 5.01) which is also perpendicular to the arc. Both the volcanic line (in the overriding lithosphere) and the downgoing plate itself are offset by about 40 km in a right-lateral sense near where Amlia fructure zone currently intersects the trench (173°W) (House and Jacob, 1983). The CMT solution also predicts a thrust mechanism that supports the idea of the event belonging to the main thrust zone rather than the overriding lithosphere.

Further to the east there is the event of 23 September 1984 (event 12). This earthquake has a thrust mechanism with a small strike-slip component. The *P*-axis has an EW direction, which is subparallel to the direction of subduction at this area of the arc. If the fault plane is the nodal plane that trends NNE, the strike-slip motion is right-lateral. Microearthquakes in the central Aleutians occurring as part of the interplate activity near Adak (LaForge and Engdahl, 1979) show evidence of arc-parallel extension above the main thrust zone and within the upper plate. LaForge and Engdahl (1979) show that the low-magnitude normal faulting is occurring because of the component of plate convergence that is parallel to the arc. However, the strike-slip component of the solution calculated here is very small compared to the thrust component. This observation suggests that the earthquake is located in the upper part of the main thrust zone. This is also supported by the CMT solution although the source is placed at the lower part of the main thrust zone (46 km). The *P*-axis in the CMT solution is also normal to the arc.

Finally, the 9 October 1985 earthquake (event 13) which occurred in the eastern end of the arc has been examined. The focal depth of 41 $\pm$ 1 km, determined from body-wave modelling, suggests that the focus is placed in the main thrust zone. A thrust mechanism with a considerable strike-slip component was obtained here. Assuming that the fault plane has a strike of 60° and dip of 80°, then the strike-slip is left-lateral. This suggests that the event is the result of both the plate convergence and the westward movement of material from the subducting lithosphere. The *P*-axis for this event is perpendicular to the arc consistent with the CMT solution, which is more nearly a pure dip-slip mechanism.

6.4.2 Source models

Synthetic seismograms were generated for five of the events (8, 9, 10, 11, and 13), using two-dimensional Savage (1966)-type source models. A flat multi-layered crustal structure was used. As discussed in Chapter 4, such a structure is not a realistic approximation for velocity structures near plate boundaries, and it may not be appropriate for all recording stations. However, for most events examined here, this assumption had no clear systematic effects and a good agreement between the observed and the synthetic waveforms was obtained. For events 12 and 14, it is possible that velocity structure anomalies at the epicentral region and/or source complexity produced complicated records and these were not modelled.

The radius of the source varied between 3.5 and 8.0 km and was positively correlated to the earthquake size. The most successful models were obtained for events 8, 9 and 11, where the synthetic seismograms match the observed waveforms well. Seismic wave pulse durations, polarities and amplitudes of the different body wave phases were accurately reproduced. This implies that a simplistic kinematic source model assumption, such as the Savage-type model used here, is a good representation of the real source. The velocity at which the rupture propagated from the centre of the model source toward its edge varied from 2.1 to 4.5 km s^{-1} for the different events. These values are included in the range of rupture velocities (0.6 - 0.9 β) predicted by the dynamic models of Madariaga (1976) and Das and Kostrov (1988). The best fitting attenuation correction factor (t^*) showed some variation (0.2 - 1.0 s) with azimuth for some of the events (9, 10) in that seismograms recorded at stations to the SE of the arc were generally more attenuated than those from the rest of the stations. This is probably due to path effects toward those stations rather than rupture propagation at the source (Doppler effect), which would produce a more systematic pattern of *P*-wave duration variation around the focal hemisphere. Event 11, however, showed a systematic pattern of *P*-wave duration variation with azimuth and that was interpreted as a directivity effect. Indeed, an elliptical source model that was assumed for this event, with the rupture starting at the upper focus of the ellipse and propagating downward, reproduced on the synthetics the observed azimuthal variation in amplitude and duration.

Stress drops typical for interplate earthquakes (Kanamori and Anderson, 1975; Chung and Kanamori, 1980) were obtained for the events studied here. The high stress drop (213 bar) and high rupture velocity of event 11 is explained by its deep focus (183.5 km), well within the subducting Pacific plate. As amplitudes were different at different

stations, an azimuthal variation of the model stress drop was observed and a mean value used for the best estimate.

Seismic moments calculated in this study for events 9, 10, 11 and 13, are similar to those given in the CMT solutions for the same events. Since measured moment is generally dependent on the frequency of the recording instrument (i.e. Christensen and Ruff, 1986; Monfret and Romanowicz, 1986), it might have been expected that the CMT moments would in general have greater values than the ones obtained here. One possible explanation for the good agreement could be the relatively smaller surface-wave magnitude of the events under examination when compared to their body-wave magnitude. As seismic rays travel mainly through oceanic crust to arrive at the recording stations, no Airy phases are created that could give high surface-wave magnitudes. As a result, low-amplitude surface waves will yield moments comparable to those obtained using body waves. No published moment values exist for event 8; the value obtained is similar to the rest of the moments calculated here.

6.5 SUMMARY & CONCLUSIONS

Seven moderate-sized earthquakes associated with the Aleutian Islands subduction zone have been studied in this Chapter. Clearly-recorded body waves provided sufficient information to determine uniquely their focal mechanisms. Indeed, the fault plane solutions for all the events were tightly constrained (to within $\pm$ 5°) using the relative amplitude method. The events are representative of the various seismotectonic zones (Fig. 1.02) that can be found in subduction environments. Event 8 occurred in the oceanic crust under the trench, and is characterized by normal faulting with the tensional axis perpendicular to the arc. Events 9, 10, 12, 13 and 14, are located in the main thrust zone. They have thrust mechanisms and fault strikes consistent with the coupling of the two colliding lithospheres. The strike-slip component that is present on the solutions of events 13 and 14 could be due to westward translation of material of the subducting lithosphere and the presence of the Amlia fracture zone respectively. The hypocentre of event 11 is situated within the subducting lithosphere in the upper part of the double Benioff zone, resulting from the subduction of the Pacific plate under Kamchatka. The down-dip direction of compression suggested by the orientation of the *P*-axis is consistent with unbending stresses in the upper half of the subducting lithosphere.

Other source parameters (focal depth, source dimensions, rupture velocity, stress drop and seismic moment) were determined for five events by body-wave modelling. The focal depth was determined using the time difference between *pP*- and *P*-wave, and was well constrained in most cases. Source models were assumed to be circular or elliptical

with the radius varying from 3.5 to 8 km depending on body-wave magnitude. All the events had typical stress drop values for interplate earthquakes (~ 30 bar), except event 11 which occurred at a depth of 183.5 km within the subducting lithosphere and can be characterized as an intraplate earthquake. The rupture velocities obtained (2.1 - 4.5 km s^{-1}) lie toward the inertial upper limit determined by the shear wave velocity. Seismic moment values obtained here are similar to CMT determinations although the latter were calculated using much lower frequency seismic waves. This could mean either that the moments are underestimated by the CMT method, or that longer period waves are more attenuated than body waves for events in the Aleutian arc.

CHAPTER 7

COMPARISON AND DISCUSSION

7.1 INTRODUCTION

In this Chapter the earthquake source parameters determined for the Hellenic arc are compared to those obtained for the Aleutian arc events. First the results from Chapters 4 and 6 are combined and discussed. Uncertainties in the modelling procedure are subsequently presented. Results from both areas studied are compared to those from other studies elsewhere in the world, and explanations for the observed phenomena are considered and their significance is discussed.

7.2 COMPARISON OF EARTHQUAKE SOURCE PARAMETERS

The earthquake source parameters determined for the two study areas are combined and compared in this section. Relationships between various parameters are plotted in Figs. 7.01 - 7.06.

7.2.1 Focal mechanisms

The focal mechanisms of the fourteen earthquakes studied generally agree with the stress regime of the two subduction zones. Events with epicentres in the main thrust zone, where the coupling between the two colliding lithospheres occurs, have thrust mechanisms with the P-axis parallel to the direction of subduction. Normal faulting caused by extension within the bending subducting slab is resolved for the events that occurred in that area. Local strike-slip tectonic features, i.e. the right-lateral transform fault of the Ionian Islands in the Hellenic arc, and the right-lateral Amlia fracture zone in the Aleutian arc, affect the type of focal mechanisms of the associated seismicity and this is confirmed by the solutions obtained for the related events. The focal mechanisms determined using the relative amplitude method (Pearce, 1977, 1980), apart from a few cases of insufficient data, are very well constrained ($\leq \pm 5°$). For some events the amplitude ratio between NS and EW components of *SH*-waves critically affected the results. It is important to mention that in many cases nodal phases and null vector observations are predicted by the solutions although this information was not inserted in their calculation. This highlights the advantages of the above method compared with

first-motion or other whole body waveform inversion techniques. Table 7.1 shows the focal mechanisms determined in this study (expressed in Aki and Richards' (1980) convention), together with the CMT results for the same events.

Fault plane solutions for most earthquakes studied show differences when compared to the CMT solutions. These differences are sometimes large (events 6, 13, 12, 14,) and they predict different source orientations. For example, event 14 it is found to have a thrust mechanism with a considerable right-lateral strike-slip component, explained by the right-lateral character of the Amlia fracture zone. However, the CMT solution, while having a strike and dip of fault plane similar to the ones obtained here, predicts a pure thrust mechanism. Moreover, the CMT solution of event 6 was shown to be incorrect as two negative *P*-wave observations occur in the compressional quadrant of the CMT solution.

For those events for which body-wave modelling was carried out here, the correct source orientation is further confirmed by the successful reproduction of the polarities and amplitudes of *P*-, *pP*-, and *sP*-waves at a number of GDSN stations at teleseismic distances.

7.2.2 Magnitude and seismic moment

Fig. 7.01 shows the relationship between m_b and M_0. The seismic moment generally seems to increase with the body-wave magnitude for earthquakes from both study areas. Event 10 however has a very small moment despite its large magnitude.

Fig. 7.02 shows the relationship between M_s and M_0 for both arcs and also includes the global relationship found by Ekström and Dziewonski (1988). All the Hellenic arc earthquakes have moments lower than those predicted by the global relationship, whereas most of the Aleutian events have moments higher than those predicted by the global relationship.

7.2.3 Moment, radius, stress drop and depth

The relationship between the seismic moment (M_0) and the radius of the fault is shown in Fig. 7.03. In the cases where an elliptical fault plane was resolved in the body-wave modelling, the radius of the circle that has the same area as the ellipse is used in the plotting. As expected, moment increases as the dimensions of the fault increase. The abnormally high moment value obtained for the relatively small source of event 11 is due to the high stress drop value for this earthquake (213 bar), since seismic moment is also proportional to stress drop.

Table 7.1 Source parameters of all earthquakes studied. Focal mechanism determinations (ϕ, δ, λ) are expressed in Aki and Richards' (1980) convention.

Event	Date	This study					CMT				
		ϕ (°)	δ (°)	λ (°)	M_0 (x10^{18} Nm)	Depth (km)	ϕ (°)	δ (°)	λ (°)	M_0 (x10^{18} Nm)	Depth (km)
1	10 Mar 81	*120*	*50*	*90*	-	-	-	-	-	-	-
2	16 Nov 82	*0*	*80*	*30*	-	-	*297*	*35*	*54*	0.32	10.0
3	17 Jan 83	*127*	*84*	*60*	5.71	8.0	*34*	*14*	*153*	24.00	10.0
4	19 Mar 83	*300*	*30*	*110*	0.16	65.0	*358*	*39*	*131*	0.33	65.0
5	21 Jun 84	*220*	*30*	*160**	-	-	*79*	*7*	*-128*	0.22	34.0
6	27 Sep 85	*250*	*70*	*170*	-	-	*135*	*76*	*13*	0.33	44.0
7	13 Sep 86	*196*	*44*	*-86*	1.02	5.5	*350*	*46*	*-130*	0.98	15.0
8	3 May 80	*150*	*60*	*-116*	0.35	15.0	-	-	-	-	-
9	21 Nov 80	*242*	*42*	*100*	1.73	35.0	*258*	*26*	*111*	1.31	40.0
10	1 Jul 82	*200*	*28*	*70*	0.27	36.5	*251*	*32*	*93*	0.69	49.5
11	24 Jul 83	*242*	*77*	*106*	2.33	183.5	*315*	*11*	*7*	2.35	177.4
12	23 Sep 84	*170*	*40*	*64*	-	-	*244*	*32*	*87*	0.82	46.0
13	9 Oct 85	*66*	*82*	*56*	5.38	41.1	*246*	*16*	*99*	8.67	31.8
14	18 Jan 86	*290*	*40*	*30*	-	-	*22*	*45*	*108*	0.24	35.8

* no well-constrained solution

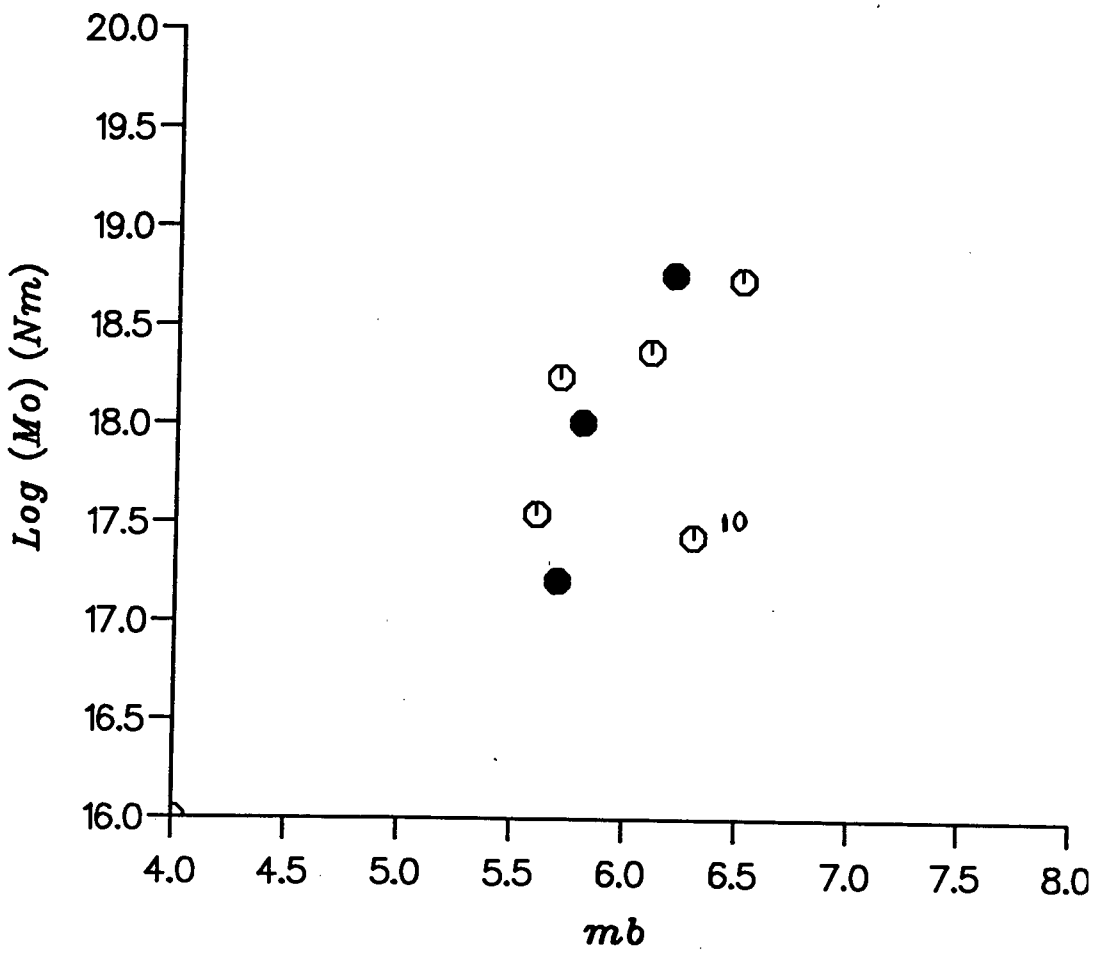

Figure 7.01. Body-wave magnitude against seismic moment for all earthquakes studied. Solid symbols represent Hellenic arc events and open symbols represent Aleutian arc events.

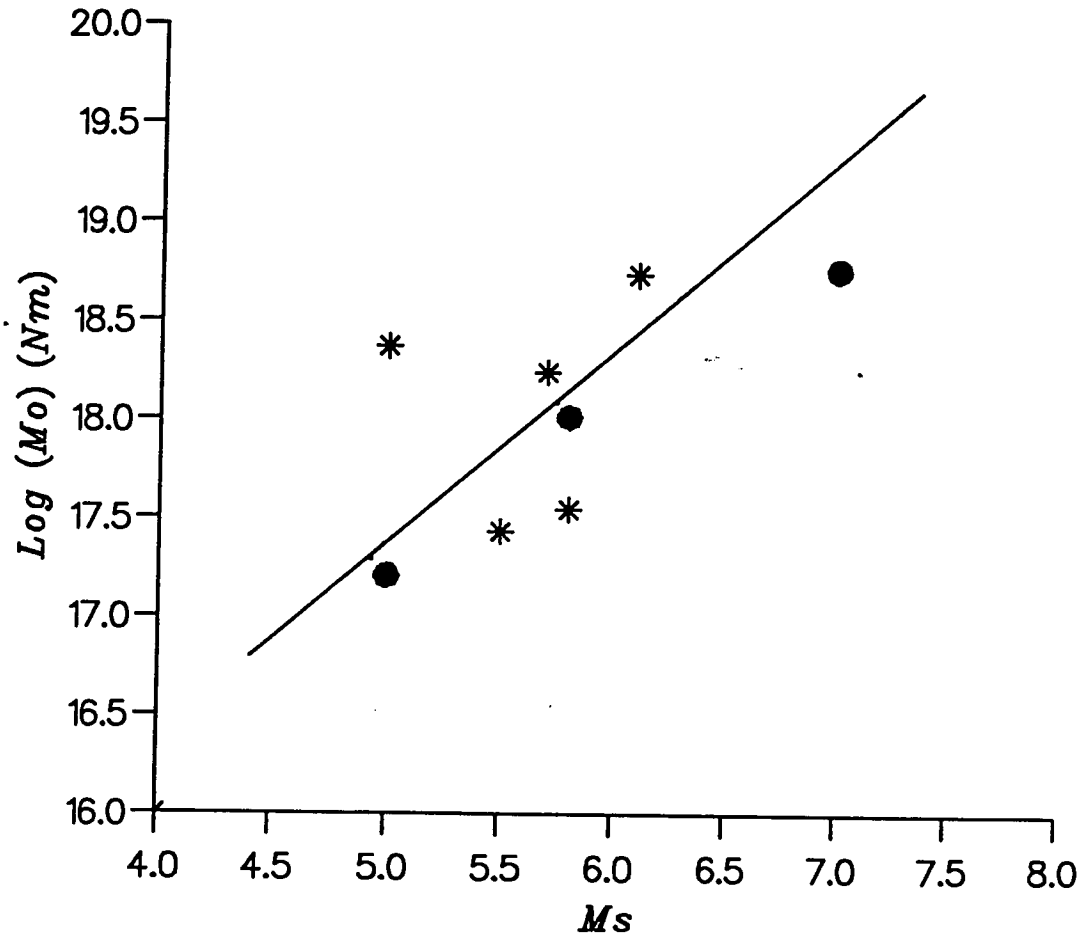

Figure 7.02. Surface-wave magnitude against seismic moment for all earthquakes studied. Solid symbols represent Hellenic arc events and asterisks represent Aleutian arc events. The solid line shows the M_o - M_s global relationship of Ekström and Dziewonski (1988).

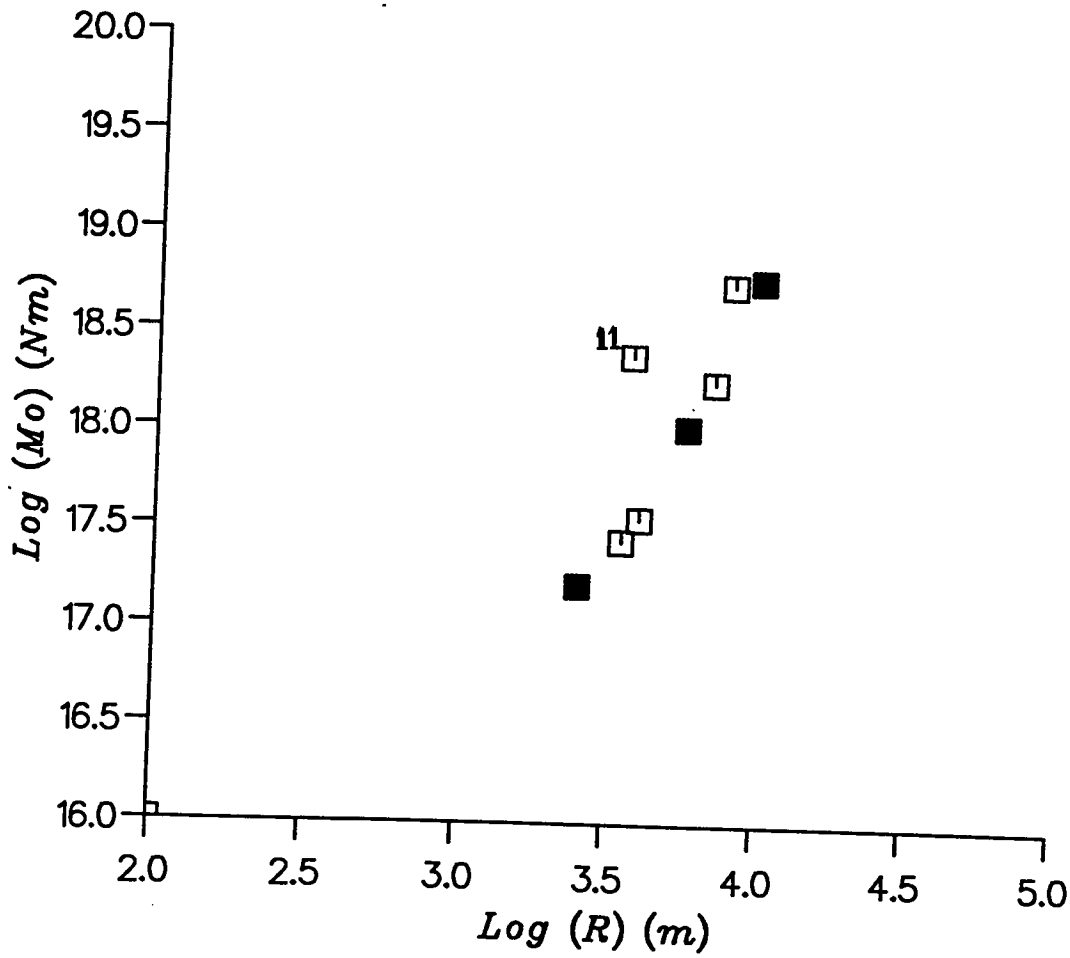

Figure 7.03. Source radius against seismic moment for all earthquakes studied. Solid symbols represent Hellenic arc events and open symbols represent Aleutian arc events.

When the stress drop is plotted against seismic moment on a log-log diagram (Fig. 7.04) an average value of about 30 bar is obtained for earthquakes examined in both the Hellenic and the Aleutian arcs. Event 11 has much higher stress drop possibly due to its deeper (183.5 km) source. No specific relationship is observed between seismic moment and depth, as can be seen in Fig. 7.05.

7.3 DISCUSSION

7.3.1 Uncertainties in the body-wave modelling

Seismic waveform inversion is fraught with difficulties. The form of a seismogram as it arrives at the receiver is determined not only by the source itself, but also by the structure of the earth between the source and the receiver, and the local site conditions at the receiver itself. Der *et al.* (1990) demonstrate that most LP waveform modelling studies are much less accurate than claimed. A good model of the waveform filtered around 20 s (LP) may be a poor fit at the periods at which the source radiates most of its energy. Modelling of broadband waveforms (~ 0.2 - 10 s) is therefore more accurate for events of the size studied in the present work, as the best fit will be to the principal waveform (~3 - 10 s). The summing of multiple sub-events has often been shown to produce excellent fits to observed seismograms (e.g. Bezzeghoud *et al.*, 1986, Stavrakakis *et al.*, 1987). Other recent studies (i.e. Choy and Kind, 1987, Choy and Dewey, 1988, Yamamoto and Mitchell, 1988) also model earthquakes as a combination of sub-events, using a variety of modelling and inversion techniques. Earthquake faults are thought to be mechanically or geometrically heterogeneous and so this approach might well be expected to model earthquakes successfully. However, it is extremely difficult to establish the uniqueness of such complex, multiple sub-event solutions. This is especially observed in studies (e.g. Bezzeghoud *et al.*, 1986, Stavrakakis *et al.*, 1987) using inversion techniques such as that of Kikuchi and Kanamori (1982), which sum up to ten sub-events. Christensen and Ruff (1985) show that for large ($M_S > 6.5$) shallow (< 60 km) earthquakes, there is a significant trade-off between source time function and depth. Errors in depth determination of a few kilometres require extremely complex source models to match the seismograms of a simple event. Das and Kostrov (1988) show by numerical experiment that not all the "ripples" on the source time function (and therefore small pulses on the seismograms) are necessarily separate sub-events. In this study simple sources were used for all the events studied.

Another effect that must be considered when waveform modelling is performed is the source structure. Most studies use horizontal plane layered structures at both source

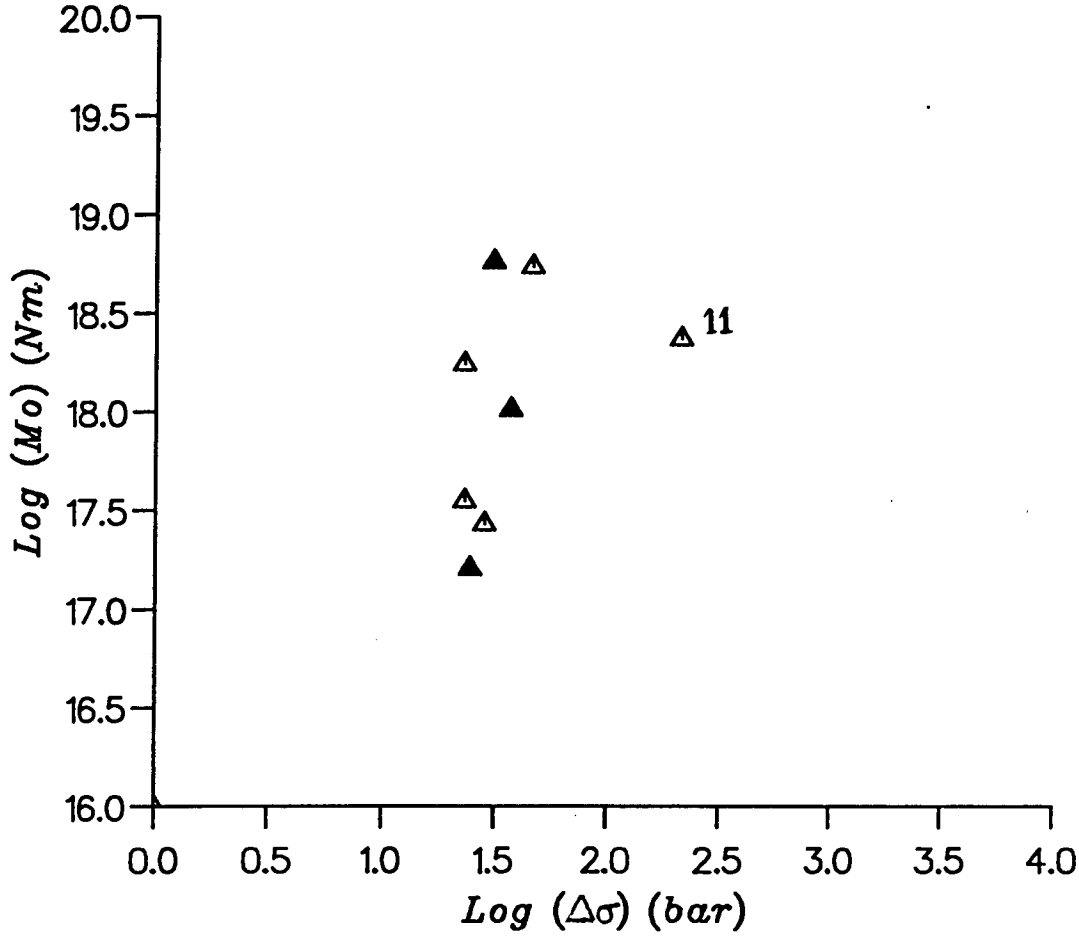

Figure 7.04. The relationship between seismic moment and stress drop for all earthquakes studied. Solid symbols show results from Hellenic arc events and open symbols represent results from Aleutian arc events.

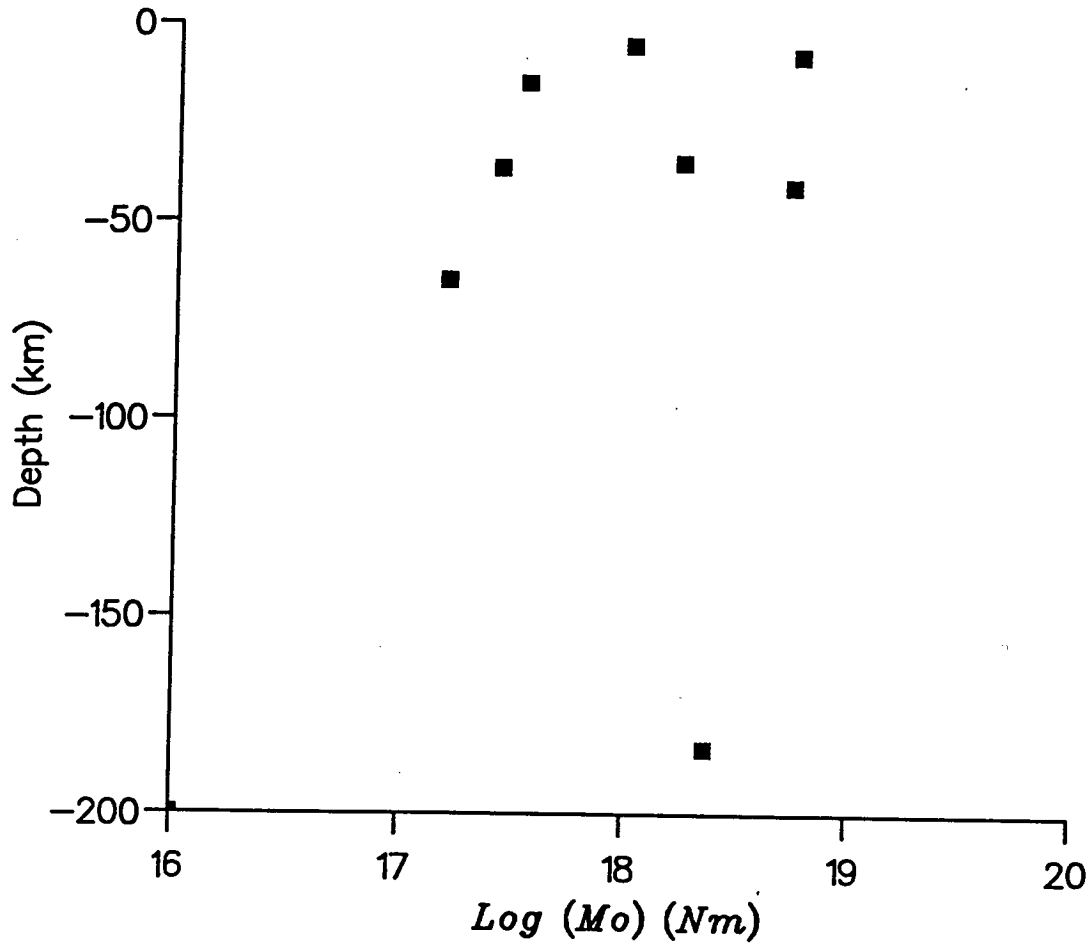

Figure 7.05. Variation of seismic moment with focal depth of the events studied.

and receiver, alteration of which has little effect on synthetic body wave seismograms (e.g. Soufleris and Stewart, 1981, Wiens, 1989). In contrast, Wiens (1987, 1989) and Lundgren *et al.*, (1989) investigate the effects of dipping layers, and find that dips of only a few degrees, especially in the sea floor, can result in extremely complex seismograms from simple earthquakes. Such dips are very likely in the Hellenic and Aleutian subduction zones because of the down-going direction of the subducting lithospheres. Wiens (1989) explores the effects of dipping near-source bathymetry and structure on long period teleseismic body waveforms from shallow subduction zone earthquakes. Synthetics for shallow double-couple sources and velocity structures incorporating planar dipping interfaces, suggest that *P*-waves are more sensitive to water depth and sea bottom orientation than to sediment thickness and dip of the sediment-crust and crust-mantle interfaces. The above study also shows that the distorting effect of the water layer gives rise to systematic differences in *P*-wave complexity between shallow events near the seismic front, which occur beneath a thick water layer and show numerous later arrivals, and deeper, arcward events which occur beneath a thin water layer and show simple waveforms. It is possible that the complexity observed for some events (5, 12 and 14) may be due to one or both the above causes.

Before using the deconvolved broadband seismograms to obtain source parameters it is necessary to correct for the effects of anelastic attenuation along the raypath from the source to the receiver. In this study the attenuation correction factor (t^*) used has average values of 0.6 s for the Hellenic arc earthquakes and between 0.2 and 0.3 s for the Aleutian arc events. This implies that attenuation is greater in the Hellenic arc. However, for a few cases these values were increased to 0.6 or 1.0 s because of the lower frequency content of seismograms at some stations compared to records from other stations for the same event. As can be seen in Fig. 7.06, increasing the t^* decreases the amplitude of the *P*-wave whilst increasing the pulse duration. Since attenuation decreases exponentially with decreasing frequency it is usually assumed to be independent of frequency. For example, if t^* is 0.2 s then the recorded amplitude of a 2 s pulse is decreased by 15%, whereas that of a 5 s pulse is decreased by only 5%. If t^* is 0.6 s the above two pulses show a decrease in amplitude of 34% and 16% respectively. A consideration of the effects of the attenuation operator shows that small changes in t^* below 0.6 s have very little effect on the predominant ($\simeq$ 7 s) period of the broadband pulses like the ones investigated in the present study. It is found by simple calculation that if t^* is increased from 0.2 s to 0.6 s, the duration of a 2 s pulse is increased by 20% and that of a 5 s pulse is increased by 6 %. Although no great effects are observed on the amplitude and duration of the pulses of the events studied with changes of t^* between 0.2 and 0.6 s, smaller values (0.2 - 0.3 s) were preferred so that no overestimate of attenuation was

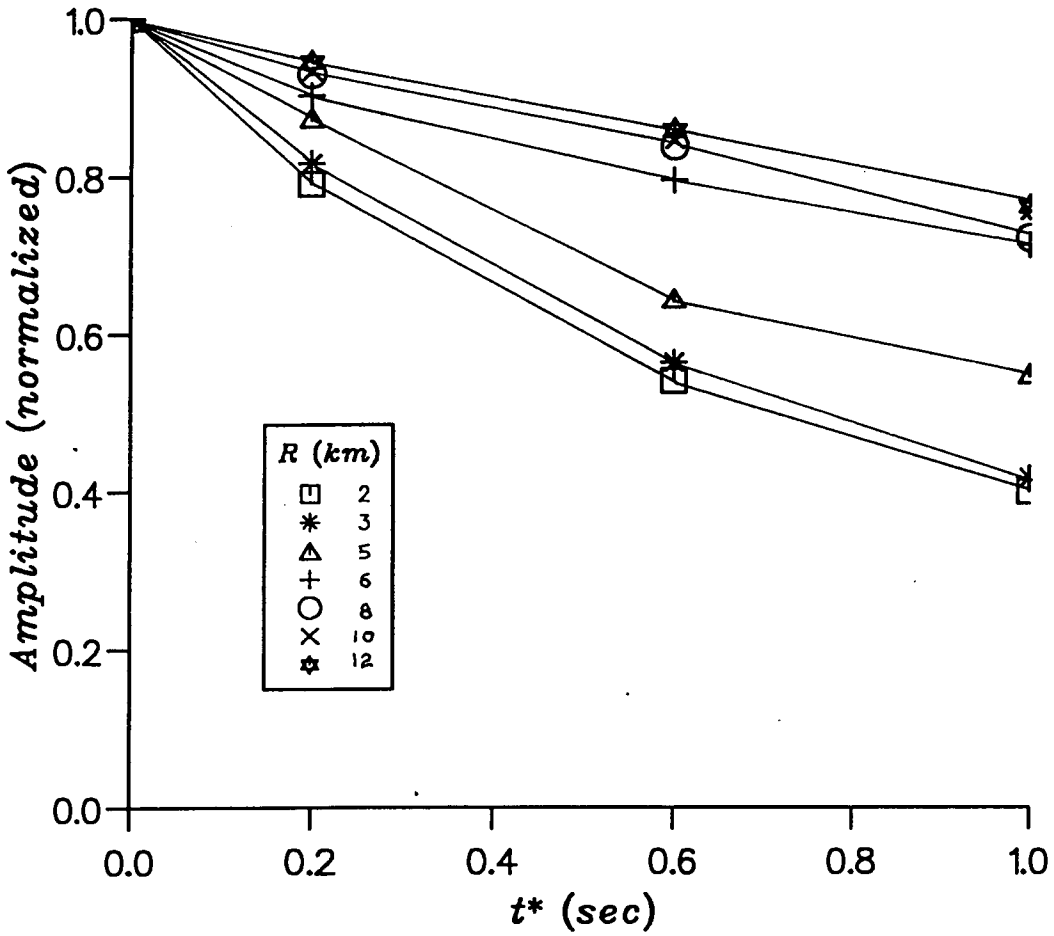

Figure 7.06. Effects of the attenuation factor (t^*) on the amplitude of the direct *P*-wave pulse for different source sizes.

made. Moreover, Stewart (1984) finds that some transmission paths have an average attenuation factor lower than the 1.0 s which is often used when modelling LP seismograms at teleseismic distances. Abercrombie (1991) finds that $t^* = 0.2$ s is more appropriate for back-arc Aegean earthquakes. Although it seems that seismograms from Hellenic arc earthquakes are more attenuated while travelling from the source to receiver than those from the Aleutian arc, no systematic evidence is present and therefore no conclusions can be drawn from this study.

Short period and broadband seismograms of three of the events in both the Hellenic and Aleutian subduction zones show too much complexity to be modelled by a simple source. This, as discussed above, could be due to a number of reasons: source complexity; source velocity structure; path effects between the source and the receiver; and receiver velocity structure. Most explosion seismograms observed at teleseismic distances are simple which suggest that complexity is not due to transmission within the mantle (Douglas *et al.*, 1990). Receiver structure effects are easily recognisable because they are systematic and similar for all recorded events. Therefore they can be easily removed. One widely accepted explanation of the complexity of earthquake *P* seismograms seems to be that it results from reverberation in the crust of the upward radiated pulses of *P* and particularly *S* with conversion of *S* to *P* (Douglas *et al.*, 1974). Engdahl and Kind (1986) studied broadband seismograms of eleven central Aleutian earthquakes, and attribute the observed complexity of the records with depth to the increase in the number of overlying boundaries, which results in the generation of multiple reflected phases that complicate the *P* coda. Moreover, unknown details in the complexity of structure around the source may also increase, giving rise to complex reflections and scattered waves. These effects need to be carefully examined with extensive waveform modelling, using a variety of possible arc structures. Plate modelling by Spencer and Engdahl (1983) suggests another possible cause of the increased complexity with depth along the dipping seismic zone: if the top and the bottom of the slab are rather sharp interfaces, they may give rise to reverberations of the direct *P* and its reflected phases within the downgoing plate. This would be more apparent at stations that record downgoing waves. However, this explanation was not always the case (Engdahl and Kind, 1986).

7.3.2 Discussion of results

One of the most important earthquake parameters that needs to be accurately determined is the focal depth. The exact location of the earthquake source provides essential information for determining the shape, size and downward extent of the slab in

subduction zones. When the depth of the hypocentre is known accurately, then other source parameters such as focal mechanism and stress drop can be interpreted in terms of the tectonic and rheological environment of the source. Depth is also significant for source mechanism determination. ISC estimations are usually overestimates as sea surface reflected phases of the direct *P*-waves (*pwP*) are frequently regarded to be *pP* (Hong and Fujita, 1981). In this study, the time interval between the *pP* and *P* phases (which were more clearly identifiable on the broadband records) was taken into account in the determination of focal depths. For the very shallow events (3 and 7), where *P* and *pP* interfere, depth was determined by body-wave modelling.

The seismic moments determined in this study for two of the three events from the Hellenic arc are lower by up to a factor of 3 or 4 than those obtained from the CMT solutions (Table 7.1, Fig. 7.07). In contrast, seismic moments for five Aleutian earthquakes are comparable with the CMT results (Fig. 7.07). Many studies (e.g. Silver and Jordan, 1983) have shown that seismic moment is dependent on frequency, and increases as the period from which it is derived increases. Seismic moment is defined as being proportional to the area of the fault and the average slip (Aki, 1966). At teleseismic distances this is proportional to the area under the far field displacement pulse, which is equivalent to the amplitude of the zero-frequency of the amplitude spectrum (e.g. Keilis-Borok, 1959; Pilant, 1979). Therefore, the best estimate of moment as it is defined should come from the lowest available frequencies, e.g. CMT solutions using surface and mantle waves (150 - 180 s). Various authors have also found, both theoretically and in practice, that when an earthquake is recorded and studied at wavelengths short enough to observe complexity and sub-events, the combined moment of these sources is significantly less than that determined from longer period data which assumes the earthquake to be a point source (e.g. Madariaga, 1979; Choy and Dewey, 1988; Vaccari *et al.*, 1990). Main and Burton (1990) determine two moment-magnitude relationships for Aegean earthquakes ($M_S > 5.5$). They find that moments calculated from surface waves (at periods of 60 - 30 s) are on average twice the size of moments calculated from 20 s body waves. In common with Vaccari *et al.* (1990) the seismic moment determined from very long period mantle and surface waves is considered the most accurate measure of the moment in an earthquake, following its original definition by Aki (1966).

Abercrombie (1991) argues that source complexity is extremely unlikely to be the cause of low moments (with respect to M_S) found in the Aegean by Ekström and Dziewonski (1988). In that study, earthquakes modelled as complex sources had a total moment considerably smaller than the moment determined from a simple source, using longer periods. A considerable amount of moment release must, therefore, occur at frequencies too low to be seen by broadband (> 0.1 Hz) seismograms. It is worth noting

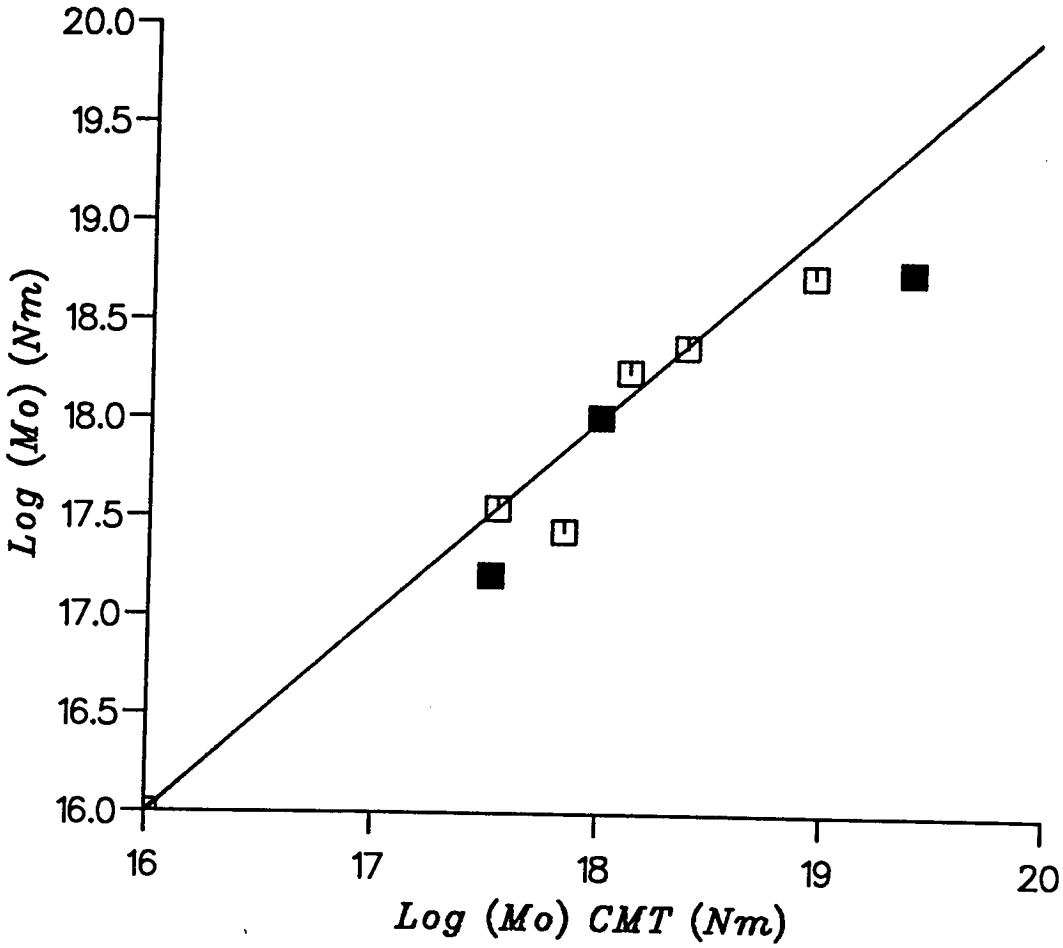

Figure 7.07. Seismic moments obtained in this study versus CMT results for the same earthquakes. The solid line represents the 1:1 relationship. Solid symbols represent Hellenic arc events and open symbols represent Aleutian arc events.

that the effect of measuring period can be discounted in the work of Ekström and Dziewonski (1988), as they use long period CMT solutions. The shallow depth of Aegean earthquakes could be a reason for the anomaly. Surface waves from shallow sources have significantly greater amplitudes than those from deeper earthquakes of the same size (Marshall and Basham, 1973), and no correction is made for this or for the path type when M_S is determined. Therefore it is highly probable that the moments determined from long period studies are correct, but the magnitudes are too high. However, depth cannot be the only factor involved, as Ekström and Dziewonski (1988) find that earthquakes in regions of continental extension (shallow) have low M_0 with respect to M_S, whereas mid-ocean ridge earthquakes (also shallow) have higher M_0, and subduction earthquakes show no simple pattern. Higher M_S values than expected are seen for thrust earthquakes along the Tonga-Kermadec subduction zone, whereas events from the Aleutian Islands exhibit the opposite effect.

Marshall and Basham (1973) describe how high amplitude Airy phases are able to travel along continental paths, but not through oceanic crust, so when the measured amplitude of the surface wave is that of an Airy phase, the M_S value will be large compared to the value determined from a wave train with no Airy phase. They calculate that M_S could be underestimated by an average of 0.2 (up to 0.5, depending on the period) from waves travelling along oceanic and mixed paths, compared to those travelling predominantly through continental crust. This effect could cause the magnitudes of earthquakes at mid-oceanic ridges to be underestimated with respect to those from continental areas, as all paths to the former are predominantly oceanic, while those to the latter are nearly all continental. The paths of surface waves from subduction zones are a mixture (some oceanic, some continental), with a bias towards one or the other caused by the location of the seismicity zone and the world-wide distribution of stations. These two effects of depth and path type are of the correct size and sense, when combined, to explain the anomalies in the global M_S - M_0 distribution observed by Ekström and Dziewonski (1988). This hypothesis could also explain why the seismic moments for Aleutian Island earthquakes estimated in the present study, using shorter period waves than the CMT solutions, are of similar size to those of the CMT solutions. Choy and Dewey (1988) find that frequency-dependence of moment is not a strong feature for moderate to large earthquakes in Chile.

Therefore, a frequency-dependence of moment together with overestimation (or underestimation) of M_S could result in the discrepancy (or agreement) observed between the moments determined here and those of the CMT solutions, for the Hellenic and Aleutian arc respectively.

Stress drop values typical of interplate earthquakes were found for both arcs. Kanamori and Anderson (1975) found that large interplate earthquakes align with a very small scatter between the lines for 10 and 100 bar with an average of 30 bar. This agrees with results obtained for all events with depth less than 100 km. Event 11 has a focal depth of 183.5 km and its stress drop was found to be 213 $\pm$ 165 bar. From a study of shallow and deep South American earthquakes, Wyss (1970) suggests that changes of the average stress with depth reflect changes of the strength of the earthquake zone as a function of depth. The strength increases with increasing depth and reaches a maximum at about 100 km. At greater depth the stress decreases again, until at 600 km it reaches about the same value as at the surface. This pattern is believed to be an expression of the temperature-pressure conditions in a slab of lithosphere of predominantly olivine rheology which plunges into the mantle. With increasing pressure the strength increases until the slab is heated enough to be progressively weakened by increasing temperature. Therefore, the difference in stress before and after an earthquake (stress drop) increases with depth, as the material becomes stronger, reaches a maximum at about 100 km and decreases again with the decreasing strength. This has also been observed by Chung and Kanamori (1980), who found that stress drop can vary between 20 and 230 bar for depths between 100 and 220 km within a descending slab, consistent with the high stress drop value inferred for event 11.

For seismic sources, measurements show that the rupture velocity, v_r, is $\leq \beta$; representative estimates from laboratory simulations and seismogram analysis indicate $v_r \sim 2.5$ km s^{-1} for rupture along crustal faults. For the events presented in this study, v_r ranges between 0.60 β to 0.95 β. These values are precisely predicted by the dynamic models of Madariaga (1976) and Das and Kostrov (1988).

The effects of directivity are apparent on the broadband waveforms of event 11 (Fig. 6.14). The azimuthal variation of the direct *P*-wave pulse observed on the broadband records can be explained by a unilateral rupture propagation at the source toward the southwest. The two-dimensional finite source model of Savage (1966) produces variation in duration of *P*-waves when the fault plane is assumed to be elliptical, and the rupture, starting from one focus, propagates outward until it reaches the edge of the fault plane. This assumption produced waveforms that matched very well the observed records. The variation in duration could also be considered as a result of differences in attenuation along the different raypaths from the source to the recording stations. However, this would have the same effect on the reflected as well as the direct *P*-waves. Douglas *et al.* (1990) show evidence that downward fracture propagation has the effect of reducing the amplitude (and increasing the duration) of the surface reflections *pP* and *sP*, relative to

the direct *P*-wave. This is observed on the broadband seismograms of event 11 and supports the directivity explanation for the observed duration variation.

Taymaz (1992) reviewed the rupture characteristics of 13 shallow earthquakes of different magnitudes, tectonic settings and mechanisms. All 13 events broke the surface, had numerous aftershocks, and showed an emergent nature in the seismic moment release as a function of time. This is thought to be due to the unbroken barriers, the natural sites of stress concentration and the sources of aftershocks. If the barriers are completely broken there may not be aftershocks within the main-shock fault plane. Events 3 and 7 of this study have broken the surface and had a number of aftershocks. It is observed that these events exhibit an emergent character in the onset of the direct *P*-wave. Intermediate depth (185 km > depth > 30 km) events from the Hellenic and the Aleutian arc show more impulsive onsets. Taymaz *et al.* (1990) have also observed simple impulsive source time functions for some Hellenic trench events. The lack of aftershocks and absence of emergent seismic moment release in intermediate and deep focus earthquakes may be due to homogeneity of material strength along the plane of rupture (Taymaz, 1992).

7.4 SUMMARY

Source parameters obtained for the two groups of earthquakes studied here do not show any significant differences. Source orientation generally is associated with and results from the prevailing stress regime, which is mainly compressional in both regions. Simple two-dimensional finite sources were assumed in the body-wave modelling and they proved to be a very good approximation of the real earthquake source for events from both regions. The relationships between the various parameters show similar patterns. Seismic moment generally increases with earthquake size and source dimensions, and does not show any specific trend with depth. Complexity observed on seismograms for three events can be attributed to source complexity and/or path effects. To avoid over-correction for attenuation along the ray path, smaller values of t^* were preferred (0.2 - 0.3 s), except in cases where the low frequency content of the seismogram required higher t^* values (0.6 -1.0 s).

The only significant difference between the two arcs, identified from the events studied, is the different relationship of seismic moments compared to CMT results. Hellenic arc earthquakes have systematically lower seismic moments than the CMT solutions, whereas the Aleutian arc events have comparable seismic moments to CMT results. This could be due to different seismic ray paths (continental or oceanic) between the study areas and the recording stations.

In the next Chapter the overall conclusions of this study are presented.

CHAPTER 8

CONCLUSIONS

8.1 CONCLUSIONS

The aim of this thesis was to study the source properties of earthquakes in two subduction zones using global body-wave seismograms. Results from the two areas were to be compared between them as well as with results from other studies obtained using different methods. For this purpose a selection of moderate-sized earthquakes from the Hellenic and the Aleutian Island subduction zones was made. The use of the relative amplitude method for determining focal mechanisms, together with broadband waveform modelling, has enabled reliable source orientation, moment and stress drop calculations to be made. The results not only increase our knowledge about earthquake source properties but also add to our understanding of the earthquake nucleation process and the neotectonics of the two subduction zones under examination. The main conclusions are summarized below:

1. Broadband records deconvolved from short period seismograms for three Hellenic and five Aleutian moderate-sized earthquakes are in excellent agreement with recorded broadband seismograms within the frequency range of interest (0.05 to 10 Hz). The advantages of using high quality broadband data are immediately apparent. For example, onset polarities of all *P*-wave phases can be clearly seen on all such records.

2. The relative amplitude method which was used to determine the source orientations of the earthquakes studied put tight constraints on the fault plane solutions ($\leq \pm 5^{\circ}$ in general). This method makes use of the maximum information extracted from a seismogram and therefore, even in cases of few data, the compatible orientations occupied a small fraction of the total orientation space. In some cases nodal and null vector observations, that were not inserted in the computation of the focal mechanism, were reproduced accurately on the synthetic seismograms generated for the same solutions.

3. Significant differences between the focal mechanisms obtained here and those from other studies (CMT) were observed for a number of earthquakes, and explained.

4. A two-dimensional finite dislocation source model was preferred in this study because a point source approximation is not valid when the data include such short wavelengths (corresponding to about 5 s). Although the same model is simple compared to more recent complex dynamic models, this two-dimensional model proved to give a very good approximation of the real earthquake source. Synthetic seismograms, generated using this source model and assuming a layered velocity structure at the source and receiver areas, were in very good agreement with the observed records.

5. A sensitivity analysis of the source model to changes in different parameters showed that small changes in the model parameters affect the synthetic seismograms significantly. Therefore, model parameters can be well constrained. The parameters in order of increasing sensitivity are: radius, rupture velocity, stress drop and depth.

6. Source finiteness was observed for most events, and this allowed the discrimination between fault and auxiliary plane.

7. Accurate focal depths were calculated for most events. Surface reflected (*pP* and *sP*) phases were easily identifed on the broadband records and constrained the depths to $\leq \pm$ 2 km. Accurate focal depth measurement is very important when connections are made between the focal mechanism and the tectonic environment in which an earthquake occurs, and this cannot be achieved without proper analysis of surface reflections.

8. An elliptical source model with downgoing rupture propagation was resolved for one of the events (event 11). The directivity effect, or variation in duration and amplitude of the direct *P*-wave and its surface reflections with azimuth, was observed on all the broadband records of this event, and was successfully reproduced on the synthetics using the finite source model.

9. Stress drop values typical of interplate earthquakes (~ 30 bar) were found in both areas studied. For the Hellenic arc, these are larger than those found by other studies for back-arc events (~ 10 bar). In addition the increase of stress drop down to a certain depth, observed by others, is confirmed by the high stress drop value (213 $\pm$ 165 bar) found for the deepest earthquake of this study (event 11, depth = 183.5 $\pm$ 1 km).

10. Seismic moments for earthquakes in both study areas showed a general increase with magnitude and source dimensions. When compared to the global M_o - M_s

relationship, seismic moments estimated for the Hellenic arc earthquakes are lower than expected. On the other hand, Aleutian arc events do not show any specific pattern. This implies that surface-wave magnitudes of Hellenic arc earthquakes are systematically overestimated.

11. Hellenic arc earthquakes have systematically lower seismic moments than those estimated by the centroid moment tensor (CMT) method. Aleutian arc events however, are comparable to the CMT results. The frequency-dependence of moment does not appear to be the only reason for the discrepancy between the moments obtained here and those from the CMT method for the Hellenic arc, because it would have the same effects on the relationship between the two different moment estimations for the Aleutian arc events. However, path type (continental or oceanic) effects are probably, at least partly, responsible for the above discrepancy and agreement of moments respectively.

12. Thrust mechanisms, obtained here for most events studied, are consistent with the prevailing stress regime (compressional) of the Hellenic and the Aleutian Islands subduction zones. However, normal fault type mechanisms obtained for events 7 and 8 are in agreement with the active extensional regime at the back-arc area and the unbending stresses in the upper half of the subducted lithosphere respectively. The strike slip component that is present on the solutions of events 3 and 14 provides new evidence for the existence of the right lateral transform fault west of Cefallonia and the presence of the Amlia fracture zone respectively.

13. Clearly recorded body-waves provided sufficient information to determine uniquely, in most cases, the source mechanisms of the events studied here, by the relative amplitude method. Although the CMT method gives generally correct solutions for earthquakes with magnitude greater than 6, it can give unreliable results in cases of moderate-sized earthquakes ($m_b \sim 5.5$) or smaller, for which the available data are either poorer or fewer. It is therefore important, when such earthquakes are examined individually in order to obtain their focal mechanism, that a more reliable method such as the relative amplitude method, should be used. Errors in the fault mechanism could affect significantly the determination of the stress regime of a specific area and also the source parameter determination achieved by body-wave modelling.

8.2 SUGGESTIONS FOR FURTHER WORK

It can be concluded that detailed study of individual earthquakes is needed when studying the earthquake source characteristics, and this must include the frequency band within which the seismic source radiates most of its energy, and hence the maximum information. However, there is much more work that needs to be done in order to investigate all the possible factors that affect the rupture dynamics and the seismic wave propagation. The installation of more seismic arrays will provide high quality data for studing moderate-sized earthquakes. In addition, oceanic bottom stations will provide a better azimuthal coverage of the focal hemisphere for teleseismic studies. An increase of our knowledge of the 3-D earth structure will reduce the number of unknown parameters (uncertainties) involved in the seismic body-wave modelling. Finally, the deployment of a variety of methods and a wide range of data will enable differentiation between the real seismic source properties and the method biases.

BIBLIOGRAPHY

Abercrombie, R. E., 1991. Earthquake rupture dynamics and neotectonics in the Aegean area. *PhD Thesis*, University of Reading, U.K., 234pp.

Aki, K., 1966. Generation and propagation of G waves from the Niigata earthquake of June 16, 1964. *Bull. Earthquake Res. Inst., Tokyo Univ.*, **44**: 23-88.

Aki, K., 1967. Scaling law of seismic spectrum. *J. Geophys. Res.*, **72**: 1217-1231.

Aki, K. and Richards, P. G., 1980. Quantitative Seismology: Theory and Methods, (2 vols.), *W.H. Freeman*, San Francisco.

Anderson, H. and Jackson, J., 1987. Active tectonics of the Adriatic Region. *Geophys. J. R. astr. Soc.*, **91**: 937-983.

Angelier, J., Lyberis, N., Le Pichon, X. and Huchon, P., 1982. The tectonic development of the Hellenic Trench and Sea of Crete: a synthesis. *Tectonophysics*, **86**: 159-196.

Archuleta, R. J. and Brune, J. N., 1975. Surface strong motion associated with a stick-slip event in a foam rubber model of earthquakes. *Bull. Seism. Soc. Am.*, **65**: 1059-1071.

Beisser, M., Wyss, M. and Kind, R., 1990. Inversion of source parameters for subcrustal earthquakes in the Hellenic Arc. *Geophys. J. Int.*, **103**: 439-450.

Boatwright, J. and Choy, G.L., 1986. Teleseismic estimates of the energy radiated by shallow earthquakes. *J. Geophys. Res.*, **91**: 2095-2112.

Bott, M. H. P., 1982. The interior of the Earth. *Edward Arnold*, London, pp. 403.

Boyd, T. M. and Creager, K. C., 1991. The geometry of Aleutian subduction: three-dimensional seismic imaging. *J. Geophys. Res.*, **96**: 2267-2291.

Brune, J. N., 1970. Tectonic stress and the spectra of seismic shear waves from earthquakes. *J. Geophys. Res.*, **75**: 4997-5009.

Brune, J. N., 1971. Correction. *J. Geophys. Res.*, **76**: 5002.

Byrne, D.E., Davis, D.M., and Sykes, L.R., 1988. Loci and maximum size of thrust earthquakes and the mechanics of the shallow region of subduction zones. *Tectonics*, 7: 833-857.

Chen, A., Frohlich, C., and Latham, G., 1982. Seismicity of the forearc marginal wedge (accretionary prism). *J. Geophys. Res.* **87**: 3679-3690.

Choy, G. L. and Boatwright, J., 1981. The rupture characteristics of two deep earthquakes inferred from broadband GDSN data. *Bull. Seism. Soc. Am.*, **71**: 691-711.

Choy, G. L. and Boatwright, J., 1982. Broadband analysis of the extended foreshock sequence of the Miyiaki-Oki earthquake June 12, 1978. *Bull. Seism. Soc. Am.*, **72**: 2017-2036.

Choy, G. L. and Kind, R., 1987. Rupture complexity of a moderate sized (m_b 6.0) earthquake: broadband body wave analysis of the north Yemen earthquake of 13 December 1982. *Bull. Seism. Soc. Am.*, 77: 28-46.

Choy, G. L. and Dewey, J. W., 1988. Rupture process of an extended earthquake sequence: teleseismic analysis of the Chilean earthquake of March 3, 1985. *J. Geophys. Res.*, **93**: 1103-1118.

Christensen, D. H. and Ruff, L. J., 1986. Rupture process of the March 3, 1985 Chilean earthquake. *Geophys. Res. Lett.*, **13**: 721-724.

Citron, G. P., Kay, R. W., Kay, S. M., Snee, L. W. and Sutter, J. F., 1980. Tectonic significance of early Oligocene plutonism on Adak Island, central Aleutian Islands, Alaska. *Geology*, **8**: 375-379.

Creager, K. C. and Boyd, T. M., 1991. The geometry of Aleutian subduction: three-dimensional kinematic flow model. *J. Geophys. Res.*, **96**: 2293-2307.

Das, S., 1985. Application of dynamic shear crack models to the study of the earthquake faulting process. *Intl. J. Frac.*, **27**: 263-276.

Das, S. and Kostrov, B. V., 1987. On the numerical boundary method for three-dimensional dynamic shear crack problems. *J. Appl. Mech.*, **109**: 99-104.

Das, S. and Kostrov, B. V., 1988. An investigation of the complexity of the earthquake source time function using dynamic faulting models. *J. Geophys. Res.*, **93**: 8035-8050.

Davies, J. N. and House, L., 1979. Aleutian subduction zone seismicity, volcano-trench separation, and their relation to great thrust-type earthquakes. *J. Geophys. Res.*, **84**: 4583-4591.

Davison, F. C. and Scholz, C. H., 1985. Frequency-moment distribution of earthquakes in the Aleutian arc: a test of the characteristic earthquake model. *Bull. Seism. Soc. Am.*, **75**: 1349-1361.

Der, Z. A., Shumway, R. H. and Hirano, M. R., 1990. Time domain waveform inversion: a frequency domain view. How well do we need to match waveforms? *Bull. Seism. Soc. Am., submitted.*

Dewey, J. F. and Sengor, A. M. C., 1979. Aegean and surrounding regions: complex multiplate and continuum tectonics in a convergent zone. *Bull. Geol. Soc. Am.*, **90**: 84-92.

Douglas, A., Hudson, J. A. and Blamey, C., 1972. A quantitive evaluation of seismic signals at teleseismic distances - III. Computed *P* and Rayleigh wave seismograms. *Geophys. J. R. astr. Soc.*, **28**: 385-410.

Douglas, A., Young, J. B. and Hudson, J. A., 1974. Complex *P*-wave seismograms from simple earthquake sources. *Geophys. J. R. astr. Soc.*, **37**: 141-150.

Douglas, A., Hudson, J. A. and Barley, B. J., 1981. Complexity of short period P seismograms: what does scattering contribute? *AWRE Report No. o 3/81*, HMSO, London.

Douglas, A., Richardson, L. and Hutchins, M., 1990. Surface reflections and *S*-to-*P* conversions on *P* seismograms. *Geophys. J. Int.*, **100**: 303-314.

Dziewonski, A. M. and Woodhouse, J.H., 1983. An experiment in the systematic study of global seismicity: centroid-moment tensor solutions for 201 moderate and large earthquakes of 1981. *J. Geophys. Res.*, **88**: 3247-3271.

Dziewonski, A. M., Chou, T. A. and Woodhouse, J. H., 1981. Determination of earthquake source parameters from waveform data for studies of global and regional seismicity. J. Geophys. Res., **86**: 2825-28-52.

Dziewonski, A. M., Friedman, A. and Woodhouse, J. H., 1983b. Centroid-moment tensor solutions for January-March 1983. *Phys. Earth Planet. Inter.*, **33**: 71-75.

Dziewonski, A. M., Friedman, A., Giardini, D. and Woodhouse, J. H., 1983a. Global seismicity of 1982: centroid-moment tensor solutions for 308 earthquakes. *Phys. Earth Planet. Inter.*, **33**: 76-90.

Dziewonski, A. M., Franzen, J. E. and Woodhouse, J. H., 1984. Centroid-moment tensor solutions for July-September 1983. *Phys. Earth Planet. Inter.*, **34**: 1-8.

Dziewonski, A. M., Franzen, J. E. and Woodhouse, J. H., 1985a. Centroid-moment tensor solutions for April-June 1984. *Phys. Earth Planet. Inter.*, **37**: 87-96.

Dziewonski, A. M., Franzen, J. E. and Woodhouse, J. H., 1985b. Centroid-moment tensor solutions for July-September 1984. *Phys. Earth Planet. Inter.*, **38**: 203-213.

Dziewonski, A. M., Franzen, J. E. and Woodhouse, J. H., 1986a. Centroid-moment tensor solutions for July-September 1985. *Phys. Earth Planet. Inter.*, **42**: 205-214.

Dziewonski, A. M., Franzen, J. E. and Woodhouse, J. H., 1986b. Centroid-moment tensor solutions for October-December 1985. *Phys. Earth Planet. Inter.*, **43**: 185-195.

Dziewonski, A. M., Ekström, G., Franzen, J. E. and Woodhouse, J. H., 1987a. Centroid-moment tensor solutions for January-March 1986. *Phys. Earth Planet. Inter.*, **45**: 1-10.

Dziewonski, A. M., Ekström, G., Franzen, J. E. and Woodhouse, J. H., 1987b. Centroid-moment tensor solutions for July-September 1986. *Phys. Earth Planet. Inter.*, **46**: 305-315.

Dziewonski A. M., Ekström, G., Franzen, J. E. and Woodhouse, J. H., 1989. Global seismicity of 1982 and 1983: Additional centroid-moment tensor solutions for 553 earthquakes. *Phys. Earth Planet. Inter.*, **53**: 17-45.

Ekström, G. and Dziewonski, A. M., 1988. Evidence of bias in estimations of earthquake size. *Nature*, **332**: 319-323.

Ekström, G. and Engdahl, E. R., 1989. Earthquake source parameters and stress distribution in the Adak Island area of the central Aleutian Islands, Alaska. *J. Geophys. Res.*, **94**: 15499-15519.

Ekström, G. and England, P., 1989. Seismic strain rates in regions of distributed continental deformation. *J. Geophys Res.*, **94**: 10231-10257.

Engdahl, E. R., 1977. Seismicity and plate subduction in the central Aleutians. In *Island Arcs and Deep Sea Trenches and Back-arc Basins*. M. Ewing Ser. 1, ed. M. Talwani and W. Pittman, III. Washington, D.C.: American Geophysical Union. pp. 259-272.

Engdahl, E. R. and Scholz, C. H., 1977. A double Benioffzone beneath the central Aleutians: an unbending of the lithosphere. *Geophys. Res. Letts.*, **4**: 473-476.

Engdahl, E. R. and Billington, S., 1986. Focal depth determination of central Aleutian earthquakes. *Bull. Seism. Soc. Am.*, **76**: 77-93.

Engdahl, E. R. and Kind, R., 1986. Interpretation of broadband seismograms from central Aleutian earthquakes. *Annal. Geophys.*, **4**: 3233-3240.

Engdahl, E. R. and Gubbins, D., 1987. Simultaneous travel time inversion for earthquake location and subduction zone structure in the Central Aleutian Islands. *J. Geophys. Res.*, **92**: 13855-13862.

Engdahl, E. R., Billington, S. and Kisslinger, C., 1989. Teleseismically recorded seismicity before and after the May 7, 1986, Andreanof Islands, Alaska, earthquake. *J. Geophys. Res.*, **94**: 15481-15498.

Engebretson, D. C., Cox, A. and Gordon, R. G., 1986. Relative motion between oceanic and continental plates in the Pacific Basin. *Spec. Publ. 206*, Geol. Soc. Am., Boulder, Colo.

Fitch, T. J., 1972. Plate convergence, transcurrent faults, and internal deformation adjacent to southeast Asia and the western Pacific. *J. Geophys. Res.*, **77**: 4432-4460.

Gates, G. and Gibson, W., 1956. Interpretation of the configuration of the Aleutian Ridge. *Geol. Soc. Am. Bull.*, **67**: 127-146.

Geist, E. L., Childs, J. R. and Scholl, D. W., 1987. Evolution and petroleum geology of the Amlia and Amutka intra-arc summit basins, Aleutian Ridge. *Mar. Pet. Geol.*, **4**: 333-352.

Geist, E. L., Childs, J. R. and Scholl, D. W., 1988. The origin of summit basins of the Aleutian ridge: implications for block rotation on an arc massif. *Tectonics*, **7**: 327-341.

Green, H. W., and Burnley, P. C., 1989. The mechanism of failure responsible for deep-focus earthquakes. *Nature*, **341**: 733-737.

Grow, J. A., 1973. Crustal and upper mantle structure of the Central Aleutian Arc. *Geol. Soc. Am. Bull.*, **84**: 2169-2192.

Hartzell, S., 1980. Faulting process of the May 17, Gazli, USSR earthquake. *Bull. seism. Soc. Am.*, **70**: 1715-1736.

Harvey, D. and Choy, G. L., 1982. Broadband deconvolution of GDSN data. *Geophys. J. R. astr. Soc.*, **69**: 659-66

Hatzfeld, D., Pedotti, G., Hatzidimitriou, P., Panagiotopoulos, D., Scordilis, M., Drakopoulos, I., Makropoulos, K., Delibasis, N., Latousakis, I., Baskoutas, J. and Frogneux, M., 1989. The Hellenic subduction beneath the Peloponnesus: first results of a micro-earthquake study. *Earth and Planet. Sci. Letts.*, **93**: 283-291.

Hirosawa, T. and Stauder, W., 1965. On the seismic waves from a finite moving source. *Bull. Seismol. Soc. Amer.*, **55**: 1811-1842.

Hobbs, B. E. and Ord, A., 1988. Plastic instabilities: Implications for the origin of intermediate and deep focus earthquakes. *J. Geophys. Res.*, **93**: 10521-10540.

Hong, T. L. and Fujita, K., 1981. Modelling the depth phases and source processes of some central Aleutian earthquakes. *Earth Plan. Sci. Let.*, **53**: 333-342.

House, L. S. and Jacob, K. H., 1982. Thermal stresses in subducting lithosphere can explain double seismic zones. *Nature*, **295**: 587-589.

House, L. S. and Jacob, K. H., 1983. Earthquakes, plate subduction and stress reversals in the eastern Aleutian arc. *J. Geophys. Res.*, **88**: 9347-9373.

Hudson, J. A., 1969a. A quantitive evaluation of seismic signals at teleseismic distances - I. Radiation from point sources. *Geophys. J. R. astr. Soc.*, **18**: 233-249.

Hudson, J. A., 1969b. A quantitive evaluation of seismic signals at teleseismic distances - II. Body waves and surface waves from an extended source. *Geophys. J. R. astr. Soc.*, **18**: 353-370.

Hudson, J. A., Pearce, R. G. and Rogers, R. M., 1989. Source type plot for inversion of the moment tensor. *J. Geophys. Res.*, **94**: 765-774.

Isacks, B. and Molnar, P., 1971. Distribution of stresses in the descending lithosphere from a global survey of focal mechanisms of mantle earthquakes. *Rev. Geophys.*, **9**: 103-174.

Jackson, J. A. and McKenzie, D. P., 1988. The relationship between plate motions and seismic moment tensors, and the rates of active deformation in the Mediterranean and Middle East. *Geophys. J.*, **93**: 45-73.

Jarrard, R. D., 1986. Relations between subduction parameters. *Rev. Geophys.*, **24**: 217-284.

Kanamori, H., 1977. The energy release in great earthquakes. *J. Geophys. Res.*, **82**: 2981-2987.

Kanamori, H. and Anderson, D.L., 1975. Theoretical basis of some empirical relations in seismology. *Bull. Seism. Soc. Am.*, **65**: 1073-1095.

Keilis-Borok, V., 1959. On estimation of the displacement in an earthquake source and of source dimensions. *Ann. Geof., (Rome)*, **12**: 205-214.

Kiratzi, A. A. and Langston, C. A., 1991. Moment tensor inversion of the 1983 January 17 Kefallinia event of the Ionian Islands (Greece). *Geophys. J. Int.*, **105**: 529-535.

Kiratzi, A. A., Karakaisis, G. F., Papadimitriou, E. E. and Papazachos, B. C., 1985. Seismic source-parameter relations for earthquakes in Greece. *Pageoph*, **123**: 27-41.

Kirby, S., 1987. Localized polymorphic phase transformations in high pressure faults and applications to the physical mechanism of deep earthquakes. *J. Geophys. Res.* **92**: 13789-13800.

Kissel, C. and Laj, C., 1988. The Tertiary geodynamical evolution of the Aegean Arc: a paleomagnetic reconstruction. *Tectonophysics.*, **146**: 183-201.

Kondopoulou, D. P., Papadopoulos, G. A. and Pavlides, S. B., 1985. A study of deep seismotectonics in the Hellenic arc. *Bol. Geofisica Teorica et Appplicata*, 27: 197-207.

Koto, B., 1893. On the cause of the great earthquakes in central Japan, 1981. *Tokyo, Imperial University College of Science Journal*, **5**: 295.

LaForge, R. and Engdahl, E. R., 1979. Tectonic implications of seismicity in the Adak Canyon region, Central Aleutians. *Bull. Seism. Soc. Am.*, **69**: 1515-1532.

Langston, C. A. and Helmberger, D. V., 1975. A procedure for modelling shallow dislocation sources. *Geophys. J. R. astr. Soc.*, **42**: 117-130.

Le Pichon, X. and Angelier, J., 1979. The Hellenic arc and trench system: a key to the neotectonic evolution of the eastern Mediterranean area. *Tectonophysics*, **60**: 1-42.

Le Pichon, X. and Angelier, J., 1981. The Aegean Sea. *Phil. Trans. R. Soc. Lond.*, **A300**: 357-372.

Ligdas, C. N., Main. I. G. and Adams, R. D., 1990. 3-D structure of the lithosphere in the Aegean region. *Geophys. J. Int.*, **102**: 219-229.

Lonsdale, P. and Smith, D., 1986. Kula Plate not kula. *EOS Trans. AGU*, **67**: 1199.

Lundgren, P. R., Okal, E. A. and Wiens, D. A., 1989. Rupyure characteristics of the 1982 Tonga and 1986 Kermadec earthquakes. *J. Geophys. Res.*, **94**: 15521-15539.

Lyon-Caen, H., Armijo, R., Drakopoulos, J., Baskoutass, J., Delibasis, N., Gaulon, R., Kouskouna, V., Latoussakis, J., Makropoulos, K., Papadimitriou, P., Papanastrassiou, D. and Pedotti, G., 1988. The 1986 Kalamata (south Peleponnesus) earthquake: detailed study of a normal fault, evidence for east-west extension in the Hellenic Arc. *J. Geophys. Res.*, **93**: 14967-15000.

Madariaga, R., 1976. Dynamics of an expanding circular fault. *Bull. Seism. Soc. Am.*, **66**: 636-666.

Main, I. G. and Burton, P. W., 1989. Seismotectonics and the earthquake frequency-magnitude distribution in the Aegean area. *Geophys. J. Int.*, **98**, 575-586.

Main, I. G. and Burton, P. W., 1990. Moment-magnitude scaling in the Aegean area. *Tectonophysics*, **179**: 273-285.

Makris, J., 1976. Crustal structure of the Central Aegean Sea and the islands of Evia and Crete, obtained by refractional seismic experiments. *J. Geophys.* **42**: 329-341.

Makris, J., 1977. A dynamic model of the Hellenic arc deduced from geophysical data. *Tectonophysics*, **36**: 339-346.

Makris, J., 1978a. Some geophysical considerations of the geodynamic situation in Greece. *Tectonophysics*, **46**: 251-268.

Makris, J., 1978b. The crust and upper mantle of the Aegean region from deep seismic soundings. *Tectonophysics*, **46**: 269-284.

Makropoulos, K. C. and Burton, P. W., 1984. Greek tectonics and seismicity. *Tectonophysics*, **106**: 275-304.

Marlow, M. S., Scholl, D. W., Buffington, E. C. and Alpha, T. R., 1973. Tectonic history of the central Aleutian Arc. *Geol. Soc. Am. Bull.*, **84**: 1555-1574.

Marshall, P. D. and Basham, P. W., 1973. Rayleigh wave magnitude scale M_S. *Pur. Appl. Geophys.*, **103**: 406-414.

McGarr, A., Green, R. W. E. and Spottiswoode, S. M., 1981. Strong ground motion of mine tremors: some implications for near source ground motion parameters. *Bull. Seism. Soc. Am.*, **71**: 295-319.

McKenzie, D. P., 1972. Active tectonics of the Mediterranean region. *Geophys. J. R. astr. Soc.*, **30**: 109-185.

McKenzie, D. P., 1978. Active tectonics of the Alpine-Himalayan belt: the Aegean Sea and surrounding regions. *Geophys. J. R. astr. Soc.*, **55**: 217-254.

Mercier, J. L., Carey, E., Philip, H. R. and Sorel, D., 1976. La neotectonique plio-quaternaire de l'arc egeen externe et de la Mer egeen et ses relations avec seismicite. *Bull. Soc. geol. France*, **18**: 159-176.

Monfret, T. and Romanowicz, B., 1986. Importance of on scale observations of first arriving Rayleigh wave trains for source studies: Example of the Chilean event of March 3, 1985, observed in the Geoscope and IDA networks. *Geophys. Res. Lett.*, **13**: 1015-1018.

Morris, A., 1990. Palaeomagnetic studies of the Mesozoic-Tertiary tectonic evolution of Cyprus, Turkey and Greece. *PhD Thesis*, University of Edinburgh, 341pp.

Nabelek, J., 1984. Determination of earthquake source parameters from inversion of body waves. *PhD Thesis*, Mass. Inst. Technol., Cambridge, U.S.A., 360pp.

Nabelek, J., 1985. Geometry and mechanism of faulting of the 1980 El Asnam, Algeria earthquake from inversion of teleseismic body waves and comparison with field observations. *J. Geophys. Res.*, **90**: 12713-12728.

Papazachos, B. C., 1990. Seismicity of the Aegean and surrounding area. *Tectonophysics*, **178**: 287-308.

Papazachos, B. C. and Comninakis, P. E., 1971. Geophysical and tectonic features in the Aegean arc. *J. Geophys. Res.*, **76**: 8517-8533.

Papazachos, B. C., Kiratzi, A. and Papadimitriou, E., 1991. Regional focal mechanisms for earthquakes in the Aegean area. *Pageoph.*, **136**: *in press.*

Papazachos, B. C., Kiratzi, A. A., Hatzidimitriou, P. M. and Rocca, A. C., 1984. Seismic faults in the Aegean area. *Tectonophysics*, **106**: 71-85.

Papazachos, B. C., Kiratzi, A., Hatzidimitriou, P. and Karacostas, B., 1986. Seismotectonic properties of the Aegean area that restrict valid geodynamic models. Wegener/Medlas Conf. Athens, May 14-16, 1986, 1-20.

Papazachos, B. C., Kiratzi, A. A., Karacostas, B., Panagiotopoulos, D., Scordilis, E. and Mountrakis, D. M., 1988. Surface fault traces, fault plane solution and spatial distribution of the aftershocks of the September 13, 1986, earthquake of Kalamata (southern Greece). *Pageoph.*, **126**: 55-68.

Pearce, R. G., 1977. Fault plane solutions using relative amplitudes of *P* and *pP*. Geophys. J. R. astr. Soc., 50: 381-394.

Pearce, R. G., 1979. Earthquake focal mechanisms from relative amplitudes of *P*, *pP*, *sP*: method and computer program. *AWRE Report* No. O41/79, HMSO publication, London, England.

Pearce, R. G., 1980. Fault plane solutions using relative amplitudes of P and surface reflections: further studies. Geophys. *J. R. astr. Soc.*, **60**: 459-487.

Pearce, R. G. and Rogers, R. M., 1989. Determination of earthquake moment tensors from teleseismic relative amplitude observations. *J. Geophys. Res.*, **94**: 775-786.

Peterson, E. T. and Seno, T., 1984. Factors affecting seismic moment release rates in subduction zones. *J. Geophys. Res.*, **89**: 10233-10248.

Pilant, W. L., 1979. Elastic waves in the earth. *Elsevier*, Amsterdam, The Netherlands.

Reid, H. F., 1911. The elastic rebound theory of earthquakes. *Bull. Dep. Geol. Univ. Calif.*, **6**: 412-444.

Riedesel, M. A. and Jordan, T. H., 1985. Multiple band estimation of moment tensors at low frequencies and their uncertainties. Abstract, IASPEI General Assembly, 1985.

Ritsema, A. R., 1974. The earthquake mechanisms of the Balkan region. *Sci. Rep. R. Neth. Meteorol. Inst.* De Bilt, *74-4*: 1-36.

Rogers, R. M. and Pearce, R. G., 1987. Application of the Relative Amplitude Moment Tensor Program to three intermediate-depth IASPEI earthquakes. *Phys. Earth Planet. Ints.*, **47**: 93-106.

Savage, J. C., 1966. Radiation from a realistic model of faulting. *Bull. Seism. Soc. Am.*, **56**: 577-592.

Scordilis, E. M., Karakaisis, B. G., Panagiotopoulos, D. G., Comninakis, P. E. and Papazachos, B. C., 1985. Evidence for transform faulting in the Ionian Sea: The Cephalonia Island earthquake sequence of 1983. *Pageoph*, **123**: 388-397.

Silver, P. G. and Jordan, T. H., 1983. Total-amount spectra of fourteen large earthquakes. *J. Geophys. Res.*, **88**: 3273-3293.

Sipkin, S., 1982. Estimation of earthquake source parameters by the inversion of waveform data: synthetic waveforms. *Phys. Earth Planet. Ints.*, **30**: 242-259.

Soufleris, C. N. and Stewart, G. S., 1981. A source study of the Thessaloniki (northern Greece) 1978 earthquake sequence. *Geophys. J. R. astr. Soc.*, **67**: 343-358.

Soufleris, C., Jackson, J. A., King, G. C. P., Spencer, C. P. and Scholz, C. H., 1982. The 1978 earthquake sequence near Thessaloniki (northern Greece). *Geophys. J. R. astr. Soc.*, **68**: 429-458.

Spakman, W., 1990. Tomographic images of the upper mantle below central Europe and the Mediterranean. *Terra Nova*, **2**: 542-553.

Spence, W., 1977. The Aleutian arc: tectonic blocks, episodic subductionary strain diffusion, and magma generation. *J. Geophys. Res.*, **82**: 213-230.

Spence, W., 1987. Slab pull and the seismotectonics of subducting lithosphere. *Revs. Geophys.*, **25**: 55-69.

Spencer, C. P. and Engdahl, E. R., 1983. A joint hypocentre location and velocity inversion technique applied to the central Aleutians. *Geophys. J. R. astr. Soc.*, 72: 399-415.

Stavrakakis, G. N., Tselentis, A. G. and Drakopoulos, J., 1987. Iterative deconvolution of teleseismic *P* waves from the Thessaloniki (N. Greece) earthquake of June 20, 1978. *Pur. appl. Geophys.*, **124**: 1039-1050.

Stewart, R. C. and Douglas, A., 1983. Seismograms from phaseless seismographs. *Geophys. J. R. astr. Soc.*, 72: 517-521.

Stimpson, I. G., 1987. The relative amplitude moment tensor method applied to the IASPEI deep earthquakes. *Phys. Earth Planet. Ints.*, **47**: 150-158.

Stimpson, I. G. and Pearce, R. G., 1987. Moment tensors and source processes of three deep Sea of Okhotsk earthquakes. *Phys. Earth Planet. Ints.*, **47**: 107-124.

Taber, J. J., Billington, S. and Engdahl, E. R., 1989. Seismicity of the Aleutian Arc. in: D. B. Slemmons *et al.* (eds.), 'Neotectonics of North America', Geol. Soc. Am., Boulder, Colo., *in press*.

Taymaz, T., 1992. Observations on source time functions of earthquakes obtained from inversion of teleseismic body waveforms. *Geophys. J. Int.*, **180**: 273-280.

Taymaz, T., Jackson, J. and Westaway, R., 1990. Earthquake mechanisms in the Hellenic Trench near Crete. *Geophys. J. Int.*, **102**: 695-731.

Taymaz, T., Jackson, J. and McKenzie, D., 1991. Active tectonics of the north and central Aegean Sea. *Geophys. J. Int.*, **106**: 433-490.

Tselentis, G. A., Stavrakakis, G., Makropoulos, K., Latousakis, J. and Drakopoulos, J., 1988. Seismic moments of earthquakes at the western Hellenic arc and their application to the seismic hazard of the area. *Tectonophysics.*, **148**: 73-82.

Vaccari, F., Suhadolc, P. and Panza, G. F., 1990. Irpinia, Italy, 1980 earthquake: waveform modelling of strong motion data. *Geophys. J. Int.*, **101**: 631-647.

Wdowinski, S., O'Connell, R. J. and England, P., 1989. A continuum model of continental deformation above subduction zones. Application to the Andes and the Aegean. *J. Geophys. Res.*, **94**: 10331-10346.

Wiens, D. A., 1987. Effects of near source bathymetry on teleseismic *P* waveforms. *Geophys. Res. Lett.*, **14**: 761-764.

Wiens, D. A., 1989. Bathymetric effects on body waveforms from shallow subduction zone earthquakes and application to seismic processes in the Kurile trench. *J. Geophys. Res.*, **94**: 2955-2972.

Woodhouse, J. H. and Dziewonski, A. M., 1984. Mapping the upper mantle: three dimensional modelling of Earth structure by inversion of seismic waveforms. *J. Geophys. Res.*, **89**: 5953-5986.

Wyss, M., 1970. Stress estimates for south American shallow and deep earthquakes. *J. Geophys. Res.*, **75**: 1529-1544. 1970.

Yamamoto, J. and Mitchell, B. J., 1988. Rupture mechanics of complex earthquakes in Southern Mexico. *Tectonophysics.*, **154**: 25-40.

Yoshii, T., 1979. A detailed cross-section of the deep seismic zone beneath northeastern Honshu, Japan. *Tectonophysics*, **55**: 349-360.

APPENDIX A

Location of seismic stations used in the present study

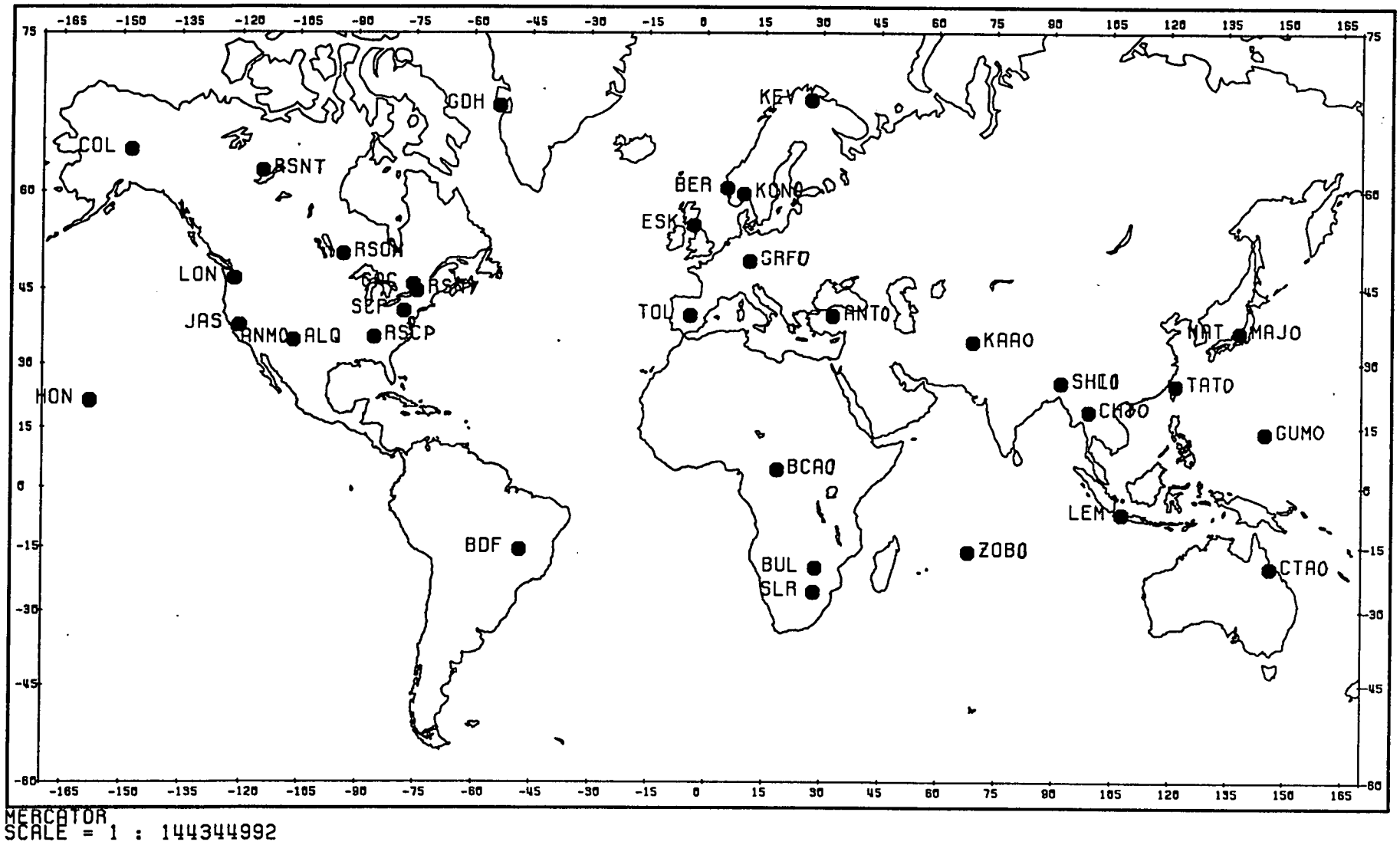

MERCATOR
SCALE = 1 : 144344992

Figure A 1. Seismic stations used in the present study.

Station	Type	Latitude (°)	Longitude (°)
ALQ	DWWSSN	34.94N	106.46W
ANMO	SRO	34.95N	106.46W
ANTO	SRO	39.86N	32.79E
BCAO	SRO	4.43N	18.54E
BDF	DWWSSN	15.66S	47.90W
BER	DWWSSN	60.37N	5.33E
BUL	WWSSN	20.14S	28.61E
CHTO	SRO	18.79N	98.98E
COL	DWWSSN	64.89N	147.79W
CTAO	ASRO	20.09S	146.25E
ESK	WWSSN	55.32N	3.21W
GAC	SRO	45.70N	75.48W
GDH	DWWSSN	69.25N	53.53W
GRFO	SRO	49.69N	11.22E
GUMO	SRO	13.59N	144.87E
HON	DWWSSN	21.32N	158.00W
JAS	DWWSSN	37.93N	120.42W
KAAO	SRO	34.54N	69.04E
KEV	DWWSSN	69.76N	27.01E
KONO	ASRO	59.65N	9.59E
LEM	DWWSSN	6.83S	107.62E
LON	DWWSSN	46.75N	121.81W
MAJO	ASRO	36.54N	138.21E
MAT	WWSSN	36.54N	138.20E
RSCP	RSTN	35.58N	85.56W
RSNT	RSTN	62.48N	114.59W
RSNY	RSTN	44.55N	74.53W
RSON	RSTN	50.86N	93.70W
SCP	DWWSSN	40.79N	77.86W
SHIO	SRO	25.57N	91.88E
SHL	WWSSN	25.57N	91.88E
SLR	DWWSSN	25.73S	28.28E
TATO	SRO	24.98N	121.49E
TOL	DWWSSN	39.88N	4.05W
ZOBO	ASRO	16.27S	68.13W

APPENDIX B

Data used in the determination of focal mechanisms

10 March 1981

Latitude 39.48000
Longitude 20.69000

	P			pP			sP			S(N)			S(E)		
	Pol	Min	Max	Pol	Min	Max	Pol	Min	Max	Pol	Min	Max	Pol	Min	Max
BCAO	+	1.	100.0	U	1.	100.0				-	1.	100.0	+	1.	100.0
KAAO	+	1.	100.0	U	1.	100.0				U	1.	100.0	O	1.	100.0
CHTO	+	1.	100.0	U	1.	100.0									
SCP	+	1.	100.0	U	1.	100.0									

16 NOV 82 ALBANIA

Latitude 40.82000
Longitude 19.58000

	P			pP			sP			S(N)			S(E)		
	Pol	Min	Max	Pol	Min	Max	Pol	Min	Max	Pol	Min	Max	Pol	Min	Max
KEV										U	1.	100.0	S	1.	100.0
BCAO										U	1.	100.0	O	1.	100.0
GAC										U	1.	100.0	O	1.	100.0
COL	+	1.	100.0	U	1.	100.0				-	1.	100.0	+	1.	100.0

17jan83 Ionian sea

Latitude 38.07000
Longitude 20.25000

	P			pP			sP			S(N)			S(E)		
	Pol	Min	Max	Pol	Min	Max	Pol	Min	Max	Pol	Min	Max	Pol	Min	Max
RSCP	+	1.	100.0	U	1.	100.0									
BUL	-	1.	100.0	U	1.	100.0									
COL	+	1.	100.0	U	1.	100.0				+	1.	100.0	-	1.	100.0
ESK	+	1.	100.0	U	1.	100.0									
KEV	+	1.	100.0	U	1.	100.0									
MAT	+	1.	100.0	U	1.	100.0									
SHL	+	1.	100.0	U	1.	100.0									
MAJO	+	1.	100.0	U	1.	100.0				+	1.	100.0	-	0.	100.0
LON	+	1.	100.0	U	1.	100.0				U	1.	100.0	O	1.	100.0
SCP	+	1.	100.0	U	1.	100.0				+	1.	100.0	-	1.	100.0
TATO	+	1.	100.0	U	1.	100.0				U	1.	100.0	S	1.	100.0
BDF	-	1.	100.0	U	1.	100.0				U	3.	300.0	S	1.	50.0
ZOBO	-	1.	100.0	U	1.	100.0									
RSNT	+	1.	100.0	U	1.	100.0				+	1.	100.0	-	1.	100.0
RSON	+	1.	100.0	U	1.	100.0				+	1.	100.0	-	1.	100.0
RSNY	+	1.	100.0	U	1.	100.0				+	1.	100.0	-	1.	100.0
ANMO										U	1.	100.0	O	1.	100.0
LEM	+	1.	100.0	U	1.	100.0				U	1.	150.0	S	1.	100.0
BCAO	-	1.	100.0	U	1.	100.0				-	1.	100.0	+	2.	200.0
GAC										+	3.	300.0	-	1.	100.0

19march 83 S.Crete

Latitude 35.02000
Longitude 25.32000

	P			pP			sP			S(N)			S(E)		
	Pol	Min	Max	Pol	Min	Max	Pol	Min	Max	Pol	Min	Max	Pol	Min	Max
KEV	+	2.	3.00	U	0.	0.50	U	0.	0.50	U	5.	10.0	1	1.	5.00
SCP	+	2.	3.00	U	0.	1.00	U	0.	1.00						
RSON	+	2.	3.00	U	0.	1.00	U	0.	1.00	+	1.	10.0	-	20	100.0
COL	+	2.	3.00	U	0.	0.80	U	0.	0.80						
MAJO	+	1.	2.00	U	0.	0.40				U	1.	10.0	U	20	100.0
LON	+	2.	3.00	U	0.	1.00	U	0.	1.00						
GAC										+	1.	100.0	-	1.	100.0
LEM	+	1.	10.0	U	1.	10.0									
BUL	-	1.	10.0	U	11	15.0									
TATO										U	1.	10.0	+	1.	10.0

21 june 1984 SW of Crete

Latitude 35.36000
Longitude 23.24000

	P			pP			sP			S(N)			S(E)		
	Pol	Min	Max	Pol	Min	Max	Pol	Min	Max	Pol	Min	Max	Pol	Min	Max
RSON										+	1.	100.0	-	1.	100.0
RSNT										+	1.	100.0	-	1.	100.0
CHTO										U	1.	100.0	S	1.	100.0
GAC										+	1.	100.0	-	1.	100.0
RSNY													-	1.	100.0
COL										U	1.	100.0	O	1.	100.0
RSCP										+	1.	100.0	-	1.	100.0
MAJO										U	1.	100.0	O	1.	100.0
BOCO										U	1.	100.0	O	1.	100.0
BDF										U	1.	100.0	S	1.	100.0
SLR										-	1.	100.0	+	1.	100.0
LON										U	1.	100.0	O	1.	100.0
ANMO										U	1.	100.0	O	1.	100.0

27 sep 1985 SE of Crete

Latitude 34.50000
Longitude 26.55000

	P			pP			sP			S(N)			S(E)		
	Pol	Min	Max	Pol	Min	Max	Pol	Min	Max	Pol	Min	Max	Pol	Min	Max
KEV	+	1.	100.0	U	1.	100.0									
CHTO	-	1.	100.0	U	1.	100.0									
TATO										U	1.	100.0	+	1.	100.0
LON	+	1.	100.0	U	1.	100.0									
RSON	-	1.	100.0	U	1.	100.0									
RSNT	-	1.	100.0	U	1.	100.0									

13 SEPTEMBER 1986 Kalamata

Latitude 37.03000
Longitude 22.20000

	P			pP			sP			S(N)			S(E)		
	Pol	Min	Max	Pol	Min	Max	Pol	Min	Max	Pol	Min	Max	Pol	Min	Max
BCAO	-	1.	100.0	U	1.	100.0				+	1.	100.0	+	1.	100.0
GDH	-	1.	100.0	U	1.	100.0				-	1.	100.0	+	1.	100.0
SLR										U	1.	100.0	S	1.	100.0
CHTO	-	1.	100.0	+	1.	100.0	+	1.	100.0	+	15	20.0	-	30	40.0
RSON	-	1.	100.0	U	1.	100.0				U	1.	100.0	S	1.	100.0
COL	-	1.	100.0	U	1.	100.0				+	1.	100.0	U	1.	100.0
TATO	-	1.	100.0	U	1.	100.0				U	1.	100.0			
LON	-	1.	100.0	U	1.	100.0									
BOCO										U	1.	100.0	S	1.	100.0
MAJO	-	1.	100.0	U	1.	100.0				+	10	100.0	-	18	100.0

3 May 80 Aleutian Islands

Latitude 51.21000
Longitude 173.64999

	P			pP			sP			S(N)			S(E)		
	Pol	Min	Max	Pol	Min	Max	Pol	Min	Max	Pol	Min	Max	Pol	Min	Max
MAJO	-	1.	100.0	+	1.	100.0				+	10.	12.00	+	18.	22.00
GUMO										U	100	200.0	S	50.	80.00
ANMO	-	1.	100.0	+	1.	100.0	+	1.	100.0	+	1.	100.0	-	1.	100.0
SHIO	-	12	18.00	+	20	30.00	U	8	10.0	+	1.	100.0	+	1.	100.0
CHTO	-	1.	100.0	+	1.	100.0				+	1.	100.0	+	1.	100.0
KONO	-	1.	100.0	+	1.	100.0	+	1.	100.0	+	1.	100.0	-	1.	100.0
KAAO	-	1.	100.0	U	1.	100.0									
CTAO										U	120	16.00	S	3.0	4.000
GRFO	-	1.	120.0	+	1.	80.0	+	1.	100.0	+	1.	100.0	-	1.	100.0

21 November 1980 Aleutian Islands

Latitude 51.78000
Longitude -176.64999

	P			pP			sP			S(N)			S(E)		
	Pol	Min	Max	Pol	Min	Max	Pol	Min	Max	Pol	Min	Max	Pol	Min	Max
MAJO	+	60	100.0	U	1.	20.00				U	10	12.0	S	10	22.0
JAS	+	1.	100.0	U	1.	100.0				U	1.	100.0	+	1.	100.0
ANMO	+	1.	100.0	-	1.	100.0				U	100	12.0	+	100	32.0
CHTO	+	50	100.0	-	1.	30.00				U	1.	100.0	S	1.	100.0
KAAO	+	60	100.0	-	1.	30.00				U	180	22.0	S	10	18.0
CTAO	+	50	100.0	-	1.	20.0				-	10	100.0			
GUMO										S	10	12.0	-	10	22.0
TATO										U	1.	100.0	S	1.	100.0

01july1982 Aleutian Islands

Latitude 51.39000
Longitude -179.94099

	P			pP			sP			S(N)			S(E)		
	Pol	Min	Max	Pol	Min	Max	Pol	Min	Max	Pol	Min	Max	Pol	Min	Max
MAJO	+	1.	100.0	U	1.	100.0				U	1.	100.0	S	1.	100.0
LON	+	1.	100.0	U	1.	100.0				+	1.	100.0	+	1.	100.0
GUMO	+	1.	100.0	U	1.	100.0				U	1.	100.0	S	1.	100.0
TATO										U	1.	100.0	O	1.	100.0
ANMO	+	1.	100.0	U	1.	100.0				U	1.	100.0	+	1.	100.0
ALQ	+	1.	100.0	U	1.	100.0				U	1.	100.0	+	1.	100.0
KEV	+	1.	100.0	U	1.	100.0				U	1.	100.0	+	1.	100.0
GAC	+	1.	100.0	U	1.	100.0				U	1.	100.0	+	1.	100.0
SCP	+	1.	100.0	U	1.	100.0				+	1.	100.0			
BER	+	1.	100.0	U	1.	100.0									
KONO	+	1.	100.0	U	1.	100.0				U	1.	100.0	+	1.	100.0
CTAO	+	1.	100.0	U	1.	100.0				-	1.	100.0	-	1.	100.0
GRFO	+	1.	100.0	U	1.	100.0				U	1.	100.0	+	1.	100.0
TOL	+	1.	100.0	U	1.	100.0									

24july1983

Latitude 53.91000
Longitude 158.36000

	P			pP			sP			S(N)			S(E)		
	Pol	Min	Max	Pol	Min	Max	Pol	Min	Max	Pol	Min	Max	Pol	Min	Max
TATO										-	1.	100.0	+	1.	100.0
RSNT										-	1.	100.0	-	1.	100.0
LON	+	1.	100.0	U	1.	100.0				-	1.	100.0	-	1.	100.0
KEV	-	1.	100.0	U	1.	100.0				-	1.	100.0	-	1.	100.0
JAS	+	1.	100.0	-	1.	100.0				-	1.	100.0	-	1.	100.0
RSON	+	1.	100.0	-	1.	100.0				-	1.	100.0	-	1.	100.0
RSSD	+	1.	100.0	-	1.	100.0				-	1.	100.0	-	1.	100.0
BER	-	1.	100.0	-	1.	100.0	+	1.	100.0	-	1.	10.00	-	1.	21.00
KONO	-	1.	100.0	-	1.	100.0	+	1.	100.0	-	1.	12.0	-	1.	25.0
ANMO	+	1.	100.0	U	1.	100.0				-	1.	10.0	-	1.	25.0
GAC										-	10	100.0	-	10	100.0
RSNY	+	1.	100.0	U	1.	100.0				-	1.0	100.0	-	1.	100.0
GRFO	-	1.	100.0	-	1.	100.0	+	1.	100.0	-	10	20.00	-	10	20.00
LEM										-	10	20.00	+	10	30.00
SCP	+	1.	100.0	-	1.	100.0				-	1.	100.0	-	1.	100.0
CTAO	+	10	100.0	U	1.	10.00	U	1.	5.00	+	10	100.0	+	10	100.0
RSCP										-	1.	100.0	-	1.	100.0
TOL	-	1.	100.0	-	1.	100.0	+	1.	100.0	U	1.	100.0	S	1.	100.0

23 Sept 84 No25 Aleutian Islands

Latitude 53.56000
Longitude -165.41000

	P			pP			sP			S(N)			S(E)		
	Pol	Min	Max	Pol	Min	Max	Pol	Min	Max	Pol	Min	Max	Pol	Min	Max
MAJO										U	1.	100.00	S	1.	100.00
GUMO										U	1.0	100.0	-	1.0	100.0
ANMO										-	1.	100.0	+	1.	100.0
CHTO	+	1.	100.0	U	1.	100.0				-	1.	100.0	-	1.	100.0
CTAO	+	1.	100.0	U	1.	100.0				U	1.	100.0	-	1.	100.0
GRFO	+	1.	100.0	U	1.	100.0									
KONO	+	1.	100.0	U	1.	100.0									
TATO										U	1.	100.0	-	1.	100.0
SCP	+	1.	100.0	U	1.	100.0									
ANTO	+	1.	100.0	U	1.	100.0				+	1.	100.0	+	1.	100.0

09oct1985 Aleutian Islands

Latitude 54.72000
Longitude -159.64000

	P			pP			sP			S(N)			S(E)		
	Pol	Min	Max	Pol	Min	Max	Pol	Min	Max	Pol	Min	Max	Pol	Min	Max
HON	-	1.	100.0	U	1.	100.0				-	7.	70.00	-	4.	40.00
RSON										+	1.	100.0	+	1.	100.0
ANMO	-	1.	10.0	-	3.	30.0	+	2.	20.0	U	1.	10.0	+	3.	30.00
GDH	+	1.	100.0	U	1.	100.0				U	1.	100.0	S	1.	100.0
MAJO	+	1.	100.0	U	1.	100.0									
RSNY										+	1.	100.0	+	1.	100.0
SCP	+	1.	100.0	U	1.	100.0				+	1.	100.0	+	1.	100.0
KEV	+	1.	100.0	U	1.	100.0									
GUMO	+	1.	100.0	U	1.	100.0				+	1.	100.0	-	1.	100.0
TATO	+	1.	100.0	U	1.	100.0				U	2.	20.0	O	3.	30.0
KONO	+	1.	100.0	U	1.	10.00	-	1.	100.0						
SHIO	+	1.	100.0	U	1.	10.0	-	1.	100.0						
ANTO	+	1.	100.0	U	1.	50.00	-	1.	100.0	+	1.	10.0	+	1.	10.0
CTAO	+	1.	10.0	U	1.	10.0				U	1.	2.00	-	3.	5.00
GAC										U	2.	3.00	+	4.	6.00
GFRO	+	1.	10.0	U	1.	5.00	-	1.	6.00	U	1.	2.00	+	3.	5.00

18 JAN 86 central Aleutian Islands

Latitude 51.57000
Longitude -173.12000

	P			pP			sP			S(N)			S(E)		
	Pol	Min	Max	Pol	Min	Max	Pol	Min	Max	Pol	Min	Max	Pol	Min	Max
ANMO	+	1.	100.0	U	1.	100.0									
JAS	+	1.	100.0	U	1.	100.0									
LON	+	1.	100.0	U	1.	100.0									
CHTO										-	60	70.0	-	90	130.0
CTAO	+	1.	100.0	U	1.	100.0				-	80	100.0	+	40	50.0
GRFO	+	1.	100.0	U	1.	100.0				-	1.	100.0	-	1.	100.0
KEV										U	1.	100.0	-	1.	100.0
KONO										-	50	70.0	-	100	130.0
TATO										-	1.	100.0	-	1.	100.0
SCP	+	1.	100.0	U	1.	100.0									
ANTO										U	50	70.0	S	90	150.0

Tectonophysics, 200 (1991) 233–248
Elsevier Science Publishers B.V., Amsterdam

Source mechanisms of recent earthquakes in the Hellenic arc from broadband data

F. Liakopoulou, R.G. Pearce and I.G. Main

Department of Geology and Geophysics, University of Edinburgh, James Clerk Maxwell Building, Mayfield Road, Edinburgh EH9 3JZ, UK

(Received March 5, 1991; revised and accepted July 5, 1991)

ABSTRACT

Liakopoulou, F., Pearce, R.G. and Main, I.G., 1991. Source mechanisms of recent earthquakes in the Hellenic arc from broadband data. *Tectonophysics*, 200: 233–248

Three-component long-period seismograms from the Global Digital Seismic Network (GDSN) are used to determine the focal mechanisms of recent large ($m_b > 5.5$) earthquakes in the Hellenic arc, using the relative amplitude method. Results are consistent with the regional stress regime obtained from other methods but they are better constrained. Broadband seismograms have been deconvolved from GDSN short-period data and preliminary modelling of the P-phases has been carried out using a two-dimensional finite dislocation model. This results in better fits to the data than earlier models using point-source trapezoids as a source-time function. The relatively shallow hypocentral depths and stress drops typical of interplate contact zones (30 bar) are consistent with previous observations. This latter contrasts with the relatively low intraplate earthquake stress drops (< 15 bar) reported for back-arc events using the same technique.

Introduction

Our aim is to study the source mechanisms of recent earthquakes from the Hellenic arc, where the African lithosphere is subducting under the Aegean lithosphere in a roughly SW–NE direction (Papazachos and Comninakis, 1971; Makropoulos and Burton, 1984; Kondopoulou, et al., 1985; Spakman, 1990; Wortel et al., 1990). Subduction has resulted in the creation of a compressional regime along the arc, whereas the back-arc region is dominated by extension. Figure 1 shows the main seismotectonic features of the area together with the fault plane solutions for earthquakes with magnitudes greater than 5.5 which occurred between 1970 and the present (Table 1). Studies of the distribution of earthquake hypocentres have shown that the African slab beneath the Aegean has a broad amphitheatre-like shape (Papazachos and Comninakis, 1971; Makropoulos and Burton, 1984; Kondopoulou et al., 1985) although most of the focal depths have not been obtained with high precision. Additional work is needed to define more accurately the types of faulting which occur in the subducting slab and in the overlying Aegean lithosphere. For a true reflection of the stress distribution in the area it is also important to determine the exact location of earthquake hypocentres, i.e. whether they lie in the Aegean lithosphere or in the underthrusting African lithosphere.

The seismicity along the Hellenic arc is confined to small- to moderate-sized, shallow- to intermediate-depth earthquakes. Although some fault plane solutions based on first-motion polarities are available (McKenzie, 1972, 1978; Ritsema, 1974; Papazachos et al., 1986), their quality is not always sufficient for accurate studies, especially when using smaller events. All the earthquakes which occurred in this region during the

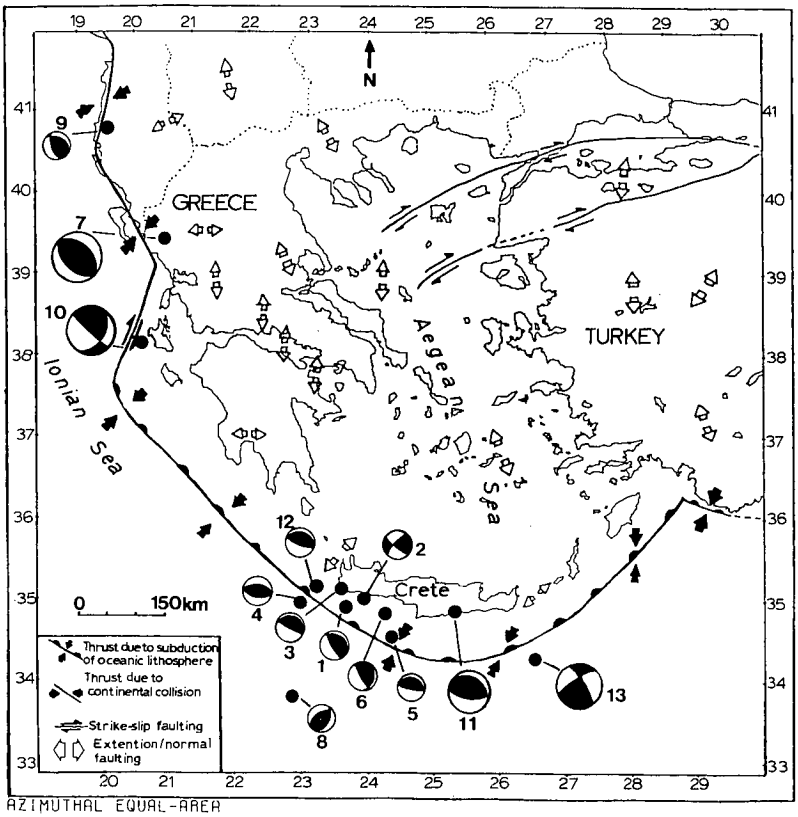

Fig. 1. Main seismotectonic features of the Hellenic arc and the Aegean sea. Earthquakes with epicentres on the arc and $m_b > 5.5$ for the time period 1970 until the present are shown numbered according to Table 1 together with fault plane solutions according to the references cited in that Table. The larger spheres (events 7, 10 and 13) represent computed results of this paper.

last 15 years had magnitudes less than 6.5. This introduces difficulties for teleseismic focal mechanism studies based solely on long-period first-motion polarities. However, the use of amplitude information in the relative amplitude method, introduced by Pearce (1977, 1980) enables the

TABLE 1

Earthquakes along the Hellenic arc with $m_b > 5.5$ for the time period between 1970 and present

Event	Date	Time	Lat (° N)	Long (° E)	m_b	Reference
1	4 May 72	21:39	35.1	23.6	5.9	1
2	29 Nov 73	10:57	35.1	23.8	5.7	2
3	18 Aug 77	9:27	35.2	23.5	5.5	2
4	11 Sep 77	23:19	34.9	23.0	5.8	2
5	15 May 79	6:59	34.6	24.5	5.5	2
6	15 Jun 79	11:34	34.9	24.2	5.5	2
7	10 Mar 81	15:16	39.3	20.7	5.6	4
8	17 Aug 82	22:22	33.7	22.9	6.0	2
9	16 Nov 82	23:41	40.8	19.6	5.5	3
10	17 Jun 83	12:41	38.1	20.2	6.2	4
11	19 Mar 83	21:41	35.0	25.3	5.7	4
12	21 Jun 84	10:43	35.3	23.3	5.8	2
13	27 Sep 85	16:39	34.4	26.5	5.6	4

Fault plane solutions from: 1: Kiratzi and Langston (1989); 2: Taymaz et al. (1990); 3: Dziewonski et al. (1983); 4: this study.

maximum source information to be extracted from the whole seismogram, even if the P-wave first motion polarity cannot be read unambigiously.

In this paper we present the source parameters for all of the earthquakes which were recorded by the GDSN between 1980–1986 and have their epicentres on the Hellenic arc; details are given in Table 2.

Data–methodology

Our data were taken from digitally recording stations of the GDSN. For the time period that GDSN data were available (1980–1986), only six earthquakes with $m_b > 5.5$ and with epicentres on the Hellenic arc were recorded by this network (Table 2). Three of those events (A, B, C) were recorded by an adequate number of stations with sufficiently high signal to noise ratio to be studied by the methods described below. The other three events (D, E, F) have either few or poorer quality recordings, so that only limited constraints can be placed on focal mechanisms and source parameters.

First, both long- and short-period three-component seismograms were used to calculate the fault plane solutions of the earthquakes by the relative amplitude method assuming a double couple source mechanism (Pearce, 1977, 1979, 1980). Where possible, additional information was obtained from long-period (LP) World Wide Standard Seismograph Network (WWSSN) records in order to improve coverage of the focal sphere. Since the events were shallow, only the polarities and amplitudes of the direct body waves (P, SH, SV) could be reliably used in the computation. The pP and sP surface reflections interfered with the direct P-waves in the case of event B and they were not identifiable for the other events.

Details of the rupture process are often suppressed in conventional narrowband representations but are obvious in broadband (BB) records which contain spectral information about the corner frequency of larger earthquakes. This matching of instrumental response to the source duration is important when considering the dynamics of the source (e.g., Choy and Boatwright, 1981, 1982; Choy and Dewey, 1988). Another advantage of using BB recordings for shallow earthquakes is that the depth phases are often better resolved than on LP records.

To obtain broadband seismograms we have divided out the instrument response of the short period records (in the frequency domain) and multiplied by the broadband (0.1–10.0 Hz) response. Figure 2 shows a short-period record and its broadband conversion. Choy and Boatwright (1981, 1982), Harvey and Choy (1982), Choy and Dewey (1988) have produced similar broadband seismograms from simultaneous deconvolution of short- and long-period data. However, Abercrombie (1991) has shown that long-period records do not contribute significantly to the conversion for events of the magnitude considered in the present work ($m_b < 6.5$). Short-period data alone, with an instrument response centred on 1s, are nevertheless sufficiently broadband to yield reliable records by the deconvolution process described above, for events of this magnitude, with duration of up to a few seconds. For example, in Fig. 3 broadband velocity waveforms for event B, pro-

TABLE 2

Published (ISC) source parameters for six earthquakes in the Hellenic arc, 1980–1986

Event	Date	Time (h:m)	Lat (°N)	Long (°E)	m_b	M_s	Depth (km)	M_0 ($\times 10^{17}$ Nm)
A	19 Mar 83	21:41	35.02	25.32	5.7	5.0	65	3.3
B	17 Jan 83	12:41	38.07	20.25	6.2	7.0	17	240.0
C	27 Sep 85	16:39	34.40	26.54	5.6	5.2	44	3.3
D	10 Mar 81	15:16	39.48	20.69	5.6	5.2	31	–
E	16 Nov 82	23:41	40.82	19.58	5.5	5.7	20	3.2
F	21 Jun 84	10:43	35.36	23.24	5.8	5.9	39	22.0

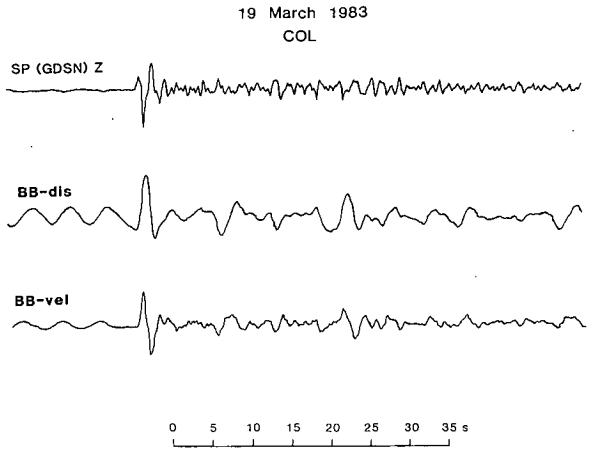

Fig. 2. An example of a short-period record (top trace) and its broadband conversions (other two traces) for the 19 Mar 83 event. The middle trace represents the broadband displacement record and the bottom trace is the broadband velocity record.

duced by deconvolving short-period records at four GDSN stations, are shown together with the broadband velocity records obtained by direct recording at the same stations. The agreement is excellent.

Consequently, body-wave modelling has been carried out to determine the source characteristics of three earthquakes with sufficient signal-to-noise ratio to justify such forward modelling. Observed BB records of displacement were then compared with synthetics generated by a source model. We used the method of Hudson (1969a,b) and Douglas et al. (1972) which considers a finite two-dimensional Savage-type source (Savage, 1966) with a homogeneous plane-layered velocity structure near the source and receiver, and an average anelastic attenuation for the whole path. The source model parameters are adjusted by trial and error until the best possible fit to the waveforms around the focal sphere is obtained.

Results

In this section we examine the results obtained from studing the earthquakes listed in Table 2.

Event A – 19 March 1983, Southern Crete

Figure 4a shows the data used to obtain the fault plane solution. Despite the fact that the reported depth (~ 60 km) is sufficient in theory to resolve surface reflections on long period records (ISC catalogues, PDE bulletins, Beisser

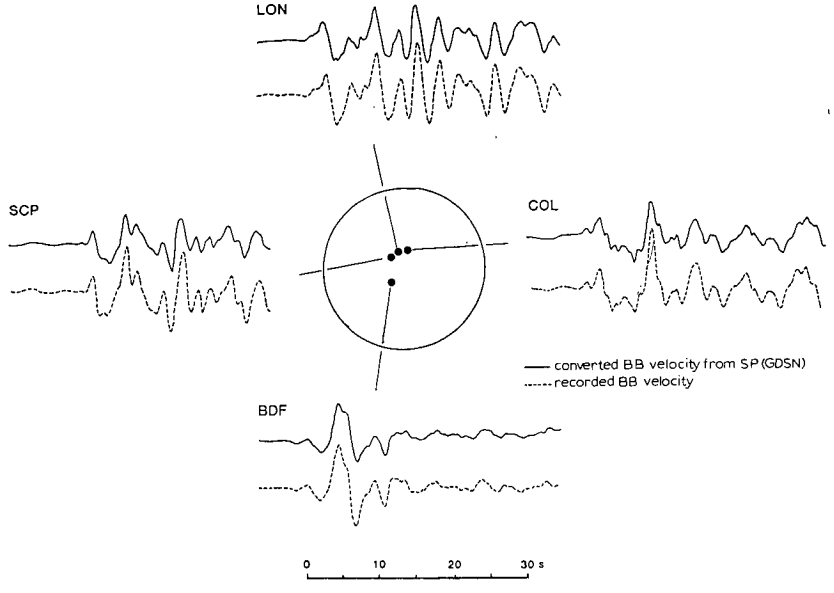

Fig. 3. Broadband velocity waveforms (converted from SP) for event B at four GDSN stations are plotted around the focal sphere (solid lines). Underneath, in dashed lines are shown the broadband velocity records as they were recorded at the same stations. The agreement is excellent.

et al., 1990), no surface reflections were detectable on the available GDSN records. Figure 4b shows the two source orientations found here to be compatible with the data displayed on a vectorplot according to the relative amplitude method. On these plots each vector represents an acceptable source orientation defined by its fault plane strike, σ, angle of dip, δ, and slip angle in the fault plane, ψ (Pearce 1977). Both the fault plane solutions show a thrust mechanism with $\sigma = 120°$, $80°$, $\delta = 150°$, $150°$ and $\psi = 70°$, $120°$ respectively. [This differs from the more common convention given in Aki and Richards (1980), in that our slip angle refers to slip of the footwall rather than the hanging wall (see Pearce, 1977)].

In Fig. 5, SP, BB and calculated synthetic BB displacement seismograms for event A are plotted about the focal sphere as solid and dashed lines respectively. The lack of depth phases at the GDSN stations KEV, LON, SCP, COL and MAJO is apparent on the SP as well as the BB records. However, this is because these stations lie close to the null vector on the upper focal hemisphere. By contrast, LP data from the WWSSN stations at LEM and BUL, which are

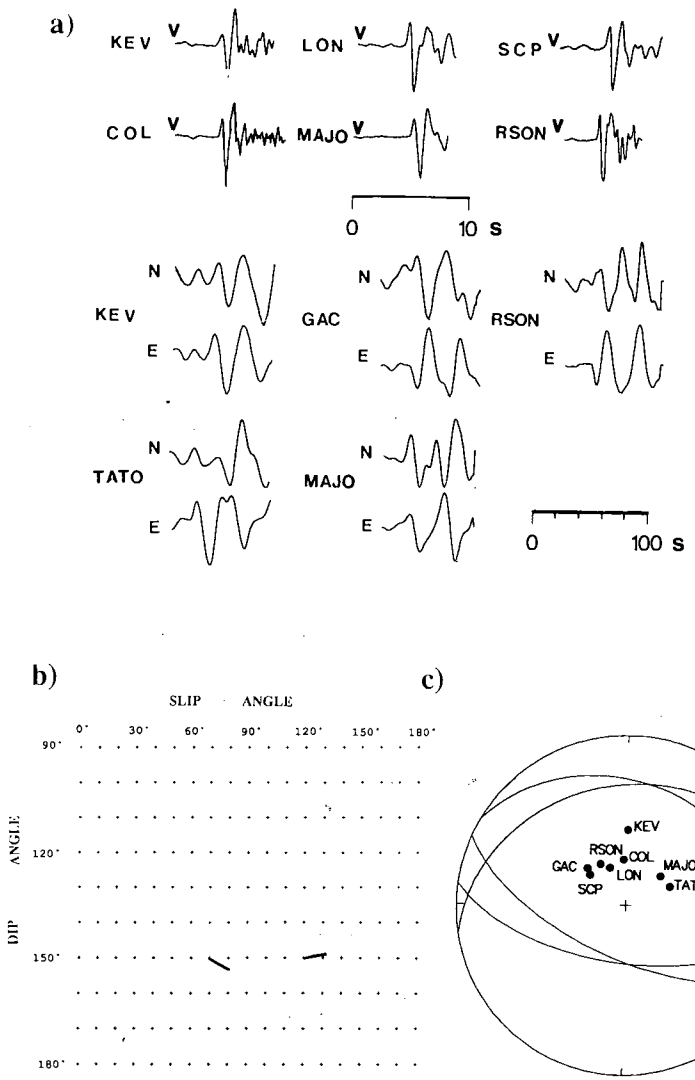

Fig. 4. (a) Data used to obtain the fault plane solution for event A. The vertical (V) components are SP GDSN P-waves and the horizontal components (N, E) are LP GDSN S-waves. (b) The two compatible solutions for the same event plotted on a vectorplot. The strike is measured clockwise from the North to the direction of the vector. The dip is measured downwards and the slip across. (c) The fault plane solutions shown in (b) now plotted on an equal area projection of the lower focal hemisphere.

well away from the null vector, display phases which can be identified as pP (consistent with a depth of approximately 65 km).

We used the fault plane solution with a strike of 120°, dip of 150° and slip angle in the fault plane of 70° to generate the synthetics as it gave the best fit to the data. The four-layer crustal model used was based on the studies of Makris (1978a,b) and Panagiotopoulos and Papazachos (1985), and is described in Table 3a. In addition, the effect of velocity structure beneath the receiver was added and an average anelastic attenuation for the path was chosen to match the dominant period of the signal. The latter parameter is defined as the travel-time in seconds divided by the average quality factor Q, and it is denoted by t^*. Here we have set $t^* = 0.6$.

A satisfactory fit is obtained for a circular fault with a radius of 2.5 km. A rupture velocity of 2.1 km s^{-1} was assumed and the average stress drop used over all the stations was 25 bar. In the Savage-type model of the source, the slip is instantaneous, so the stress drop does not relate to any time constants of the source function. In an elastic medium the stress drop is, therefore, pro-

TABLE 3

Crustal models

(a) Event A

V_p (km s^{-1})	V_s (km s^{-1})	Density (g cm^{-3})	Thickness (km)
4.0	2.1	2.2	1.5
6.1	3.4	2.8	18.0
6.5	3.6	2.9	12.0
7.7	4.7	3.3	50.0
7.8	4.8	3.4	Halfspace

(b) Event B

V_p (km s^{-1})	V_s (km s^{-1})	Density (g cm^{-3})	Thickness (km)
1.5	0.0	1.0	2.0
3.5	2.0	2.2	1.0
6.0	3.4	2.8	17.0
6.2	3.5	2.9	9.0
7.7	4.7	3.3	Halfspace

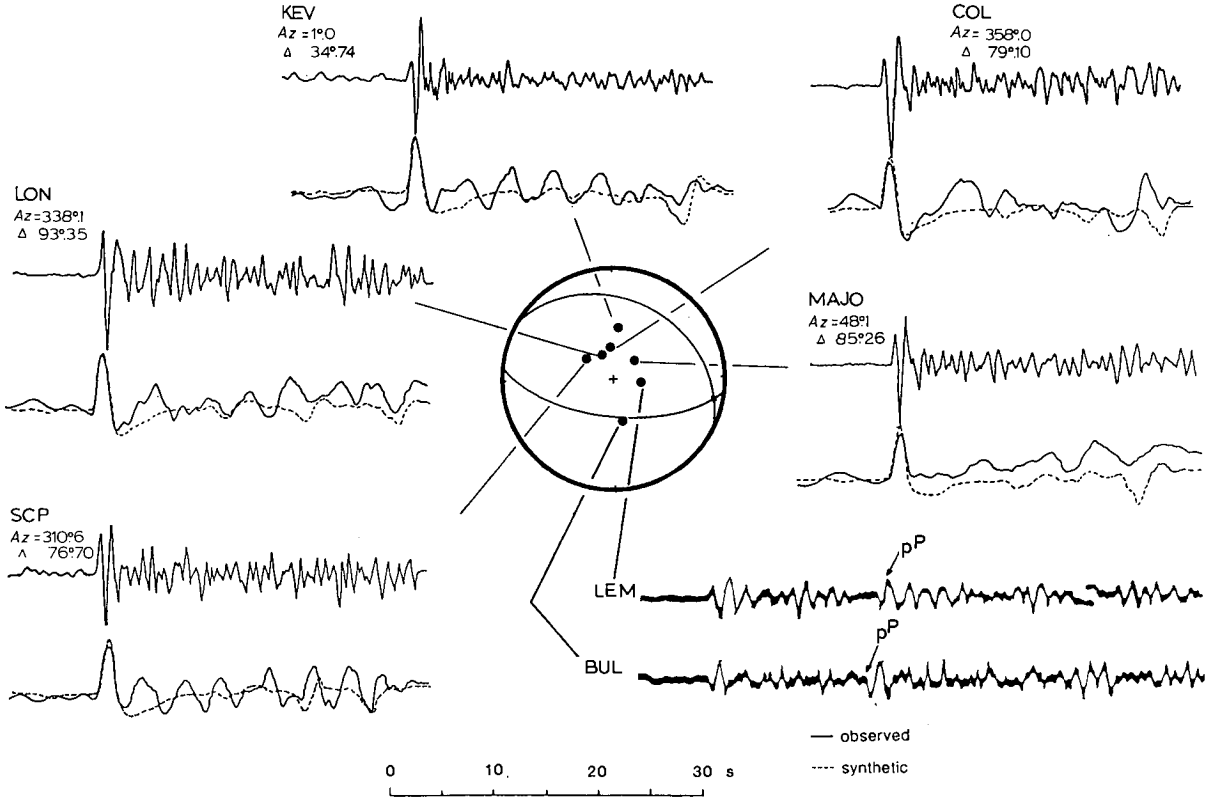

Fig. 5. P-wave displacement seismograms for event A. The GDSN SP data (top) and their BB conversion (bottom) are plotted as solid lines; the synthetic BB displacements are plotted as dashed lines. WWSSN LP data are shown for the stations LEM and BUL.

portional only to the pulse amplitude, and is independent of the pulse duration, which is controlled mainly by the fault area and rupture velocity. The stress drop is used in the modelling mainly to give an exact (peak-to-peak) amplitude fit of the main P-phases at each station. The calculated static moment was 1.5×10^{17} Nm (Table 4).

TABLE 4

Source parameters for events A and B

Event	Depth (km)	M_0 ($\times 10^{17}$ Nm)	$\Delta\sigma$ (bar)	R (km)	V_r (km s^{-1})
A	65	1.5	25	2.5	2.1
B	8	57.1	30	10.0	2.4

Event B – 17 January 1983, Ionian Islands

This event had a surface-wave magnitude of 7.0 and was well recorded by both WWSSN and GDSN stations. The large surface-wave magnitude compared to a body-wave magnitude of 6.2 is consistent with a shallow depth. To determine the fault plane solution, seismograms from sta-

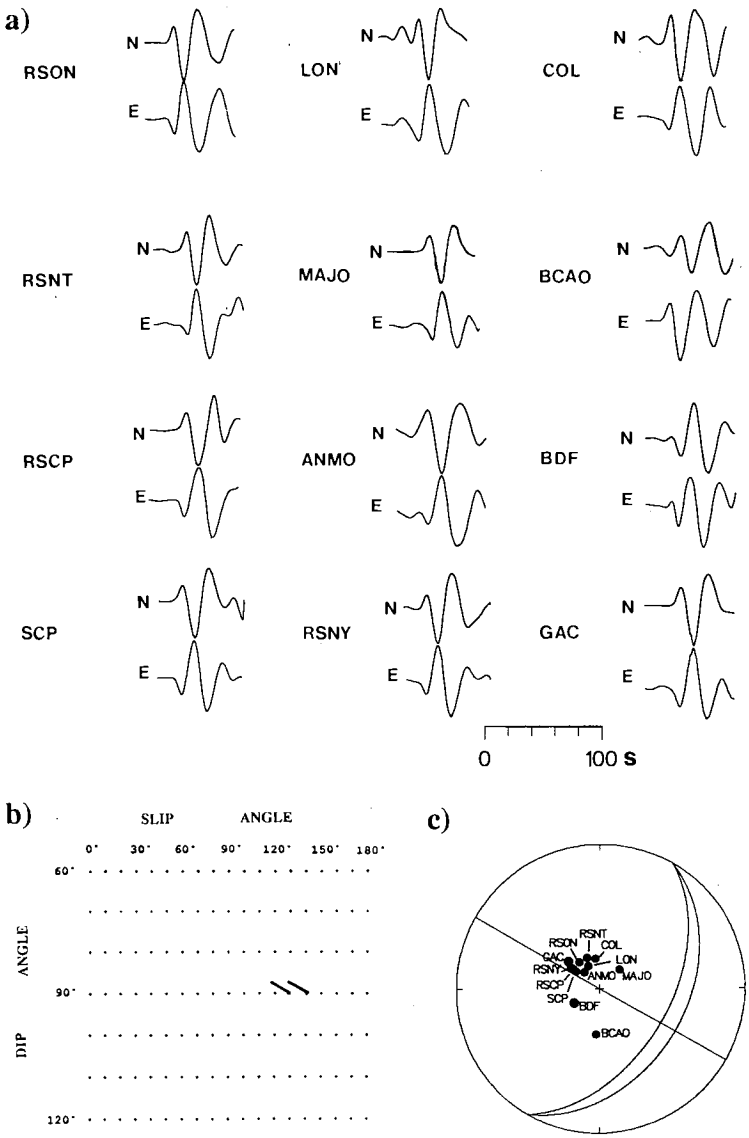

Fig. 6. (a) Part of data used to calculate the fault plane solution for event B. (b), (c) Vectorplot and focal mechanism for event B as in Fig. 4b,c.

tions of the two global seismic networks with epicentral distances in the range of 30–90° were used. The polarities of the P-, SV- and SH-waves together with their amplitudes were inserted in the calculation (Fig. 6a). The solutions which are compatible with these observations are plotted on a vectorplot (Fig. 6b). They show a near vertical dip slip thrust fault with a strike-slip component with a strike of $300 \pm 10°$, a dip of $95 \pm 5°$ and a slip angle in the fault plane of $130 \pm 10°$. A solution with $\sigma = 307.5°$, $\delta = 96.0°$ and $\psi = 130.0°$ was used in the calculation of synthetic seismograms since it produced the best match between synthetic and observed waveforms.

Plotted around the focal sphere, in Fig. 7, are the BB displacement pulses (middle solid traces), deconvolved from the GDSN SP records (top traces). Six SP GDSN stations at suitable epicentral distances have clearly recorded the event with a high signal-to-noise ratio. However, because the event is larger, its longer source signal duration yields complex waveforms on short-period records, making it impossible to identify the polarities of P-waves. This problem does not occur on the BB records where the wider frequency response, which includes the dominant signal frequency, allows a better representation of the true pulse at the source. The velocity structure model used to calculate the synthetic seismograms is given in Table 3b and it is based on the studies of Makris (1978a,b). The event is shallow, therefore the depth phases are likely to interfere. A good agreement is obtained between the synthetic (dashed lines in Fig. 3) and the observed BB pulses, assuming a circular fault with a radius of 10 km, a rupture velocity of 2.4 km s^{-1}, an attenuation correction (t^*) of 0.6 and a hypocentre depth of 8 km. The mean stress drop used was 30 bar and the calculated seismic moment was 57.0×10^{17} Nm (Table 4). These

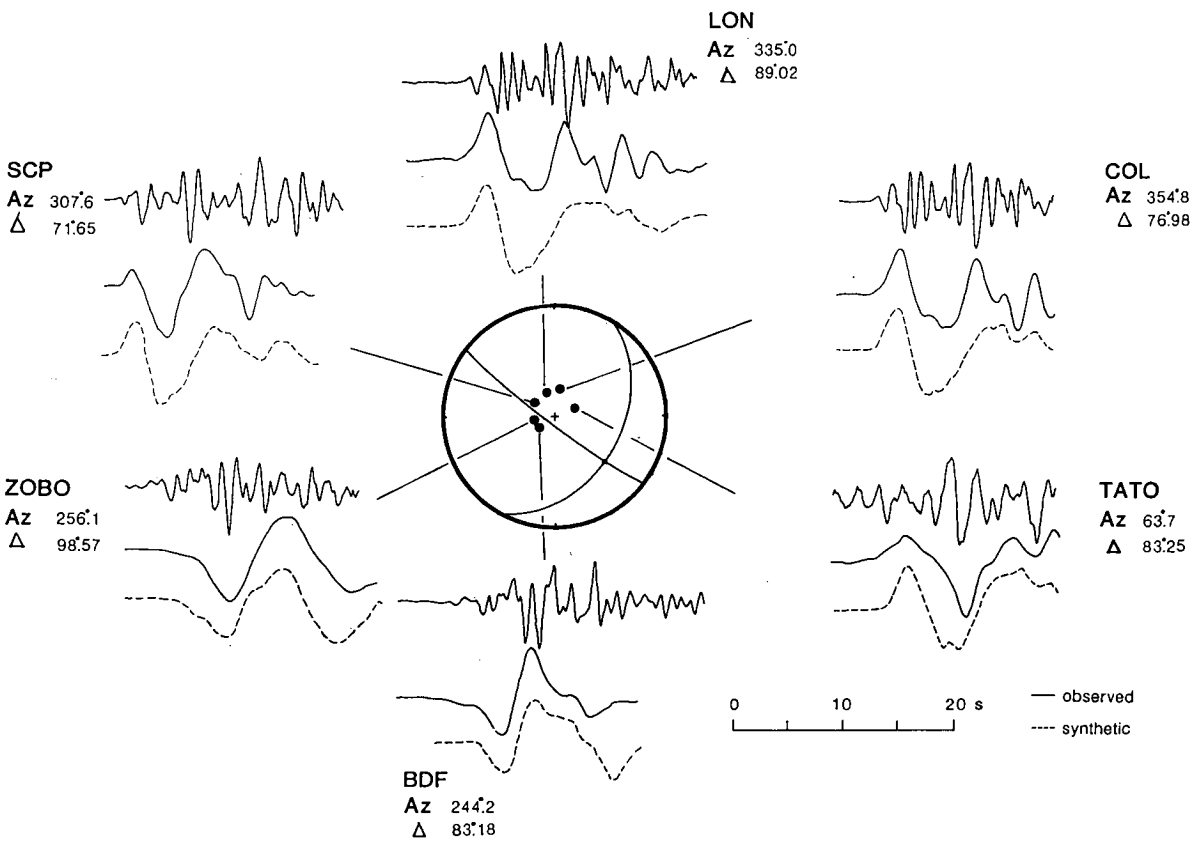

Fig. 7. GDSN SP P wave displacement seismograms (top solid lines), BB converted from SP (middle solid lines) and BB synthetics (dashed lines) are plotted about the focal sphere for event B.

values are corrected for the surface break of 12 km, which results from the difference in length between the assumed fault radius (10 km) and the estimated depth (8 km). No verification of this predicted surface break can be made at this stage, because it lies on the Ionian Sea floor.

Event C – 27 September 1985, southeast of Crete

Figure 8 shows the range of acceptable fault plane solutions using the relative amplitude method. Although only SP P-wave polarities from 5 GDSN stations were available for this event, they are able to place a strong constraint on the source orientation; this is shown schematically by the shaded areas in Fig. 8, where the solid lines represent the two nodal planes estimated by Dziewonski et al. (1986). There is a disagreement between the fault plane solutions obtained by the two methods. SP records at two GDSN stations (RSON and RSNT) have recorded the P-wave first motion as a dilatation. This is confirmed by the deconvolved BB records, where the negative

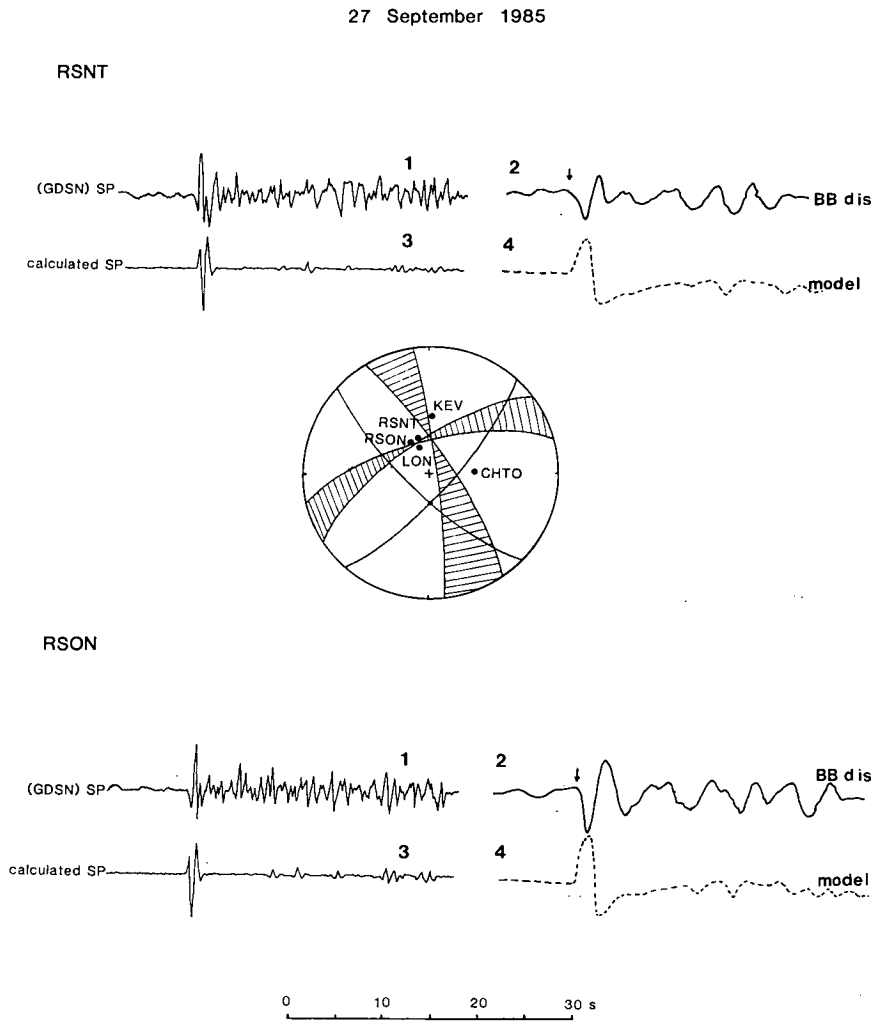

Fig. 8. Allowed fault plane solutions schematically plotted on an equal-area projection of the lower focal hemisphere, calculated using RAMP, for event C (shaded areas). On the same projection the two thicker lines represent the two nodal planes of the CMT solution for the same event. For the stations RSON (lower diagram) and RSNT (upper diagram) the following P-wave data are shown: (*1*) GDSN SP; (*2*) BB converted from SP; (*3*) synthetic SP using the CMT fault plane solution; (*4*) synthetic BB using the CMT fault plane solution.

polarities are more obvious. However, the CMT solution predicts compression at these sites, and furthermore, BB displacement synthetics computed using this solution do not show any similarity to the observed records (Fig. 8). This implies that the CMT solution is incorrect in this case.

Events D, E, F

The data used to calculate the fault plane solution of the 10 March 1981 earthquake (event D) are shown in Fig. 9, together with the vectorplot showing the range of solutions compatible

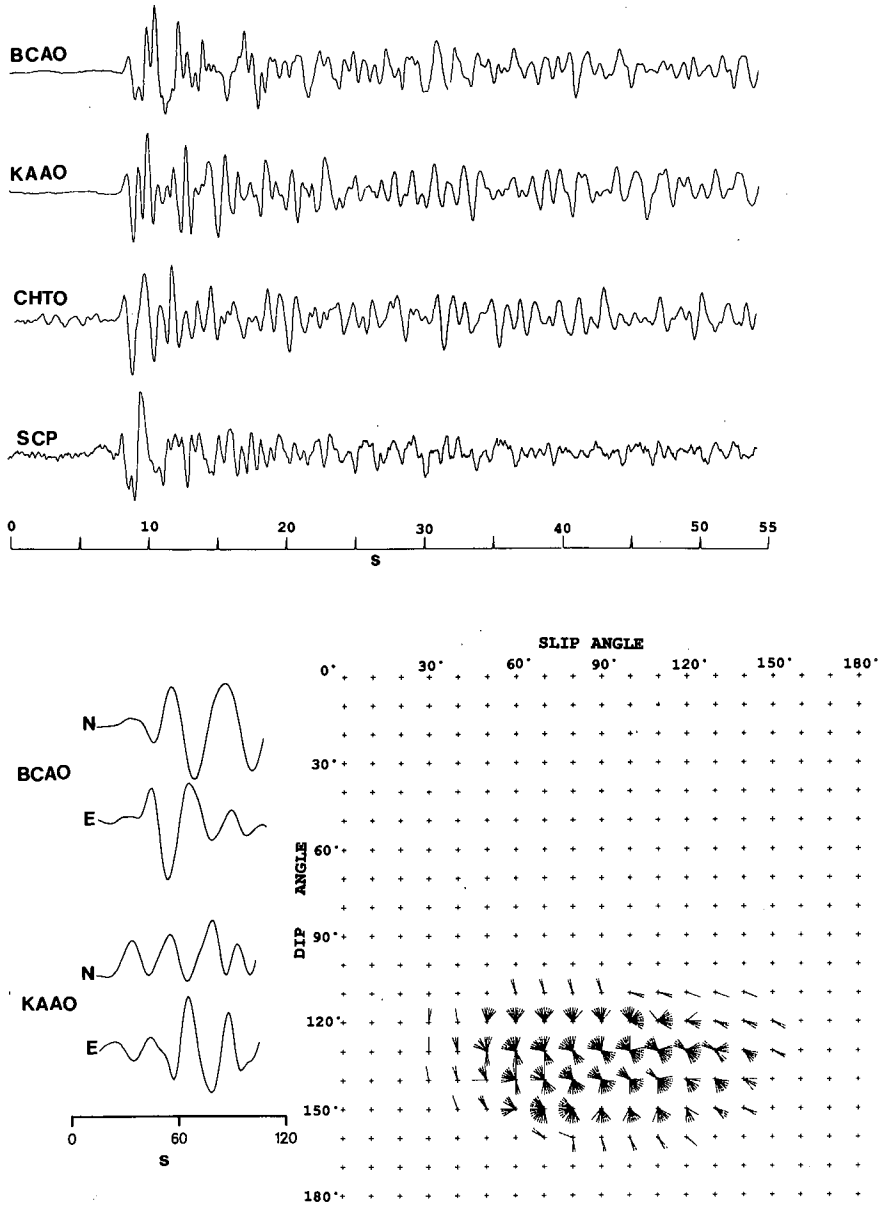

Fig. 9. Data used to calculate the fault plane solution of event D. The four top traces represent the available GDSN SP seismograms. The horizontal components (*N*, *E*) are GDSN LP S-wave seismograms. The compatible solutions obtained for this event are shown on the vectorplot.

with these data. The constraints on the fault plane cannot be characterized as tight, but they do indicate a thrust mechanism. The four top traces of Fig. 9 show the GDSN SP seismograms from the stations BCAO, KAAO, CHTO and SCP for event D (10 March 1981, NW Greece). Although the records show sufficient signal-to-noise ratio, their complexity does not allow for unambiguous body-wave modelling of the source function.

Similarly, Fig. 10 presents the LP S-wave seismograms (lower traces) used to calculate the fault plane solution for the earthquake of 16 November 1982 (Albania). The solutions obtained are shown on a vectorplot. One of the solutions suggests pure strike slip mechanism, and the other two include a dip-slip component. SP records from three stations (BCAO, SCP, COL) are available for this earthquake. These are shown in the top half of Fig. 10. Because the SP records

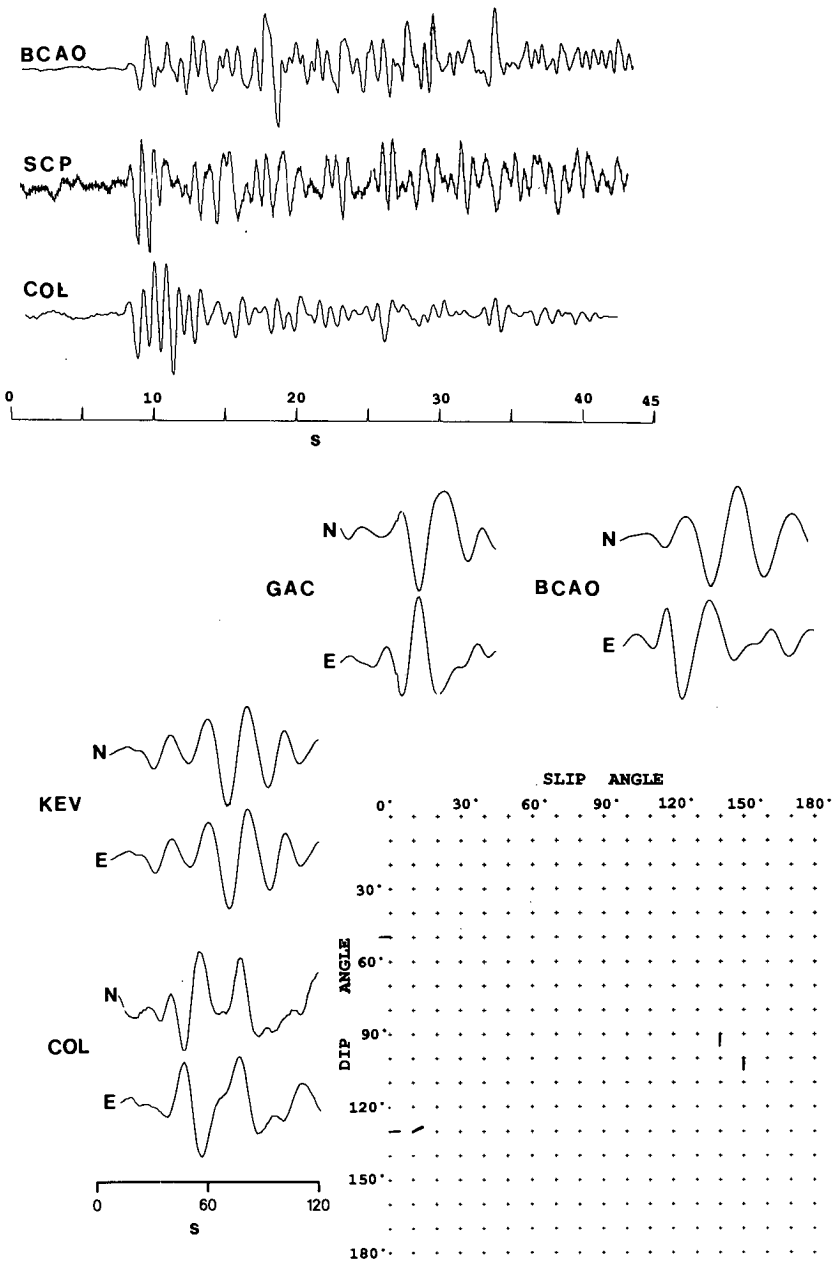

Fig. 10. As Fig. 9, for event E.

are few and have a low signal-to-noise ratio, body-wave modelling has not been attempted for this event.

Finally, the earthquake of the 21st June 1984 (west of Crete, event F) is examined. LP S-wave polarities, and relative polarities, from six GDSN stations were the input data for the fault plane solution calculation (Fig. 11). The allowable solutions occupy a large fraction of the total vectorplot area (same figure), due to limited data. However, most of the solutions lie in the area of low angle thrust mechanisms, suggesting that such a mechanism is more probable for this event. This earthquake was recorded by 10 GDSN stations at epicentral distances 30–90°. Figure 12 shows the SP seismograms recorded at three GDSN stations (LON, MAJO, CHTO) and their BB conversions, both displacement and velocity. The positive onset of the P-waves is apparent on the BB records, although on the BB velocity record small precusors seem to precede the main event. This is observed at all stations. Furthermore, the complexity of the seismograms, both SP and BB, do not allow any clear identification of surface re-

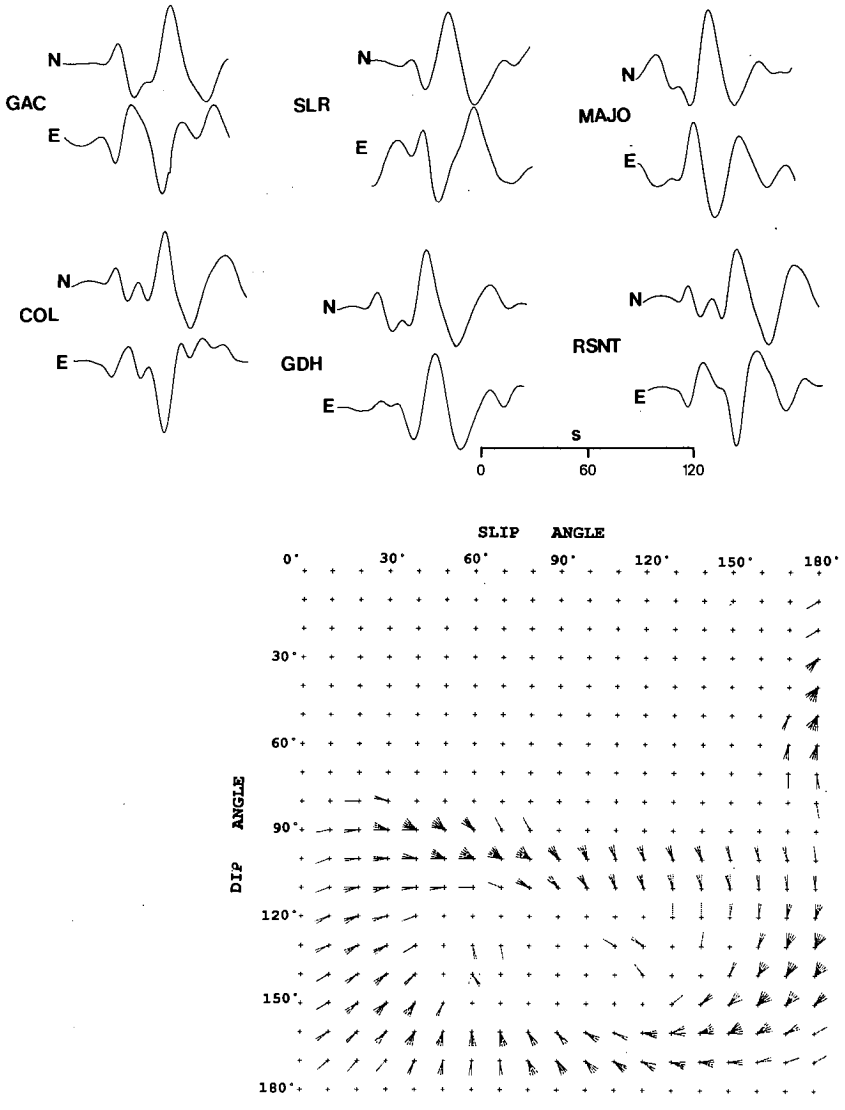

Fig. 11. LP S-wave seismograms (horizontal components) from six GDSN stations used to calculate the fault plane solution of event F. The vectorplot with the three acceptable solutions is shown at the bottom-right part of the figure.

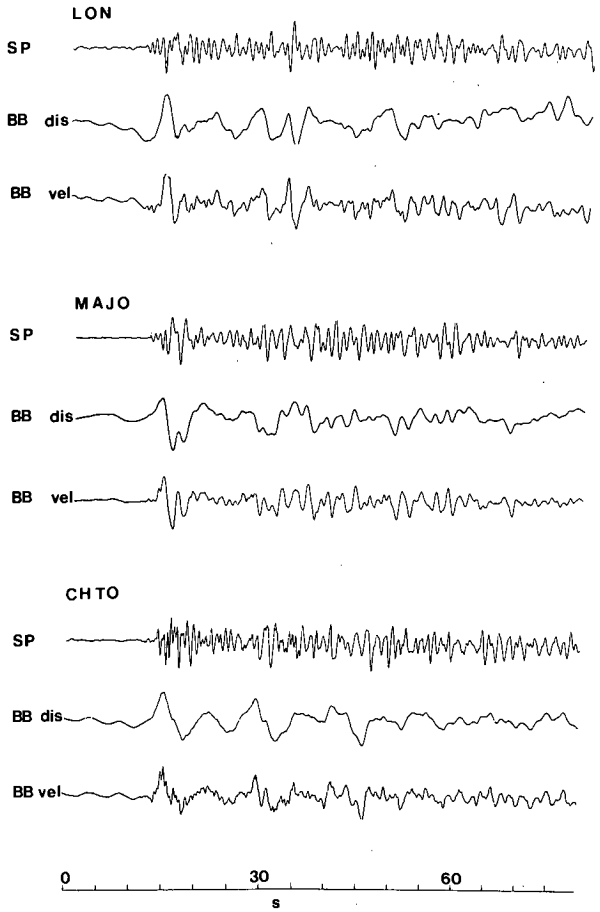

Fig. 12. SP seismograms for event F (top trace), recorded at three GDSN stations and their broadband conversion. The middle trace represents the broadband displacement record and the bottom trace is the broadband velocity record.

flections, so that body-wave modelling has so far proved to be impossible.

Discussion

For moderate-sized earthquakes it is essential to model the seismic source using broadband data, so that the frequency range where most of the energy is contained is included in the band-pass, if detailed rupture characteristics are to be determined. It has been demonstrated that short-period digital records with a sufficient signal-to-noise ratio can be converted to give broadband seismograms that are in exellent agreement with recordings (Douglas et al., 1990; Abercrombie, 1991), and this has been confirmed in the present study (Fig. 3).

We compare now the fault plane solutions obtained using the relative amplitude method with those calculated by other studies. For event A, which has a thrust mechanism, the solutions determined using the centroid (CMT) method (Dziewonski et al., 1983), the inversion of WWSSN LP P- and SH-waves (Taymaz et al., 1990), and the method of one-station inversion (Beisser et al., 1990) are similar with regard to the type of mechanism but they differ in the strike of the two nodal planes.

Our solution for event B, an almost vertical dip-slip fault with a strike-slip component, is compared with the CMT solution (Dziewonski et al., 1983), which gives dip-slip with a very small strike-slip component, and with the solution obtained using first-motion polarities read from WWSSN seismograms (Anderson and Jackson, 1987), which gives almost pure dip-slip. Scordilis et al. (1985) have found a fault plane solution for this event using first motion polarities from a local network, which gives a strike-slip fault with a thrust component. They support the idea for the existence of a similar fault west of the Ionian Islands which strikes in an about NE–SW direction and dips to the southeast. McKenzie (1978) proposes that the deformation of northwestern Greece is taken up by a number of right-lateral strike-slip faults which connect the deformation of northwestern Greece to the Hellenic arc. Dewey and Sengör (1979) believe in the existence of a right lateral transform fault between Cephalonia and Zakynthos because of the northward termination of the Hellenic arc and an offset in seismicity. However, Kissel and Laj (1988) believe that the geographical extension of the arc has been underestimated by different models (e.g., LePichon and Angelier, 1979) since paleomagnetic evidence from Corfu and Epirus, more to the north, show that they have undergone significant rotation.

For event C, although only first motions from a small number of stations were used, the range of acceptable solutions is well defined and occupies a small fraction of the whole orientation space. There is a significant difference between

our solution and the CMT solution in that both nodal planes dip in the opposite sense. This highlights an advantage in the accuracy of the relative amplitude method over the CMT method when targeting specific suitable events.

The fault plane solutions for events D, E, and F, are not well constrained. Therefore, a comparison between them and those published by others is not attempted here. Nevertheless, all are consistent with thrust mechanisms so that generally they agree with the compressional stress regime of the area.

The synthetic seismograms obtained are highly sensitive to variations in the modelling parameters (Abercrombie, 1991). The focal depth, the source region seismic wave velocities, the layer thicknesses and densities can all be perturbed from their initial values in order to maximize the waveform match between theoretical and observed seismograms by trial and error. Errors due to insensitivity of the model are tiny compared to other sources of error, e.g., radiation pattern and site and path effects.

We acknowledge that a flat, multi-layered crustal structure is not a realistic approximation for velocity structures near plate boundaries and it may not be appropriate for all recording stations. However, no systematic effects were observed on the expected dissimilarities between observed and synthetic seismograms.

The stress drops used (around 30 bar) are typical for interplate earthquakes (Kanamori and Anderson, 1975). This compares with relatively low intraplate stress drops of ~ 15 bar reported for shallow earthquakes in the Aegean back-arc by Abercrombie (1991), using the same technique. Seismic moments were found to be systematically lower than those estimated by others (Dziewonski et al., 1983). Kiratzi et al. (1985), Tselentis et al. (1988) and Main and Burton (1990) have produced relations between surface wave magnitude (M_s) and seismic moment for earthquakes from the whole Aegean area. In all cases our scalar moments are towards the lower limits of their calculations. This is probably due to the differences in frequencies of the waves used by the other methods. The CMT method uses very long period waves and Main and Burton (1990) have used surface waves with a period range of 30–50 s. Kiratzi et al. (1985) and Tselentis et al. (1988) have used published moments which have been calculated using surface waves. Many recent studies comparing moment as a function of bandwidth (e.g., Silver and Jordan, 1983; Boatwright and Choy, 1986), have found that moment is a frequency-dependent quantity; it generally increases with increasing period. Moments obtained from long-period body waves (Christensen and Ruff, 1986), and very long-period Rayleigh waves (Monfret and Romanowicz, 1986), progressively increase in size. Variations in frequency dependent moment far exceeding a factor of 4 have been observed by Silver and Jordan (1983) in the frequency range 1.0–10.0 mHz for great earthquakes. Therefore, the discrepancy between moments obtained here, using intermediate-period body waves, and those using longer-period waves is consistent with the conclusions of those studies.

Conclusions

Broadband seismograms deconvolved from GDSN short-period data are in excellent agreement with directly recorded broadband seismograms. Therefore, the method of obtaining displacement broadband seismograms from SP records is valid for moderate-sized earthquakes ($m_b < 6.5$). Forward modelling using BB data yields important information about the earthquake source for teleseismically recorded events. The source parameters for the events studied here are comparable with those determined by other workers. This work also demonstrates that the relative amplitude method places relatively tight constraints on fault plane solutions, even in cases where only a limited number of seismograms are available. Finally, this study highlights the importance of analysing earthquakes individually in order to gain information about the seismotectonic stress regime of a specific area.

Acknowledgement

This work was supported by a grant from the State Scholarship Foundation of Greece (F.L.).

References

Abercrombie, R.E., 1991. Earthquake rupture dynamics and neotectonics in the Aegean area. Ph. D. thesis, University of Reading, U.K.

Aki, K. and Richards, P.G., 1980. Quantitative Seismology: Theory and Methods (2 vols.). W.H. Freeman, San Francisco, CA.

Anderson, H. and Jackson, J., 1987. Active tectonics of the Adriatic Region. Geophys. J.R. Astron. Soc., 91: 937–983.

Beisser, M., Wyss, M. and Kind, R., 1990. Inversion of source parameters for subcrustal earthquakes in the Hellenic Arc. Geophys. J. Int., 103: 439–450.

Boatwright, J. and Choy, G.L., 1986. Teleseismic estimates of the energy radiated by shallow earthquakes. J. Geophys. Res., 91: 2095–2112.

Choy, G.L. and Boatwright, J., 1981. The rupture characteristics of two deep earthquakes inferred from broadband GDSN data. Bull. Seismol. Soc. Am., 71: 691–711.

Choy, G.L. and Boatwright, J., 1982. Broadband analysis of the extended foreshock sequence of the Miyiaki-Oki earthquake June 12, 1978. Bull. Seismol. Soc. Am., 72: 2017–2036.

Choy, G.L. and Dewey, J.W., 1988. Rupture process of an extended earthquake sequence: teleseismic analysis of the Chilean earthquake of March 3, 1985. J. Geophys. Res., 93: 1103–1118.

Christensen, D.H. and Ruff, L.J., 1986. Rupture process of the March 3, 1985 Chilean earthquake. Geophys. Res. Lett., 13: 721–724.

Dewey, J.F. and Sengör, A.M., 1979. Aegean and surrounding regions: Complex multiplate and continuum tectonics in a convergent zone. Geol. Soc. Am. Bull., 90: 84–92.

Douglas, A., Hudson, J.A. and Blamey, C., 1972. A quantitative evaluation of seismic signals at teleseismic distances—III. Computed P and Rayleigh wave seismograms. Geophys. J.R. Astron. Soc., 28: 385–410.

Douglas, A., Richardson, L. and Hutchins, M., 1990. Surface reflections and S-to-P conversions on P seismograms. Geophys. J. Int., 100: 303–314.

Dziewonski, A.M., Friedman, A. and Woodhouse, J.H., 1983. Centroid-moment tensor solutions for January-March, 1983. Phys. Earth Planet. Inter., 33: 71–75.

Dziewonski, A.M., Franzen, J.E. and Woodhouse, J.H., 1986. Centroid-moment tensor solutions for July–September 1985. Phys. Earth Planet. Inter., 45: 205–214.

Harvey, D. and Choy, G.L., 1982. Broadband deconvolution of GDSN data. Geophys. J.R. Astron. Soc., 69: 659–66.

Hudson, J.A., 1969a. A quantitative evaluation of seismic signals at teleseismic distances—I. Radiation from point sources. Geophys. J.R. Astron. Soc., 18: 233–249.

Hudson, J.A., 1969b. A quantitative evaluation of seismic signals at teleseismic distances—II. Body waves and surface waves from an extended source. Geophys. J.R. Astron. Soc., 18: 353–370.

Kanamori, H. and Anderson, D.L., 1975. Theoretical basis of some empirical relations in Seismology. Bull. Seismol. Soc. Am., 65: 1073–1095.

Kiratzei, A.A. and Langston, C.A., 1989. Estimation of earthquake source parameters of the May 4, 1972 event of the Hellenic arc by the inversion of waveform data. Phys. Earth Planet. Inter., 57: 225–232.

Kiratzi, A.A., Karakaisis, G.F., Papadimitriou, E.E. and Papazachos, B.C., 1985. Seismic source-parameter relations for earthquakes in Greece. Pure Appl. Geophys., 123: 27–41.

Kissel, C. and Laj C., 1988. The Tertiary geodynamical evolution of the Aegean arc: a paleomagnetic reconstruction. Tectonophysics, 146: 183–201.

Kondopoulou, D.P., Papadopoulos, G.A. and Pavlides, S.B., 1985. A study of deep seismotectonics in the Hellenic arc. Bol. Geofis. Teor. Appl., 27: 197–207.

Le Pichon, X. and Angelier, J., 1979. The Hellenic arc and trench system: a key to the neotectonic evolution of the eastern Mediterranean area. Tectonophysics, 60: 1–42.

Main, I.G. and Burton, P.W., 1990. Moment-magnitude scaling in the Agean area. Tectonophysics, 179: 273–285.

Makris, J., 1978a. Some geophysical considerations of the geodynamic situation in Greece. Tectonophysics, 46: 251–268.

Makris, J., 1978b. The crust and upper mantle of the Aegean region from deep seismic soundings. Tectonophysics, 46: 269–284.

Makropoulos, K.C. and Burton, P.W., 1984. Greek tectonics and seismicity. Tectonophysics, 106: 275–304.

McKenzie, D.P., 1972. Active tectonics of the Mediterranean region. Geophys. J.R. Astron. Soc., 30: 109–185.

McKenzie, D.P., 1978. Active tectonics of the Alpine-Himalayan belt: the Aegean Sea and surrounding regions. Geophys. J.R. Astron. Soc., 55: 217–254.

Monfret, T. and Romanowicz, B., 1986. Importance of on scale observations of first arriving Rayleigh wave trains for source studies: Example of the Chilean event of March 3, 1985, observed in the Geoscope and IDA networks. Geophys. Res. Lett., 13: 1015–1018.

Panagiotopoulos, D.G. and Papazachos, B.C., 1985. Travel times of P_n waves in the Aegean and surrounding area. Geophys. J.R. Astron. Soc., 80: 165–176.

Papazachos, B.C. and Comninakis, P.E., 1971. Geophysical and tectonic features in the Aegean arc. J. Geophys. Res., 76: 8517–8533.

Papazachos, B.C., Kiratzi, A., Hatzidimitriou, P. and Karacostas, B., 1986. Seismotectonic properties of the Aegean area that restrict valid Geodynamic models. Wegener/Medlas Conf. Athens, May 14–16, 1986, pp. 1–20.

Pearce, R.G., 1977. Fault plane solutions using relative amplitudes of P and pP. Geophys. J.R. Astron. Soc., 50: 381–394.

Pearce, R.G., 1979. Earthquake focal mechanisms from relative amplitudes of P, pP, sP: method and computer program. AWRE Rep. No. O41/79, HMSO publication, London, England.

Pearce, R.G., 1980. Fault plane solutions using relative amplitudes of P and surface reflections: further studies. Geophys. J.R. Astron. Soc., 60: 459–487.

Ritsema, A.R., 1974. The earthquake mechanisms of the Balkan region. Sci. Rep. R. Neth. Meteorol. Inst. De Bilt, 74-4: 1–36.

Savage, J.C., 1966. Radiation from a realistic model of faulting. Bull. Seismol. Soc. Am., 56: 577–592.

Scordilis, E.M., Karakaisis, B.G., Panagiotopoulos, D.G., Comninakis, P.E. and Papazachos, B.C., 1985. Evidence for transform faulting in the Ionian Sea: The Cephalonia island earthquake sequence of 1983. Pure Appl. Geophys., 123: 388–397.

Silver, P.G. and Jordan, T.H., 1983. Total-Moment spectra of fourteen large earthquakes. J. Geophys. Res., 88: 3273–3293.

Spakman, W., 1990. Tomographic images of the upper mantle below central Europe and the Mediterranean. Terra Nova, 2: 542–553.

Taymaz, T., Jackson, J. and Westaway, R., 1990. Earthquake mechanisms in the Hellenic Trench near Crete. Geophys. J. Int., 102: 695–731.

Tselentis, G.A., Stavrakakis, G., Makropoulos, K., Latousakis, J. and Drakopoulos, J., 1988. Seismic moments of earthquakes at the western Hellenic arc and their application to the seismic hazard of the area. Tectonophysics, 148: 73–82.

Wortel, M.J.R., Goes, S.D.B. and Spakman, W., 1990. Structure and seismicity of the Aegean subduction zone. Terra Nova, 2: 554–562.